THE OPTIMIZATION OF MULTIPLE ANTENNA BROADBAND WIRELESS COMMUNICATIONS

Y.A.S Dia'meh

Ph.D.

2013

THE OPTIMIZATION OF MULTIPLE ANTENNA BROADBAND WIRELESS COMMUNICATIONS

A study of propagation, space-time coding and spatial envelope correlation in Multiple Input, Multiple Output radio systems

Yousef Ali Dia'meh

B.Eng., M.Sc.

Submitted for the Degree of

Doctor of Philosophy

School of Engineering, Design and Technology

University of Bradford

2013

Abstract

THE OPTIMIZATION OF MULTIPLE ANTENNA BROADBAND WIRELESS COMMUNICATIONS

A study of propagation, space-time coding and spatial envelope correlation in Multiple Input, Multiple Output radio systems

Keywords

Multiple Output Multiple Input (MIMO) ; Orthogonal Frequency-Division Multiplexing (OFDM); Space Time Block Coding (STBC); Diversity; Spatial Envelope Correlation; Indoor Channel Propagation; IEEE 802.11n, WiMAX

This work concentrates on the application of diversity techniques and space time block coding for future mobile wireless communications.

The initial system analysis employs a space-time coded OFDM transmitter over a multipath Rayleigh channel, and a receiver which uses a selection combining diversity technique. The performance of this combined scenario is characterised in terms of the bit error rate and throughput. A novel four element QOSTBC scheme is introduced, it is created by reforming the detection matrix of the original QOSTBC scheme, for which an orthogonal channel matrix is derived. This results in a computationally less complex linear decoding scheme as compared with the original QOSTBC. Space time coding schemes for three, four and eight transmitters were also derived using a Hadamard matrix.

The practical optimization of multi-antenna networks is studied for realistic indoor and mixed propagation scenarios. The starting point is a detailed analysis of the throughput and field strength distributions for a commercial dual band 802.11n MIMO radio operating indoors in a variety of line of sight and non-line of sight scenarios. The physical model of the space is based on architectural schematics, and realistic propagation data for the construction materials. The modelling is then extended and generalized to a multi-storey indoor environment, and a large mixed site for indoor and outdoor channels based on the Bradford University campus.

The implications for the physical layer are also explored through the specification of antenna envelope correlation coefficients. Initially this is for an antenna module configuration with two independent antennas in close proximity. An operational method is proposed using the scattering parameters of the system and which incorporates the intrinsic power losses of the radiating elements. The method is extended to estimate the envelope correlation coefficient for any two elements in a general (N,N) MIMO antenna array. Three examples are presented to validate this technique, and very close agreement is shown to exist between this method and the full electromagnetic analysis using the far field antenna radiation patterns.

Table of Contents

Acknowledgment

I would like to express my deepest appreciation and thankful to my supervisors, **Prof. Raed A. Abd-Alhameed** and **Dr. Steve Jones**. I am most grateful to them for advice, assistance, support and their continuous encouragement during the difficult times, sharing with me the exciting times and for being consistently supportive throughout this work. I will never forget the many opportunities that they gave me in facilities, publications, teaching and travel during the years of my PhD study.

I would like also express my special thanks to Mr. Mark Child for his continuous help and kindness through the time of this research work. My appreciation is also to extend to Dr N. J. McEwan, Mr. Fernando Salazar-Quiñonez, Dr. D. Zhou and Dr. C. H. See for their generous assistances.

My thanks are also extended to all the other people in the antenna and electromagnetic research group; Dr. T. Sadeghpour , I.E.T. Elfergani, H. Hragh and Dr. M. M. Musa.

Last but by no means least; I convey my warmest thanks to my parents, brothers and sisters for their endless support throughout my life and for providing me the chance to reach this far with my studies.

Acronyms

AMC	Adaptive Modulation and Coding
AWGN	Additive white Gaussian noise
BPF	Bandpass Filter
BER	Bit error rate
CSI	Channel state information
CCI	Co-channel interference
CP	Cyclic prefix
DMLD	Diagonalized maximum likelihood detector
DZFD	Diagonalized zero forcing detector
DWT	Discrete Wavelet transform
EGC	Equal gain combining
EVCM	Equivalent virtual channel matrix
FFT	Fast Fourier transform
FDTD	Finite Difference Time Domain
FEM	Finite Element Method
FIT	Finite Integration Technique
4G	Fourth Generation

FDMA	Frequency Division Multiple Access
FDM	Frequency division multiplexing
HPF	High pass filter
ICI	Inter carrier interference
ISI	Inter symbol interference
IFFT	Inverse Fast Fourier transform
LTE	Long Term Evolution
LPF	Low pass filter
MRC	Maximal ratio combining
ML	Maximum likelihood
MCM	Multicarrier modulation
MIMO	Multiple input multiple output
N-LOS	None line of sight
OFDM	Orthogonal frequency division multiplexing
OSTBC	Orthogonal space time block code
PR	Perfect reconstruction
PIFA	Planar Inverted F-antennas
QAM	Quadrature Amplitude Modulation
QOSTBC	Quasi orthogonal space time block code

SC	Selection combining
SBR	Shoot and Bounce Ray
SNR	Signal to noise ratio
SISO	Single input single output
SVD	Singular value decomposition
STBC	Space time block code
STTC	Space time trellis code
ρ_e	Spatial envelope correlation
STC	Space time coding
SIC	Successive interference cancellation
TDMA	Time Division Multiple Access

List of Tables

List of Figures

CHAPTER 1

Introduction

1.1 Introduction

The demand for new telecommunications services such as video calls, multimedia applications, high speed internet access and other high-speed applications drives the search for improved technologies. 4G technologies such as WiMAX and LTE (Long Term Evolution) require high data rates to provide an appropriate quality of service to the end users, therefore wireless communications has to be pushed to the physical limits of the radio channel. The channel capacity or the data rate is limited by the bandwidth and the transmission power. The upper bound of the maximum achievable data rate for the ideal Additive White Gaussian Noise (AWGN) channel is the Shannon Nyquist criterion [1-2]. Assuming the available bandwidth is w and signal to noise ratio SNR, then the maximum transmit data rate is:

$$C = w\log_2(1+SNR) \quad \text{bits/s} \qquad (1)$$

From equation (1), the channel capacity or data rate can only be increased by increasing the bandwidth or transmission power, but it is expensive to increase the spectrum usage and increasing signal power is unhelpful in interference limited systems, and undesirable for power-limited applications involving battery-powered terminals, and also from a safety and sustainability point of view.

Introducing an antenna array at both transmitter and receiver can increase the channel capacity linearly with the number of the antennas under certain conditions; this system

with multiple antennas at the both ends is referred to as MIMO (Multiple-Input Multiple-Output). The idea of improving the capacity of multiple-antenna fading channels using an antenna array at both ends was first proposed by Winters in 1987 [3]. However, ten years later these system were re-invented by Foschini and Gans [4,5], and Telatar [6]. Since then, a great effort has been directed towards research and development of MIMO systems.

Recently there has been a large interest in using multiple antennas in wireless systems commonly known as MIMO system where multiple antennas at the transmitter and the receiver are used [7].

In [8] it was shown that the capacity of a MIMO system increases linearly with the number of transmit and/or the receive antennas under the assumption that the number of transmit and receive antennas are identical.

4G systems employ Multiple Input Multiple Output (MIMO) with Orthogonal Frequency Division Multiplexing (OFDM). Like other 4G systems, Long Term Evolution (LTE) also employs a MIMO-OFDM air interface. MIMO increases the throughput and OFDM converts the frequency selective fading channel to multiple flat-fading sub-channels which facilitate equalization. In high data rate systems, OFDM has the advantage over single-carrier systems that it mitigates the effect of inter symbol interference (ISI) caused by delay spread.

Over the last ten years, wireless communications systems have been experiencing an increasing demand for higher data rates, wider network capacity and a better quality of

service from fixed wireless and mobile solutions. Traditionally, wireless communications were designed for voice transmission with moderate data rates, while nowadays wireless equipment is required to provide high data rate applications such as video streaming or file transfer. The real challenge for these systems is to achieve a reliable connection to fulfil all these requirements, operating in a limited radio frequency spectrum and considering the complex space-time varying wireless environments [9].

MIMO systems achieve a higher spectral efficiency, making use of diversity techniques [10-12] to counteract fading. The effectiveness of these characteristics will be the driving force for the next generation in telecommunications systems.

As with many other modern wireless systems, in order to achieve a reliable communication performance in specific environments, MIMO requires a propagation channel model. This enables studies to validate the behaviour of wireless equipment in real world applications. This propagation models can be organized in two general groups: analytical and deterministic (site–specific) models.

Deterministic models are tending to replace the analytic or statistical models, since those techniques are inaccurate for small cell sizes and generally not applicable for spatial channel characterisations [13].

In the telecommunications field, methodologies, models and even measurement procedures are being designed in order to facilitate accurate channel modelling of real world wireless systems. The incorporation of computing systems technology into a detailed deterministic or site specific model has been one of the most important fusions

over the last century for planning tools. Software tools that run over simulated channel models in realistic designed environments predict how and where the wireless equipment will be able to achieve the higher performance.

The three dimensional (3D), deterministic, shoot and bounce ray-tracing model (SBR) is one of the most promising techniques utilised for propagation modelling [14], since low computational effort is required for a conventional PC to perform the analysis. Although requiring significantly greater processing time, with current advances in processing speeds and available memory, it is also become increasingly feasible to make use of some numerical Maxwell equation methods like finite-difference time-domain (FDTD), finite integration technique (FIT) or finite element method (FEM) [15-17] to perform simulations in order to achieve an accurate representation of the channel propagation for a specific environment.

Many methods and techniques have been successfully applied in the research field to model a propagation channel, but not all of them reproduce all attributes of the real channel which are required to accurately predict the performance of complex broadband systems exploiting both time, frequency and spatial decorrelation.

Some previous research like that presented in [15], demonstrate the importance of using the comparison of path loss measurements with simulation using FIT as a propagation solving method, obtaining accurate results but requiring a high computational effort. Another particular analysis in [16] considers the channel characterisation as a result of measurements of specific parameters i.e. Received Signal Strength indicator (RSSI) values, Data rate or Power delay profile, etc. introducing useful information for realistic

channel characterisation. Finally, the results obtained in [17] describe the measurement procedure for a data rate achieved over different locations, and compares statistically which one provides a better estimation for 802.11 devices.

Having reviewed numerous studies that have been performed in the field to support channel simulation using models characterised by measurements [18-20], the optimal method to evaluate a propagation model for a MIMO wireless system is the 3D SBR. This is because it requires only moderate computing effort and can obtain an acceptably accurate prediction over a large scale indoor environment when compared with physical measurements. It is also reaffirmed that the throughput analysis for the newest IEEE standards is necessary to obtain a full performance for wireless equipment, in this case 802.11n.

1.2 Aim, Objectives and New Contribution of the Present Research

The aim of this research is to contribute towards the optimisation of broadband, multi-antenna communications systems.

Objectives identified towards this aim were to:

- Understand and be able to model and simulate current broadband MIMO communications systems.
- Identify, simulate and validate spatial channel models suitable for performance evaluation of broadband MIMO systems and techniques.
- Contribute new techniques which enhance the performance of broadband MIMO systems.

New contributions of the research include: development of new space time block codes (Chp. 4); evaluation of the performance of a MIMO-OFDM system using Adaptive Modulation and Coding (Chp. 5); channel measurement and modelling (Chp. 6,7); development of an improved method to calculate the envelope correlation between antenna elements of an 2-element array (Chp. 8) and an N-element array (Chp. 9) which includes intrinsic power losses in the antenna elements.

1.3 State of the Art

It has been proved that a complex orthogonal design of STBCs that provides full diversity and full transmission rate is not possible for more than two transmit antennas [21]. To achieve full-rate transmission while maintaining much of the orthogonality benefits of Orthogonal Space Time Block Code (OSTBC), Quasi Orthogonal Space Time Block Code (QO-STBC) has been proposed. Three groups of researchers have independently proposed such codes at about the same time. They are Jafarkhani, Tirkkonen, Boariu and Hottinen, and Papadias and Foschini [22-24]. They gave different names to their codes. For example, Jafarkhani named his code QO-STBC [22], which indicates the property of the code and has been adopted in the literature. On the other hand, Boariu and Hottinen named their code ABBA [23] which describes the code structure. Papadias and Foschini did not name their code [24].

Achievable MIMO diversity gain will depend not only on the location and arrangement of antenna array elements and the angle of arrival/departure spectrum for a particular

channel, but also on coupling effects between antenna elements. The envelope correlation provides a useful method for optimising element separation for the average rich scattering channel. A simple method for the computation of the envelope correlation for two antenna elements using scattering parameters was presented in [25]. This method avoids intensive computations using the radiation field patterns of the antenna system, and may be straightforwardly generalised to the envelope correlation of an N-antenna system [26]. This formulation has received widespread adoption in discussing antenna diversity issues [27, 28]. The spatial correlation was derived and tested in [29]; however, the computations in [25] and [26] do not include the power losses in the antenna structures. This accounts for the discrepancy between the envelope correlation results obtained by this method and those computed directly from the radiation field patterns of the two antenna elements [28].

A new QOSTBC scheme for four transmit elements is proposed in this thesis by reforming the detection matrix of the original QOSTBC scheme. An orthogonal channel matrix was derived that results in a simpler linear decoding scheme compared to the original OSTBC. The proposed scheme showed a better performance than the conventional scheme, where performance gains of about 2 dB are achieved. Also a space time block code for three, four and eight transmitters is proposed using Hadamard matrix. As noted, MIMO technology offers significant enhancement in the quality and robustness of voice, data and video transmissions. This is illustrated in the recently developed standard 802.11n that allows users to achieve up to 300 Mbps in a single transmission. Due to the recently emerged standard applied to this technology, further research is not only encouraged but also necessary. Although many authors have provided evidence on the effectiveness of this technology in field strength distribution, throughput or

propagation-simulation environments, results based on all parameters combined is limited. Thus the comparison of these perspectives in this work has focused on the operational performance of physical measurements, throughput and the field strength distribution over an indoor environment as evaluated using an 802.11n MIMO 2x3 dual band (2.4 & 5 GHz) system. Applying a 3D SBR technique, the path loss was simulated to compare the accuracy with results obtained from measurement. The actual environment for the measurement and analysis of the MIMO system was the third floor corridor in B wing of the Chesham building at the University of Bradford UK.

An extended simulation model for the University of Bradford campus was created to evaluate the channel propagation for indoor multi-storey, indoor- outdoor, outdoor-outdoor and outdoor-indoor scenarios, the model includes the details of the buildings in terms of the physical measurements and the materials used where the received signal strength and path loss were evaluated.

In MIMO systems, more than two antennas can be employed, thus the correlation between any two antennas in an antenna array is required. The calculation of the envelope correlation for an (N,N) MIMO antenna array in terms of the system's scattering parameters was modified to include power losses. This represents a major simplification with respect to the conventional use of the radiation field patterns of the antennas. The accuracy of the technique is illustrated by five examples.

1.4 Organization of the Report

Chapter 2: This chapter provides an introduction to multicarrier modulation systems. It describes the basic principle of generating and receiving an OFDM signal. Mitigation of

the effects of Inter-Carrier Interference (ICI) and Inter-Symbol Interference (ISI) in OFDM systems is described. Also this chapter gives a mathematical description of the transmitted and received OFDM signal.

Chapter 3: This chapter gives an introduction to MIMO systems and diversity techniques. Two different types of diversity that can be used to exploit the MIMO channels are presented. A survey of Space Time Block Coding is presented.

Chapter 4: This chapter presents conventional QOSTBC and proposes a new approach for a QOSTBC scheme for four transmit elements achieved by re-forming the detection matrix of the original QOSTBC scheme, where an orthogonal channel matrix was derived. This scheme results in a simpler linear decoding scheme compared to the original OSTBC. An Orthogonal space time block code for three, four and eight transmitters is also proposed using Hadamard matrix.

Chapter 5 discusses MIMO technology over a multipath channel and how transmission of parallel multi-channel data enhances the spectral efficiency of the wireless system while maintaining the original transmission bandwidth and power. In addition, the performance of a MIMO-OFDM system based on WiMax is investigated. A space-time coded OFDM transceiver using Adaptive Modulation and Coding (AMC) and Selection Combining at the receiver is designed and evaluated in terms of the achievable Bit Error Rate (BER) and Throughput.

Chapter 6: Presents an evaluation using an 802.11n MIMO 2×3 dual band (2.4 & 5 GHz) system to make physical measurements of throughput and the field strength distribution

over an indoor environment. Applying a 3D SBR technique, the path loss is simulated and the accuracy compared to the results obtained from measurements. Different propagation scenarios have been studied.

Chapter 7: An extended simulation model for University of Bradford campus is developed to evaluate the channel propagation for indoor multi-storey, indoor- outdoor, outdoor-outdoor and outdoor-indoor scenarios, the model includes the details of the buildings in terms of the physical measurements and the materials used, where the received signal strength and path loss were evaluated.

Chapter 8: A simple method for the computation of the envelope correlation for two antenna elements using scattering parameters is presented to avoid intensive computations using the radiated field patterns of the antenna system. The calculation of the envelope correlation for a lossy, two-antenna system has been evaluated in terms of the scattering parameters and the intrinsic power losses of the antenna structures. Examples were demonstrated to show the accuracy of the proposed correlation equation.

Chapter 9: The calculation of the envelope correlation for an (N,N) MIMO antenna array in terms of the system's scattering parameters is modified in this chapter to include power losses. This represents a major simplification with respect to the conventional use of the radiated field patterns of the antennas. The accuracy of the technique is illustrated by five examples.

Chapter 10: The overall work is summarized and a review provided of the outcome of the research work. The conclusions drawn from the studies and further extensions of the work are discussed in this chapter.

CHAPTER 2

Multicarrier Modulation Overview

2.1 Introduction

Orthogonal frequency division multiplexing (OFDM) is a flexible multicarrier modulation technique adopted by a wide variety of high data rate communication systems, including digital subcarriers lines, wireless LANs (802.11a/g/n), digital audio and video broadcast (DAB, DVB-T), Flash-OFDM (developed by Flarion now QUALCOM), and 3G LTE , WiMax and fourth generation cellular systems. In highly dispersive channels, OFDM is an efficient technique for high data rate applications due to its ability to avoid inter symbol interference (ISI).

In high data rate systems, as the channel delay spread τ becomes increasingly larger than the symbol time T_s, the inter symbol interference (ISI) becomes more severe. Since the number of symbols sent per second is high then it is expected to have $\tau \gg T_s$. In non-line of sight (NLOS) systems such as Mobile WiMAX, that are designed to transmit over long distances, the delay spread frequently becomes large. In addition, over short distances, wireless broadband systems of all types will be generally affected by ISI; therefore the transmission process needs some techniques to overcome the ISI. The vast majority of the 802.16 standards have applied the OFDM mode, and this has been adopted as the preferred mode by the WiMAX Forum [29].

OFDM is a special case of multicarrier modulation (MCM) that divides a communication channel spectrum into a number of equally spaced frequency bands, where it can be

described as a modulation or multiplexing technique. One of the main reasons for using OFDM is to increase robustness against frequency selective channels and narrowband interference. In single carrier systems, one fade or interferer can cause an entire link to fail, but in multicarrier systems only a small percentage of the subcarriers will be affected. The basic concept of OFDM is to divide high data rate transmissions into parallel, lower data rate streams and transmit them over a number of orthogonal subcarriers, in which each subcarrier is orthogonal to other subcarriers and it carries a portion of the user transmitted information [30, 31, and 32]. Hence, OFDM is different from the commonly used *Frequency Division Multiplexing* (FDM).

There are several differences between OFDM and FDM even though OFDM uses the same fundamental principle as FDM modulation. FDM allocates each channel to a unique frequency range, where this frequency range determines both the centre frequency and channel bandwidth. Since these channels are non-overlapping, multiple users can operate simultaneously by using different channels in the frequency domain.

The centre frequencies that are used by an FDM system are spaced so as to operate within separate spectral allocations. At the receiver, each FDM signal is individually received by using a frequency-tuneable bandpass filter (BPF) to selectively remove unwanted frequencies [33, 34, and 35].

In OFDM transmission, all data channels are combined into a single multiplexed stream of data, which is modulated over different subcarrier frequencies. Due to the orthogonal nature of these subcarriers [36, 37, 38, and 39], all these different subcarriers within the

OFDM transmission signal are time and frequency synchronized with each other allowing interference between these subcarriers to be controlled without causing ICI.

2.2 Multicarrier Modulation

In modern communications where wideband multipath channels are needed to deliver today's applications, the symbol time T_s becomes smaller than the channel delay spread thus severe inter symbol interference is introduced. Error probability increases rapidly in the presence of ISI and as T_s becomes equal to, or smaller than, the delay spread τ the bit error rate becomes large. In order to have a channel without ISI, the symbol time T_s has to be much larger than the channel delay spread τ. Multicarrier modulation (MCM) is a principle of transmitting data by dividing the input into L symbol streams each of which has lower data rate with symbols of duration $T = T_s \times L$. These sub-streams are used to modulate L subcarriers, maintaining the overall data rate.

If the subcarrier frequency spacing is chosen to be $f_{sc} = \frac{1}{T}$, then the modulated subcarrier spectra are overlapping, yet orthogonal. Such multicarrier modulation is referred to as OFDM. However, the sub-channels are orthogonal to each other only in stationary propagation channels. The data rate of each sub-channel is much lower than the total data rate, so the sub-channel bandwidth is also much lower than the total bandwidth of the system. The number of sub-streams is chosen in a way that ensures that the sub-channel bandwidth is lower than the coherence bandwidth of the channel. In this case the sub-channels will experience relatively flat fading, and thus ISI on each of them is small.

The multicarrier technique has an interesting property in the time domain and in the frequency domain where in time domain the symbol duration on each of L subcarriers will increase to $T = LT_s$, so increasing L ensures that the symbol duration exceeds the

channel delay spread , $T \gg \tau$, which prevents ISI. In the frequency domain the subcarrier bandwidth will be $B/L \ll B_c$ which lead to flat fading on each subcarrier and therefore prevent ISI.

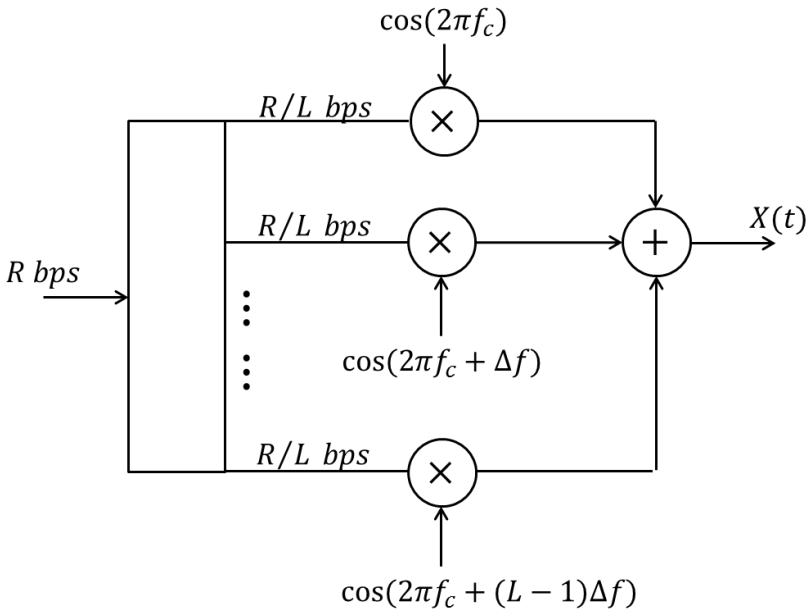

Figure 2. 1: A basic multicarrier transmitter: a high data stream of R bps is divided into L parallel sub-streams each of which with rate of R/L and then multiplied by different carrier frequencies [29].

A simple illustration of a multicarrier transmitter is shown in Figure 2.1.Consider the MC transmitter shown in Figure 2.1 with signal data rate R bps and bandwidth B, the signal data rate R will be divided into L parallel sub-streams each with rate R/L and passband bandwidth of B/L.

As long as the number of the subcarriers is large enough to make sure that the coherence bandwidth is much greater than the subcarrier bandwidth, that is $B_c \gg B/L$ which ensures that each subcarrier experiences flat fading, then the mutually orthogonal signals can be individually detected as illustrated in Figure 2.2.

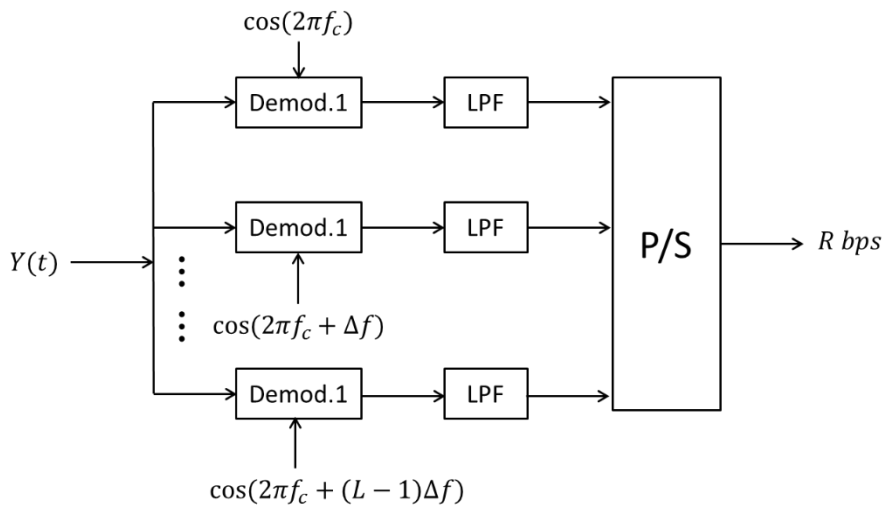

Figure 2. 2 : A basic MC receiver, where L independent receivers are required to detect each signal [29].

2.3 Basic Principle of OFDM

OFDM signals are generated digitally, since generating the signal by analogue means is very difficult due to the need of large number of synchronised oscillators. [39]. Figure 2.3, illustrates the basic OFDM transmitter scheme. The OFDM mode is based on Fourier transform theory where the OFDM subcarriers in the frequency domain are modulated using the IFFT process to produce the OFDM signal in the time domain and demodulated using an FFT, in order to overcome the requirement of a complex system of oscillators in both the transmitter and in the receiver.

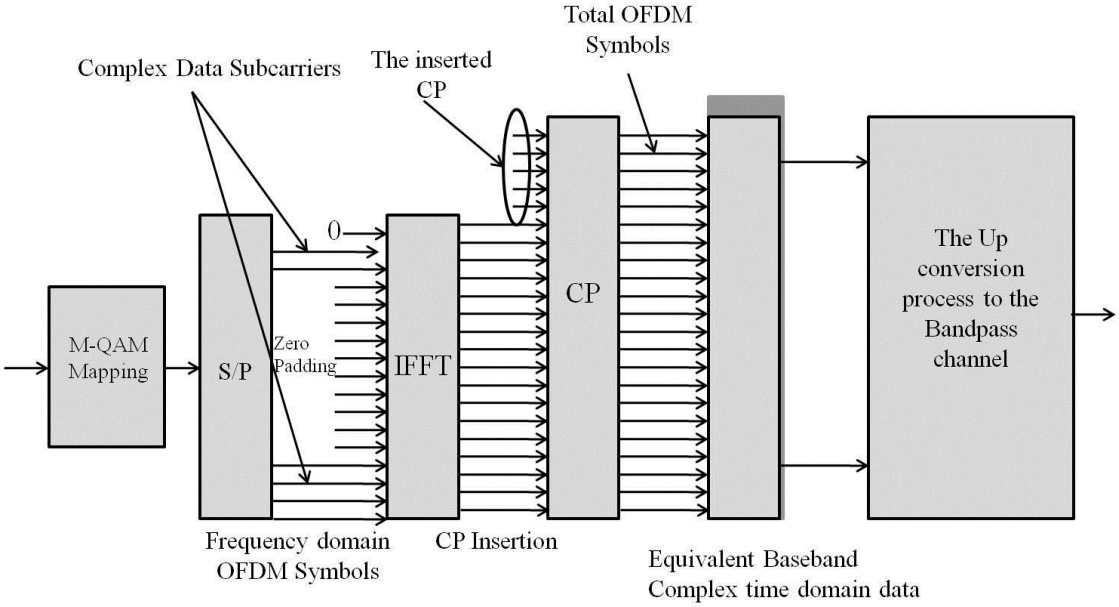

Figure 2. 3: The basic OFDM transmitter scheme [29].

Zero padding is implemented at the input to the IFFT block to make the design of an anti-aliasing filter ahead of the digital to analogue converter (D/A) practicable. The total number of subcarrier (IFFT size) is given by $(N = N_d + N_s)$, where N_d is the input complex data subcarrier and N_s is the is the number of zeros that are added by the zero padding.

Transmission over the wireless channel is subject to both frequency dispersion and time dispersion. Frequency dispersion is caused by Doppler Spread, which results in orthogonality loss between the subcarriers, and therefore some error will be introduced. Frequency dispersion also introduces the so called Inter Carrier Interference (ICI) due to loss of orthogonality of the overlapping side lobes of the OFDM subcarriers. Transmitter pulse shaping (of the time-domain output from the IFFT) to reduce the effect of ICI has been investigated by some researchers [40, 41, 42].

Time dispersion is caused by multipath fading; OFDM offers robustness against time dispersion by inserting a cyclic prefix (CP), which is defined as a copy of the last portion of the OFDM symbol, inserted at the start of the OFDM symbol. Although the CP reduces the symbol rate of the OFDM signal, it provides protection against ISI caused by time dispersion of the channel.

The real and imaginary parts of the equivalent baseband complex time domain samples produced by the IFFT and extended by addition of the CP are separated and transmitted

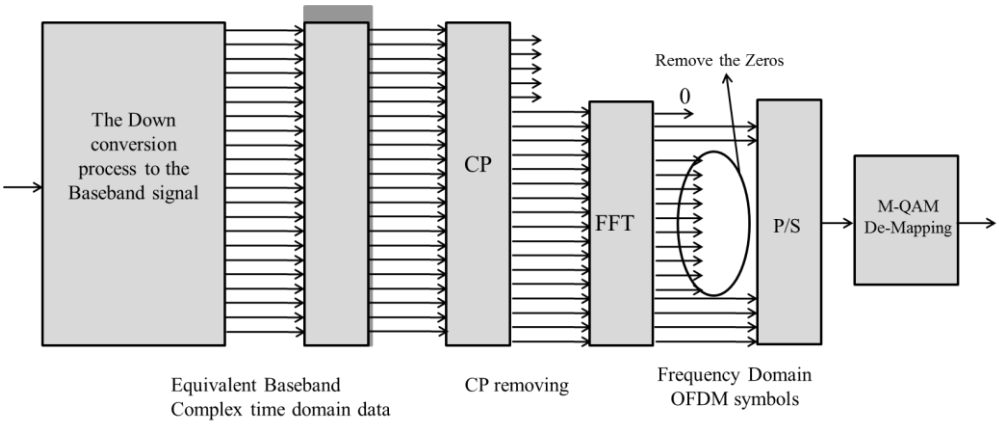

Figure 2. 4 : OFDM Receiver diagram [29].

serially via two digital to analogue converters and low pass filters. The real and imaginary baseband components are then up converted and summed to create the bandpass channel by mixing respectively with in-phase (I) and quadrature (Q) signals at the carrier frequency.

In the receiver side shown in Figure 2.4, the reverse operation is applied by down converting the received bandpass signal to its equivalent complex baseband signal and then converting from analogue to digital. The CP is removed and the received time domain OFDM signal is applied to the FFT process to demodulate the complex subcarriers. Then the zeros are removed to extract the desired complex data subcarriers.

Equalisation is typically applied at this stage and then the data subcarriers are used as input to the coherent demodulator (De-Mapper) to reconstruct the data bits, which are finally converted to a serial stream.

2.3.1 Data Subcarrier Mapping

In OFDM systems, the incoming serial data stream is mapped using a modulation scheme into amplitude and phase that is represented by a complex data vector ($S_d,\ d = 1{:}\,N_d$), where N_d is the number of the complex data subcarriers. The modulation scheme determines how many bits will be accommodated for each complex data subcarrier where the number of bits per data subcarrier for the M-QAM modulation is given by:

$$B_{sub} = log_2 M \tag{2.1}$$

By applying equation (2) to BPSK and QPSK modulations the bits assigned to each data subcarrier will be stated by the following:

$$\begin{aligned} B_{sub}^{BPSK} &= 1bit \\ B_{sub}^{QPSK} &= 2bit \end{aligned} \tag{2.2}$$

Using QPSK modulation will double the number of bits of the serial data input in comparison with BPSK which means more capacity.

2.3.2 Data De-Mapping

In the mobile wireless communication environment, multiple scattering such as that caused by buildings and other physical obstacles in the propagation channel might create a severe multipath propagation, which makes the design of a reliable communication system difficult. Time delay dispersion from the multipath effect due to scattering, and

frequency dispersion due to the movement of the mobile station in addition to the additive white Gaussian noise (AWGN) (introduced by the thermal noise) causes a rapid random variation in the amplitude and phase of the received signal [43].

Due to the multipath propagation channel characteristics, the OFDM signal constellation will be attenuated and phase distorted, therefore at the receiver channel equalization is attempted to estimate the most likely original transmitted vector of each point [44,45].

2.3.3 Serial to Parallel Conversion

The main principle of OFDM is that the transmitted data signal is transformed into several parallel data subcarriers, each of which carries a small portion of the information data. In this way the bit rate of each subcarrier is much lower than the total bit rate, that reduces the effect of the inter symbol interference (ISI) significantly.

In ordinary serial data systems as FDMA and TDMA, the data symbols (data subcarriers) are transmitted sequentially, where the frequency spectrum of each data symbol is allowed to occupy the entire available bandwidth.

On the other hand, OFDM provides two advantages over serial systems. Firstly, since each subcarrier occupies a small portion of the bandwidth, the equalization is simpler than for serial systems. Secondly, under severe multipath fading, even with perfect equalisation, every symbol of a conventional broadband serial transmission will be adversely affected by a high level of noise and ISI, whilst in OFDM the ill-effects of the channel will be concentrated in only a proportion of the symbols associated with those subcarriers experiencing deep flat fading and hence reduced SNR, whilst other subcarriers experience no fading or even enhancement.

2.3.4 Zero Padding

In principle, zero padding can be applied in either to the time or the frequency domains. It has the effect of increasing the size of the FFT/IFFT transform and hence the resolution in the other domain. For this reason, it is sometimes referred to as oversampling. In OFDM, zero padding is applied in the frequency domain, i.e. before the IFFT in the transmitter.

This is done in order to prevent OFDM symbols from interfering with other adjacent systems by providing guard bands and also to enable a realisable interpolation filter to be used after the digital to analogue conversion. A number of subcarriers at the upper and lower edges of the pass band are modulated to zero. The total number of subcarriers is given by:

$$N = N_d + N_s \tag{2.3}$$

where N_d is the number of parallel complex data subcarriers and N_s is the number of zero subcarriers.

Equal numbers of zero subcarriers are added above the upper sideband subcarriers and below the lower sideband to provide a frequency guard band between adjacent systems and reduce the complexity in analogue anti-aliasing and reconstruction filter designs. Because the IFFT algorithm is organised such that the lower sideband components appear above the upper sideband components [29], the zeros are added in the middle, as illustrated in Figure 2.3.

2.3.5 Adding the Cyclic Prefix

In single carrier communication systems the data symbols of rate R_s are transmitted sequentially in which, each data symbol has duration of T_s that is inversely proportional to the symbol rate ($T_s = \frac{1}{R_s}$).

The frequency selective fading channel can be characterized by an impulse response with delay spread represented by the time domain. Figure 2.5 shows an impulse response of the two paths selective fading channel, where τ_{max} is the time delay between the first and second paths.

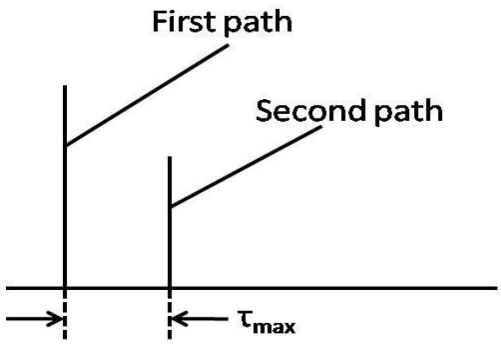

Figure 2. 5: Impulse response of a frequency selective fading channel [29].

In this channel, the first path generates the desired signal and the second path generates the delayed signal at the receiver. In order to overcome the delay spread in wireless channels, a Cyclic Prefix (CP) is usually added in the OFDM systems. Adding CP will increase the actual OFDM symbol period from T_s to $T = T_S + T_g$. A cyclic prefix will be added to the transmitted signal as shown in Figure 2.6.

The FFT is a lower-complexity algorithm that implements a DFT. The FFT is most efficient for sizes where $N = 2^m$ where m is an integer. The channel must provide a circular

convolution to insure that, IFFT/FFT creates an ISI-free channel as discussed in section (2.3.4).

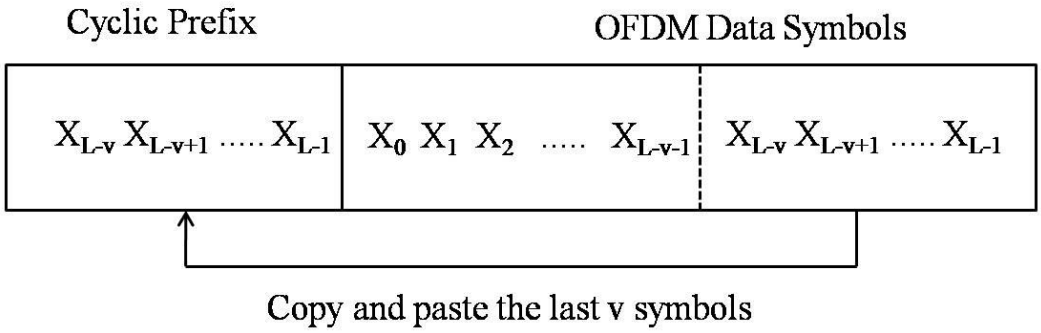

Figure 2. 6: Adding the Cyclic Prefix to the OFDM transmitted data [29].

Let's consider a channel that has a maximum delay spread duration of v+1 samples and thus by adding the guard interval that is equivalent of at least v samples between the OFDM symbols makes the OFDM symbols independent of those arriving before and after the same symbol. Thus one OFDM symbol can be considered at a time. An OFDM symbol of length L can be represented in time domain as:

$$x = [x_0 \quad x_1 \quad x_2 \quad ..... \quad x_L] \tag{2.3}$$

After applying a cyclic prefix of length v, the transmitted signal will be:

$$x_{cp} = [x_{L-v} \quad x_{L-v\mp1} \quad ..... \quad x_L \quad x_0 \quad x_1 \quad x_2 \quad ..... \quad x_L] \tag{2.4}$$

The signal received after the channel can be defined as $y_{cp} = h * x_{cp}$, where y_{cp} is the output signal of length $(L+v)+(v+1) = L+2v$ samples. The first v samples contains the interference from previous OFDM symbols therefore they are discarded and the last v samples dissipated into the subsequent OFDM symbol and also discarded. y_{cp} is the channel impulse response during the OFDM symbol; note the channel can be assumed to be constant over an OFDM symbol since the OFDM symbol time is less than the channel coherence time. After omitting the $2v$ samples that will leave the only L

desired samples for the output y which is the required number of samples needed to recover data symbols transmitted over x, [29].

The cyclic prefix is simple; however, it has some drawbacks on both bandwidth and power consumption. The bandwidth required for transmitting the OFDM symbols will increase from B to $B(L+v)/L$ because of the v added redundant symbols. Also the transmitted power will increase by $10log_{10}(L+v)/L$ due to the additional v transmitted added symbols. The overall losses resulting from the use of the cyclic prefix in terms of the power loss and rate loss can be given by the following:

$$Rate\ Loss = Power\ Loss = \frac{L}{L+v} \tag{2.5}$$

By increasing the number of the subcarriers, the efficiency wasted by using the cyclic prefix can be minimized. One way to overcome the waste of the transmit power is by using Zero Prefix [29], however, this will distort the received symbols, since there is no longer true cyclic convolution.

2.3.6 Spectral Efficiency

The spectral efficiency defines the amount of information data that the system can carry in a given amount of spectrum. In cellular communications it is measured by *bits/s/Hz.* It also quantifies the efficiency of the radio performance thus a higher spectral efficiency will leads to better quality of service (QoS) for the end user at any traffic load.

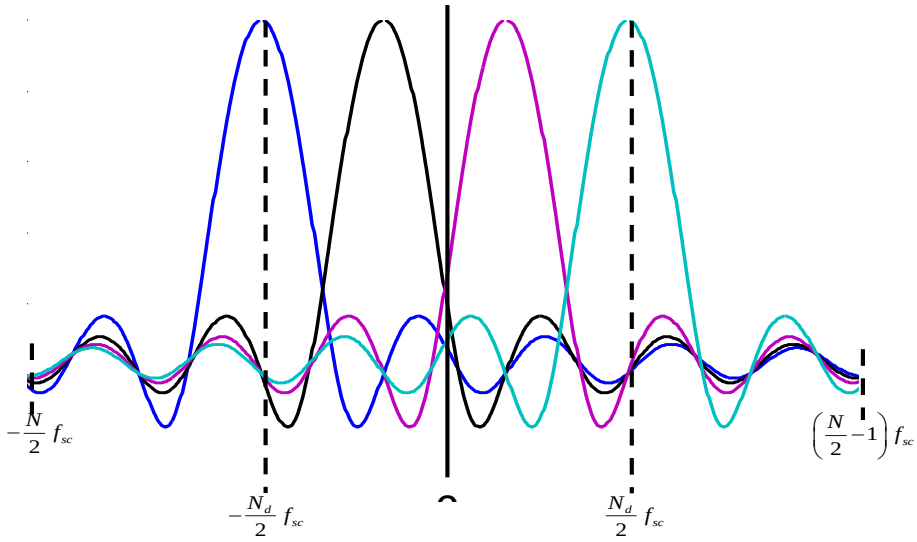

Figure 2. 7: Bandwidth allocated for OFDM signals; OFDM symbol with e.g. N_d=4 data sub-carriers.

From Figure 2.7 the OFDM system bandwidth is the distance between the maximum subcarrier frequency and the minimum subcarrier frequency, given by:

$$BW = \frac{N_d}{2} f_{sc} - \left(\frac{-N_d}{2} f_{sc} \right) = N_d f_{sc} \tag{2.6}$$

The spectral efficiency in terms of bit rate per unit bandwidth can be rewritten as:

$$\eta = \frac{R_b}{BW} = \frac{R_b}{N_d f_{sc}} \tag{2.7}$$

where R_b is the bit rate.

Then the total number of bits that can be modulated by R_d data subcarriers OFDM symbol using an M-QAM modulation technique is given by:

$$N_{tot} = N_d \, log_2 M \tag{2.8}$$

In order to achieve bit rate of R_b bps, each OFDM symbol with time duration T_s must carry N_{tot} bits that is equivalent to the total number of bits per OFDM symbol.

$$N_{tot} = R_b \times T_s \tag{2.9}$$

From equations (2.8) and (2.9) the number of data carriers per OFDM symbol can be given as follow:

$$N_d = R_b \times \frac{T_s}{log_2 M} \tag{2.10}$$

Using equation 2.10 one can write the spectral efficiency as follows:

$$\eta = \frac{R_b}{\frac{T_s \times R_b}{log_2 M} \times f_{sc}} = \frac{log_2 M}{T_s f_{sc}} \tag{2.11}$$

When $(T_s f_{sc}) = 1$, the spectral efficiency is maximized which ensures the orthogonality between the OFDM subcarriers and there is an integer number of cycles for OFDM sub-carriers in this time duration, which is called the useful OFDM time duration ($T_u = \frac{1}{f_{sc}}$), by substituting $(T_s f_{sc}) = 1$ in equation 2.11 then the spectral efficiency can be written as:

$$\eta = log_2 M \quad \text{bits/s/Hz} \tag{2.12}$$

Applying a cyclic prefix (CP) to an OFDM system the total OFDM symbol duration will be:

$$T_t = T_u + T_g$$

In this case the spectral efficiency given by equation 2.14 will be yields to:

$$\eta = \frac{log_2 M}{1 + T_g / T_u} \tag{2.14}$$

2.4 Frequency Equalization

To estimate the received symbols, each of the subcarriers' complex channel gains must be known, which correspond to the knowledge of the amplitude and phase for each subcarrier. In simple modulation technique such as QPSK the knowledge of the phase is enough within the transmit information compared to the symbol amplitude.

Thus, applying FFT at the receiver side the data symbols can be estimated using a one tap frequency equalizer (or FEQ) as:

$$\hat{X}_l = \frac{Y_l}{H_l} \tag{2.15}$$

Where H_l is the complex response of the channel at frequency $f_c + (l-1)\Delta f$, thus it corrects the phase and equalises the amplitude before the decision made on the symbols [29].

2.5 OFDM system

2.5.1 Representing the OFDM system in Vector Notation

In the OFDM communication system shown in Figure 2.8, the encoding and decoding are done in the frequency domain where X, Y and $\hat{X}$ contains the L transmitted, received and estimated data symbols respectively.

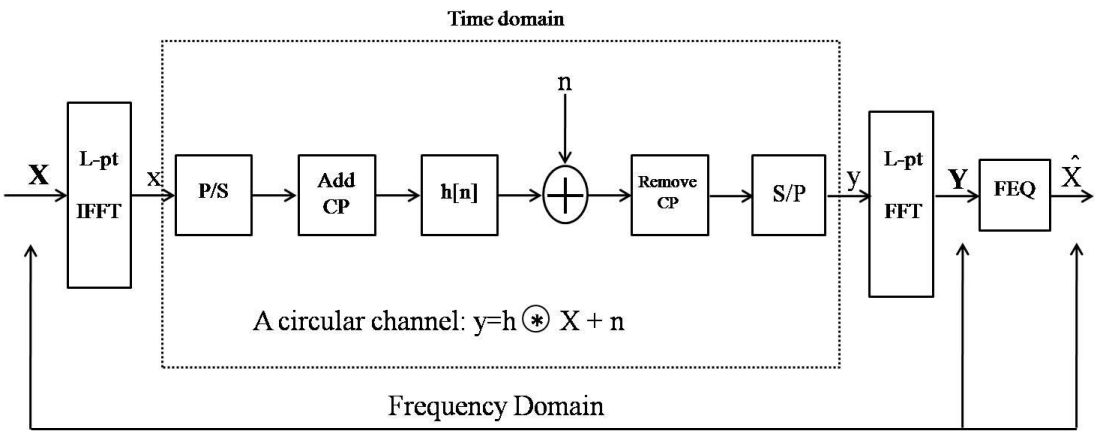

Figure 2. 8 : Vector representation of OFDM transceiver [29]

Let us now describe the main transmission steps in an OFDM system. Note that Figure 2.8 disregards some practical issues since it is assumed that the receiver knows the channel (CSI) and the transmitter and the receiver are synchronized. In addition it makes the following assumptions.

- The wideband signal of bandwidth B is divided into L subcarriers each of which has B/L bandwidth. The transmission will maintain the symbol rate but each subcarrier will experience flat fading (ISI free communication) as long as a CP that exceeds the delay spread is used.
- The subcarriers are modulated using IFFT in order to use a single wideband instead of using L narrowband channels.
- A CP of length v must be added after the IFFT, so that the IFFT/FFT decompose the ISI channel into orthogonal subcarriers, then the resulting symbols of length $(L + v)$ are sent over the wideband channel serially.
- At the receiver end the, L received symbols are demodulated using FFT after the CP is removed. The result will be L data symbols each of which form $Y_l = H_l X_l + N_l$ where l is the subcarrier number.

- The subcarriers can be equalized by dividing each of them by its complex channel gain H_l. The received signal can be written as $\hat{X}_l = X_l + \frac{N_l}{H_l}$.

2.5.2 OFDM Example: WiMAX

OFDM is simple in concept but it can be confusing if each signal processing step is not understood. In this example a passband system is discussed and then the important design values are stated for a WiMAX system.

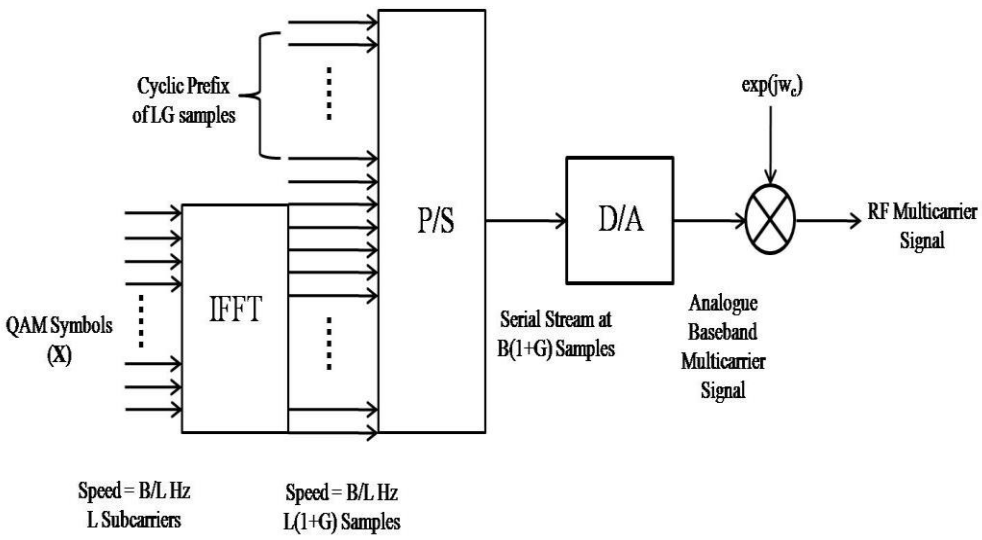

Figure 2. 9: OFDM Baseband transmitter [29].

The input of the OFDM modulation scheme shown in Figure 2.9 is the set of L QAM symbols (**X**), where these symbols are modulated on separate subcarriers. The symbols can be generated from the original bit stream by data mapping and then applying serial to parallel conversion. The L point IFFT creates a vector in the time domain (**x**) which has length of L(1+G) due to adding the cyclic prefix. G is the length of the added cyclic prefix (LG = v). Then this longer vector is converted from parallel to serial into a wideband signal at which the amplitude modulates a carrier of frequency $f_c = \frac{w_c}{2\pi}$.

To make it more realistic, the main OFDM parameters as summarized in Table 2.1, will be used for an example.

Table 2. 1: OFDM Parameters (WiMAX)

Symbol	Description	Relation	Example WiMAX value
B^*	Nominal Bandwidth	$\boldsymbol{B = 1/T_s}$	10MHz
L^*	Number of subcarriers	Size of IFFT/FF	1024
G^*	Guard Interval	% of L for CP	1/8
L_d^*	Data subcarrier	L pilot/null subcarriers	768
T_s	Sample time	$T_s = \boldsymbol{1/B}$	1 μ sec
N_g	Guard symbols	$N_g = \boldsymbol{GL}$	128
T_g	Guard time	$\boldsymbol{T_g = T_s}N_g$	12.8 μ sec
T	OFDM symbol time	$\boldsymbol{T = T_s(L + N_g)}$	115.2 μ sec
B_{sc}	Subcarrier bandwidth	$\boldsymbol{B_{sc} = B/L}$	9.76 KHz

() Denotes the WiMAX specified parameters, the other parameters can be calculated from these values.*

As an example let us assume 16 QAM modulation is used ($M = 16$). Therefore without coding the data rate of the WiMAX system will be:

$$R = \frac{B}{L}\frac{L_d \log_2(M)}{1+G} = \frac{10^7 MHz}{1024} \times \frac{768 \times \log_2(16)}{1.125} = 24Mbps \tag{2.16}$$

In other words each L_d data subcarriers of bandwidth B/L carry $log_2(M)$ bits of the data.

2.6 Model Design of OFDM Transceiver Using MATLAB-SIMULINK

The OFDM system is modelled using MATLAB-SIMULINK to allow various parameters of the system simulated and tested. The OFDM system parameters used in the simulation are:

- Data mapping: M-QAM
- IFFT, FFT size: 256-points
- Channel used: AWGN, multipath Rayleigh
- Guard interval size: 9 samples
- OFDM frame size: 201

The OFDM system with M-QAM mapping is shown in Figure 2.10.

- Binary source: frame based binary data is generated using the random Bernoulli binary generator, at the output 48 samples per frame are used for data rate 1 Mbps.
- Data Mapping: the input serial data stream is converted into parallel data stream according to the digital modulation scheme. The data stream is transmitted in parallel by assigning each data word to a carrier in the transmission process. After allocating the symbols to a subcarrier they are phase mapped depending on the modulation scheme, which is represented by In-phase and Quadrature-phase vectors. Each symbol of two bits correspond to a unique IQ vectors. Changing the number of bits per symbol in the IQ mapping block one can map the data for 8QAM, 16QAM and 64 QAM. Using a higher constellation scheme make it possible to transmit more bits per symbol in parallel which result in high data rate communication systems. In general the modulation scheme is selected depending on the data rate requirement and transmission robustness.

- IFFT-Frequency domain to Time domain: The IFFT converts signal from the frequency to time domain also maintaining the orthogonality between the subcarriers. At this stage IFFT mapping, zero padding and selector blocks are included, the zero padding block adjusts the size of the IFFT to L points (where L must be power of 2) since the number of the subcarrier could be less than the IFFT size [30].
- The Guard Period: to mitigate the effect of ISI on the OFDM signal, a guard interval is inserted at the beginning of each symbol, that is represented as a cyclic extension of the symbol waveform. The guard interval adds a time overhead which decreases the spectral efficiency of the system, the guard interval length should be longer than the channel delay spread [31].

The performance of a communication system is usually analysed in terms of Bit Error Rate versus SNR.

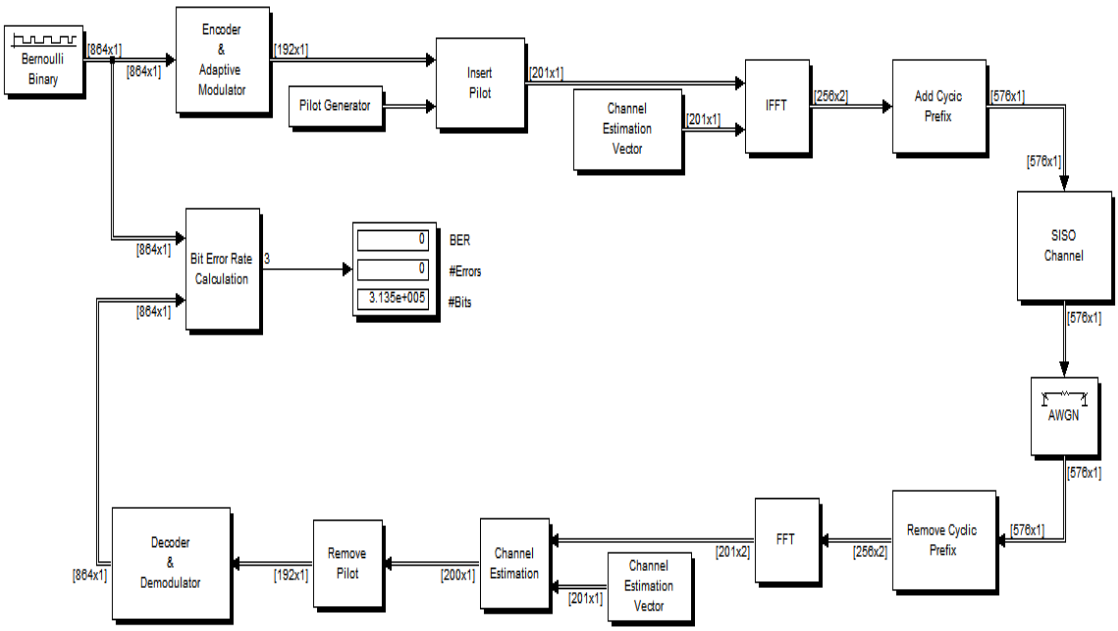

Figure 2. 10: OFDM Matlab/Simulink Model

The OFDM system is simulated using different modulation techniqes such as BPSK, QPSK and 16-QAM. The BER performance of the OFDM over these modulations is shown in Figure 2.11. It can be noticed from the figure that at low SNR the best performance is achieved by BPSK . However as the distance increases the received signal strength decreases resulting in a decreasing SNR, so a switch from lower modulation level to higher modulation level is needed.

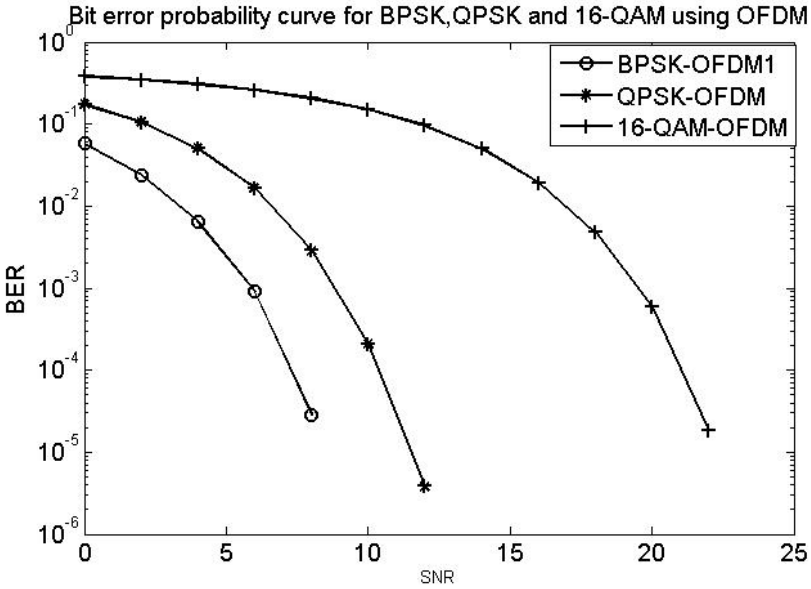

Figure 2. 11: BER performances for OFDM using BPSK, QPSK and 16-QAM.

2.7 Conclusions

The OFDM modulation technique has been presented in terms the influence of high data rate communication system and its mitigation towards the effect of ISI. The use of computationally efficient IFFT and FFT technology for modulation and demodulation respectively provides a straightforward implementation for OFDM. OFDM was tested using MATLAB-SIMULINK over M-QAM digital modulation. It can be concluded that the BER for BPSK is less for low SNR compared to that achieved by QPSK and 16-QAM modulations. This simply confirms that OFDM using BPSK is suitable for lower capacity and low power systems, whereas higher modulation schemes are suitable for high capacity and higher power systems.

CHAPTER 3

Multiple Antenna Techniques

3.1 Introduction

In this chapter the signalling schemes used to exploit Multiple Input Multiple Output (MIMO) systems are discussed, including diversity theory and techniques. In conventional mobile communication systems there is only one antenna at both the transmitter and the receiver. This system configuration is known as Single Input Single Output (SISO). A major drawback for SISO systems is that their capacity is limited by the Shannon-Nyquist criterion [33]. In order to increase the capacity of SISO systems to meet the high bit rate transmission demanded by the modern mobile communications the bandwidth and the transmit power have to increase significantly. Fortunately, using MIMO techniques has the potential to increase the capacity of a wireless system without the need to increase the transmission power or the bandwidth as discussed in [4-5].

Rayleigh fading and log-normal shadowing in wireless communications channel imposes a large power penalty on the modulation performance. One of the best techniques to mitigate the fading effects is by applying diversity combining, in which the independent fading signals are combined together, since independent paths have less probability to experience deep fades simultaneously.

In simple words, the main idea behind diversity is to send replicas of the data over independent fading paths and hence at the receiver combine these in such a way as to minimise the impact of fading on the resultant signal.

Consider a system with two antennas at the receiver that experience independent fading, the probability that they experience deep fading at the same time would be less if they are spaced apart sufficiently. At the receiver the antenna with higher signal power will be selected, a technique known as *selective combing*: thus using more than one antenna will result a better signal reliability. In this chapter the common method for achieving diversity at the transmitter and receiver will be studied and discussed.

3.2 Diversity Techniques

Diversity techniques are developed in order to mitigate fading effects; the basic principle of diversity is to have multiple version of the transmitted signal at the receiver where each replica is received though a different path or channel. Figure 3.1 shows two signals suffering independent fading Rayleigh, and their combination. When two signals are fading independently, it is unlikely that both experience a deep null at the same time. It is noticeable from Figure 3.3 that the combined signal has higher SNR compared with the branch signals.

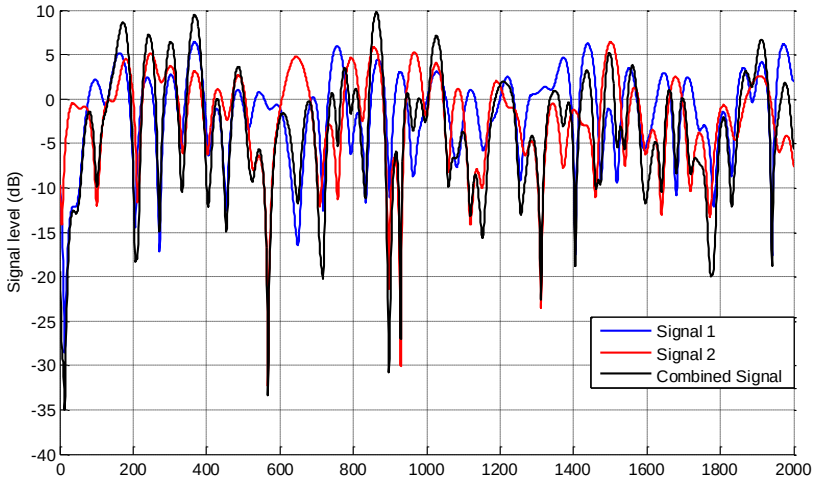

Figure 3. 1: Two replicas of the transmitted signal and the resultant combined signal.

In addition to the fading mitigation benefit a diversity technique known as Space Time Coding (STC) is used to exploit MIMO channel, this signalling scheme will be further discussed in later sections. Diversity can be categorised as shown in Figure 3.2.

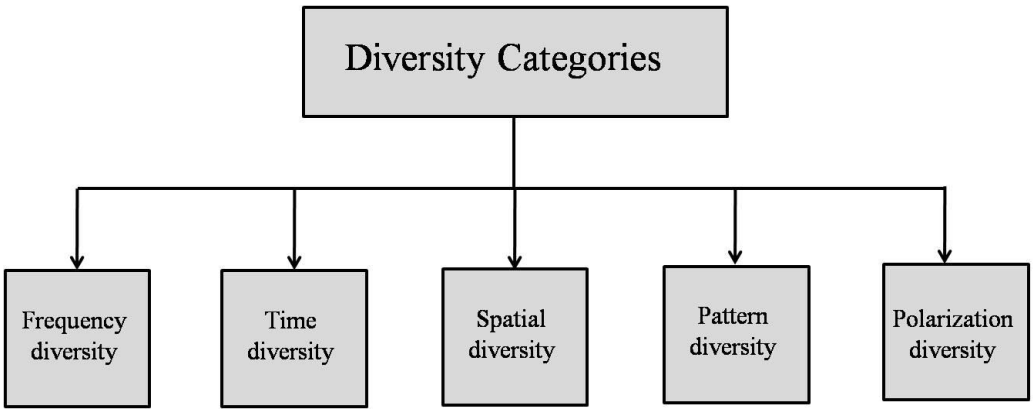

Figure 3. 2: Diversity Categories [46].

In general, there are five diversities as shown in Figure 3.2. Three of these techniques are categorised as antenna diversity which are spatial, pattern and polarization diversities, these will also be discussed later in this chapter.

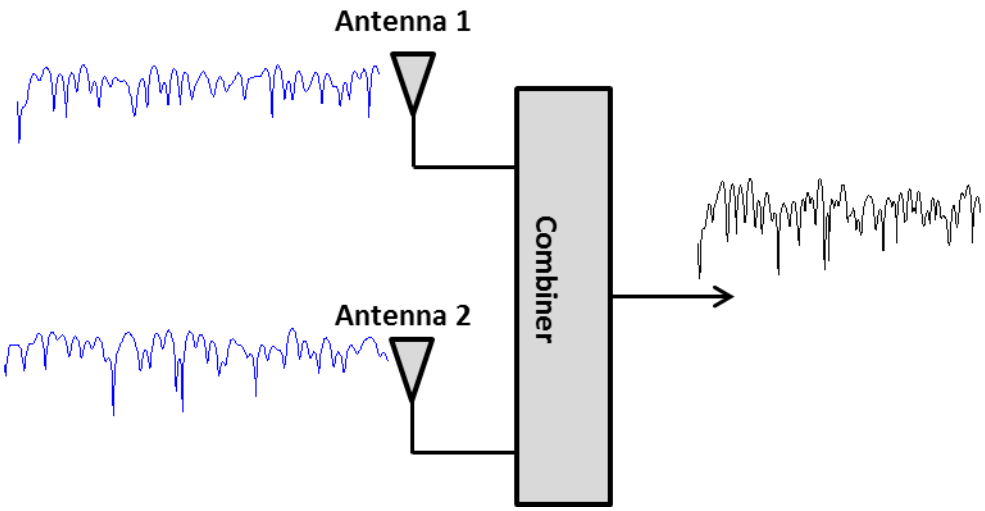

Figure 3. 3: Diagram illustrates two received signals combined using basic diversity combiner

Figure 3.3 shows a receiver with dual antenna elements, two replicas of the transmitted signals are received and combined using a diversity combining technique. In mobile communication systems, low correlation and equal power between the antennas are needed, because high correlation will result in deep fades. In addition, if the received signals have very different power levels then the weaker signal of one of the antennas is not useful even if it is less faded.

The following are the common diversity properties applied in communications systems:

- Time Diversity: time diversity can be achieved by transmitting a replica of the signal in a different time slot. This results in uncorrelated fading signals at the receiver. To achieve effective time diversity the separation between the signals should be at least or equal the coherence time of the channel.
- Frequency Diversity: to achieve frequency diversity, the signal is transmitted over different frequencies. The separation between the frequencies should be sufficient

(the coherence bandwidth of the channel should be less than the signal frequency separation) to ensure that each frequency experience independent fading.

- Spatial Diversity: also known as Antennas diversity, spatial diversity is implemented by using multiple antennas where a replicas of the original signal are transmitted between different pairs of antennas, to ensure independent fading, then the alternative antennas should spaced sufficiently.

3.3 Diversity Combining Techniques

In the previous section diversity techniques were classified according to the domain in which they were introduced. A key feature of diversity is the low probability of simultaneous deep fades in different diversity sub-channels. The performance of a wireless communication system combined with diversity techniques depends on how the multiple replicas of the signals are combined at the receiver so as to decrease the overall BER.

The diversity scheme can be classified according to the combining method used at the receiver. On this depends the implementation complexity and the amount of channel state information needed by the combining method at the receiver.

In this section different combining techniques are described in terms their operation performances. Figure 3.4 illustrates the combining diversity techniques that can be implemented at the receiver shown in Figure 3.3.

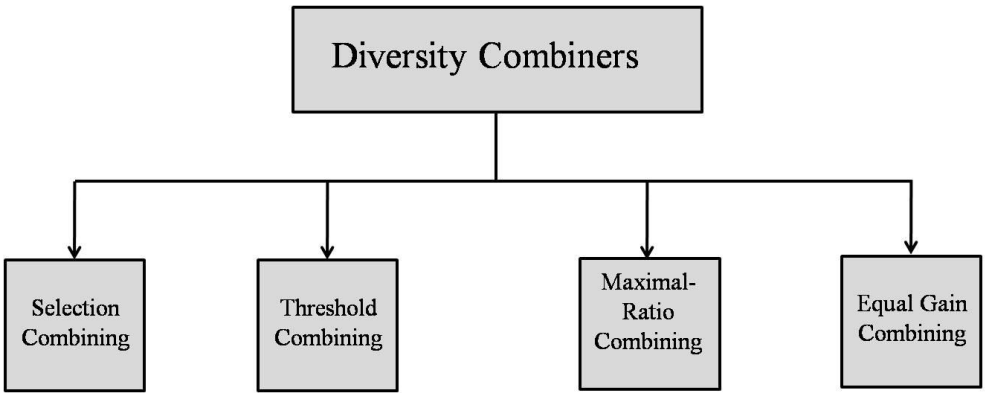

Figure 3.4: Types of the Diversity Combining Techniques [46].

3.3.1 Selection Combining

In the selection combining (SC) technique, the combiner selects the signal at the branch that experiences the highest SNR as shown in Fig. 3.5. In systems where one branch is active at a time, only one receiver is needed so the receiver switches to highest SNR branch. On the other hand, in a system that transmits continuously, a receiver at each branch is needed to monitor SNR on each of them, so the output SNR is equal to that of the best incoming signal.

Fig. 3.6 shows the effect of SC when increasing the number of receiving antennas versus SNR. It can be noticed that the SNR improvement is nonlinear with the number of receive antennas.

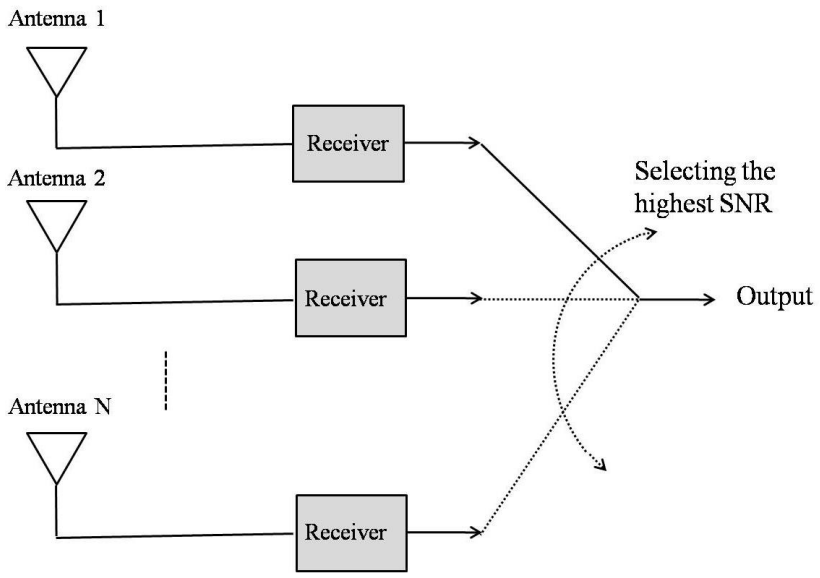

Figure 3.5: Selection Combining for N Branches [46].

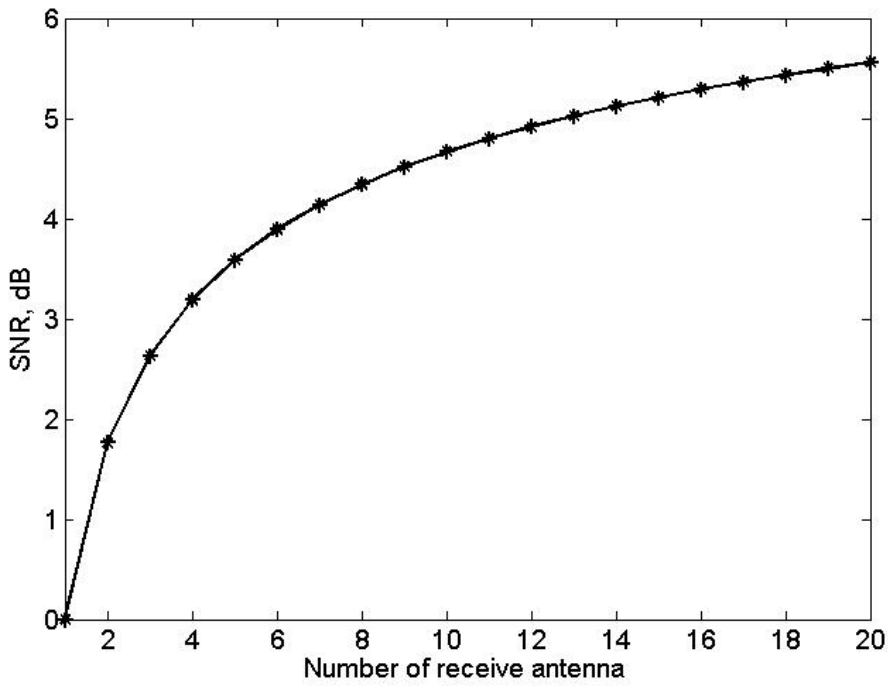

Figure 3.6: SNR improvement with Selection Combining

3.3.2 Threshold Combining

In selection combining, a receiver at each branch is needed to monitor SNR. A simpler combining technique was proposed known as Threshold Combining where one receiver is used to scan the branches sequentially and output the first signal that has SNR above a defined threshold. When a branch is selected, the combiner outputs that signal if the SNR on that branch is larger than the threshold, but if the SNR is drops below the threshold on the selected branch the combiner switches to another branch. There are several criteria used by the combiner to switch between the branches as shown in Fig. 3.7, the simplest one is to switch for another antenna randomly [47].

For both selection and threshold combining the output signal is equal to one of the diversity branches. Also they do not require any knowledge of the channel state information, thus these two diversity techniques can be used with coherent and non-coherent modulation [48].

To implement threshold combining is simple, since it does not require simultaneous monitoring of all branches.

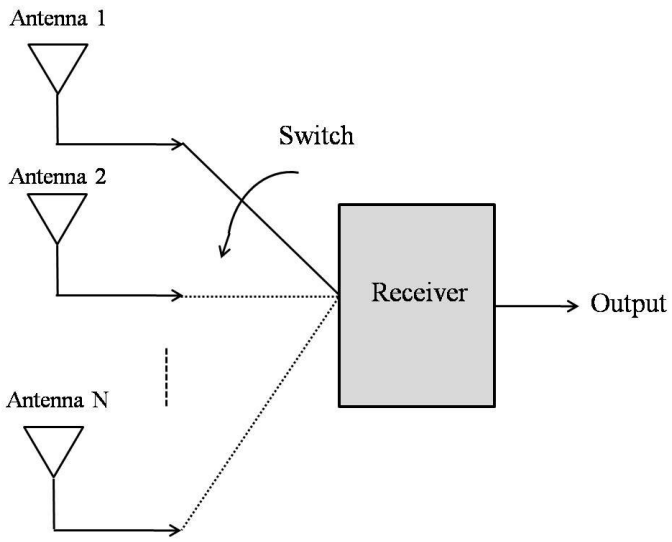

Figure 3.7: Switch Combining for N branches [46].

3.3.3 Maximal Ratio Combining

In switch combining and threshold combining, the signals at the output of the combiner will be equal to one of the signals on the branches. In Maximal Ratio Combining (MRC) the output is a weighted sum of the signals. The signals from all branches are out of phase therefore the signal must be multiplied by $a_i e^{-j\theta_i}$, where θ_i is the phase of the signal on the ith branch as shown in Fig. 3.8. In order to have a higher SNR at the output, the signal with lower SNR should have higher weighting.

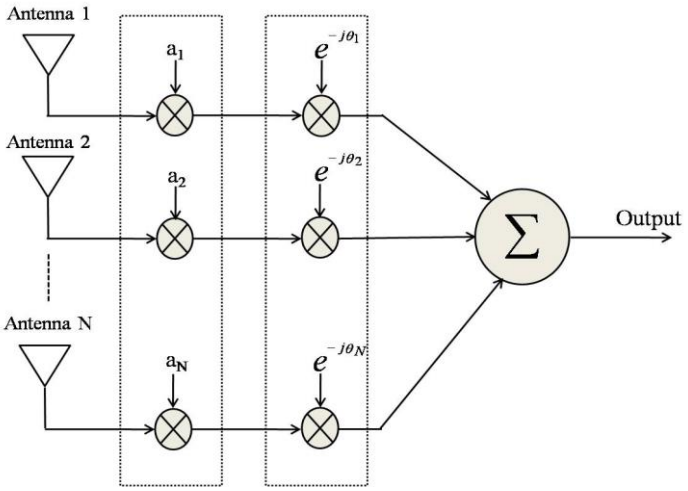

Figure 3.8: Maximal Ratio Combining for N branches [46].

3.3.4 Equal Gain Combining

Equal gain combining (EGC) is a simplified version of the MRC, where all the signals are weighted equally, i.e. $a_i = 1$ as shown in Fig. 3.9, thus each branch is co-phased by multiplying the signal with $\alpha_i = e^{-j\theta_i}$ and then all the branches are added together.

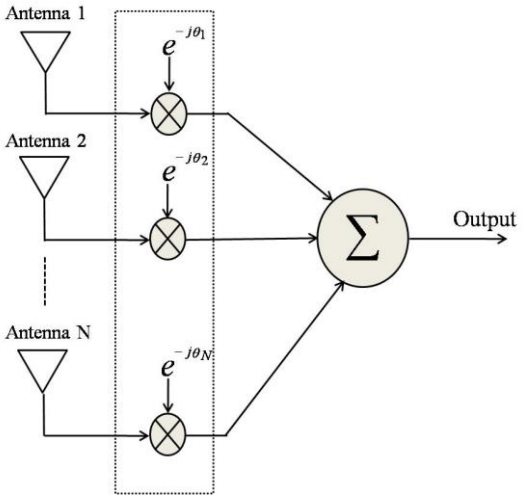

Figure 3.9: Equal Gain Combining technique for N branches [46].

SNR versus the number of receive antennas, for MRC and EGC over Rayleigh fading channel is shown in Fig. 3.10.

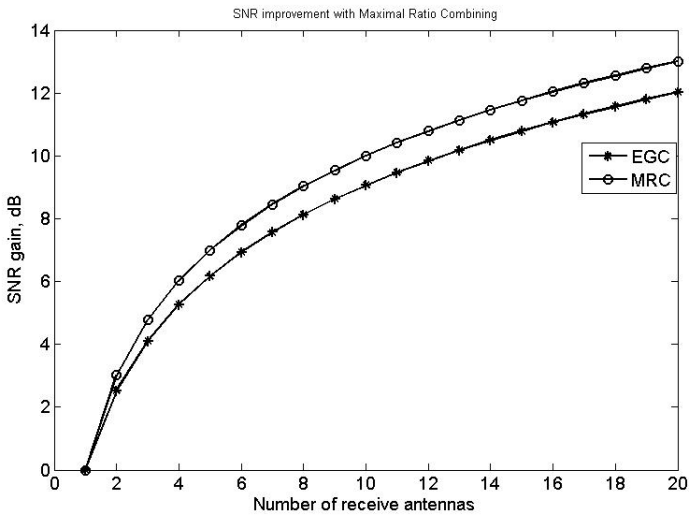

Figure 3.10: SNR versus the number of receive antennas, for both MRC and EGC over Rayleigh Fading channel

It is shown in Figure 3.10 MRC experience 1dB more that EGC, which is a power penalty paid when using EGC for the reduced complexity of the system, however the EGC performance is very close to the MRC [48][4].

3.4 Transmitter Diversity

Transmitter diversity is newer technique compared to receiver diversity. It has been implemented widely since the early 2000s. Since signals are transmitted from different antennas simultaneously, the signals superimpose, or interfere at the receiver. Thus some signal processing is needed at both the transmitted and the receiver in order to eliminate or attenuate the spatial interference. Transmitter diversity is attractive when space, power and processing complexity is available at the transmitter side rather than the receiver side; therefore transmitter diversity is implementable in downlink based systems such as WiMAX since it shifts the implementation of multiple antennas to the transmitter side, in this case is the base station. Transmit Diversity is categorised depending on the

knowledge of the channel gain at the transmitter. Thus transmit diversity and spatial multiplexing can be categorised as Closed Loop systems when the channel is known at the transmitter, a system quite similar to receiver diversity; and Open Loop when the channel is unknown at the receiver.

3.4.1 Closed Loop Transmit Diversity

A basic configuration for a Closed Loop transmit Diversity is shown in Figure 3.11 with N_t transmit antennas and one receive antenna. Let us assume that the path gain for the ith transmit antenna is h_i, where $h_i = r_i e^{j\theta_i}$ and it is known at the transmitter side, referred to as channel state information (CSI), CSI may be achieved by feedback from the receiver to the transmitter, but in systems where the channel is varying quickly like in mobile environment, Closed Loop schemes are not practical, thus they are useful primarily in low mobility and fixed systems.

Let the transmitted signal be s(t) with total signal energy E_s. The signal is multiplied by a complex gain $\alpha_i = a_i e^{-j\theta_i}$ $(0 \le a_i \le 1)$, which perform both weighting and co-phasing, then the signal is transmitted through the ith antenna. The weights of the transmitted signal must satisfy $\sum_{i=1}^{N_t} a_i^2 = 1$. The transmitted, weighted signals are added in the air therefore the signal at the receiver will be:

$$r(t) = \sum_{i=1}^{N_t} a_i r_i s(t) \tag{3.1}$$

At high SNR, the transmit diversity order with MRC is N_t, thus the transmitter and receiver MRC, EGC and SC diversity achieve full diversity order. The complexity in

transmitter diversity comes from obtaining the channel phase and the channel gain at the transmitter although they can be measured using the pilot technique at the receiver and then feedback to the transmitter. There are two important types of closed loop transmit diversity: Transmit Selection Diversity and Linear Diversity Precoding,

The simplest form of transmit diversity known as Transmit Selection Diversity proposed by Winters [49]. A subset of the available transmit antennas are used at a given time, where this subset of the antennas represent the best channels between the transmitter and the receiver, the advantages of this technique are:

- Less complexity and reduced hardware costs.
- Less spatial interference.
- Higher diversity order even when only a subset of the transmit antennas are used.

Linear diversity precoding, is a special case of Linear precoding, where the data rate is maintained unlike Linear precoding which improves the data rate and/or the link reliability [50][51].

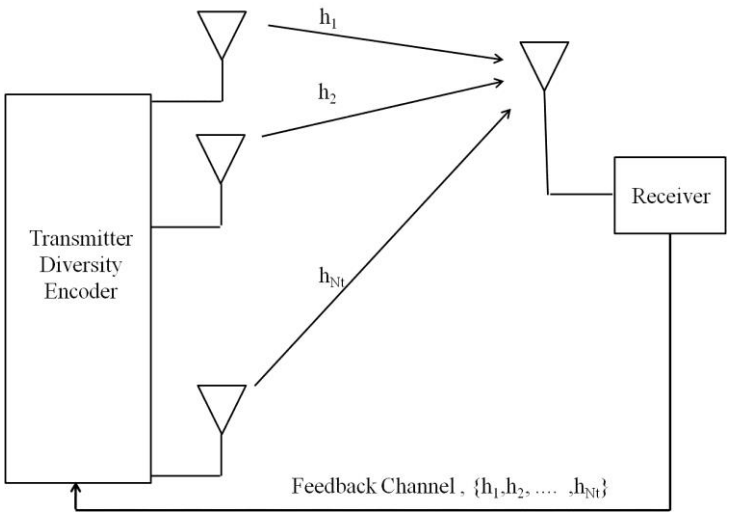

Figure 3.11: Closed Loop Diversity [29].

3.4.2 Open Loop Diversity

Space Time coding is the most known open loop diversity scheme, where a code known by the receiver is used at the transmitter.

Space time coding (STC) is performed in both spatial and temporal domain, introducing redundancy between signals transmitted from different antennas in different time slots, STC research focuses on improving the system performance by increasing the number of transmission antennas. The design of STCs has to trade-off between three main goals: simple decoding, minimizing bit error rate, and maximizing the information rate.

The question is how to maximize the data rate and minimize the bit error rate by using simple encoding and decoding algorithm.

There are two different space time codes methods, namely space time trellis codes (STTC) and space time block coding (STBC), in this chapter STBC will be discussed since it will avoid the high decoding complexity of STTC.

A major breakthrough in late 1990s was employed by space time block code known as the Alamouti code or Orthogonal Space Time Block Code (OSTBC) [52], which introduces two transmission antennas with full diversity and full rate (one symbol per channel use). The key point in this scheme is the orthogonality between the transmitted signal vectors over the two transmitted antennas. The code has become the most popular method of achieving transmitter diversity because of its simple implementation and diversity order. The Alamouti scheme was then extended to arbitrary number of transmission antennas by using orthogonal design theory [22, 53, 54 and 55].

However, for more than two transmission antennas, no STBCs with full diversity and full rate exist, thus, many different code design methods have been proposed promising either full diversity or full rate. In one opinion [4], It is better for STBCs to provide full diversity with extremely low encoder decoder complexity.

3.5 Spatial Multiplexing

The basic idea of spatial multiplexing (SM) is to send n_T independent symbols per symbol period using the space and time dimensions. Full diversity can be achieved by transmitting the encoded bits over all n_T transmitting antennas. The basic principle of SM for two antennas implemented at the transmitter and two antennas at the receiver is illustrated in Figure 3.12.

The bit stream to be transmitted is firstly de-multiplexed into two sub-streams then modulated and transmitted over each antenna as shown in Figure 3.12. Assuming the receiver knows the channel then it can differentiate between the co-channel and the exact signals and after the demodulation of the received signals, the original bit stream can be obtained by combining the received sub-streams. The spatial multiplexing increases the MIMO channel capacity with the number of the transmit-receive antenna pairs [6].

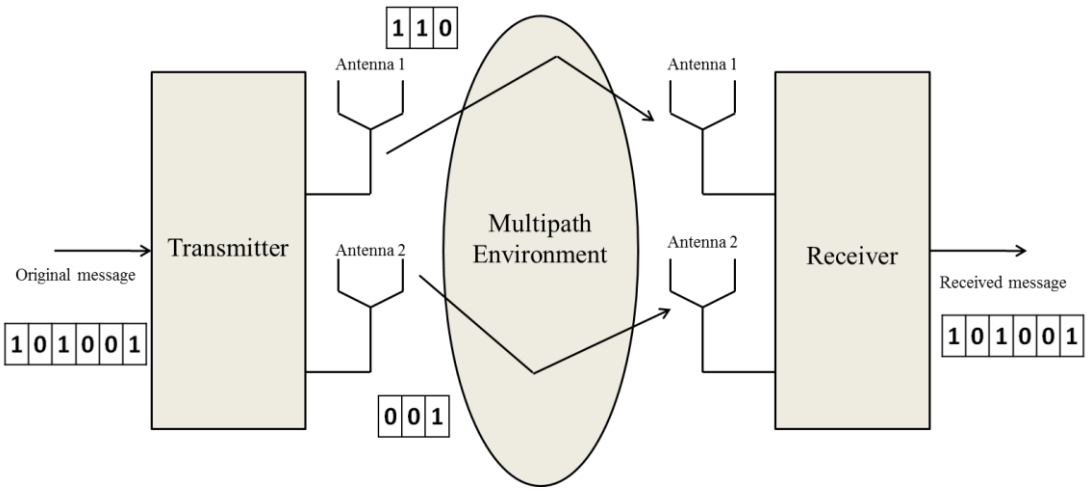

Figure 3. 12: A 2×2 MIMO system with spatial multiplexing. The original message is de-multiplexed into two sub streams and transmitted simultaneously from each transmitter [29].

If the number of the antennas at the transmitter is n_T and the receiver is n_R, then the maximum parallel channel that can be achieved in ideal MIMO system is $min(n_T, n_R)$. A considerable amount of research activity on spatial multiplexing has been carried out, research has shown that spatial multiplexing has the potential to increase the spectral efficiency [56, 57].

Further research has tried to enhance the concept of spatial multiplexing such as combining SM with other modulation schemes such as OFDM [58, 59]. Spatial multiplexing technique assumes the channel is known at the receiver and the performance can be enhanced by exploiting the channel knowledge at the transmitter. However SM does not perform well in poor SNR environments since it is more difficult for the receiver to identify the uncorrelated signal paths [60].

3.6 Space Time Block Coding

In general, STBC can be described as mapping n_N complex symbols $\{s_1\ s_2\ s_3\ \ldots\ s_N\}$ into a matrix S of dimension $n_t \times N$:

$\{s_1 \quad s_2 \quad s_3 \quad \ldots \quad s_N\} \rightarrow S$

STBC code matrix (S) taking the following form:

$$S = \sum_{n=1}^{n_N} s_n A_n + j s_n B_n \tag{3.2}$$

Where $\{s_1 \quad s_2 \quad s_3 \quad \ldots \quad s_{n_N}\}$ are the set of symbols to be transmitted, $s_{n1} = Re\{s_n\}$ and $s_{n2} = Im\{s_n\}$, and $\{A_n, B_n\}$ are fixed code matrixes with dimension of $n_t \times N$ called linear STBCs.

3.6.1 Alamouti Code

A block diagram of the Alamouti space time encoder is shown in Figure 3.13 in which the information bits are first modulated using an M-ary modulation scheme, i.e. each group of information bits m is modulated as $m = \log_2 M$ then the encoder takes the block of the two modulated symbols s_1 and s_2 in each encoding operation and transmitted over the transmission antennas according to the following code matrix:

$$S = \begin{pmatrix} s_1 & s_2 \\ -s_2^* & s_1^* \end{pmatrix} \tag{3.3}$$

The first row represent the first transmission period, where the symbols s_1 and s_2 are transmitted simultaneously from antenna one and antenna two respectively, and the

second row represent the second transmission period where, the symbols $-s_2^*$ and s_1^* are transmitted simultaneously from antenna one and antenna two respectively.

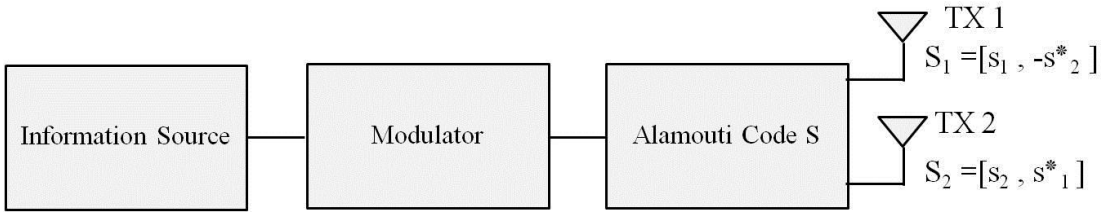

Figure 3. 13 : A block diagram of Alamouti space time encoder

Encoding is performed in both time domain (two transmission periods) and space domain (two transmission antenna). The key feature of the Alamouti scheme is that the transmit sequences from the two transmit antennas are orthogonal, since the inner product of the sequences S_1 and S_2 is zero, i.e

$$S_1.S_2 = s_1 s_2^* - s_2^* s_1 = 0 \tag{3.4}$$

Then, the code matrix has the following property:

$$\begin{aligned} S.S^H &= \begin{pmatrix} s_1 & s_2 \\ -s_2^* & s_1^* \end{pmatrix} \begin{pmatrix} s_1^* & -s_2 \\ s_2^* & s_1 \end{pmatrix} \\ &= \begin{pmatrix} |s_1|^2 + |s_2|^2 & 0 \\ 0 & |s_1|^2 + |s_2|^2 \end{pmatrix} \\ &= \left(|s_1|^2 + |s_2|^2 \right) I_2 \end{aligned} \tag{3.5}$$

where I_2 is a (2×2) identity matrix, which enables the receiver to detect s_1 and s_2 using simple linear signal processing. If it is assumed there is only one receiver antenna available, the channel fading coefficients from the first and second transmitter antenna to the receiver antenna at time t are denoted as $h_1(t)$ and $h_2(t)$ respectively. Assuming

that the fading across the channel is constant for two consecutive symbol transmission period, then they can be expressed as:

$$h_1(t) = h_1(t+T) = h_1 = |h_1| e^{j\theta_1} \qquad (3.6)$$
$$h_2(t) = h_2(t+T) = h_2 = |h_1| e^{j\theta_2}$$

where $|h_1|$ and θ_i, $i = 1,2$ are the amplitude gain and the phase shift for the path from the transmit antenna i to the receiver antenna. The received signals at t and $t+T$ can be written as:

$$r_1 = s_1 h_1 + s_2 h_2 + n_1 \qquad (3.7)$$
$$r_1 = -s_2^* h_1 + s_1^* h_2 + n_2$$

where r_1 and r_2 are the received signals at t and $+T$, n_1 and n_2 are independent complex variables representing additive white Gaussian noise (AWG) at time t and $t+T$.

Equation (3.7) can be written in matrix form as follows:

$$r = Sh + n \qquad (3.8)$$

where $h = [h_1, h_2]^T$ is the complex channel vector and n is the noise vector.

3.6.2 Combining and ML Decoding

If it can recover the channel coefficient h_1 and h_2 at the receiver then the decoder will use them as CSI. The maximum likelihood detector will select two signals $(\hat{x}_1, \hat{x}_2)$ from the signal modulation constellation to minimize the metric distance for all possible values of signals $\hat{x}_1$ and $\hat{x}_2$

$$d^2\left(r_1, h_1\hat{x}_1 + h_2\hat{x}_2\right) + d^2\left(r_2, -h_1\hat{x}_2^* + h_2\hat{x}_1^*\right) \qquad (3.9)$$
$$= \left|r_1 - h_1\hat{x}_1 - h_2\hat{x}_2\right|^2 + \left|r_2 + h_1\hat{x}_2^* - h_2\hat{x}_1^*\right|^2$$

Substituting equation (3.6) into (3.8), then the maximum likelihood decoding can be given by:

$$\left(\hat{x}_1,\hat{x}_2\right)=arg\min_{(\hat{x}_1,\hat{x}_2)\in C}\left(\left|h_1\right|^2+\left|h_2\right|^2-1\right)\left(\left|\hat{x}_1\right|^2+\left|\hat{x}_2\right|^2\right)+d^2\left(\tilde{x}_1+\hat{x}_1\right)+d^2\left(\tilde{x}_2+\hat{x}_2\right) \tag{3.10}$$

where C is the all possible constellation of the symbols $\left(\hat{x}_1,\hat{x}_2\right)$, $\tilde{x}_1$ and $\tilde{x}_2$ are the decision statistics created due to combining the two received signals with the CSI. Where $\tilde{x}_1$ and $\tilde{x}_2$ are represented by:

$$\begin{aligned}\tilde{x}_1&=h_1^*r_1+h_2r_2^*\\ \tilde{x}_2&=h_2^*r_1-h_1r_2^*\end{aligned} \tag{3.11}$$

For channel gains h_1 and h_2, the decision statistics $\tilde{x}_i$ (i=1,2) is a function of x_i (i=1,2). Therefore, the ML decoding rule in Equation (3.10) can be simplified into two decoding rules as shown in equations. (3.12) and (3.13):

$$\tilde{x}_1=arg\min_{\hat{x}_1\in S}\left(\left|h_1\right|^2+\left|h_2\right|^2-1\right)\left|\hat{x}_1\right|^2+d^2\left(\tilde{x}_1+\hat{x}_1\right) \tag{3.12}$$

$$\tilde{x}_2=arg\min_{\hat{x}_2\in S}\left(\left|h_1\right|^2+\left|h_2\right|^2-1\right)\left|\hat{x}_2\right|^2+d^2\left(\tilde{x}_2+\hat{x}_2\right) \tag{3.13}$$

3.6.3 Equivalent Virtual channel Matrix (EVCM) of Alamouti Code

Consider the conjugate of the signal r_2 (in equation 3.7) that is received in the second symbol period, it results in:

$$\begin{aligned}r_1&=s_1h_1+s_2h_2+n_1\\ r_2^*&=-h_1^*s_2+h_2^*s_1+n_2\end{aligned} \tag{3.14}$$

Thus the equation (3.14) can be written as:

$$\begin{pmatrix}r_1\\ r_2^*\end{pmatrix}=\begin{pmatrix}h_1 & h_2\\ h_2^* & -h_1^*\end{pmatrix}\begin{pmatrix}s_1\\ s_2\end{pmatrix}+\begin{pmatrix}n_1\\ n_2\end{pmatrix} \tag{3.15}$$

Or in short form as:

$$y = H_v s + n \tag{3.16}$$

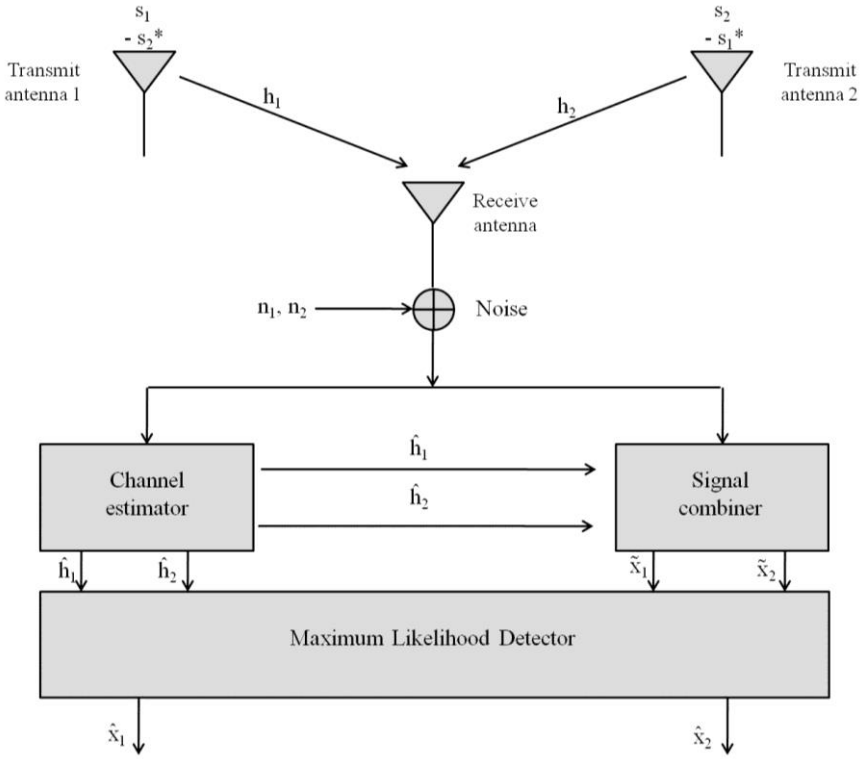

Figure 3. 14: Alamouti Receiver scheme [52].

where the modified receive vector $y = \left[r_1, r_2^* \right]^T$ has been introduced in (3.16). H_v is known as the equivalent virtual MIMO channel matrix (EVCM) of the Alamouti STBC scheme; it is given by:

$$H_v = \begin{pmatrix} h_1 & h_2 \\ h_2^* & -h_1^* \end{pmatrix} \tag{3.17}$$

Thus, by considering the elements of y in equation 3.16 as introduced from two virtual receive antennas (instead of received samples at one antenna at two time slots) one could

interpret the (2 × 1) Alamouti STBC as a (2×2) spatial multiplexing transmission using one time slot. The key difference between the Alamouti scheme and a true (2 × 2) multiplexing system lies in the specific structure of H_v. Unlike a general independent and identically distributed (i.i.d.) MIMO channel matrix, the rows and columns of the virtual channel matrix are orthogonal.

It is obvious that the EVCM depends on the structure of the code and the channel matrix. The concept of EVCM simplifies the analysis of the STBC transmission, therefore the existence of EVCM is one of the STBC characteristics.

3.6.4 Alamouti Scheme Simulation and Results

Diversity is a well-known technique to mitigate the fading effects over the communication link. Alamouti proposed a transmit diversity scheme that offers similar diversity gains, using multiple antennas at the transmitter, which was considered to be more practical, for example, where it is required to implement multiple antennas at the base station instead of multiple antennas for every mobile in a cellular communications system.

This section highlights this comparison of transmit versus receive diversity by simulating BPSK modulation over flat-fading Rayleigh channels. For the transmitter diversity, two transmit antennas are used and one receive antenna; and for receive diversity it employs one transmit antenna and two receive antennas; in addition to no-diversity link, i.e. one transmit antenna and one receive antenna.

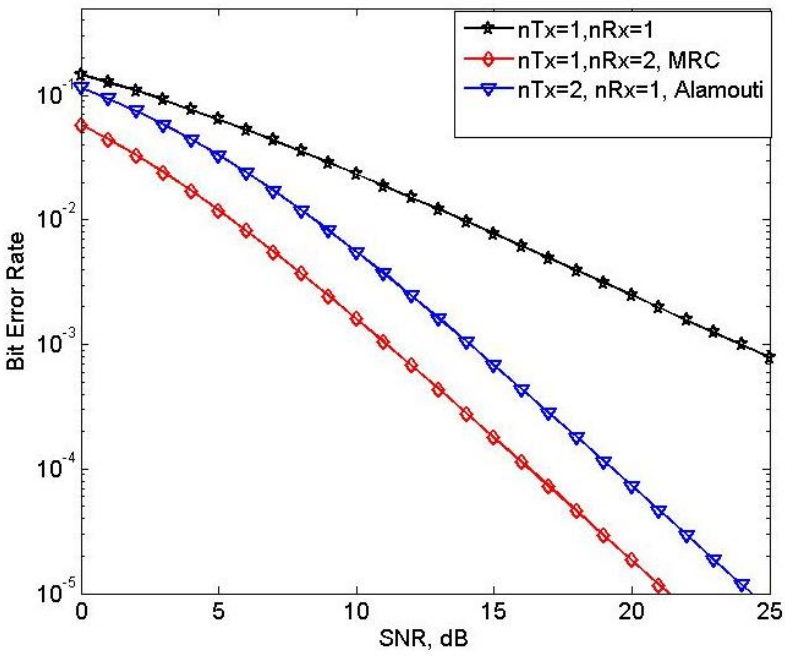

Figure 3. 15: BER for BPSK modulation with Alamouti STBC over Rayleigh channel using two transmit antennas and one receive antenna.

Figure 3.15 shows that using two transmit antennas and one receive antenna have the same diversity order as using one transmit antenna and two receiver antennas (MRC). Also it is noticeable that transmit diversity has 3 dB disadvantage compared with MRC receiver diversity because it modelled the transmitted power to be the same in both cases, but if the transmitted power is calibrated such that the received power in both cases to be same then the performance will be identical.

From Figure 3.16 it is noticeable that the (2 × 2) Alamouti scheme shows a better performance than either of the other diversity scenarios curves because the order of diversity in this case is $n_t \times n_r = 4$. In general, the Alamouti scheme with two transmit and n_r receive antennas has the same diversity gain as an MRC receive diversity scheme with one transmit and $2n_r$ receive antennas.

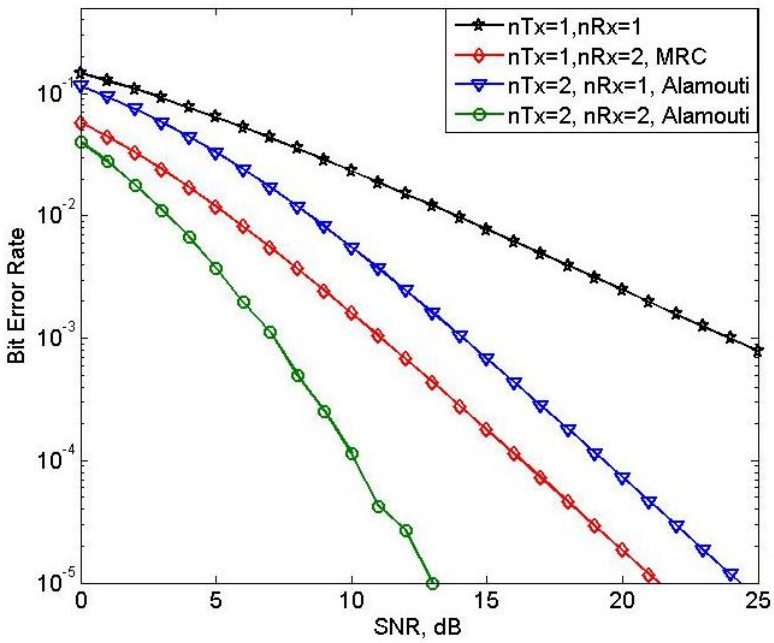

Figure 3. 16: BER for BPSK modulation for Alamouti scheme with 2 transmitters and two receivers over Rayleigh channel

3.7 Conclusions

Diversity techniques are used to improve the performance of the radio channel without any increase in the transmitted power. This chapter provides a summary of the receiver diversity techniques and their performance. Among different combining techniques, MRC has the best performance and the highest complexity while SC has the least complexity. the focus was on general principles illustrated by a few simulation examples. The simple Alamouti code and its performance were discussed in detail, where it was shown that Alamouti scheme with two transmit and n_r receive antennas has the same diversity gain as an MRC receive diversity scheme with one transmit and $2n_r$ receive antennas.

CHAPTER 4

A New Approach to Quasi-Orthogonal Space-Time Block Coding

4.1 Introduction

Traditional communication systems have a single antenna at the transmitter and a single antenna at the receiver, an arrangement known as Single Input Single Output (SISO). SISO systems have a capacity limited by the Shannon-Nyquist criterion. To meet the demand of high bit-rate transmission by modern communications systems, the bandwidth and the power of SISO systems would have to increase significantly. Fortunately, adopting a Multiple-Input Multiple-Output (MIMO) system can increase the capacity of a wireless system without the need to increase the transmission power or the bandwidth.

Transmit diversity is a well-known technique for mitigation of fading effects over a communication link. Alamouti [52] proposed a transmit diversity scheme offering maximum diversity gain using two antennas at the transmitter. This pioneering work provided the basis for the creation of orthogonal space-time block coding systems (OSTBCs) with more than two transmit antennas, starting with Tarokh's studies of the error performance associated with unitary signal matrices [55]. Sometime later, Ganesan

streamlined the derivations of many of the results associated with OSTBC and established an important link to the theory of the orthogonal and ‘amicable orthogonal’ designs [53].

It has been proved that a complex orthogonal design of STBCs which provides full diversity and full transmission rate is not possible for more than two transmit antennas [52]. To achieve full-rate transmission while largely retaining the orthogonality benefits of OSTBC, the Quasi Orthogonal Space-Time Block Code (QO-STBC) was proposed independently by three groups of researchers at about the same time: Jafarkhani [22], Tirkkonen, Boariu and Hottinen [23] and Papadias and Foschini [24]. It was Jafarkhani who named the code QO-STBC explicitly to describe the nature of the code, and this name was adopted in the literature. Boariu and Hottinen named their code ABBA after the code structure. Papadias and Foschini did not name their code [24].

A QO-STBC can achieve full rate but interference terms will appear from the neighbouring signals during signal detection. These will increase the detection complexity and decrease the gain performance.

In this chapter a new approach for Quasi-Orthogonal space-time block coding (QO-STBC) is proposed, with simple linear decoding via maximum likelihood detection. Conventional QO-STBC can achieve the full communication rate, but at the expense of decoding complexity and diversity gain due to interference terms in the detection matrix; thus, a QO-STBC scheme was proposed to eliminate interference from the detection matrix. The proposed code has improved diversity gain compared with the conventional QO-STBC scheme, and also reduced decoding complexity.

4.2 Conventional QO-STBC

In the quasi-orthogonal code structure, the columns of the transmission matrix are divided into groups. The columns within each group are not orthogonal to each other but those from different groups are orthogonal to each other. By using this quasi-orthogonal design, pairs of transmitted symbols can be decoded independently; the loss of diversity in QO-STBC is due to coupling terms between the estimated symbols.

A QO-STBC scheme for four transmit elements was proposed independently by Jafarkhani [22] and Tirkkonen [23]. Both of these proposed schemes achieve almost the same BER performance. For example the encoding matrix proposed by Tirkkonen [23] involves two (2×2) Alamouti codes X_{12} and X_{34} where:

$$X_{12} = \begin{bmatrix} x_1 & x_2 \\ -x_2^* & x_1^* \end{bmatrix} \text{ and } X_{34} = \begin{bmatrix} x_3 & x_4 \\ -x_4^* & x_3^* \end{bmatrix} \tag{4.1}$$

X_{12} and X_{34} are used in a block structure resulting in what is known as Extended Alamouti QO-STBC, X_{ABBA}, for four transmit antennas:

$$X_{ABBA} = \begin{bmatrix} X_{12} & X_{34} \\ X_{34} & X_{12} \end{bmatrix} = \begin{bmatrix} x_1 & x_2 & x_3 & x_4 \\ -x_2^* & x_1^* & -x_4^* & x_3^* \\ x_3 & x_4 & x_1 & x_2 \\ -x_4^* & x_3^* & -x_2^* & x_1^* \end{bmatrix} \tag{4.2}$$

If a code matrix X_{ABBA} from equation (4.2) is adopted over frequency-flat fading channel with four transmitter antennas and one receiver antenna, then the received signal can be given by the following:

$$r = X_{ABBA} h + n \tag{4.3}$$

where r is a vector of four successive signal samples at the receiver antenna, h contains the channel coefficients, i.e. $h = [h_1\ h_2\ h_3\ h_4]^T$, and n is the noise vector, i.e. n = [$n_1\ n_2\ n_3$

$n_4]^T$. Assuming a code matrix X_{ABBA} and a single antenna receiver, then the four received signals within successive time slots are:

$$
\begin{aligned}
r_1 &= -x_1h_1 + x_2h_2 + x_3h_3 + x_4h_4 + n_1 \\
r_3 &= -x_3h_1 + x_4h_2 + x_1h_3 + x_2h_4 + n_3 \\
r_2 &= -x_2^*h_1 + x_1^*h_2 - x_3^*h_3 + x_4^*h_4 + n_2 \\
r_4 &= -x_4^*h_1 + x_3^*h_2 - x_2^*h_3 + x_1^*h_4 + n_4
\end{aligned}
\tag{4.4}
$$

Noting the second and the fourth rows of the code matrix X_{ABBA} as complex conjugate, the received vector Y can be expressed as:

$$
Y = [r_1 r_3^* r_3 r_4^*] = H_v \cdot \begin{bmatrix} x_1 \\ x_2 \\ x_3 \\ x_4 \end{bmatrix} + n \tag{4.5}
$$

where H_v is the Equivalent Virtual Channel Matrix (EVCM) given by:

$$
H_v = \begin{bmatrix} h_1 & h_2 & h_3 & h_4 \\ h_2^* & -h_1^* & h_4^* & -h_3^* \\ h_3 & h_4 & h_1 & h_2 \\ h_4^* & -h_3^* & h_2^* & -h_1^* \end{bmatrix} \tag{4.6}
$$

H_v can be described as a highly structured, equivalent, virtual (4 × 4) MIMO channel matrix that replaces the (4 × 1) channel vector**.**

To decode the QO-STBC, the maximum ratio combining technique is applied, by multiplying the received vector Y with H_v^H it yields:

$$
\begin{aligned}
X &= H_v^H Y = H_v^H . H_v X_{ABBA} + H_v^H n \\
&= D_4 X_{ABBA} + H_v^H n
\end{aligned}
\tag{4.7}
$$

Here H_v^H is the Hermitian of H_v. Thus this concludes the derivation of $D_4 = H_v^H \cdot H_v$, the detection matrix used to decode the received signal. For the OSTBC scheme the detection matrix is always diagonal: this enables the use of simple linear decoding, but in the QO-STBC scheme this cannot be done due to non-orthogonality of the detection matrix, as shown in equation (4.8):

$$D_4 = H_v^H . H_v = \begin{bmatrix} \alpha & 0 & \beta & 0 \\ 0 & \alpha & 0 & \beta \\ \beta & 0 & \alpha & 0 \\ 0 & \beta & 0 & \alpha \end{bmatrix} \tag{4.8}$$

where the diagonal elements α represent the channel gains and elements β represent the interference from the neighbouring signals, for four transmit antennas:

$$\alpha = |h_1|^2 + |h_2|^2 + |h_3|^2 + |h_4|^2 \tag{4.9}$$

$$\beta = h_1 h_3^* + h_2 h_4^* + h_1^* h_3 + h_2^* h_4 \tag{4.10}$$

The interference terms β in the detection matrix cause performance degradation. Therefore more complex decoding methods were introduced to determine the estimate X of equation (4.7), as shown in the following:

$$\begin{aligned} X &= (H_v^H \cdot H_v)^{-1} \cdot H_v^H Y \\ &= (H_v^H \cdot H_v)^{-1} \cdot H_v^H . H_v \cdot X + (H_v^H \cdot H_v)^{-1} \cdot H_v^H . H_v \cdot n \end{aligned} \tag{4.11}$$

where

$$X = [x_1 x_2 x_3 x_4]^T$$

$$n = [n_1 n_2 n_3 n_4]^T$$

4.3 Proposed QO-STBC

In [61] a new QO-STBC scheme for three and four transmit antennas was proposed where the detection matrix of the conventional QO-STBC was to be reformed by using two Givens rotation matrices [62]. In this section we propose a new approach for the QO-STBC scheme, reforming the detection matrix using a different technique.

Assume the detection matrix D_4 given in equation (4.8) is considered for the present proposal. The properties of the eigenvalues can be simply defined by:

$$D_4.\mathrm{V} - \mathrm{V}.D = 0 \tag{4.12}$$

where D is equivalent to $D = \lambda I$, λ being the eigenvalue operator. Since D is the matrix of eigenvalues and V is the eigenvectors matrix then by definition $D_4.V = V.D$, with D and V given by the following:

$$D = \begin{bmatrix} \alpha+\beta & 0 & 0 & 0 \\ 0 & \alpha+\beta & 0 & 0 \\ 0 & 0 & \alpha-\beta & 0 \\ 0 & 0 & 0 & \alpha-\beta \end{bmatrix} \tag{4.13}$$

$$\mathrm{V} = \begin{bmatrix} 1 & 0 & -1 & 0 \\ 0 & 1 & 0 & -1 \\ 1 & 0 & 1 & 0 \\ 0 & 1 & 0 & 1 \end{bmatrix} \tag{4.14}$$

The eigenvalues matrix (D) is the interference-free matrix, which can be derived as follows:

1) From the relation between the eigenvalues (D) and eigenvectors (V) of matrix D_4:

$$D_4.V = V.D \tag{4.15}$$

2) Solving equation (4.15) for D

$$D = V^{-1} \cdot D_4 \cdot V \tag{4.16}$$

3) Substituting equation (4.8) in (4.16)

$$D = V^{-1} \cdot H_v^H \cdot H_v \cdot V \tag{4.17}$$

4) The relation between V^{-1} and V^H is given as

$$V^{-1} = \frac{1}{2} V^H \tag{4.18}$$

5) Substituting equation (4.18) in (4.17)

$$D = \frac{1}{2} V^H \cdot H_v^H \cdot H_v \cdot V \tag{4.19}$$

Thus a new channel matrix can be defined as:

$$H = H_v \cdot V \tag{4.20}$$

where

$$H = \begin{bmatrix} h_1 + h_3 & h_2 + h_4 & h_3 - h_1 & h_4 - h_2 \\ h_2^* + h_4^* & -h_1^* - h_3^* & h_4^* - h_2^* & h_1^* - h_3^* \\ h_1 + h_3 & h_2 + h_4 & h_1 - h_3 & h_2 - h_4 \\ h_2^* + h_4^* & -h_1^* - h_3^* & h_2^* - h_4^* & h_3^* - h_1^* \end{bmatrix} \tag{4.21}$$

$H^H.H$ is a diagonal matrix which can achieve simple linear decoding, because of the orthogonal characteristic of the channel matrix H. The encoding matrix X_{New} can be derived corresponding to the channel matrix H from equation (4.5), as shown in following equation (4.22):

$$X_{New} = \begin{bmatrix} x_1 - x_3 & x_2 - x_4 & x_3 + x_1 & x_4 + x_2 \\ x_4^* - x_2^* & -x_3^* + x_1^* & -x_4^* - x_2^* & x_3^* + x_1^* \\ x_1 + x_3 & x_2 + x_4 & x_3 - x_1 & x_4 - x_2 \\ -x_4^* - x_2^* & x_3^* + x_1^* & x_4^* - x_2^* & -x_3^* + x_1^* \end{bmatrix} \tag{4.22}$$

The new encoding matrix is quasi-orthogonal, and since its channel matrix H is orthogonal, ML decoding can be achieved via simple linear detection as shown:

$$\hat{X} = H^H \cdot Y = H^H H \cdot X_{New} + H^H n \tag{4.23}$$

For three antenna elements the coding matrix is derived by eliminating the last column of (4.2) as defined in (4.24),

$$X_3 = \begin{bmatrix} x_1 & x_2 & x_3 \\ -x_2^* & x_1^* & -x_4^* \\ x_3 & x_4 & x_1 \\ -x_4^* & x_3^* & -x_2^* \end{bmatrix} \tag{4.24}$$

Similarly, the detection matrix D_3 for three antenna elements scheme defined in (4.24), can be expressed as off-diagonal interference terms, given by:

$$D_3 = H_{v3}^H . H_{v3} = \begin{bmatrix} \alpha & 0 & \beta & 0 \\ 0 & \alpha & 0 & \beta \\ \beta & 0 & \alpha & 0 \\ 0 & \beta & 0 & \alpha \end{bmatrix} \tag{4.25}$$

Where H_{v3} is defined as,

$$H_{v3} = \begin{bmatrix} h_1 & h_2 & h_3 & 0 \\ h_2^* & -h_1^* & 0 & -h_3^* \\ h_3 & 0 & h_1 & h_2 \\ 0 & -h_3^* & h_2^* & -h_1^* \end{bmatrix} \tag{4.26}$$

And the interference terms α and β are defined as,

$$\alpha = |h_1|^2 + |h_2|^2 + |h_3|^2 \tag{4.27}$$

$$\beta = h_1 h_3^* + + h_1^* h_3 \tag{4.28}$$

Now, applying the similar method above to eliminate β terms and derive the channel matrix H_3 then, the quasi-orthogonal encoding matrix which results in free interference detection matrix can be stated by:

$$H_3 = \begin{bmatrix} h_1 + h_3 & h_2 & h_3 - h_1 & -h_2 \\ h_2^* & -h_1^* - h_3^* & -h_2^* & h_1^* - h_3^* \\ h_1 + h_3 & h_2 & h_1 - h_3 & h_2 \\ h_2^* & -h_1^* - h_3^* & h_2^* & h_3^* - h_1^* \end{bmatrix} \tag{4.29}$$

$$X_{3New} = \begin{bmatrix} x_1 - x_3 & x_2 - x_4 & x_3 + x_1 \\ x_4^* - x_2^* & -x_3^* + x_1^* & -x_4^* - x_2^* \\ x_1 + x_3 & x_2 + x_4 & x_3 - x_1 \\ -x_4^* - x_2^* & x_3^* + x_1^* & x_4^* - x_2^* \end{bmatrix} \tag{4.30}$$

4.4 Simulation and Results of the Proposed QO-STBC

The evaluation performance of the proposed scheme considered by equation (4.22) is investigated, over Rayleigh fading channels using a simple simulation model shown in Figure 4.1. The signals were modulated using QPSK, and the total transmit power was divided equally among the transmit antennas. The fading was assumed to be constant over four consecutive symbol periods and the channel was known at the receiver. Figure 4.2 shows the BER performance of the new scheme compared to the conventional QO-STBC for three and four transmit antennas, as given in [23]. It is clearly shown that the proposed scheme achieves better performance than the conventional scheme with about 2dB of additional power gain.

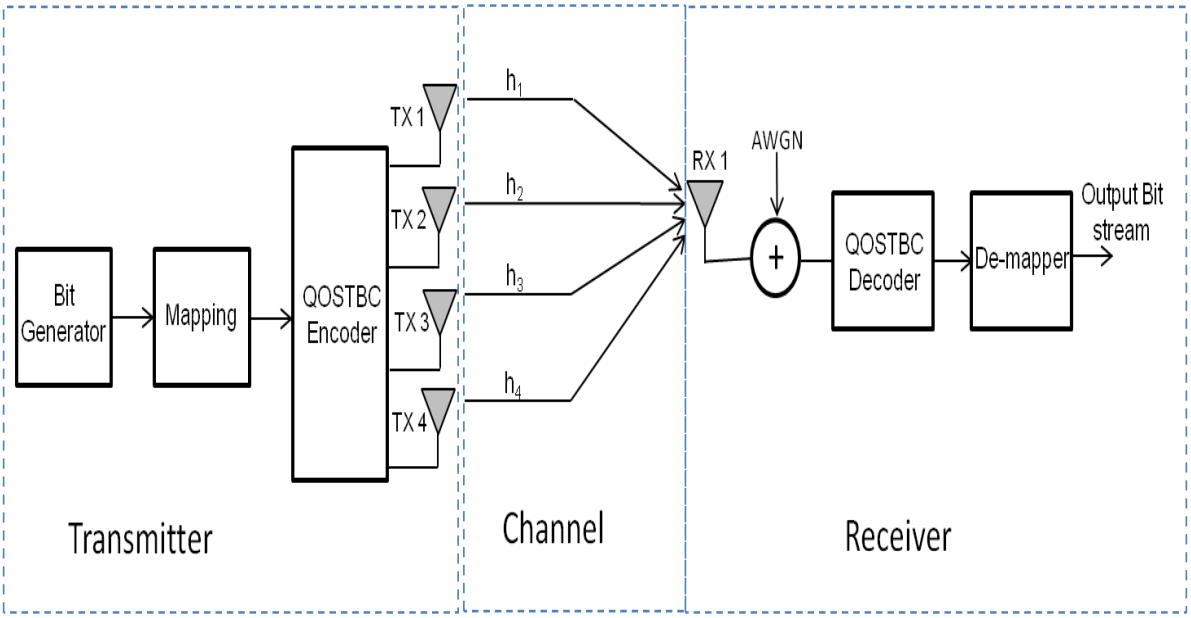

Figure 4. 1 : System Block Diagram

Figure 4.3 shows the Outage Probability of the proposed QO-STBC compared to the

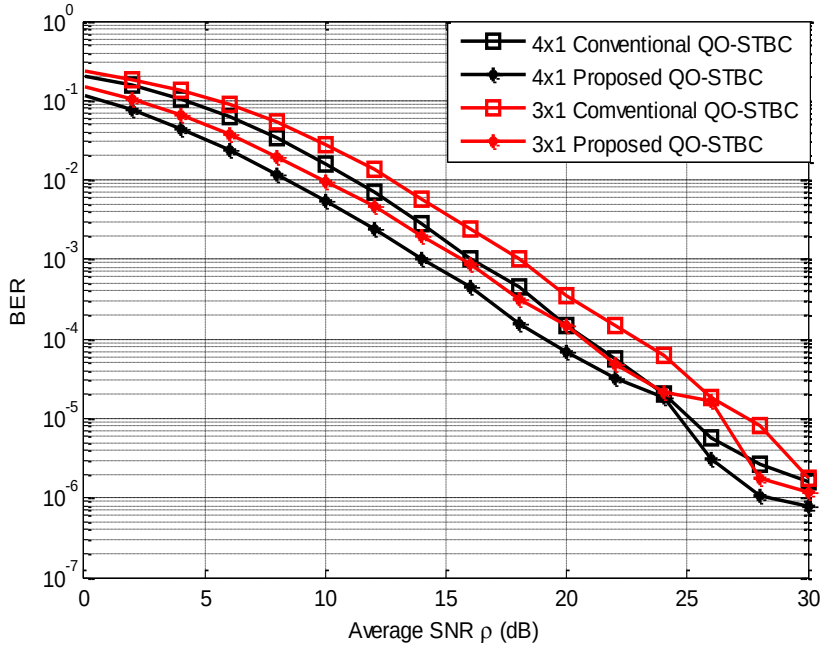

Figure 4.2: BER performance of proposed and conventional QO-STBC for 4 antennas.

conventional QO-STBC for four transmit antennas, where it can be observed that at high SNR the slope of the probability curves is equating to the diversity gain.

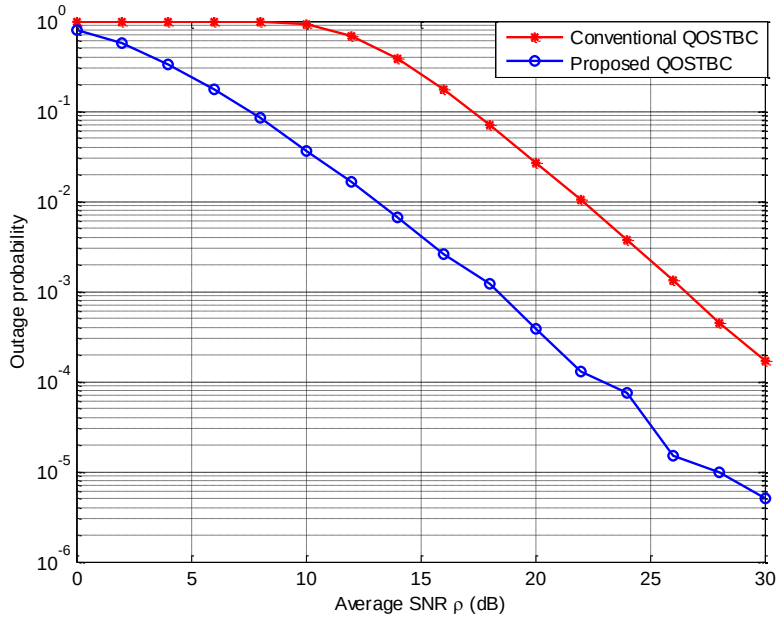

Figure 4.3: Outage Probability proposed QO-STBC compared to the conventional QO-STBC for four transmit antennas.

4.5 Space Time Code Design using Hadamard Matrix

A Hadamard matrix is an $n \times n$ matrix H_n with 1 and -1 entries that satisfy the orthogonality condition [9,10]. This matrix is given by:

$$H_n H_n^T = H_n^T H_n = nI_n \tag{4.31}$$

Where H_n^T is the transpose of H_n and I_n is the identity matrix of size n.

The Hadamard matrices are commonly used in communications systems, coding and cryptography, spectral analysis, data compression signal processing and numerical analysis [63, 64]. In this section the use of Hadamard matrix in data coding and decoding is addressed. The Hadamard matrices are popular due to their implementation simplicity and its efficient transforms [65]. An n-by-n Hadamard matrix with $n > 2$ exists only if

rem(n,4) = 0, where rem is the Remainder after division. This function handles only the cases where n, n/12, or n/20 is a power of 2.

Generally, square space time block codes are designed such that for each time slot one symbol is transmitted from one antenna, at which a Code matrix X is generated such that each row is orthogonal to another, i.e $XX^H = I$,where I is identity matrix and $(\cdot)^H$ is the complex hermitian matrix operator [13]. This section presents a novel STBC construction method based on Hadamard transform. In this regards, the generated codes are referred to as Hadamard Space-Time Block Codes (HSTBC)

4.5.1 Code Construction

Assume the transmitted symbols given by $S = [s_1, s_2, \ldots\ldots, s_N]$, then for four transmit antennas one can write the code matrix in form of a cyclic matrix as follows,

$$S_4 = \begin{bmatrix} s_1 & s_2 & s_3 & s_4 \\ s_2 & s_1 & s_4 & s_3 \\ s_3 & s_4 & s_1 & s_2 \\ s_4 & s_3 & s_2 & s_1 \end{bmatrix} \tag{4.32}$$

The Hadamard matrix of order four can be given by:

$$H_4 = \begin{bmatrix} 1 & 1 & 1 & 1 \\ 1 & -1 & 1 & -1 \\ 1 & 1 & -1 & -1 \\ 1 & -1 & -1 & 1 \end{bmatrix} \tag{4.33}$$

The resultant matrix X_4 is a HSTBC and might be expressed by:

$$X_4 = H_4 \otimes S_4 \tag{4.34}$$

$$X_4 = \begin{bmatrix} s_1 & s_2 & s_3 & s_4 \\ s_2 & -s_1 & s_4 & -s_3 \\ s_3 & s_4 & -s_1 & -s_2 \\ s_4 & -s_3 & -s_2 & s_1 \end{bmatrix} \tag{4.35}$$

Where '$\otimes$' is element-by-element multiplication.

Considering 4×1 MIMO system and utilizing the X_4 HSTBC code matrix, the system can be described as,

$$Y = h * X_4 + n \tag{4.36}$$

Where Y is the received signal matrix, $h = [h_{11} \quad h_{12} \quad h_{13} \quad h_{14}]$ is the channel matrix, X_4 is the code matrix and $n = [n_1 \quad n_2 \quad n_3 \quad n_4]$ is the noise matrix.

Hence, the virtual channel matrix can be written as;

$$H_v = \begin{bmatrix} h_{11} & h_{12} & h_{13} & h_{14} \\ -h_{12} & h_{11} & -h_{14} & h_{13} \\ -h_{13} & -h_{14} & h_{11} & h_{12} \\ h_{14} & -h_{13} & -h_{12} & h_{11} \end{bmatrix} \tag{4.37}$$

Similarly, the 8×1 MIMO system HSTBC code matrix for transmitted symbols $S = [s_1, s_2, \ldots, s_8]$ can be written as:

$$X_8 = \begin{bmatrix} s_1 & s_2 & s_3 & s_4 & s_5 & s_6 & s_7 & s_8 \\ s_2 & -s_1 & s_4 & -s_3 & s_6 & -s_5 & s_8 & -s_7 \\ s_3 & s_4 & -s_1 & -s_2 & s_7 & s_8 & -s_5 & -s_6 \\ s_4 & -s_3 & -s_2 & s_1 & s_8 & -s_7 & -s_6 & s_5 \\ s_5 & s_6 & s_7 & s_8 & -s_1 & -s_2 & -s_3 & -s_4 \\ s_6 & -s_5 & s_8 & -s_7 & -s_2 & s_1 & -s_4 & s_3 \\ s_7 & s_8 & -s_5 & -s_6 & -s_3 & -s_4 & s_1 & s_2 \\ s_8 & -s_7 & -s_6 & s_5 & -s_4 & s_3 & s_2 & -s_1 \end{bmatrix} \tag{4.38}$$

For 3×1 MIMO system HSTBC code matrix for transmitted symbols $S=[s_1,s_2,s_3]$ can be derived from X_4 code matrix by nulling the fourth time slot as follows,

$$X_3=\begin{bmatrix} s_1 & s_2 & s_3 & 0 \\ s_2 & -s_1 & 0 & -s_3 \\ s_3 & 0 & -s_1 & -s_2 \\ 0 & -s_3 & -s_2 & s_1 \end{bmatrix} \tag{4.39}$$

4.5.2 Space Time Block code from Diagonalized Hadamard Matrix (DHSTBC)

In this section a full rate and full diversity order of Diagonalized Hadamard Space Time code (DHSTBC) is presented. The codes generated using this method are orthogonal spate time codes, such as $XX^H=D$, where D is a diagonal matrix.

The generated codes are able to provide full rate and full diversity when the number of the receiver antennas are at least equal to the number of transmit antennas, the code matrices for DHSTBC are limited to the Hadamard matrices size ($N=2^n$, where $n\geq1$).

The application of (4.34) using matrix multiplication with N=2, i.e., $S_2=[s_1 \quad s_2]$ and Hadamard Matrix H_2 given by,

$$H_2=\begin{bmatrix} 1 & 1 \\ 1 & -1 \end{bmatrix} \tag{4.40}$$

Results in a code matrix given by:

$$X_2=\begin{bmatrix} s_1+s_2 & s_1+s_2 \\ s_1-s_2 & s_2-s_1 \end{bmatrix} \tag{4.41}$$

For N=4 and $S_4=[s_1 \quad s_2 \quad s_3 \quad s_4]$, the DHSTBC coding matrix X_4 can be defined by,

$$X_4 = \begin{bmatrix} s_1+s_2+s_3+s_4 & s_1+s_2+s_3+s_4 & s_1+s_2+s_3+s_4 & s_1+s_2+s_3+s_4 \\ s_1-s_2+s_3-s_4 & s_2-s_1-s_3+s_4 & s_1-s_2+s_3-s_4 & s_2-s_1-s_3+s_4 \\ s_1+s_2-s_3-s_4 & s_1+s_2-s_3-s_4 & s_3-s_2-s_1+s_4 & s_3-s_2-s_1+s_4 \\ s_1-s_2-s_3+s_4 & s_2-s_1+s_3-s_4 & s_2-s_1+s_3-s_4 & s_1-s_2-s_3+s_4 \end{bmatrix} \quad (4.42)$$

The elements of the DHSTBC matrices are linear combination of the transmitted symbols in which each STBC symbol contains information of each element of S_N.

4.5.3 Properties of DHSTBC code matrix

The generated codes using the proposed method above are orthogonal and they have the following properties:

Property 1: The product of X_N and its hermitian transpose X_N^H is diagonal matrix known as diversity product, i.e. the diversity product for X_2 is,

$$X_2 X_2^H = \begin{bmatrix} 2(s_1+s_2)^2 & 0 \\ 0 & 2(s_1-s_2)^2 \end{bmatrix} \quad (4.43)$$

And the diversity product for X_4 is,

$$X_4 X_4^H = \begin{bmatrix} 4(s_1+s_2+s_3+s_4)^2 & 0 & 0 & 0 \\ 0 & 4(s_1-s_2+s_3-s_4)^2 & 0 & 0 \\ 0 & 0 & 4(s_1+s_2-s_3-s_4)^2 & 0 \\ 0 & 0 & 0 & 4(s_1-s_2-s_3+s_4)^2 \end{bmatrix} \quad (4.44)$$

Thus, the rows of both X_2 and X_4 are orthogonal to each other.

Property 2: The summation across the columns of the code matrix returns the original transmitted symbols.

$$\sum_{n=1}^{N} X_N = [s_1, s_2, \ldots\ldots, s_N] = S \tag{4.45}$$

where n=1,2,…., N correspond to the rows of X_N, that is simply illustrated in Figure 4.4.

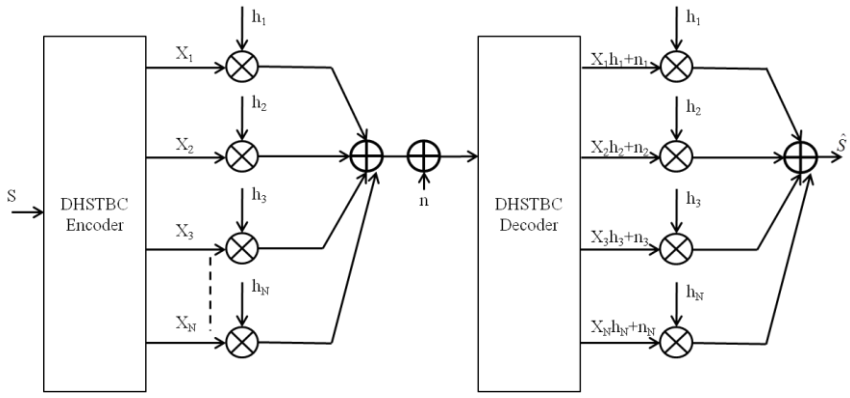

Figure 4.4: DHSTBC Encoding and Decoding

4.5.4 Simulation and Results of the Proposed DHSTBC

An evaluation of the performance of the proposed schemes in equation 4.42 over Rayleigh fading channel has been done using a simple simulation model. The signals were modulated using QPSK, and the total transmit power was divided equally among the number of transmit antennas. The fading was assumed to be constant over four consecutive symbol periods and the channel was known at the receiver. The same data bits and the same mechanism were used to evaluate all the proposed and conventional schemes.

Figure 4.5 shows the performance of the proposed DHSTBC compared to the conventional OSTBC for four transmit antennas. It is shown in Figure 4.5 that the proposed scheme achieves better performance than the conventional scheme. Figure 4.6

shows the Outage Probability of the proposed DHSTBC compared to the conventional OSTBC.

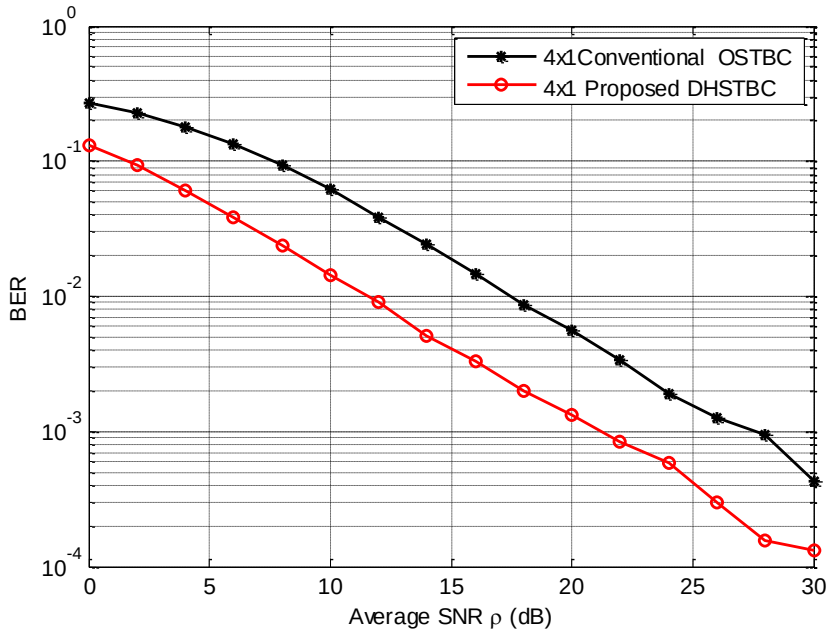

Figure 4.5: BER performance of the proposed DHSTBC compared to the conventional OSTBC.

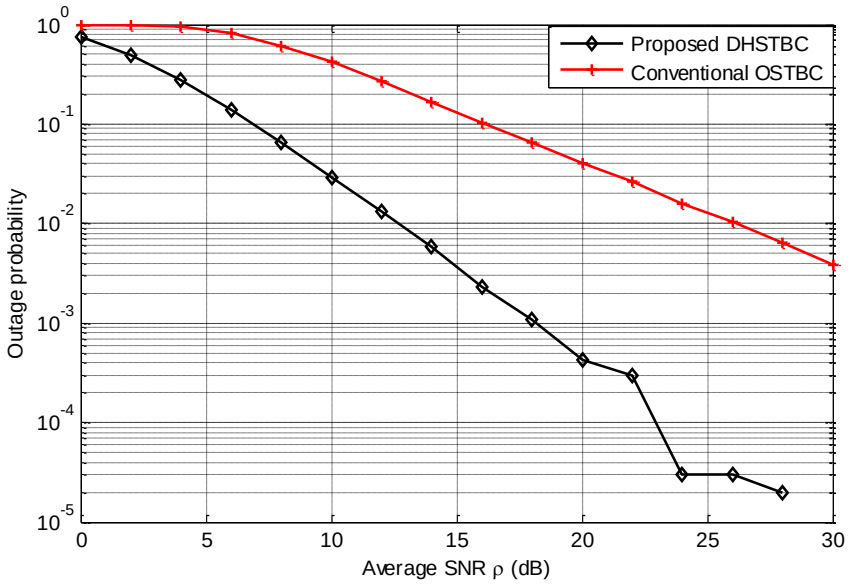

Figure 4.6: Outage Probability proposed DHSTBC compared to the conventional OSTBC.

4.6 Conclusions

In this chapter a novel QO-STBC scheme has been presented in terms of three and four transmit elements by reforming the detection matrix of the original QO-STBC scheme. An orthogonal channel matrix was derived that results in a linear decoding scheme simpler than the original OSTBC. The proposed scheme shows a better operation performance than the conventional scheme, with performance gains of about 2 dB being achieved. In addition, a Diagonalzed Hadamard space time code for four transmit antennas was proposed, the proposed scheme outperformed the conventional one due to the orthogonality of the detection matrix.

CHAPTER 5

Performance Evaluation of MIMO Selection Combining over WiMAX

5.1 Introduction

The Third Generation (3G) mobile systems, which is now being used in many parts of the world is providing good quality digital voice, video call, internet access, video/music download, video streaming and a host of other services; however the coming Fourth Generation (4G) will have the high data-rate to provide on-demand video and audio services, HD and 3D contents and many more bandwidth intensive applications.

The Worldwide Interoperability for Microwave Access WiMAX provides a robust wireless broadband solution that has much flexibility. It supports 2.3 GHz, 2.5 GHz, 3.5 GHz and 5.8 GHz spectrum [66, 67]. WiMAX was originally designed as a competitive alternative to other older wireless technologies, which has experienced four stages in its evolution [29], Local-loop narrowband system, Line-of-Sight (LOS) broadband system, Non-LOS broadband system, and Standard-based broadband system.

WiMAX supports point-to-point and point-to-multi-point Non-Line-of-Sight (NLOS) transmissions by incorporating OFDM in its physical layer and multi-antenna processing (MIMO) [29].

Traditional single carrier scheme had some inherent short falls which necessitated advancement into multicarrier modulation schemes. For instance, in single carrier, the channels are frequency selective i.e. they have different attenuation in different frequency bands making the channel unpredictable [68, 69]. These frequency selective channels introduce inter-symbol interference (ISI) at the receiver because of the spread in delay through the multipath channel.

Even if some equalization is applied at the receiver by giving higher amplification to regions in the frequency band where the attenuation is high, it will not entirely solve the problem because the noise within these bands will also be amplified, resulting in poor signal to noise ratio (SNR) and error rate probability [29].

The performance analysis of a WiMAX system adopting concatenated Reed-Solomon and Convolutional encoding with a block interleaver was presented in [70]. In [71] the effect of Rician fading and number of multipath on the MIMO systems capacity is investigated. The variation of Block Error Rate, throughput and Throughput Fraction with SNR, keeping the number of multipaths constant at 4, 8 and 12 are presented.

In [72], the throughput performance of an OFDM WiMAX (IEEE 802.16-2004) transmission system with adaptive modulation and coding (AMC) by outdoor measurements was evaluated. In [73], WIMAX transmission over noisy environment was investigated using Forward Error Correction method that applied Reed Solomon coding and Convolution coding to achieve low bit error rate.

WiMAX and other 4G systems enable the use of Multiple Input Multiple Output (MIMO) technology with Orthogonal Frequency Division Multiplexing (OFDM) to provide the high-data rate wireless access needed to achieve the high QoS that the end users have come to expect. MIMO systems have shown improved data throughput (maximum amount of useful data carried) and link range without increasing bandwidth or requiring more power. It also has higher spectral efficiency (more bits per second per hertz of bandwidth), more link reliability and reduced fading through the use of multiple transmit and receive antennas.

WiMAX is becoming a success in the market place because of its high data-rates and ease of deployment. Higher data-rates are promised for the future because the technology incorporates OFDM and MIMO showing that OFDM-MIMO is the future of wireless broadband technologies. This chapter analyses the performance of fixed WiMAX systems, as an extension for SISO systems and includes a MISO mode analysed using selection combining (SC). Bit Error Rate (BER) and throughput results are presented to highlight the operating performance of the systems.

5.2 The WiMAX PHY Layer

WiMAX uses OFDM to implement its physical layer when operating in NLOS conditions since OFDM is now recognized as a robust technique to overcome the effects of multipath [74]. By incorporating OFDM and MIMO, the latest standards of WiMAX can achieve very high peak data rates up to 70 Mbps when using the 20 MHz bandwidth and data rates of about 25 Mbps when using the 10 MHz bandwidth [75]. WiMAX supports multi-antenna (MIMO) technology, space-time coding (STC) and adaptive antenna system (AAS) [76].

WiMAX was designed by the IEEE 802.16 working group D, from the ground up, to achieve very high throughput over long distances [77]. To achieve this, very reliable and proven technologies where incorporated into it. Technologies like OFDM, TDD, FDD and QAM were used for its PHY layer implementation.

WiMAX also allows for a scalable PHY layer architecture which means that the data-rate is able to scale easily with the available bandwidth of the channel [76], thereby allowing for maximum channel utilization. The FFT can be scaled depending on the available bandwidth of the channel. Available FFT sizes may include 128, 512 or 1024 for a channel of bandwidth 1.25 MHz, 5 MHz or 10 MHz respectively. The FFT size for mobile WiMAX is scalable from 512- 4096 [78]. WiMAX Parameters are summarised in Table 5.1.

Table 5. 1: WiMAX Parameters

Parameter	Fixed WiMAX OFDM	Mobile Wimax			
FFT size	256	128	512	1024	2048
Number of used subcarriers	192	72	360	720	1440
Number of Pilots	8	12	60	120	240
Number of guardband	56	44	92	184	360
Cyclic Prefix	1/4,1/8,1/16,1/32				
Channel Bandwidth (MHz)	3.5	1.25	5	10	20
Subcarrier Spacing (KHz)	15.625	10.94			
Useful symbol time (µs)	64	91.4			
OFDM symbol duration (µs)	72	102.9			
No. OFDM symbols in 5 ms frame	69	48			
Guard time assuming 12.5% (µs)	8	11.4			

WiMAX technology is based on the IEEE 802.16 standard where IEEE 802.16-2004 and IEEE 802.16e are the physical layer (PHY) specifications. The IEEE 802.16-2004

supports multiple antenna option including Space Time Block Coding (STBC), Spatial Multiplexing and Adaptive Antenna Systems (AAS). The newer WIMAX standard (IEEE 802.16e) supports broadband applications for mobile terminals and laptops.

5.3 MIMO Implementations

There are three major approaches to implementing a MIMO system, namely Pre-coding, Spatial Multiplexing and Diversity Coding [79]. Pre-coding demands pre-knowledge of the channel while Spatial Multiplexing and Diversity Coding operate without any prior knowledge of the channel. In this chapter, diversity coding and how it builds redundancy into the system by sending data at different time slots and phase will be studied and discussed.

5.3.1 Transmitter Function

A design is presented and analysed which encodes the bits to be transmitted at the transmitter side using the OFDM approach. This comprises the following functions:

- Channel coding: There are different combinations of modulation and code rates available for the OFDMA burst. The channel coding consists of forward error correction (FEC), interleaving and modulation.
- Forward Error Correction (FEC): consisting of a Reed-Solomon (RS) outer code concatenated with a rate-compatible inner convolutional code (CC).
- Data interleaving.
- Modulation, using one of the BPSK, QPSK, 16-QAM or 64-QAM constellations specified.

- Orthogonal Frequency Division Multiplexing (OFDM) transmission is using 192 sub-carriers, 8 pilots, 256-point FFTs, and a cyclic prefix length of 24.
- Space-Time Block Coding uses an Alamouti code. This implementation uses the OSTBC encoder and combiner blocks.
- A Multiple-Input-Multiple-Output (MIMO) Rayleigh fading channel with Additive White Gaussian Noise (AWGN) for the STBC model.

5.3.2 Receiver Function

This contains the following functions,

- OFDM receiver that includes channel estimation using the inserted preambles.
- Hard-decision demodulation followed by de-interleaving, Viterbi decoding, and Reed-Solomon decoding.

5.4 Adaptive Modulation and Coding

The time-varying channel condition implies a time-varying system capacity. To achieve the optimum performance, adaptive data rate, power control, coding, bandwidth, antennas, and protocols are necessary. In wireless communication systems, link adaptation such as Adaptive Modulation and Coding (AMC) is essential if optimum use is to be made of link resources. AMC corresponds to data rate adaptation, in which changes are made to the modulation and coding format according to the channel conditions [80].

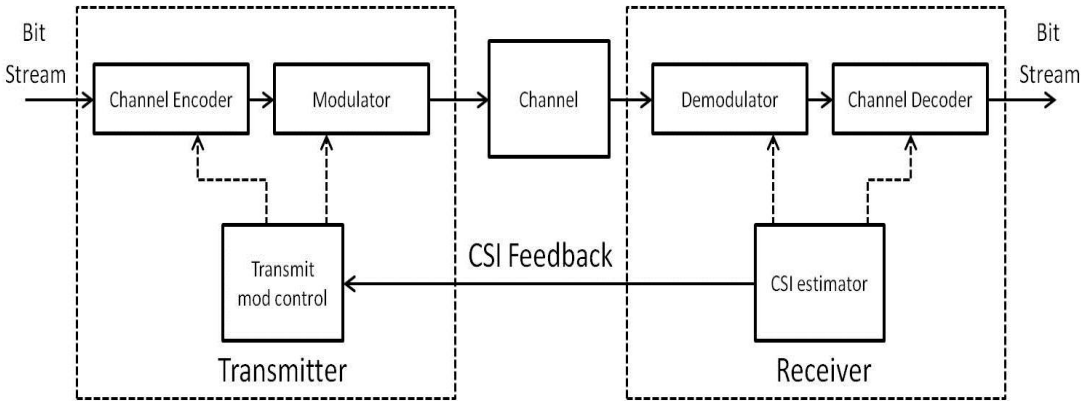

Figure 5. 1: Model for adaptive modulation and coding [76].

AMC achieves a robust and spectrally efficient transmission over time-varying channels, therefore it has been deployed in many wireless standards such as GSM, IS-95, wireless LANs, HSDPA, WCDMA and WiMAX, and also is likely to be deployed in forthcoming 4G standards. The transmitter needs to have the CSI before it can adapt its transmission scheme according to the channel condition. In a number of proposed systems, the CSI is usually estimated at the receiver, and then is fed back to the transmitter.

The power gain or the received SNR at a given time is estimated, and this information is used to adapt the modulation and coding parameters such as the data rate, transmit power, and coding parameters. These parameters are adjusted according to the received SNR at each instant, as illustrated in Figure 5.1 [76, 80, 81, 82, 83].

5.5 MIMO Configuration with Selection Combining

The Alamouti 2×1 configuration over OFDM was implemented over Rayleigh Fading Channel and AWGN using Simulink model as shown in Figure 5.2.

Figure 5.3 shows the implementation of the selection combining as discussed earlier in 3.6.4. The benefit of this diversity technique lies in its simplicity since it eliminates the

need for co-phasing of multiple branches and hence only one Branch output is allowed to go through. The overall signal-to-noise ratio gain increases as the number of antennas increases but this variation is not linear. The greatest increase is observed when going from zero diversity to two antenna diversity [29].

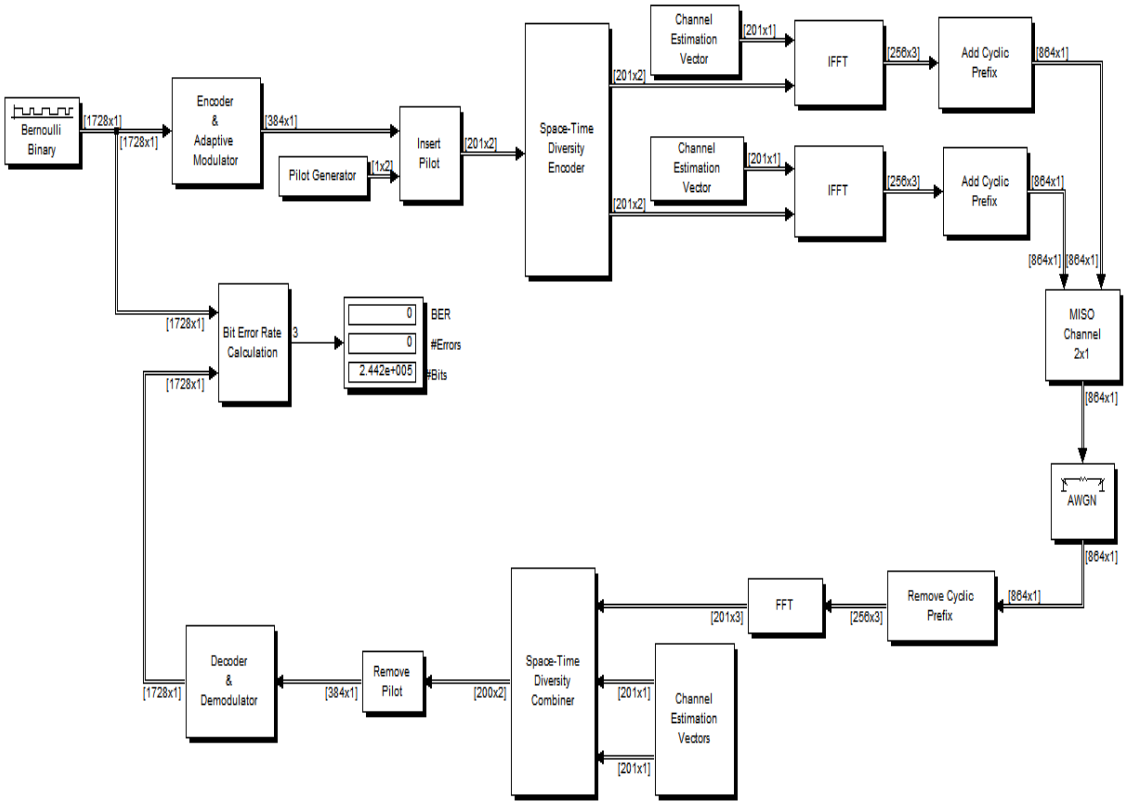

Figure 5. 2: Block diagram of the Alamouti 2x1 configuration.

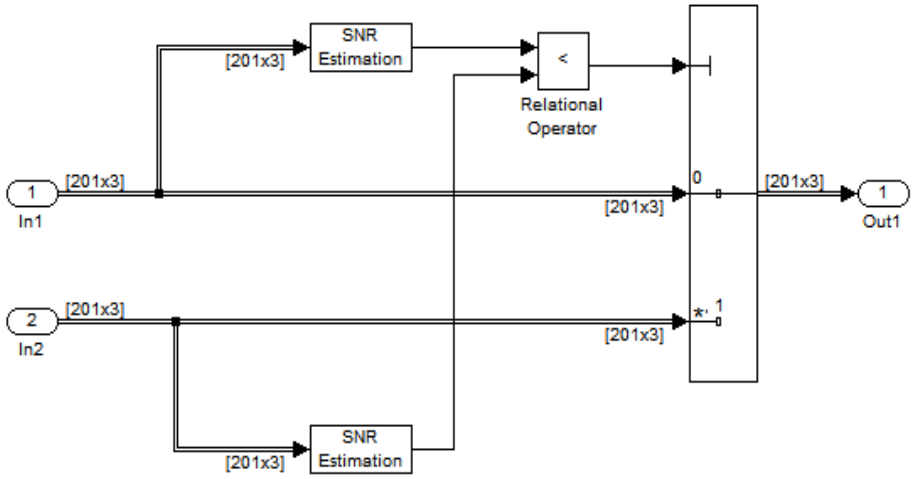

Figure 5. 3: The Selection Combining block.

Alamouti 2x2 configuration over OFDM was implemented using selection combining over Rayleigh Fading Channel and AWGN with Simulink as shown in Figure 5.4.

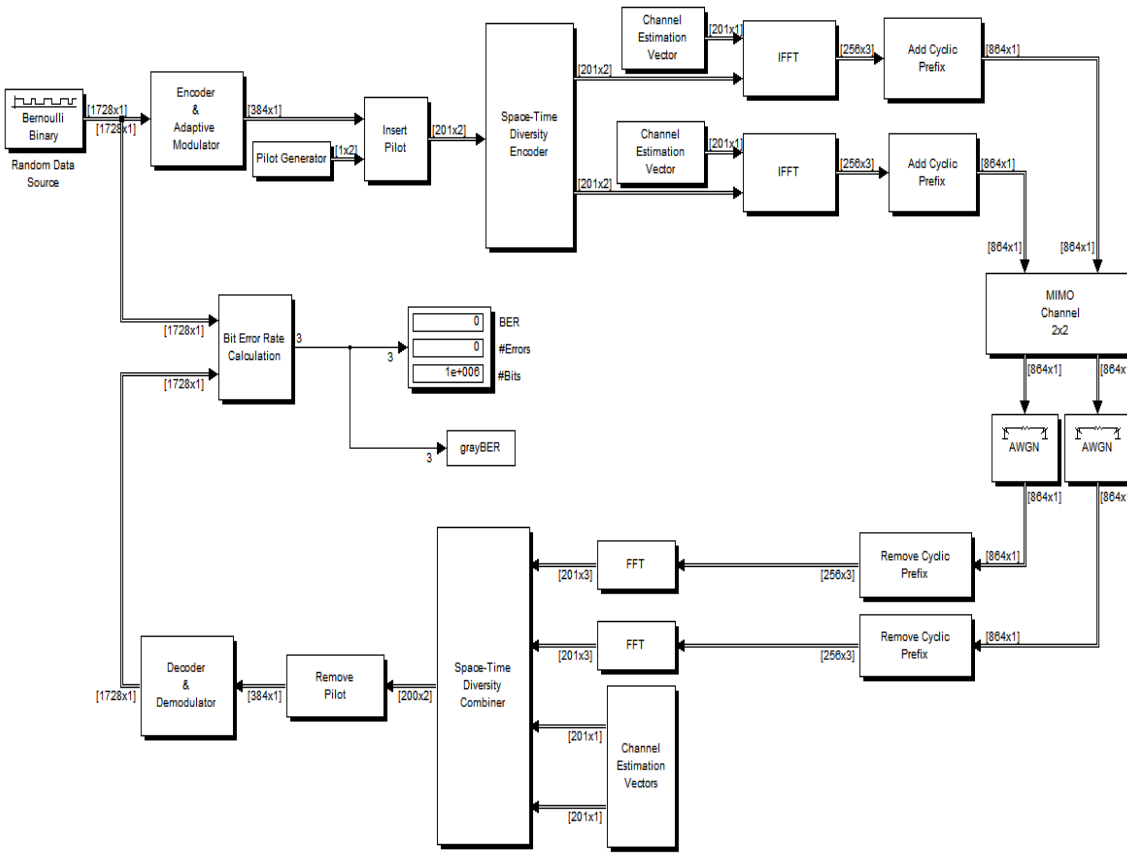

Figure 5. 4: The 2x 2 STBC Sc antenna configurations as implemented in Simulink.

5.6 Simulation and Results

In this section, BER and Throughput versus SNR results for all the required coding and modulation schemes by the IEEE 802.16d standard are presented. The system performance for two transmitters and one receiver is considered for analysis using selection combining; in addition to other examples employing two and three elements at the receiver. The simulation model was implemented in Simulink® 2010, the parameters used in this simulation are presented in Table 5.1.

5.6.1 System Bit Error Rate (BER)

The BER performance of different antenna configurations and different modulation schemes are presented. The BER graphs were evaluated using the BERTOOL. Figure 5.5 compares the BER versus SNR performance for MISO (i.e 2×1) for all possible modulations used in the IEEE 802.16d standard.

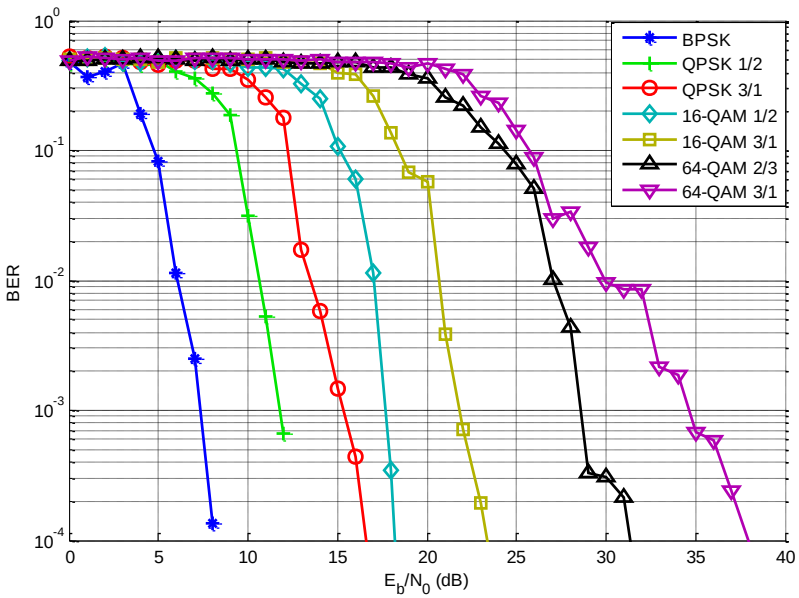

Figure 5. 5: BER vs. SNR performance for MISO**.**

Figure 5.6 shows BER versus SNR performance for 2x2 model using Selection combining at the receiver side.

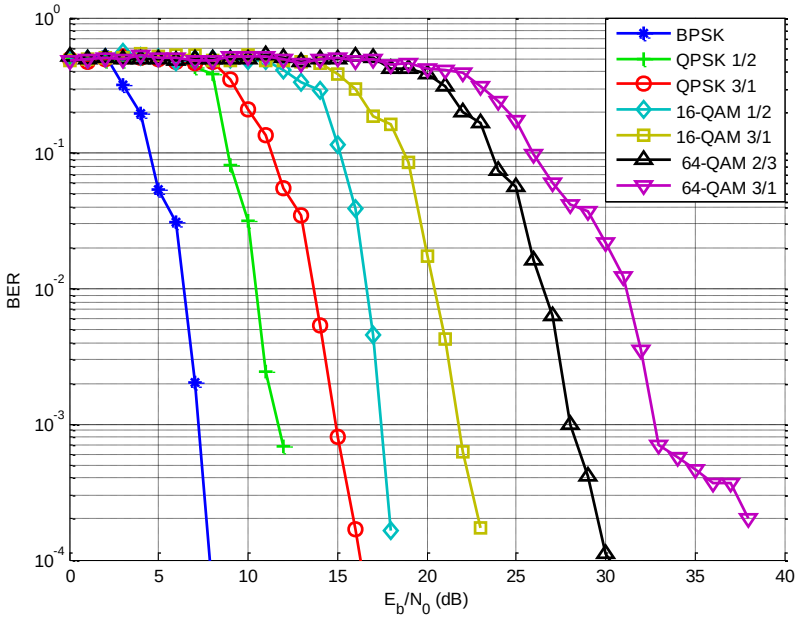

Figure 5. 6: BER versus SNR performance for 2×2 using SC.

Figure 5.7 shows BER versus. SNR performance for 2×3 model using Selection combing at the receiver side.

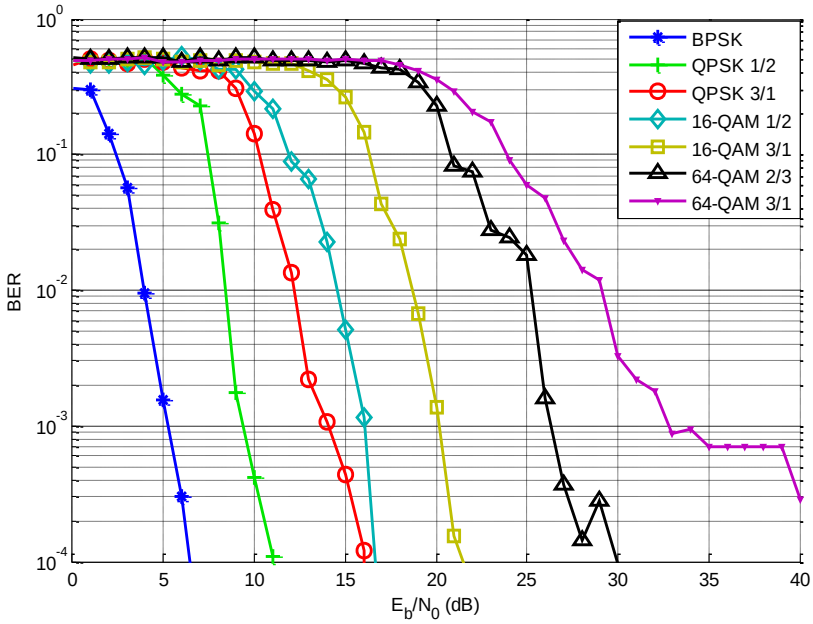

Figure 5.7: BER versus SNR performance for 2×3 using SC.

By comparing Figures 5.5, 5.6 and 5.7 one can notice that at high SNR values, the BER performance for 2×3 outperforms 2×2 and 2×1, i.e. at 20dB SNR the achievable BER for 2×3 is roughly double the one achieved by 2×2 and the BER achieved by 2×2 is roughly double the one achieved by 2×1.

5.6.2 Throughput Performance

The network throughput of a system is a very important parameter that can be used to classify network performance. Throughput refers to average rate of successful delivery of symbols over a communication channel [83]. Throughput is usually measured in bits/s or data packet/sec, in which a packet is said to be bad if one of its bits is received incorrectly and so it is discarded [76]. The equation for calculating the link throughput of a network in data packets/sec is given by,

$$C_{link} = \frac{N_D N_b R_{FEC} R_{STC}}{T_s} * (1 - PER) \tag{5.1}$$

where, PER, T_s, N_D, N_b, R_{FEC} and R_{STC} denote the Packet Error Rate, OFDMA symbol duration, the number of assigned data subcarriers, the number of bits per subcarrier, FEC coding rate, and space-time coding rate respectively.

Symbol duration T_s is given by,

$$T_s = {T_t}/{N_s} \tag{5.2}$$

Then equation (5.1) can be written as,

$$C_{link} = N_s * K * (1 - PER) \tag{5.3}$$

where K is different for each modulation scheme as shown in Table 5.2.

Table 5.2: Calculation of K for different modulation schemes

Modulation	N_D	N_b	R_{FEC}	R_{STC}	T_t	K
BPSK	192	1	0.5	1	0.1	960
QPSK 1/2	192	2	0.5	1	0.1	1920
QPSK3/1	192	2	0.75	1	0.1	2880
16-QAM 1/2	192	4	0.5	1	0.1	3840
16-QAM 3/1	192	4	0.75	1	0.1	5760
64-QAM 2/3	192	6	0.67	1	0.1	7680
64-QAM 3/1	192	6	0.75	1	0.1	8640

The relationship between PER and BER is given by,

$$PER = 1 - (1 - BER)^L \tag{5.4}$$

where L is the packet length in bits. For these calculations a packet length of one byte (8 bit) is used.

Therefore, equation (3) can be given as;

$$C_{link} = N_s * K * (1 - BER)^8 \tag{5.5}$$

Figure 5.8, 5.9 and 5.10 shows that the BPSK modulation scheme begins to experience some low throughput at a much lower SNR than the rest, but it can only achieve a maximum throughput of about 1Mbps, which is much lower than the others. The QPSK 1/2 modulation begins next to show some significant throughput but can only achieve a maximum value of about 3.8 Mbps. This is followed by QPSK 3/1, which achieves a maximum throughput of about 5.6 Mbps, while on the other hand, 16-QAM 1/2 achieves a maximum throughput of about 11.4 Mbps, 16-QAM 1/3 a maximum throughput of

about 17 Mbps, 64-QAM 2/3 a maximum throughput of about 30 Mbps, and 64-QAM 3/4 a maximum throughput of about 34 Mbps,

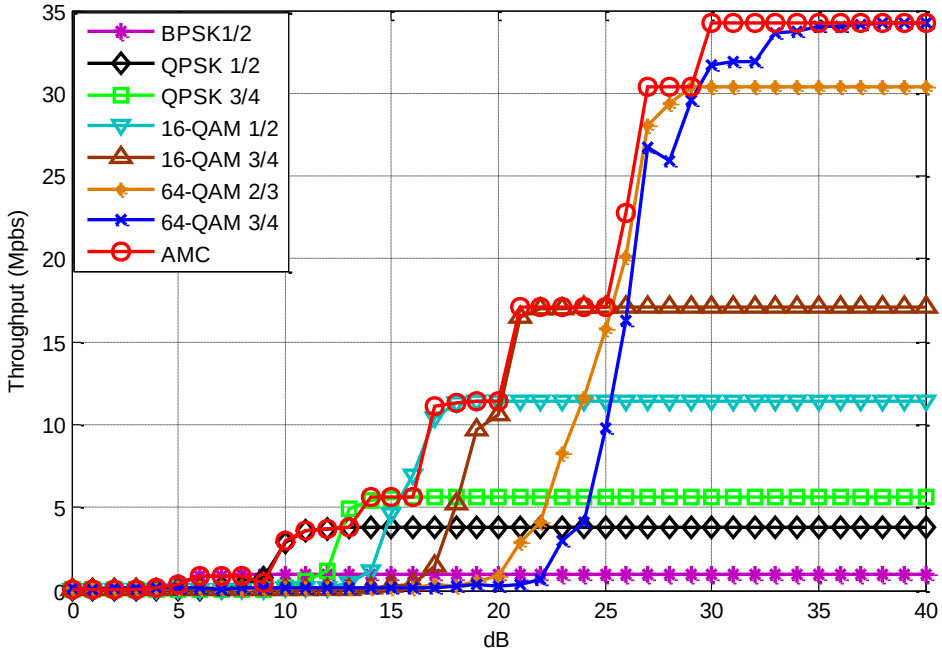

Figure 5. 8: Throughput versus the E_b/N_o for MISO (2x1).

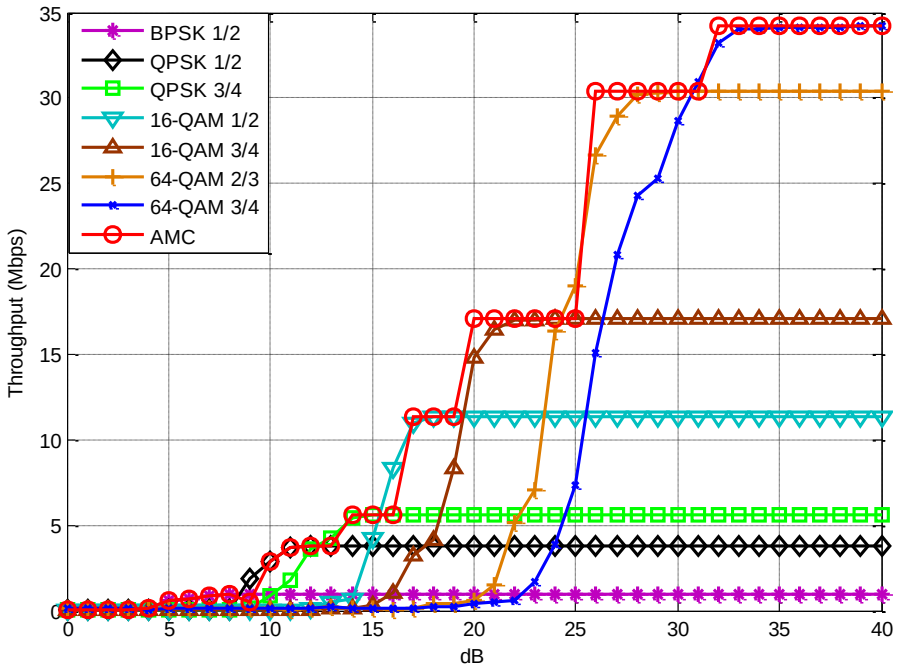

Figure 5. 9: Throughput versus the E_b/N_o for MISO (2x2) using SC.

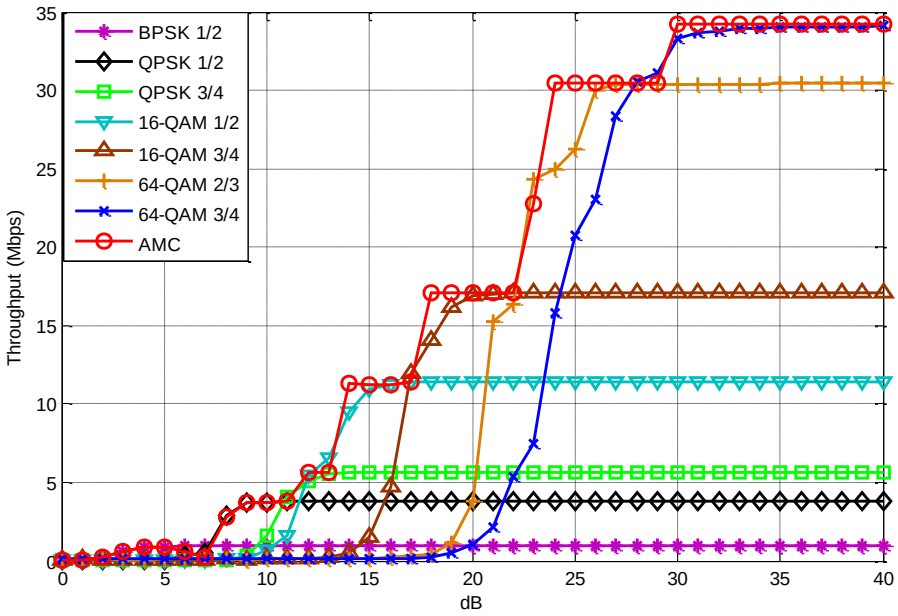

Figure 5. 10: Throughput versus the E_b/N_o for MISO (2x3) using SC

5.7 Conclusion

AMC is a great technique for potentially maximizing the overall throughput of a wireless system, however there are some challenges associated with its implementation. For instance, the mobile channel can be considered to be time-varying, thus the feedback mechanism of the system must be fast and reliable so the SNR information will not be obsolete when the next transmission is due. This limits the performance of the AMC technique for a fast time-varying channel because, if the coherence time of the channel is too small, then there may be a discrepancy between the predicted and the actual channel condition when the next transmission is due. If this occurs, it may even lead to a worse network performance because the wrong modulation scheme will be used for the wrong channel condition per time.

Furthermore, there is an increase in the complexity and cost of the transmitter and receiver units in the system. This has to be considered in making a compromise of whether to use AMC in the design of a wireless system or not.

However, in all our simulations, results and analysis, the MIMO 2×3 antenna configuration with AMC shows the best throughput performance potential of all the systems studied.

CHAPTER 6

Indoor Environment Channel Propagation Simulation and Measurements

6.1 Introduction

The performance of voice, video and data streaming applications using the recently developed standard 802.11n with its MIMO antenna options, strongly depends on the nature of the environment. Although many authors have provided evidence on the effectiveness of this technology in field strength distribution, throughput or propagation-simulation environments, work linking all of these parameters is limited. This chapter provides a comparison of these metrics for a 2×3 dual-band MIMO system operating at 2.4 and 5 GHz in a typical office building, obtained using a commercial wireless router.

The measurements are consistent with simulation results obtained using a 3D Shoot and Bounce Ray (SBR) software. Predictions of the radio propagation over an area of around 1600 m^2 required an evaluation time of less than 1 hour in a single processor computer for both frequencies. Agreement between predicted and measured Received Signal

Strength Indicator (RSSI) values are acceptable, with the conclusion that such simulation methods provide an accurate, affordable and time efficient alternative to measurements for the investigation, modelling and planning of WLAN networks using MIMO technologies.

The indoor wireless propagation channel between two antennas is influenced by numerous interactions between the transmitted signal and objects in the physical environment, creating multiple wavefronts. These interact to determine the pattern of path loss, shadowing and localised fast fading of the field. Simulation of the received signal distribution provides valuable information for wireless system applications.

Propagation models are designed using statistical and deterministic approaches. Statistical methods present several limitations, including low accuracy in small cell sizes and inapplicability to spatio-temporal channel characterization and hence to a majority of emerging wireless systems (OFDM, MIMO, UWB etc.) [84]. Therefore deterministic methods have become the preferred technique for channel propagation simulations. Deterministic models can be performed through the application of Maxwell's equation (i.e. FIT, FDTD) or by Ray tracing techniques (SBR). In view of the high number of multipath interactions involved in the calculations, either 2D or 3D simulations may be performed to provide sufficient computational accuracy for any given scenario [85].

A 3D Finite Integration Technique (FIT) approach was applied in [84] to radio propagation calculations over an area of 400 m^2. The modelling geometry was based on a building layout replicating the specified location of windows, doors and significant metallic furniture in a simulation supported by a single processor computer with

computing time less than 3 hours across the 400MHz-900MHz frequency range. Results show error standard deviation was in the range 2 - 3.7 dB which proved sufficient accuracy in the model. A similar approach was reported in [86] where simulation frequencies below 1GHz were considered for small scenarios giving insufficient reliability for higher frequencies or greater areas.

The high computing effort applied in this technique is noticeable due to the long period taken to both establish and run the simulation. This provides a substantial limitation on investigations where wider areas and higher frequencies are required, making the FIT model impractical [87], especially in terms of prediction accuracy and the spatial detailing.

Finite Difference Time Domain (FDTD) methods may be used to compute the electromagnetic response of a mixture of walls in a building. This is done by the discretizing the walls, corners and terminal locations into finite size building blocks and calculating the iterative field over the multiple scattering from the structures. FDTD provides for simple programming and a simple data base structure; however the excessive run time (55 hours) and memory requirement limits the applicability of this technique. Ray tracing requires rather complex programming, but may be applied to large scale and complex geometries [88].

Although the software code is usually complex to design and develop, a more user friendly software application can be applied to a ray based technique. This would not only overcome the commonly known disadvantage but also provide more promising solutions for the calculation of higher frequencies or wider areas.

Ray tracing combines the Shoot and Bouncing Rays (SBR) technique and the Uniform Theory of Diffraction (UTD) [89], which makes 3D SBR an efficient propagation prediction tool for simulation comparison with indoor measurements [90-93], including frequencies up to 5GHz [91].

The flexibility of the ray tracing method provides a broader scope for different network analysis tools, even for the prediction of field strength in cellular mobile networks [94], taking advantage of the detailed scenario that could be evaluated using the topology and the lossy material structure specifications that produce a realistic model and therefore a scalable accuracy in the results.

The implementation of SBR allows the comparison of commercial equipment using standardised regulations and frequencies to obtain the performance for wireless systems usually developed for Wireless Local Area Networks (WLAN), which with the use of 3D ray tracing allows evaluating several standards over real world scenarios such as 802.11b/g in [95, 96], 802.11a in [97] and even the simulation of the most recent 802.11n [98].

The study presented herein is based on a 3D SBR technique for the accurate prediction of field strength distribution over an area of 1728m^2 with frequencies of 2.4GHz and 5GHz.

6.2 Multipath Propagation Mechanisms

In a realistic environment, signal transmission follows not only the direct path, but also a number of distinct propagation paths. These paths undergo various effects depending on

the type of interaction between the wave and the surrounding objects. At the output port of the receiving antenna, the observed signal corresponds to a combination of different waves, each of them presenting a different attenuation and a different phase rotation. Moreover, each wave reaches the receiver with a distinct delay, linked to the length of the propagation path. Multipath propagation mechanisms may lead to a significant distortion of the received signal. On the other hand, a direct path, known as the line of sight (LOS) path, is not always available, which is particularly frequent in indoor configurations. In this case, so called non-line of sight (NLOS) paths are necessary to enable efficient radio communication. Figure 6.1 illustrates the concept of multipath propagation, as well as the main propagation phenomena, that result in the following:

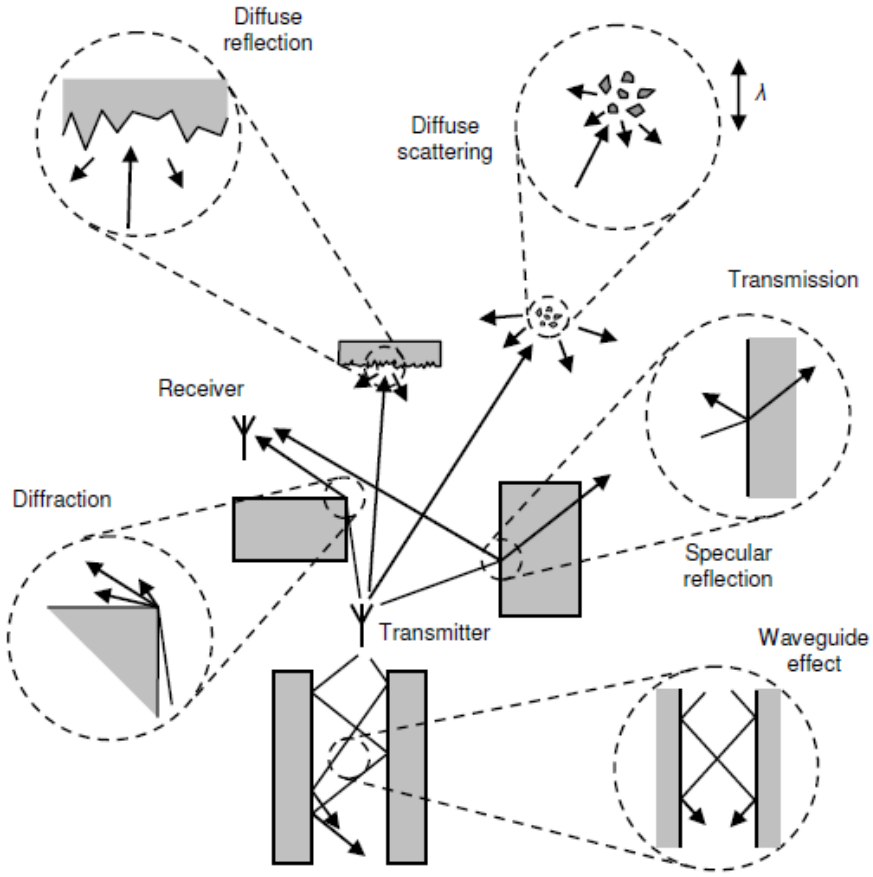

Figure 6. 1: Main Propagation mechanisms [89].

Reflection: reflection takes place on obstacles of large dimensions with respect to wavelength. When two different materials are separated by a plane surface (i.e. a surface where possible rough spots are small with respect to the wavelength), the reflection is said to be *specular*. In this case, the direction and the amplitude of the reflected ray are governed by the Snell-Descartes and Fresnel laws. When the surface separating the two materials presents non-negligible random rough spots, the reflection is called *diffuse reflection*. Most of the energy is then directed along the reflected ray, but part of the energy is diffused in neighbour directions.

Transmission: when the medium where a reflection takes place is not perfectly radio-opaque, part of the incident wave travels through the material following a so-called transmission mechanism. Most of the building materials used in indoor environments significantly attenuates the transmitted wave. For a given material, the attenuation and the direction of the transmitted signal are related to the wavelength, since the refractive index of the material varies with the frequency. Finally, for layered materials such as plasterboard, multiple reflections may occur within the material.

Diffraction: diffraction takes place on the edges of large sized obstacles with respect to the wavelength. This mechanism accounts for the electromagnetic field continuum on either side of the optical line of sight. The calculation of a diffracted field uses Huygens Principle [89, 90], which considers every point of a wave front as a secondary spherical source. Hence, diffracted waves are distributed along a geometrical cone, with an angle corresponding to the incident angle.

Diffusion: when an electromagnetic wave travels towards a group of obstacles of small dimensions with respect to the wavelength, the observed phenomenon corresponds to the superimposition of a large number of random diffractions. In this case, the behaviour of the incident wave is handled in a statistical way and the resulting phenomenon is called *diffusion*. In general, the electromagnetic wave is directed in all directions with a variable attenuation. This phenomenon is generally observed in outdoor environments, for instance in the presence of tree foliage. In indoor environments, diffusion may occur on a group of small objects.

Waveguide effect: the waveguide effect occurs in indoor environments, between two corridor walls for instance. Successive reflections on two parallel obstacles lead to a global wave motion along the guiding direction. This phenomenon also occurs in urban environments, for instance between two buildings lining a narrow street.

6.3 Model Structure Design

The actual environment, for the measurements and analysis of the MIMO systems was the corridor of the 3rd floor of B wing of the Chesham building, at the University of Bradford. The corridor dimensions were obtained from the building layout and compared with physical dimension measurements to verify the accuracy of the drawing. All of the measurements performed on this environment were taken overnight, to avoid the inference created by the human body of people walking over the corridor and to minimise interference from WLAN radio traffic. The materials of the walls, doors, ceiling, ground and windows were physically verified in order to have an approximation of the widths of each element.

The simulation was performed through 3D Shoot and Bouncing Ray (3D SBR) technique, using 0.2˚ ray spacing, 7 reflections, 2 transmissions and 0 diffractions, which allowed evaluation of the paths launched from the transmitter. Following the basic multipath mechanisms (reflection, diffraction, transmission and scattering), it was possible to determine the rays reaching the receiver and therefore to calculate the path loss. Once the ray-launching computations have identified the approximate ray-paths, use of the image technique permits a more precise determination of the ray geometries having reduced the number of structures involved in ray interactions. Depending on the scenario and required accuracy, either 2D or 3D simulations may be performed [85]. The Wireless InSite model allowed for the configuration of specific parameters for its complete simulation: waveform, antenna, transmitter, receiver, model, materials and output.

The waveform type used for the simulations was a Gaussian waveform of 5230 MHz and 2410 MHz frequencies with 23 MHz bandwidth. The antenna type implemented were linear dipoles, vertically polarized with a 6 cm length, and maximum receiver sensitivity of -100 dBm, using the Gaussian waveform previously defined. Two transmitter and three receiver dipole antennas were used with a quarter wavelength ($\lambda/4$) separation. The construction of the model followed the corridor layout used for the physical measurement. The model therefore has the same dimensions of the building corridor corresponding to 64 × 26 × 3 meters as shown in Figure 6.2.

The model was successfully completed by detailed modelling establishing two types of walls: 20 cm thick and 12 cm thick (block material) according to the floor layout seen in Figure 6.2 and Table 6.3.

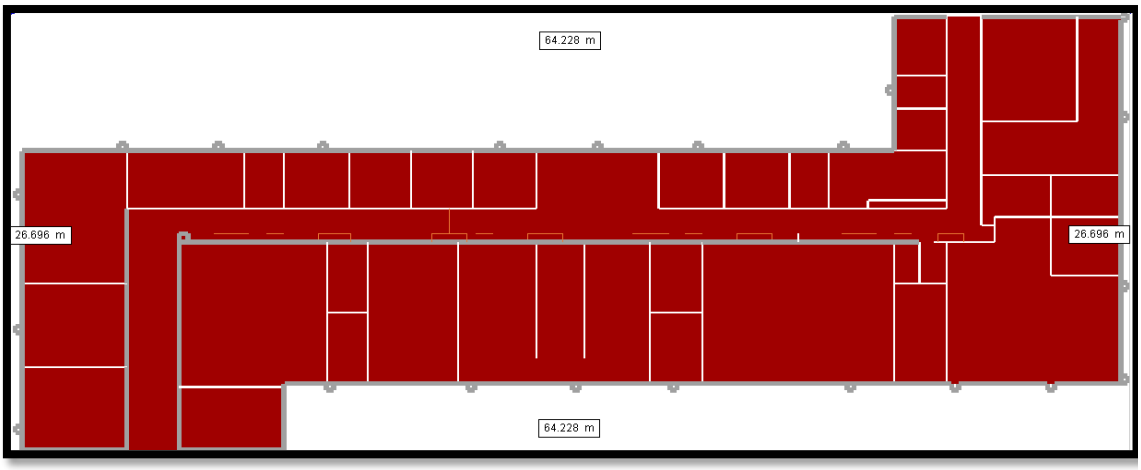

Figure 6.2: Floor Plan Simulated Model Dimensions.

Two types of doors were identified, wooden doors (office doors) and crystal doors, the latter having two sub classifications: 2 glass crystal door (meeting rooms) and the 4 glass crystal door (labs doors), shown in the Figure 6.2. Furniture such as wooden closets and door frames were also included in the model.

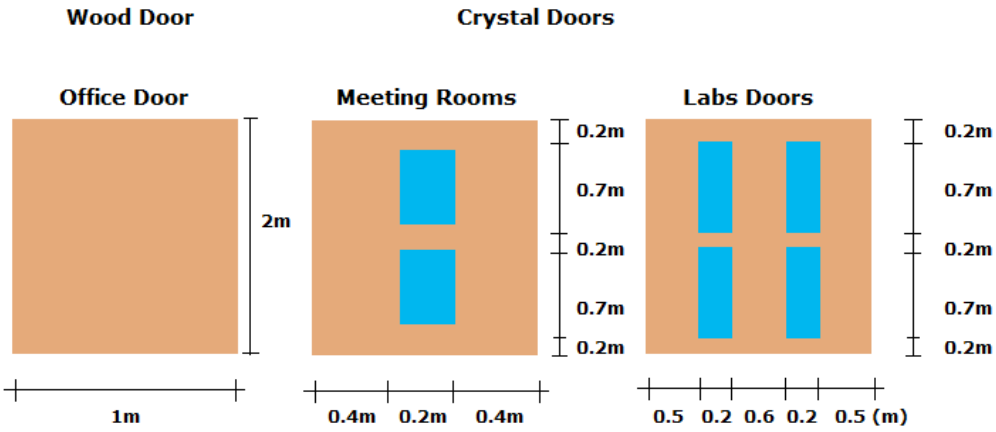

Figure 6.3: Doors Dimensions.

The floor and the ceiling, 3m above the floor, were defined as block material. A second ceiling was simulated, 2.5m above the floor, acting as the foam ceiling tiles with 3cm

thick of a soft dielectric material. Exterior windows and frames were also confirmed on a physical comparison survey.

The properties of the materials used in the model were defined according to the investigation described in [88], which defines the electrical parameters for building materials.

Table 6. 1: Wall types for indoor database.

Type	Layer Thickness
Wall	12cm - Block
Wall	20cm - Block
Door	6cm - Wood
Window	1cm - Glass

The outputs required for the overall environment was the received power over each receiver location (90 in total) as well as the power delay profile for the NLOS and LOS simulated scenarios.

6.4 RSSI Measurements Campaign

The first measurement campaign was developed to evaluate the field strength distribution using one laptop and two MIMO 2×3 systems along the corridor of 3rd floor of B wing Chesham Building at the University of Bradford.

The antennas used as part of this research were the Dlink DAP-2553 access points. These access points operates at dual band frequencies of 2.4 GHz (2400 ~ 2483.5MHz) and 5

GHz (5.15 ~ 5.35GHz and 5.47 ~ 5.725GHz for Europe), with MIMO 2×3 antennas arrangement, which means 2 antennas were used for transmitting and 3 antenna for reception. This equipment performs according to the regulatory 802.11n standard and are compatible with 802.11a/b/g. An additional feature that this antenna includes is a Power over Ethernet Port.

The particular reason to use these antennas is the flexibility to operate in a Wireless Client (WC) mode, Access Point (AP) mode or Wireless Distributed System (WDS), which will be fundamental for the chapter purposes [99]. The WDS mode, allows to connect two MIMO systems without been observed by other wireless equipment (i.e. Laptops, Access points, mobile phones).

6.4.1 Operational Parameters

This MIMO system works with adaptive modulation using BPSK, QPSK, 16QAM, 64QAM with OFDM techniques, depending on the data rate desired for the link. As the standard establish in this equipment uses CSMA/CA for the Media Access Control (MAC).

The antennas transmitting at 2.4 GHz have a maximum transmitting power of 17 dBm, while at 5 GHz the transmission power is 18 dBm. These values are determined by the modulation and coding scheme (MCS), as well as the bandwidth used [99].

6.4.2 System Configuration

The antenna must be ON and connected to the computers via Ethernet. The IP address of the antenna must be in the same domain (i.e. 192.168.0.1- 192.168.0.256). The gateway

address of the computer must be the same as the IP address of the antenna as shown in Figure 6.4

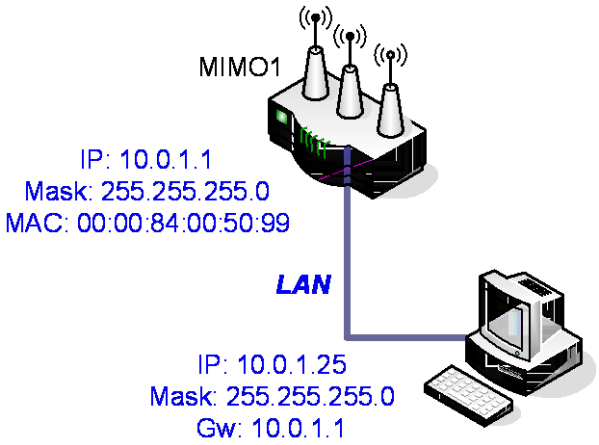

Figure 6.4: PC Connection.

The configuration of the antenna parameters is possible in three different interfaces: Telnet (Command Line Interface), HTTP (Web Browser), AP MANAGER II (SQL based Software). All of them do the same basic configurations. The easiest to manage is the Web browser interface, although the AP MANAGER II has more features for databases.

Focusing on establish a link between the two access points; the web browser interface is the quickest tool to develop this action. Once registered in the web browser interface, on the “Basic Settings/Wireless” tab contains all the basic parameters to link the two antennas together, antenna mode (WDS, AP, WC) frequency, as well as the list of visible access points. The other important section in the configurable tab is on “Advance Settings/ Performance” which contains specific parameters such as, standard and transmit power.

The same parameters must be set on the two antennas in order to achieve a successful connection. The model parameters will be defined in WDS mode connection for different frequencies and bandwidths according to the requirements of sections 6.1, 6.2. Once the connection is established in WDS mode, the “Status/ WDS Information” the system shows the equipment attached to the actual device. It’s important to notice that this software shows the signal strength connection in “signal %” not in dbm or watts values; this will be discussed in the next section.

6.4.3 Software Implementation

Due to the lack of provision in the web browser software to get the RSSI value in dBm units, independent software was applied to develop the measurements. There are two types of software designated for this purpose, the passive gateway software and the active gateway software. The passive gateway will listen to the traffic in the environment, as a packet sniffer, using direct passive devices (i.e. a wireless adapter in the laptop) to detect signals. The active gateways can be part of the network, giving more flexibility to the information received, even though is harder to implement [100].

Two types of software were used to measure the received signal strength from the antennas, “inSSIDer”, which can be downloaded from [101] and “Wavemon” downloaded from [102]. Both software packages are free to download and don’t require licenses for use. The PC system on which the software was installed was a laptop computer with the following characteristics: 3 GB RAM, AMD Athlon dual processor at 2.10, built in Windows Vista operating system. This PC will determine the path loss over the link connection (represented as PC 1 in Figure 6.6).

Once inSSIDer software was installed, the selection of the interface determined the path on which the system is to read the received signal strength from all the RF devices in the area (MIMO2 from Figure 6.6), as well as the channel location for each wireless equipment in the zone. Figure 6.5, shows how the inSSIDer screen looks when is running (the image screen might differ from version to version).

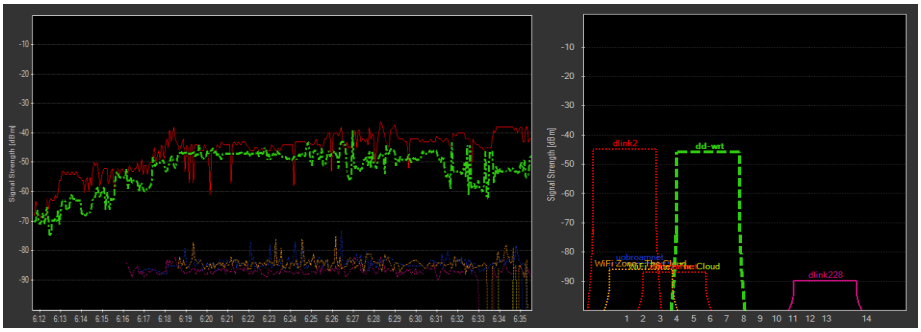

Figure 6.5: Inssider RSSI.

The Wavemon (wave monitor) software collects the packets from the antenna and converts them into an RSSI value. This software is able to work over the ethernet or WLAN interface, capturing the ESSID (Extended Service Set Identification) from the RF devices and providing such information as IP address and MAC address from the equipment in the coverage area. The reason to use two different software packages for the same purpose is to achieve an average for both RSSI values obtained from the two software packages to optimize the results.

6.4.4 System Structure

The path loss campaign was executed with two MIMO antennas, linked wirelessly in WDS mode. A laptop computer was connected to one of the antennas by ethernet port, executing the software mentioned to the capture of the RSSI value. The PC used for this

evaluation was done over a laptop for easy carry on throughout the corridor with the antenna connected as shown in Figure 6.6.

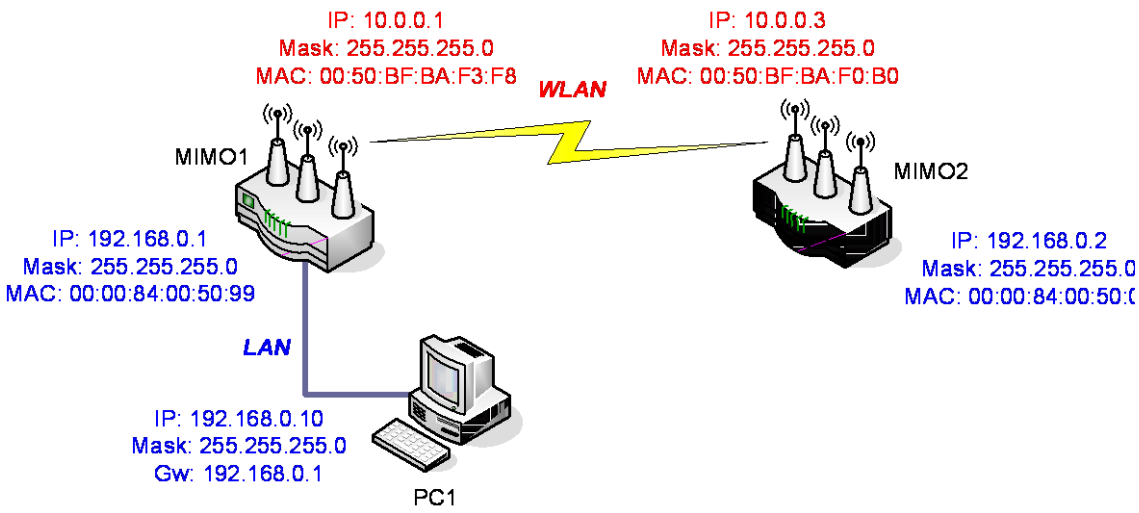

Figure 6.6 : RSSI Measurement Campaign System Structure.

6.4.5 Scenarios and Preparation

For the physical measurement through the corridor, a diagram was established to divide the entire corridor in sections of $1m^2$, as shown in Figure 6.7, obtaining a total of 90 sections. Each section was evaluated for 5 RSSI values over two frequencies (2.4 and 5GHz) using the 802.11n standard at 20 MHz bandwidth. The receiver and the transmitter antennas were located one meter above the floor. The receiver antenna (MIMO1) was the one moving along the corridor, always facing in the direction of the transmitter antenna. The antenna MIMO2 was in a fixed position on point 55 in Figure 6.7 and facing point 50 for all the measurements in this campaign.

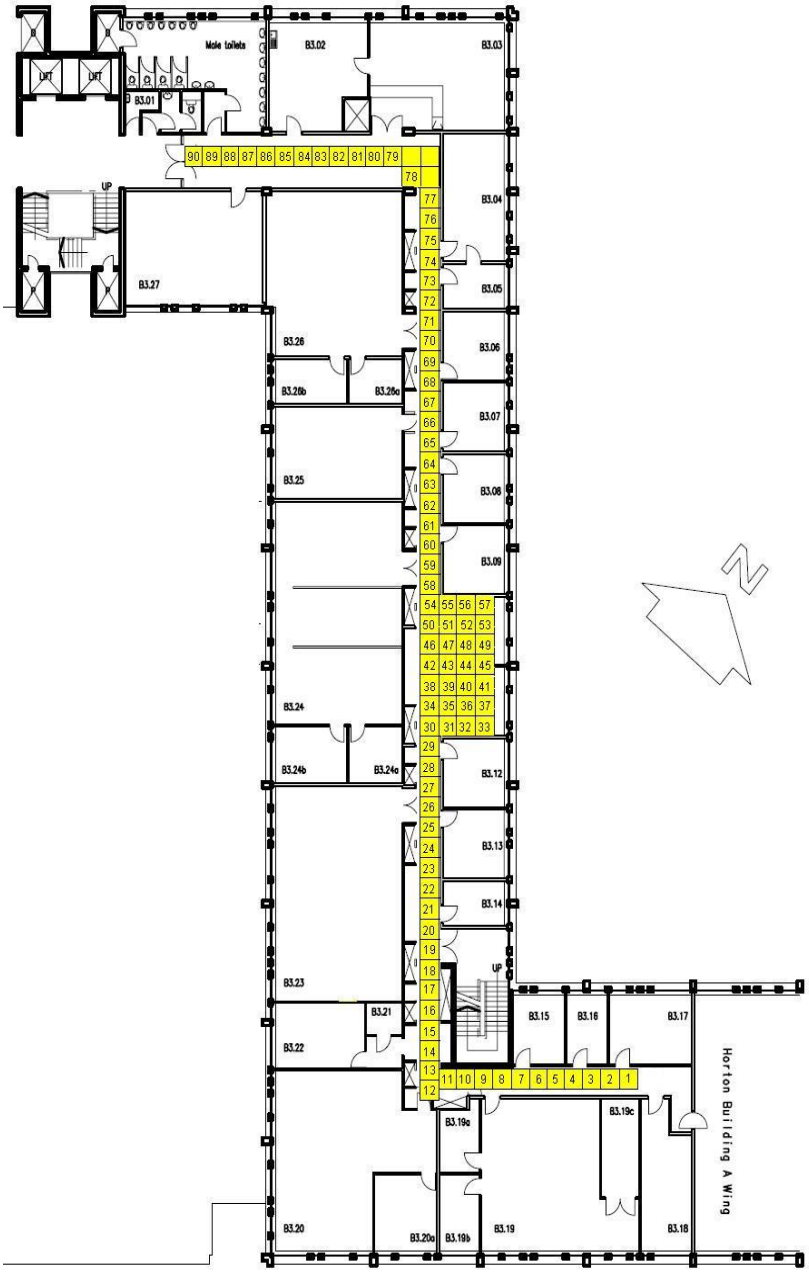

Figure 6.7: RSSI Scenario.

MIMO1 was the moving antenna that evaluated all the sections (from 1 to 90), capturing at each point 5 values of the RSSI obtained from the link to MIMO2, as shown in Figure 6.8.

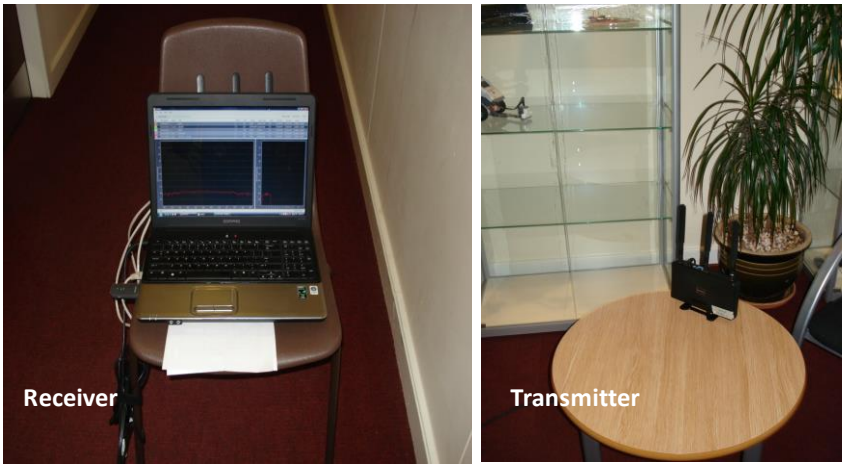

Figure 6.8: RSSI Measurement Campaign Images.

6.5 RSSI Measurement and Simulation Results

The 3D RSSI Scenario comprised of 90 receiver locations was divided into the Rx Route (69 locations), and the Rx Grid (21 locations) for practical analysis. The Rx Route is a route of receiver locations along the entire corridor; every single one with the same characteristics. The Rx Route has a partly LOS and partly NLOS receivers. The Rx Grid is a 7x3 Grid of receiver locations set in LOS, as shown in Figure 6.9.

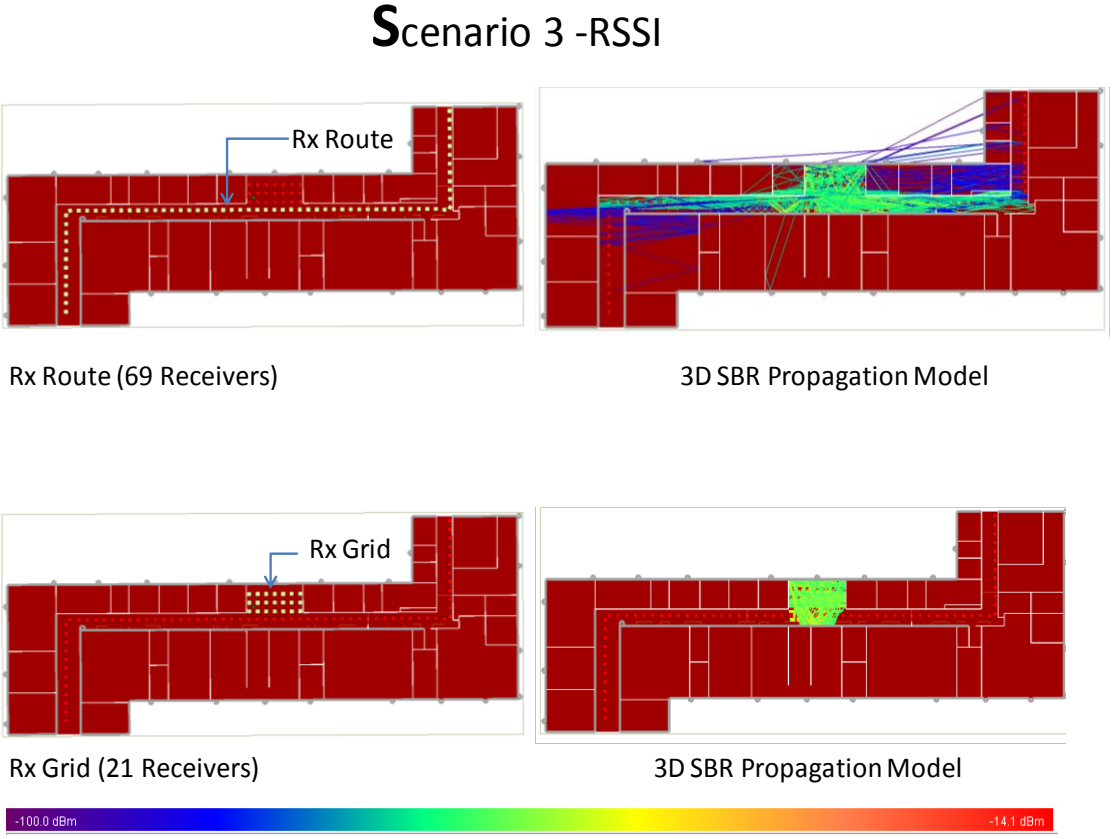

Figure 6.9: 3D RSSI Scenario Simulated Results.

Figure 6.10 shows the field strength distribution obtained from RSSI Measurements campaign along the corridor. The graph shows 13 scales from -9 to -100 dBm values, each scale using a 6.9 dBm range. The distribution was implemented for 2.4 and 5GHz measurements. Both distributions show that in 5.2 GHz configuration, the signal strength is distributed over a smaller coverage area compared with 2.4 GHz, but achieving a higher intensity at close range.

Figure 6.10 : RSSI Measurement Results for 2.4GHz and 5GHz

Two simulations were averaged to analyse the propagation behaviour; the graphs in Figure 6.11 show the comparison of the received signal strength measured per receiver location and the simulation of the 3D RSSI Scenario results. The simulated results are an average of the received signal obtained for the maximum and minimum transmission power of the antennas. At 2.4 GHz, this was from 17 to 11 dBm, and for 5 GHz from 18 to 9 dBm, confirming the similarity of the values simulated.

Measured and simulated results were analysed statistically, with the concludion that there was a correlation between simulated and measured signals of 86% at 2.4 GHz and 96% at 5 GHz. The total correlation of the physical and simulated model was of 92%. This indicates that the approximation from the simulation to the real world measurements were

in broad agreement.

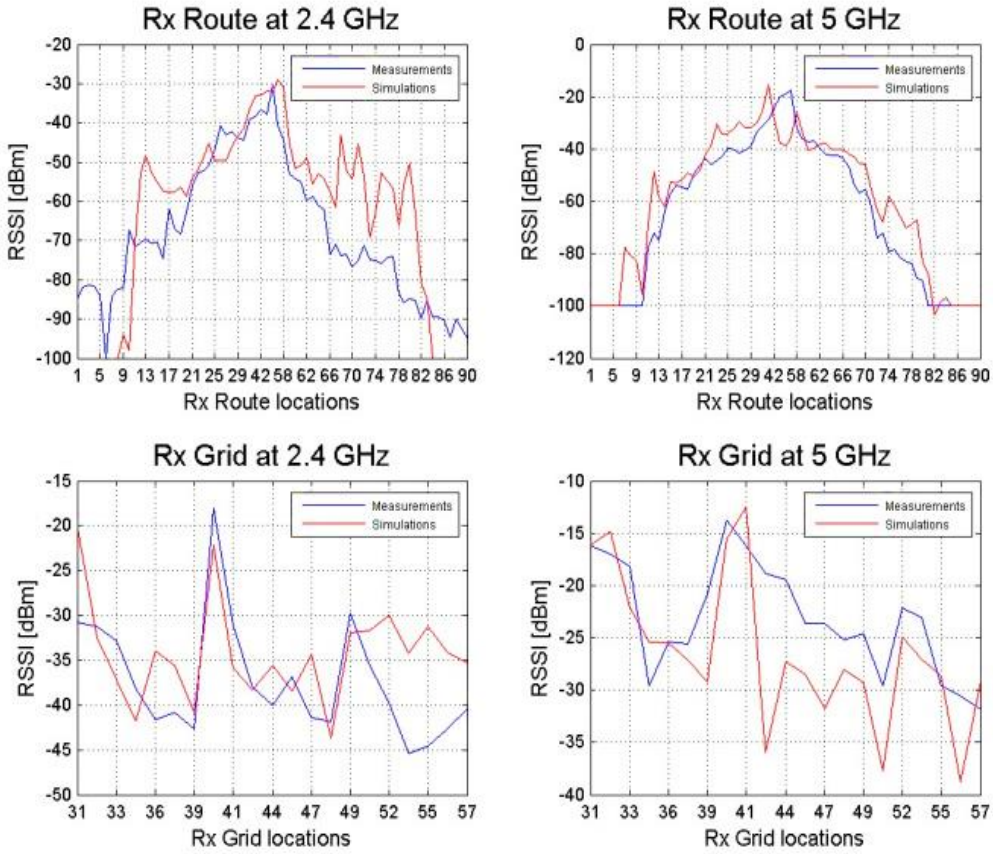

Figure 6.11: Measured and simulated RSSI.

Figure 6.12 shows the field strength distribution for the simulation with antennas operating at 5 GHz and 2.4 GHz, using the maximum transmission power, at 18 and 17 dBm respectively. This distribution shows a good agreement with the field distribution measured in the RSSI measurement campaign. The evaluation time for this simulation was of 53 minutes for 2.4 GHz and 58 minutes for 5GHz.

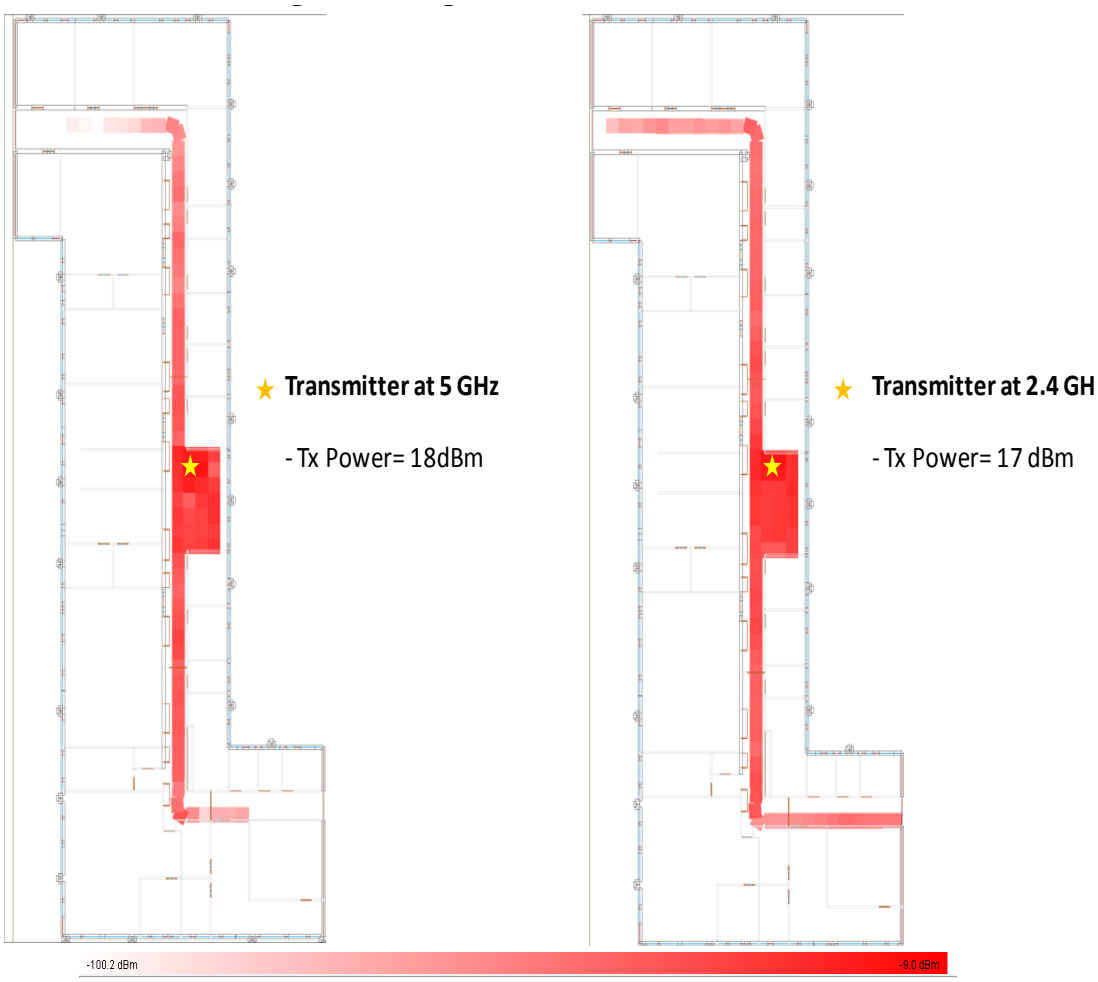

Figure 6.12: Field distribution simulated for 2.4 and 5GHz

6.6 Throughput Measurement Campaign

The throughput measurement campaign was developed to measure the data rate achievable at different locations on the 3rd floor corridor of B wing, Chesham Building at the University of Bradford. The measurements were computed by two stationary personal computers (PC), each one connected via ethernet to a commercial 802.11n wireless router having a 3×2 MIMO antenna array, evaluating the throughput obtained from MIMO2 to MIMO1as shown in Figure 6.13, which can operate at different frequencies and bandwidths.

The evaluation of each set of measurements, that is from 10m-50m, was performed in compliance with the 802.11n standard, using unoccupied channel [103].

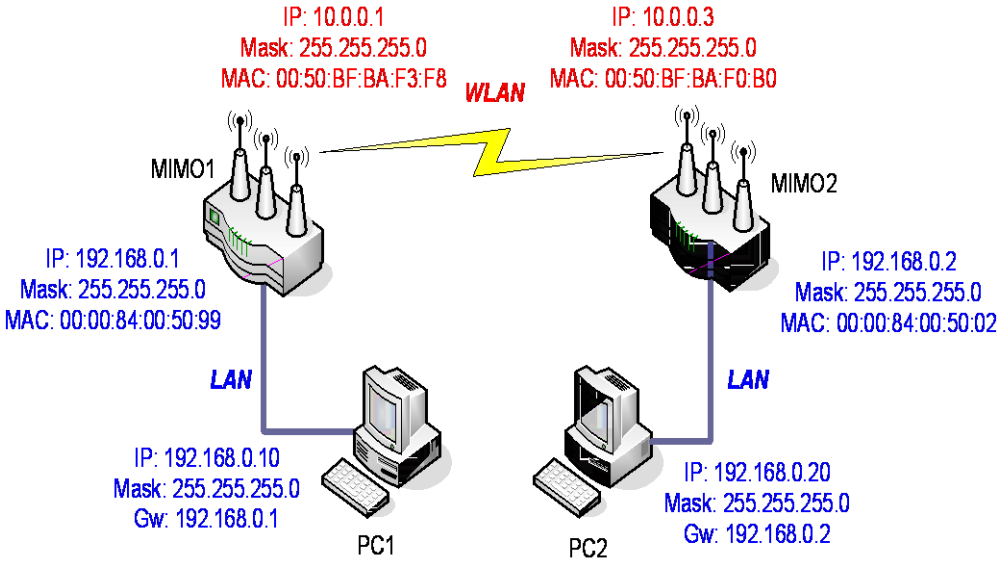

Figure 6.13: Throughput measurements system structure.

6.6.1 Software Implementation

The throughput measurements were developed on UDP throughput mode due to the fast evaluation time for each position. For this section, two different programs were applied to evaluate the throughput: IPERF and IxChariot. IPERF with its graphical interface (JPERF) provides a range of utilities to measure TCP and UDP characteristics and IxChariot is a sophisticated commercial package that enables performance assessment of network applications.

The PC characteristics included 2 GB RAM memory and a 2.6 GHz single processor, using Windows XP professional operating system. Each PC was connected to a Dlink

DAP2553 1×3 MIMO antenna via Ethernet using a Category 6 UTP cable, since it supports up to 10245 Mbps and the maximum throughput theoretically of a 2 stream MIMO systems is 300Mbps. The two antennas were linked together wirelessly in WDS mode. The software was deployed on both systems (PC1 and PC2).

6.6.2 Measurement Scenarios

Two different scenarios were established to evaluate the throughput performance on the MIMO antennas: these are the Line of Sight (LOS) Scenario and the Non Line of Sight (NLOS) Scenario. In each scenario, the antenna height was always 1m above the floor, for both the mobile (Rx) and the fixed unit (Tx).

The LOS scenario was implemented by installing the Tx antenna in a corridor in such a manner that all the measurement locations from the Rx antenna were able to achieve LOS reception. Five receiver locations were established for this scenario, separated by 10 m from each other in a linear distribution as shown in Figure 6.14. The NLOS Scenario was implemented by installing the Tx antenna in the corridor in such a way that all measurement locations from the Rx antenna were able to achieve a NLOS reception. The same five receiver locations were established for the NLOS scenario as it was for the LOS scenario.

The aim of these scenarios is to evaluate the throughput over the distance in a LOS/NLOS setting for the 2.4 and 5.2 GHz bands at 20 and 40 MHz bandwidth. An additional throughput measurement was developed, taking advantage of the LOS/NLOS scenarios and the configurable parameters from the antenna diversity analysis

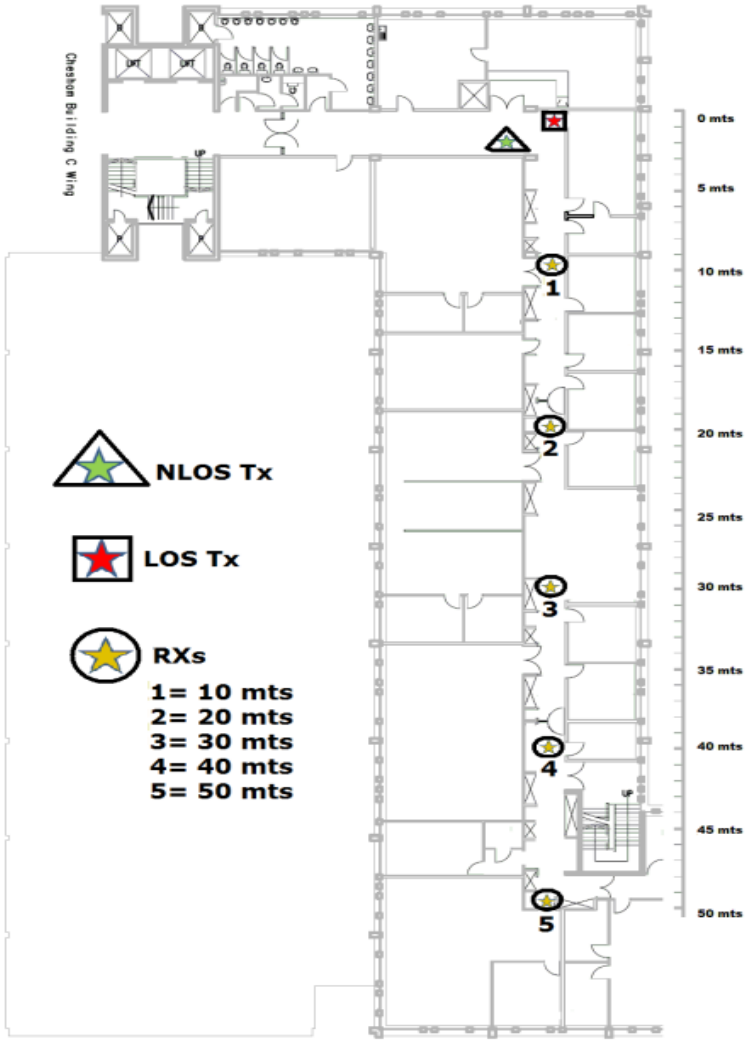

Figure 6.14: Line of sight Scenario

6.7 Throughput Campaign Results

Each value represented in Figure 6.15 was averaged over 5 measurements per location. It describes the average (mean) and the maximum (peak) values obtained from the throughput measurements obtained for the LOS scenario at each of the 5 locations. A particular observation on the achievable throughput using 40MHz bandwidth is that at some points it doubles the 20 MHz throughput. In the majority of cases using 40 MHz, 5.2 GHz achieves higher date rates compared with the 2.4 GHz configurations.

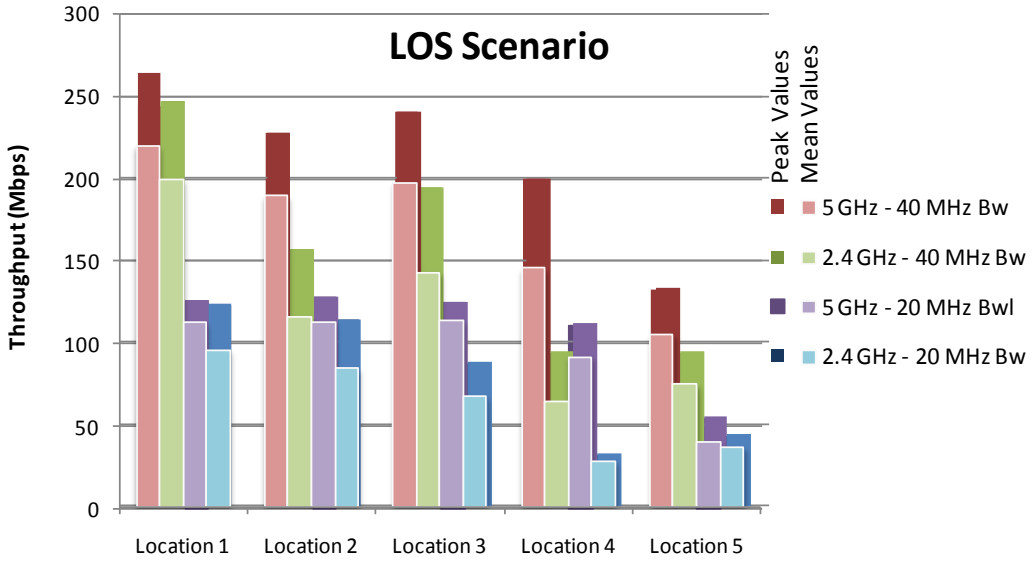

Figure 6.15: Averaged Throughput over locations for LOS scenario

Figure 6.16 shows the mean and the peak values from the throughput measurements obtained from the NLOS scenario with the system operating at 2.4 and 5.2 GHz, using 20 and 40 MHz transmission bandwidth at each of the 5 locations. In this scenario there is a noticeable decrease of throughput as the distance between the Tx and the Rx increases. Still at around 50 meters distance (location 5) the throughput is 90-100 Mbps (5GHz-40MHz), which is considered a very good performance for a NLOS scenario.

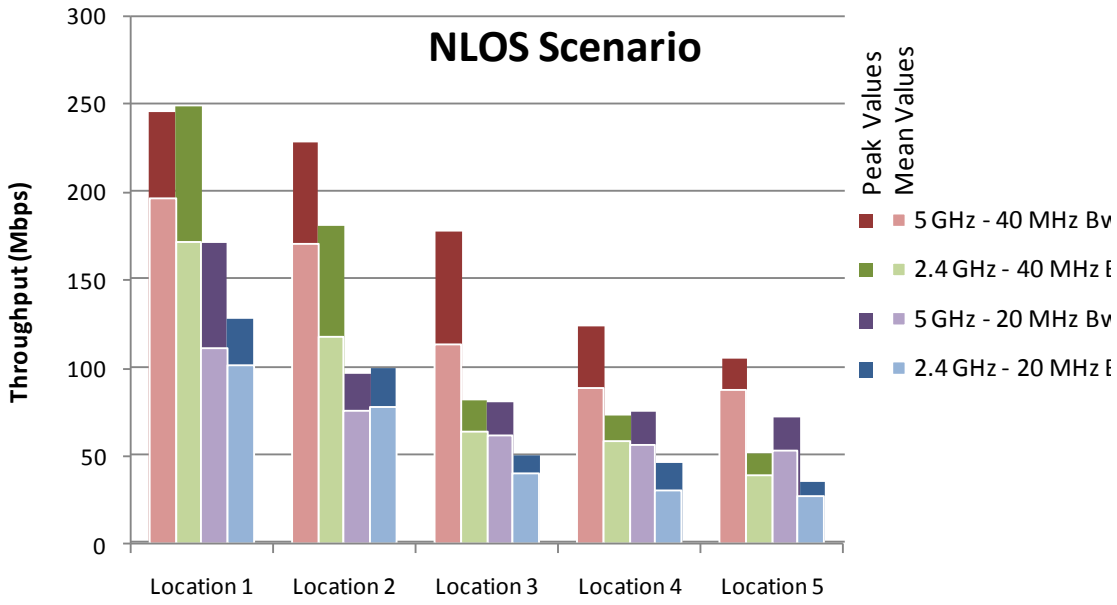

Figure 6.16: Averaged Throughput over locations for NLOS scenario

The antenna diversity measurements for the LOS and NLOS scenario shown in Figure 6.17 and Figure 6.18, compares the high throughput obtained from the MIMO configurations and demonstrates that it is directly proportional to the number of antennas.

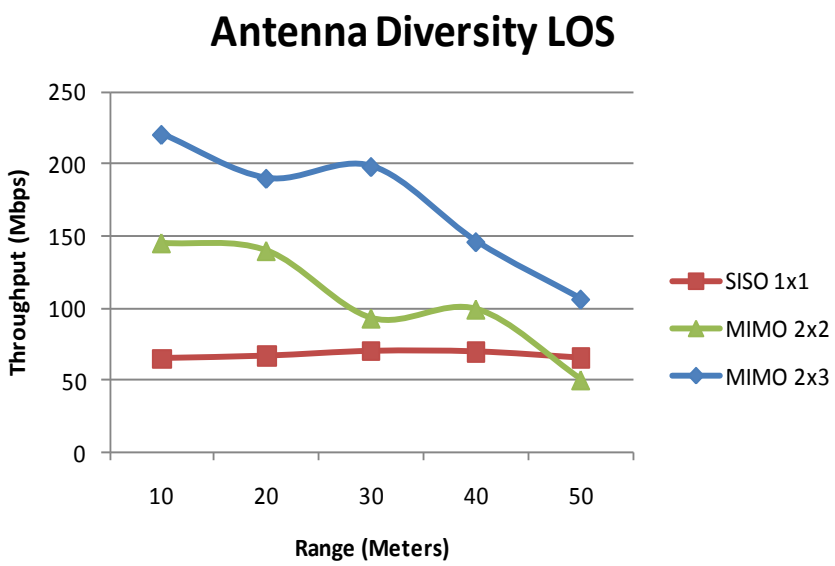

Figure 6.17: Averaged Throughput over Distance for Different Antennas Configuration in LOS

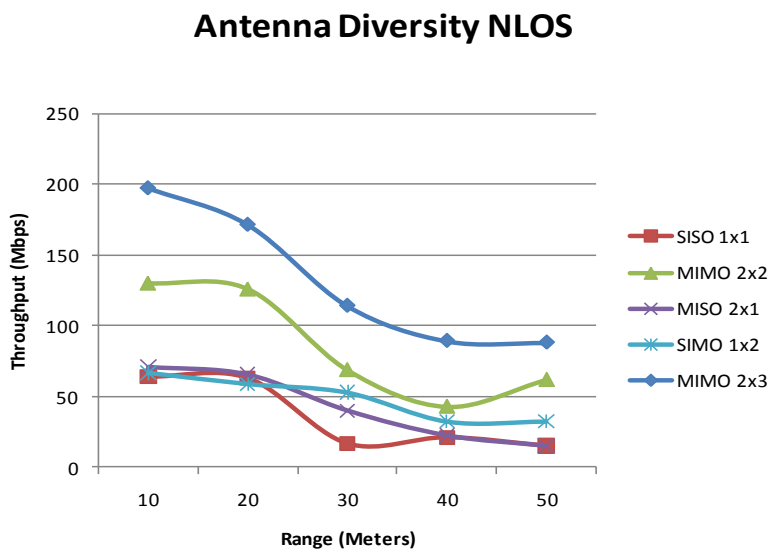

Figure 6.18: Averaged Throughput over distance for different antennas configuration in NLOS

6.8 Furnished Indoor Office Environment

The study was carried out in lab B3.26 on the third floor of B wing, Chesham Building, University of Bradford. The furniture included wooden tables, metal cabinets and a refrigerator simulated as wooden cuboids and metal cuboids respectively as shown in Figure 6.19.

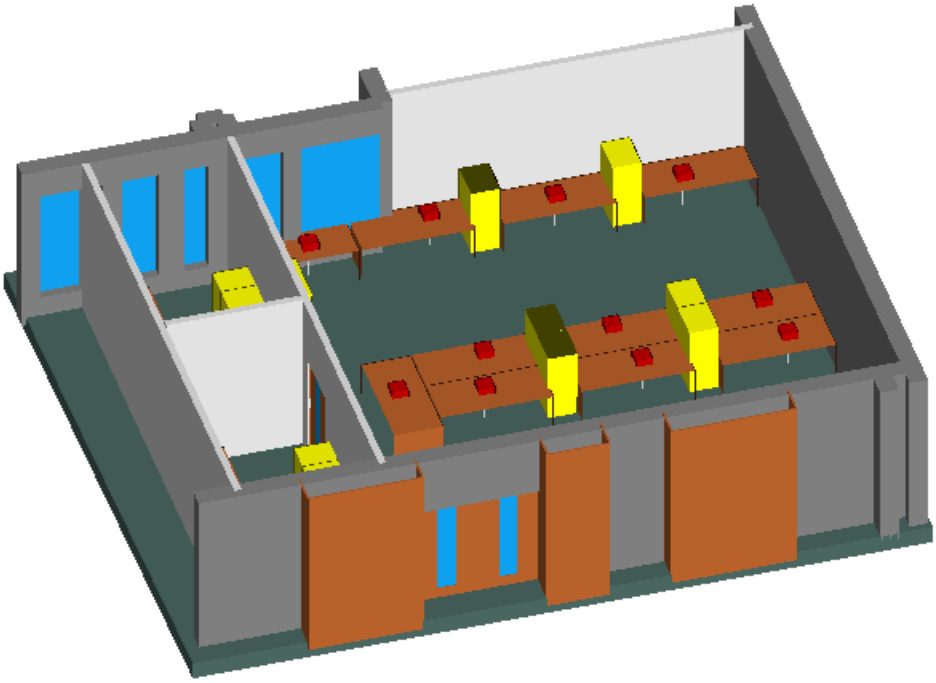

Figure 6. 19: 3D Indoor Environment Model.

The measurement campaign was developed to evaluate the field strength distribution using one laptop and two MIMO 3×2 as in section 6.5 systems along the specified receiver locations at B3.26, Chesham Building, at the University of Bradford.

The physical model was performed by defining the receivers over the tables at height obtaining total of 33 locations. The evaluation was done at three different transmitter locations and height as shown in Figure 6.19. Each section was evaluated for 5 RSSI values over two frequencies (2.4 and 5GHz) using the 802.11n standard at 20 MHz bandwidth.

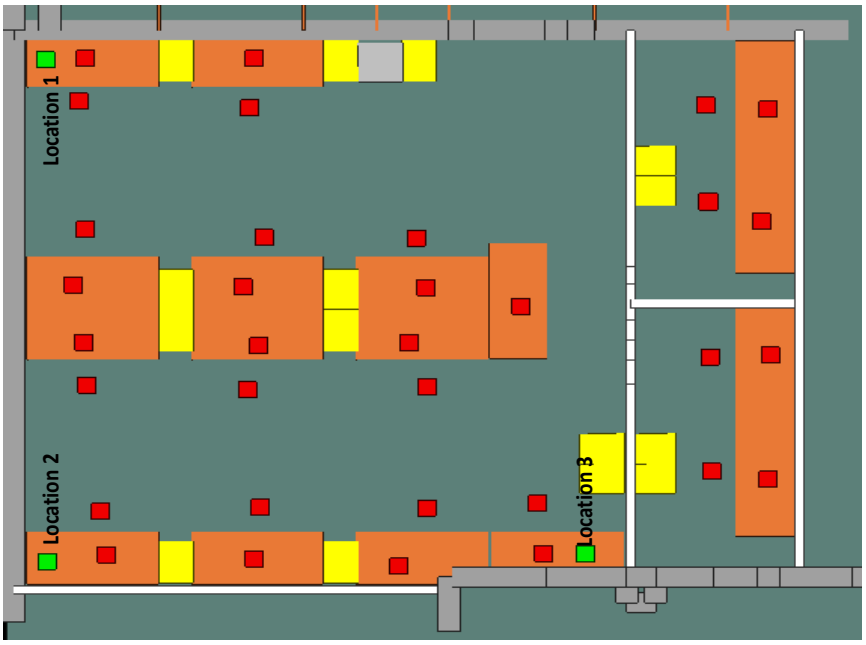

(a)

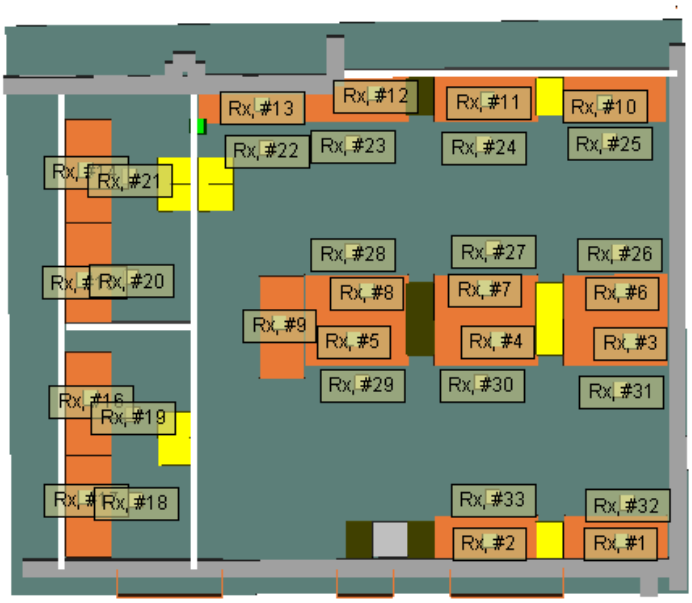

(b)

Figure 6.20: (a) Transmitters locations (Green) and Receivers locations (Red), (b) Receiver numbers.

Two simulations were averaged to analyse the propagation behaviour, Figures 6.21 to 6.24 show the comparison of the received signal strength measured per receiver location and the simulation of the 3D RSSI results at different transmitter locations and height.

The simulated results are an average of the received signal for the maximum and minimum transmission power of the antennas. At 2.4 GHz, this was from 17 to 11 dBm, and for 5 GHz from 18 to 9 dBm. The results confirm that there is a fair measure of similarity between measured and simulated values, however, the simulation appears to underestimate losses.

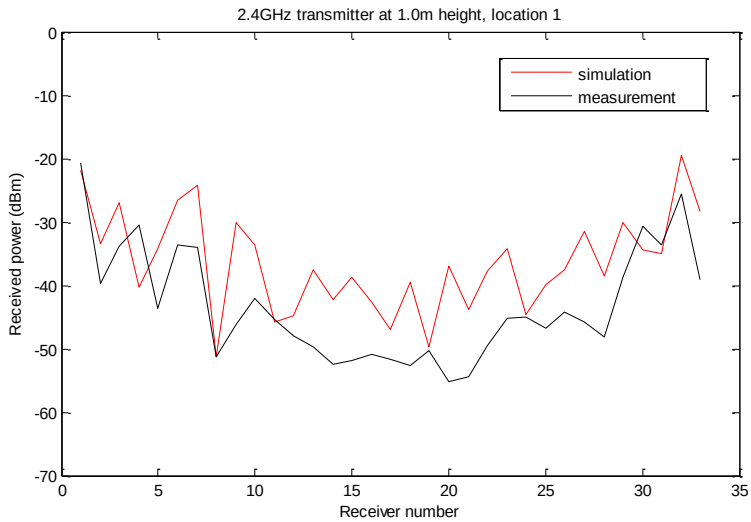

Figure 6.21: Measurements and simulation results comparison at 1.0m height location 1.

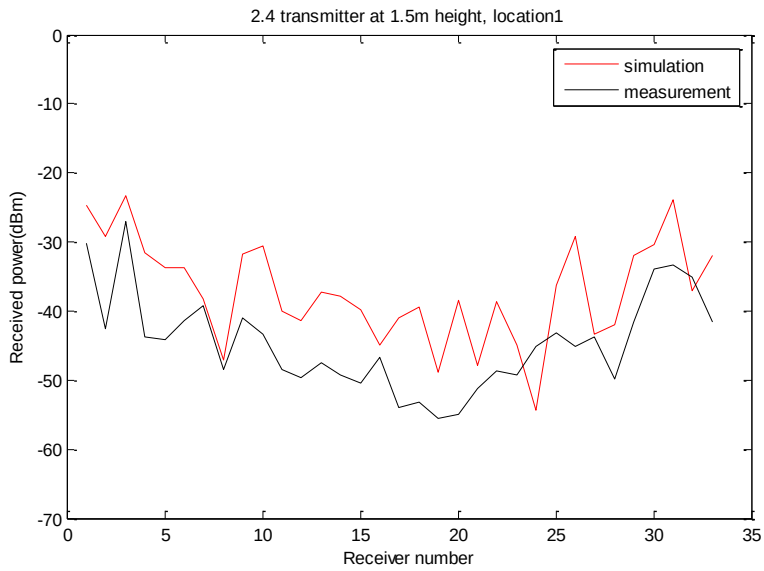

Figure 6.22: Measurements and simulation results comparison at 1.5m height location 1.

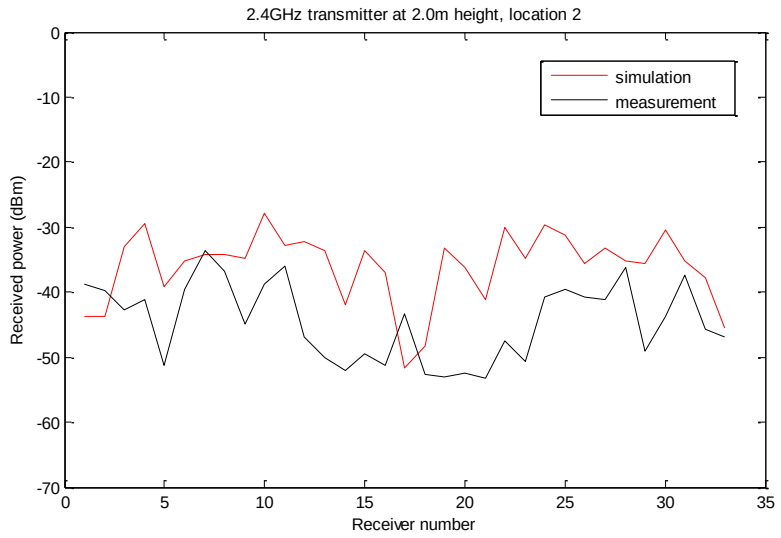

Figure 6.23: Measurements and simulation results comparisonat 2.0m height location 2.

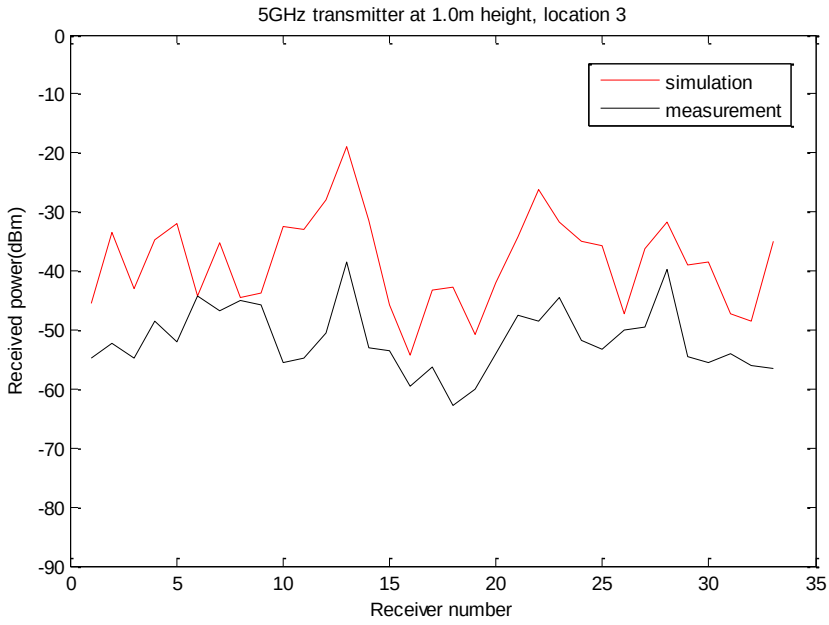

Figure 6.24: Measurements and simulation results comparison at 1.0m height location 3.

From the above results it can be noticed that there is a fair agreement between the trend of simulated and measured results with a difference of less than 10dBm at most of the receiver locations.

Figure 6.25 shows the Cumulative Density Function (CDF) of the received power for location 1 at the different heights, from which the probability that a particular value of power is received can be estimated.

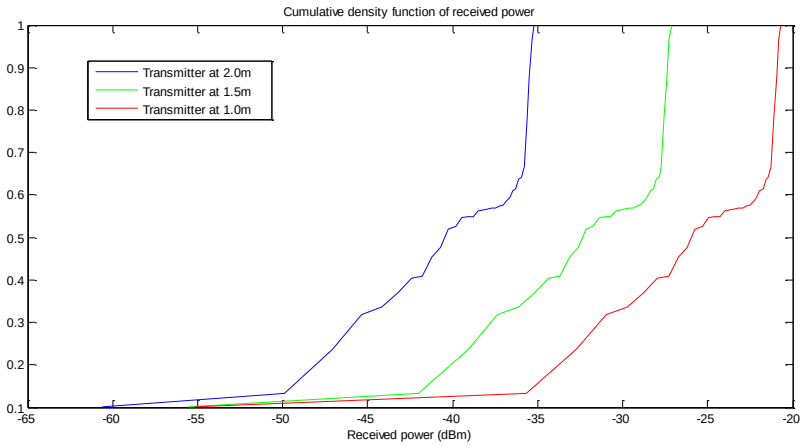

Figure 6.25: Cumulative density function of received power (dBm) with transmitter at different heights.

Figures 6.26 to 6.29 show a comparison between the performance of the 5 GHz and 2.4 GHz. The readings were generated with the transmitter at 1.0m height location 1. It can be observed that the 5GHz transmitter has less coverage compared to the 2.4 GHz. The delay spread at 5 GHz higher than at 2.4 GHz as shown in Figure 6.26.

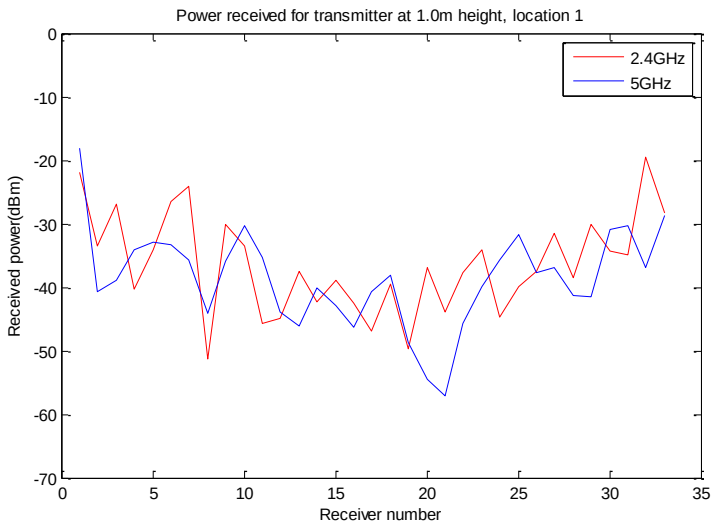

Figure 6.26: Received power versus the receiver number.

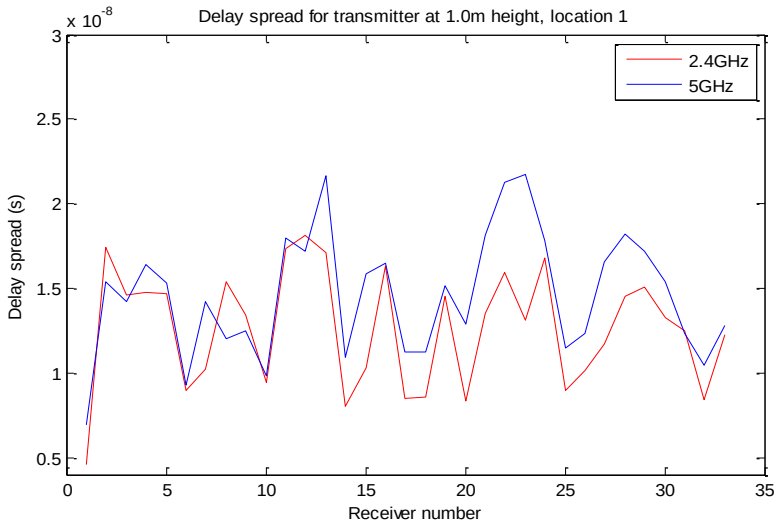

Figure 6.27: Delay spreads versus receiver number.

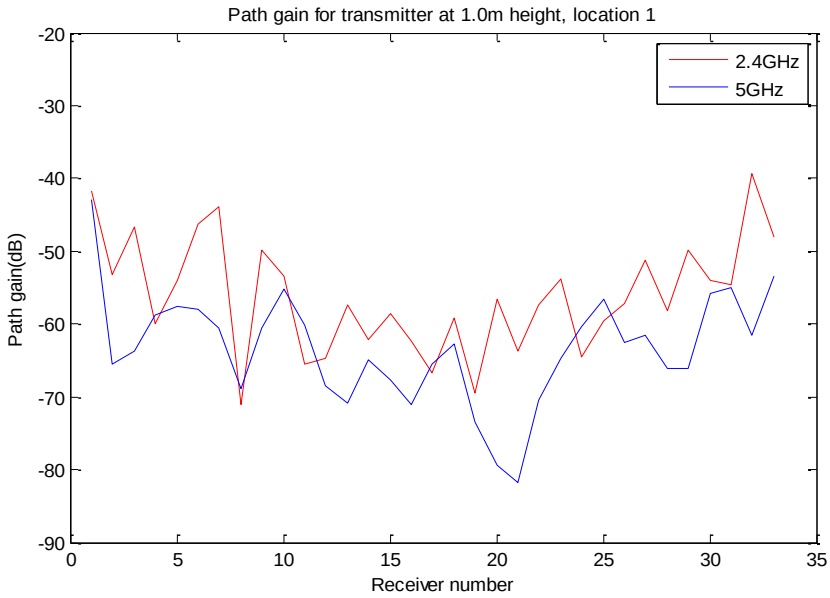

Figure 6.28: Path gain versus receiver number.

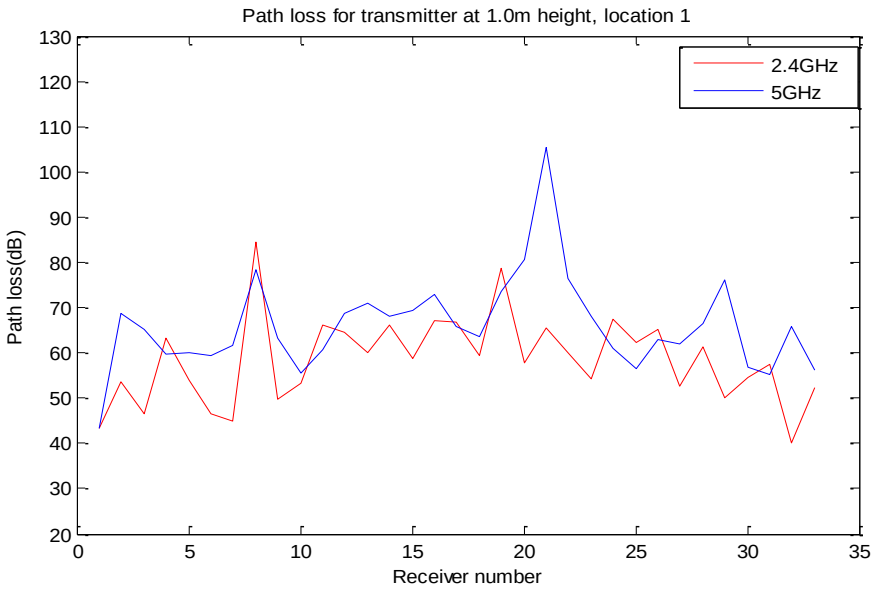

Figure 6.29: Path loss versus receiver number.

6.9 Conclusions

The analysis of throughput values obtained from Line of Sight and Non-Line of Sight scenarios provide an experimental insight into the performance of MIMO systems deployed using the 802.11n standard in a typical multi-storey office building, reaching 250 and 296 Mbps for NLOS and LOS respectively (for 10 m distance). The achievable bit rate for a MIMO system is much more reliable when compared to a SISO connection. Furthermore the 802.11n channel bonding option provides remarkable throughput increase, compared with 802.11a/b/g.

The implementation of a simulated propagation model using 3D SBR provides a good estimation of the channel propagation without demanding an extraordinary computational effort. The investigation found a high correlation for 2.4 GHz and 5.2 GHz frequencies (86% and 96% respectively) between measured and simulated data. By modelling a MIMO system in an indoor environment, it was possible to determine the signal strength distribution and its achievable throughput for different locations. Despite the accuracy of the results obtained in this investigation, the modelling process remains rather complex, which might limit its applicability in future work.

Finally, an indoor furnished office environment was simulated using Wireless Insite and the results have been compared with the measurements of the received signals. The results recorded showed a good degree of similarity with measurements. The results were quite encouraging as regards the adoption of this modelling approach in support of practical deployment as they provide a useful estimation of the propagation channel and a fairly accurate alternative to measurement, which takes a lot of time and is labour-intensive.

CHAPTER 7

Simulation of Different Channel Propagation Scenarios

7.1 Introduction

Future wireless communication systems are expected to offer high-reliabilty broadband radio access in order to meet the increasing demands of the high speed data and multimedia services. The propagation of radio in build-up areas is strongly influenced by the nature of the environment, in particular the location, size and density of the buildings.

In propagation studies a qualitative description of the environment is usually employed using terms such as rural, suburban, urban and dense urban. Dense urban areas are generally defined as dominated by tall buildings such as office blocks and other commercial buildings. On the other hand suburban areas comprise residential areas, gardens and parks. The rural term defines open land with scattered buildings, woodland and forests. These qualitative descriptions are open to different definitions by different users, which leads to doubts whether the prediction models based on measurements made in one area are generally applicable elsewhere. Therefore there is an obvious need to accurately describe the propagation area to avoid any ambiguity [105]

In this chapter the model presented in chapter 6, is extended to create a model for part of University of Bradford campus to evaluate the channel propagation for indoor multi-storey, indoor- outdoor and outdoor-outdoor scenarios. The model includes the details of the buildings in terms of the physical measurements and the materials used where the received signal strength and path loss were evaluated.

7.2 Indoor Multi-Storey Scenario

Indoor systems tend to be complex, with the radio wave encountering many obstacles that give rise to multiple diffractions and reflections. The electrical characteristics of the materials are often only vaguely known and, to make the situation more complicated, people, furniture and even walls can be moved.

Nevertheless, buildings and, in particular, high-rise office buildings contain many potential users of telecommunications systems and could provide significant revenue if a high-quality radio communication service could be delivered. Although the distances between transmitter and receiver are usually very small, the existence of multiple obstructions (such as walls and floors) means that the path loss can be quite high and difficult to predict. Recommendation ITU-R P. 1238 [106] gives some guidance. Figure 7.1 shows a detailed model for second and third floors of Chesham building, University of Bradford. The dimensions of the building layout is identical to the physical measurements and the indoor structure and materials are the same as in section 6.4.

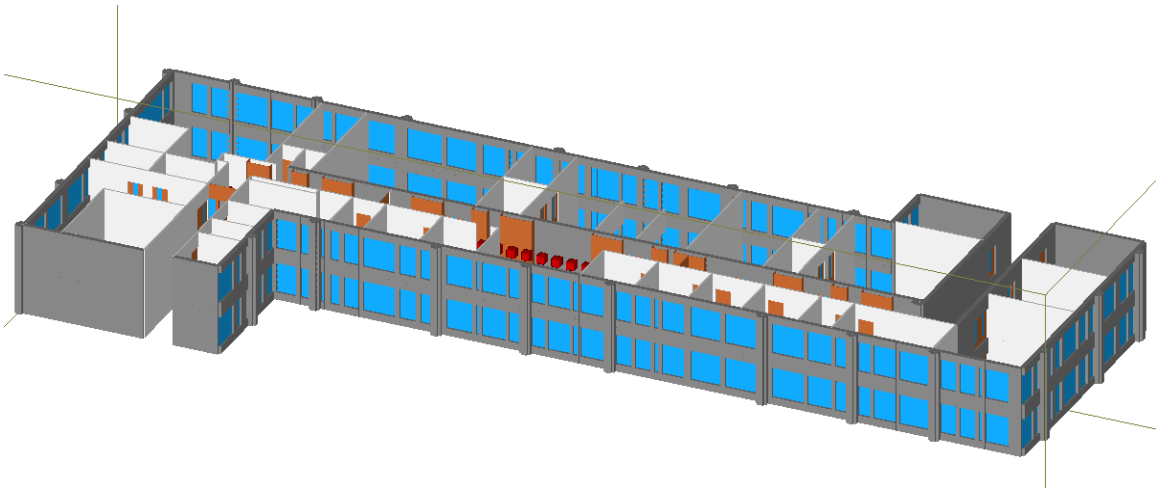

Figure 7. 1: The second and third floors for Chesham building, University of Bradford.

The waveform type used for the simulations was a Gaussian waveform of 2410 MHz frequency with a 23 MHz bandwidth. The antenna type implemented were linear dipoles, vertically polarized with a 6 cm length, and (an un-realisable) maximum receiver sensitivity of -250 dBm. Two transmitter and three receiver dipole antennas were used with a quarter wavelength (λ/4) separation. The construction of the model followed the corridor layout. 48 receiver points with 1 meter separation and 1 meter height were distributed along the corridor, and one transmitter was implemented at one meter height, this model was evaluated for three scenarios, same floor LOS, same floor NLOS, and lower floor as shown in Figure 7.2.

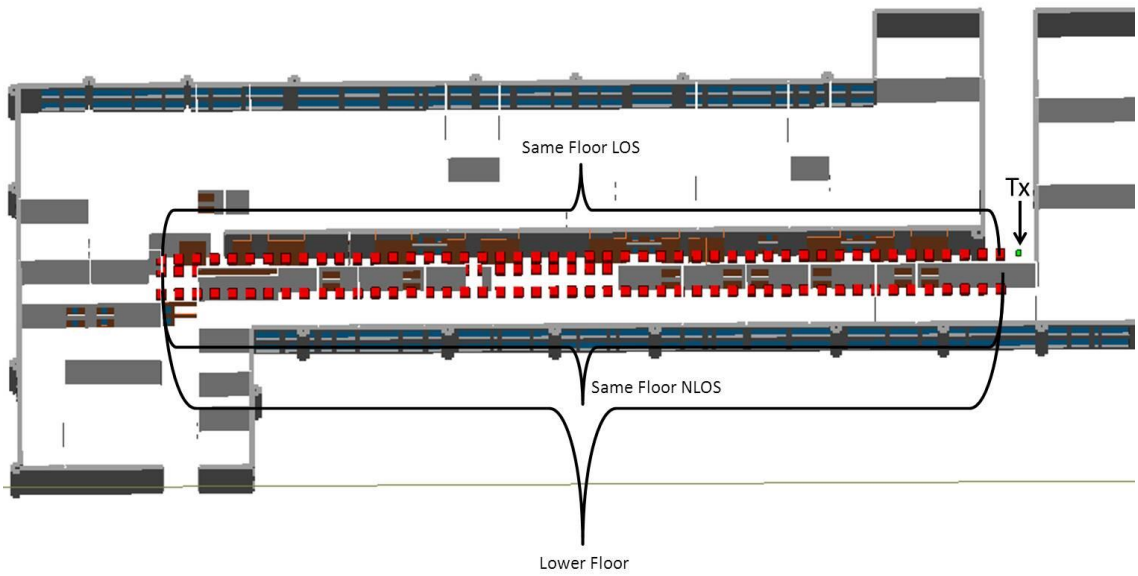

Figure 7. 2: Three evaluation scenarios, same floor LOS, same floor NLOS, and lower floor

Figure 7.3 shows the received power strength for the three different scenarios and Table 7.1 shows the standard deviation, mean and median.

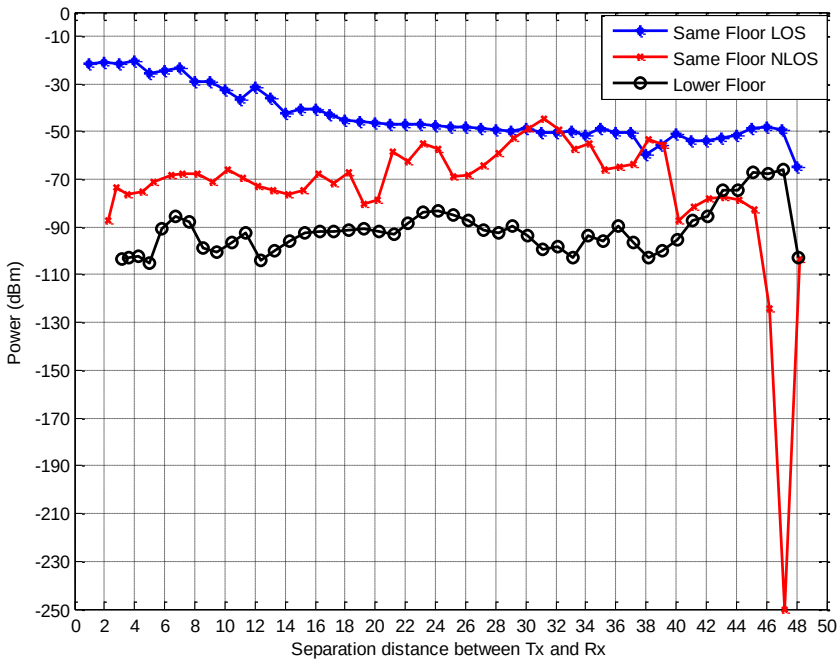

Figure 7. 3: Received power (dBm) vs. Separation distance (m) for different scenarios.

Table 7. 1: Received Power Strength (dBm) for the three different scenarios at 2.41 GHz.

Environment	*Standard Deviation*	*Mean*	*Median*
Same Floor LOS	11.1	-43.3	-47.7
Same Floor NLOS	9.5	-73.4	-68.4
Lower Floor	9.6	-91.7	-92.4

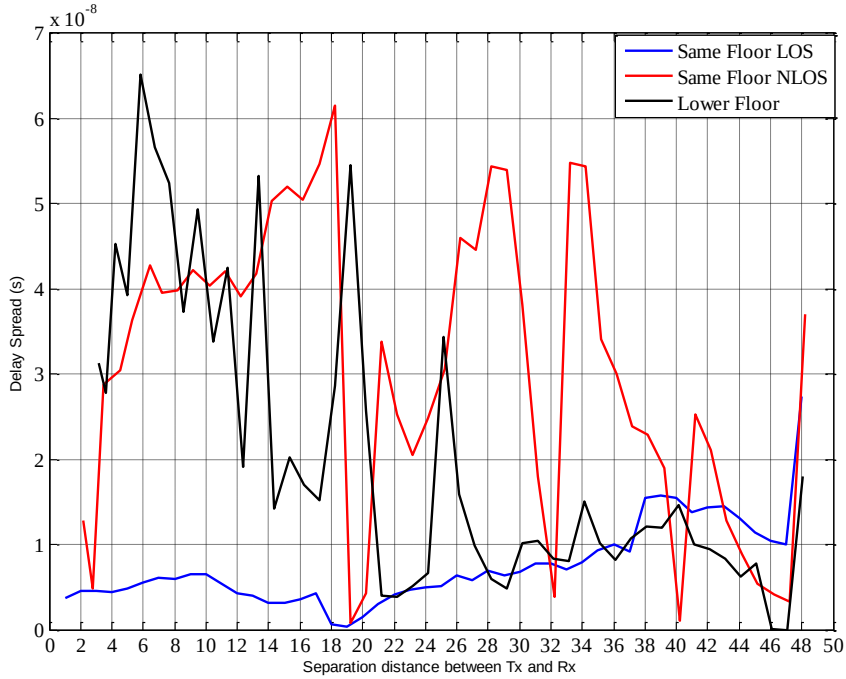

Figure 7. 4: Delay Spread vs. Separation distance (m) for different scenarios.

The delay spread of the indoor environment need to be considered by the communication system designer, and there is a little he can do beyond simply repositioning transmitters and receivers to avoid any unacceptable delay spread. Table 7.2 shows delay spared parameters for our model.

Table 7.2: Delay Spared parameters for the three different scenarios at 2.41 GHz.

Environment	*Standard Deviation*	*Mean*	*Median*
Same Floor LOS	4.9	7.5 ns	6.2 ns

Same Floor NLOS	17.3	20.8 ns	14.4 ns
Lower Floor	17.4	30.6 ns	32.1 ns

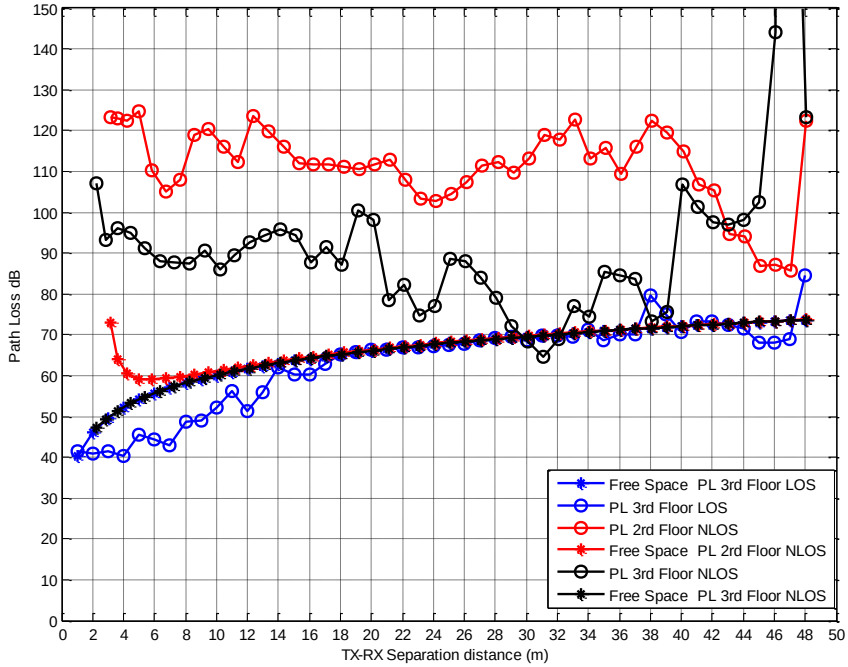

Figure 7. 5: Path loss (dB) vs. Separation distance (m) for different scenarios.

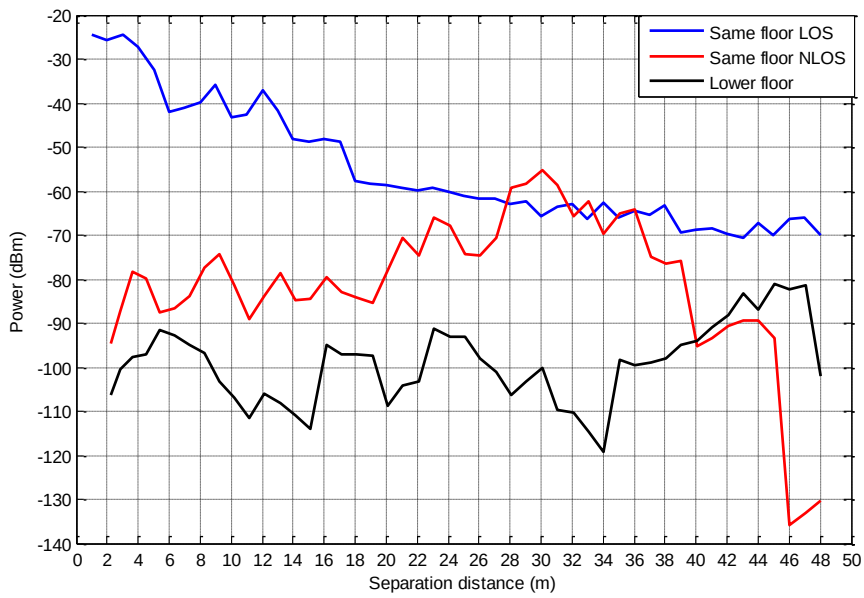

Figure 7. 6: Received power (dBm) vs. Separation distance (m) for different scenarios using three elements array at both the transmitter and the receiver.

7.3 Indoor-Outdoor Scenario (moving RX)

Knowing that the relative movement of the transmitter or the receiver or objects can introduce some channel time variation, the effect of pedestrian movement on MIMO channel capacity has been studied for an indoor environment in [107]. Results showed that for increasing MIMO antenna configurations, the number of dynamic MIMO channel increases with the number of pedestrians. Although the study was limited to an indoor environment, similar results might be expected for the outdoor scenario considered in this paper. This work studies the 4x1 MIMO case of an LTE moving receiver; calculating the received signal strength indicator (RSSI) and throughput using a distributed transmitter antenna array for a mobile speed of up to 1m/s.

The analysis for this study was carried out on a 22,400m^2 landscape, representing part of University of Bradford campus. The objects defined to represent the buildings include concrete walls, floors and ceilings, with heights varying from 5 m to 25 m, also a green area was added in the model as shown on Figure 7.7. For a given time varying channel, the analysis considers: waveform, antenna, transmitter, receiver, model type, materials composition and output. A Gaussian waveform was used for 1800 MHz signals, with 20 MHz bandwidth. In this case the antenna is limited to a linear dipole arrangement, vertically polarised, with 8.33 cm length, and a maximum receiver sensitivity set to (an un-realisable) -250dBm.

Figure 7.7 may be interpreted as a projection of the buildings characterized in the study as seen from above; the red square line represent the receiver trajectory with each point showing the specific location of the receiver at a given time where the starting point and

the end point are marked as shown in the figure, and the green rectangular points represent the transmitting base station (BTS).

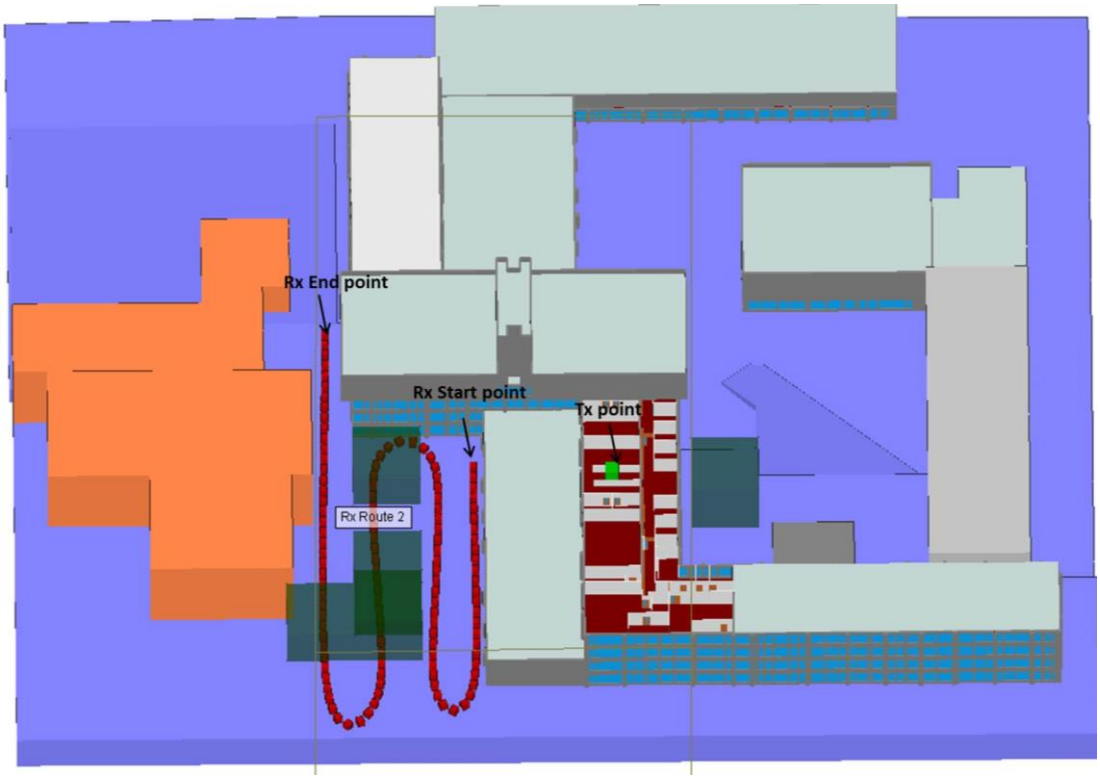

Figure 7. 7: 3D Campus Environment Model with Transmitters and Receivers locations.

The received power, at any time instant for multipath propagation signals behaves differently from a single path propagation channel. The reason for that is the interference and diffraction effects that have a direct and dramatic influence on the total received power at the receiving antenna. This is clearly illustrated in Figure 7.8 where the total received power is varying nonlinearly with time since the separation distance between the transmitter and the receiver varies with time as well.

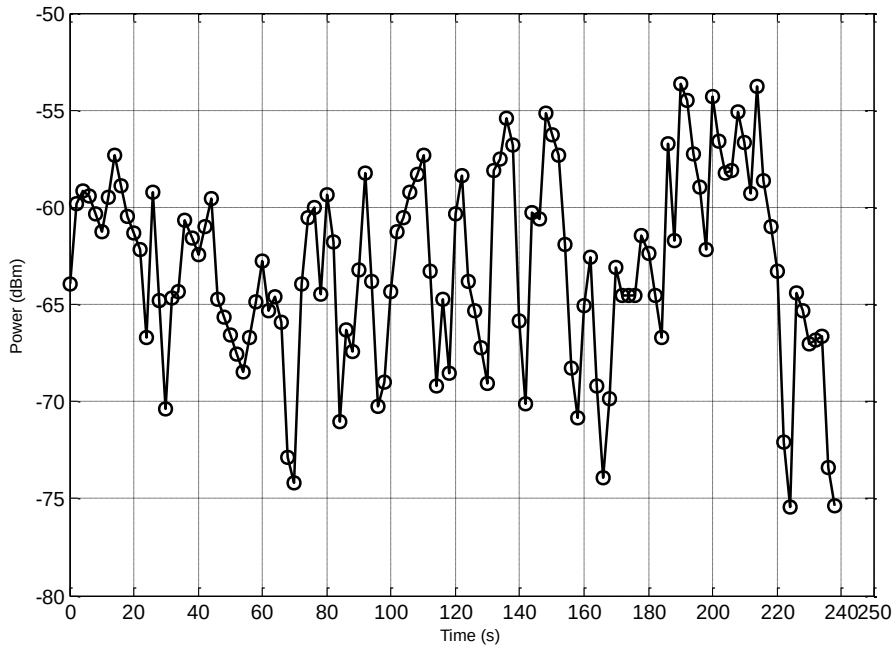

Figure 7.8: Received power (dBm) vs. time (s).

Path loss (PL) of the propagation channels in dB is the mean signal power loss in the propagation channel. It normally follows an inverse power law versus distance. Path Loss is frequency dependent and it do not depend on the antenna gain or transmitted power level. Figure 7.9 shows the path loss the simulated scenario verses time

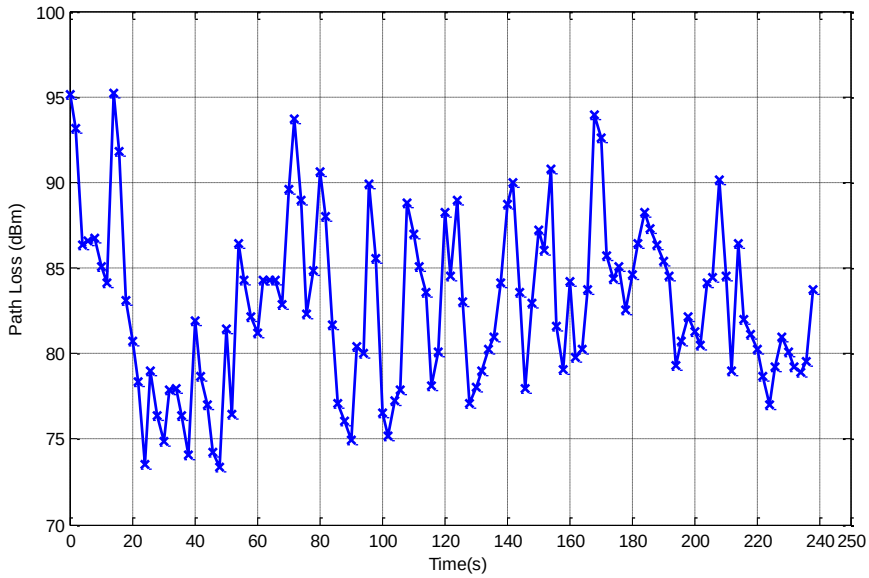

Figure 7.9: Path loss vs. time (s).

7.4 Outdoor-Outdoor Scenario (moving)

The analysis for this scenario was carried out on the same landscape as in section 7.3. The transmitter was moved to the top of the building as shown in Figure 7.12 at height of 25 m also the multipath propagation components are shown as well.

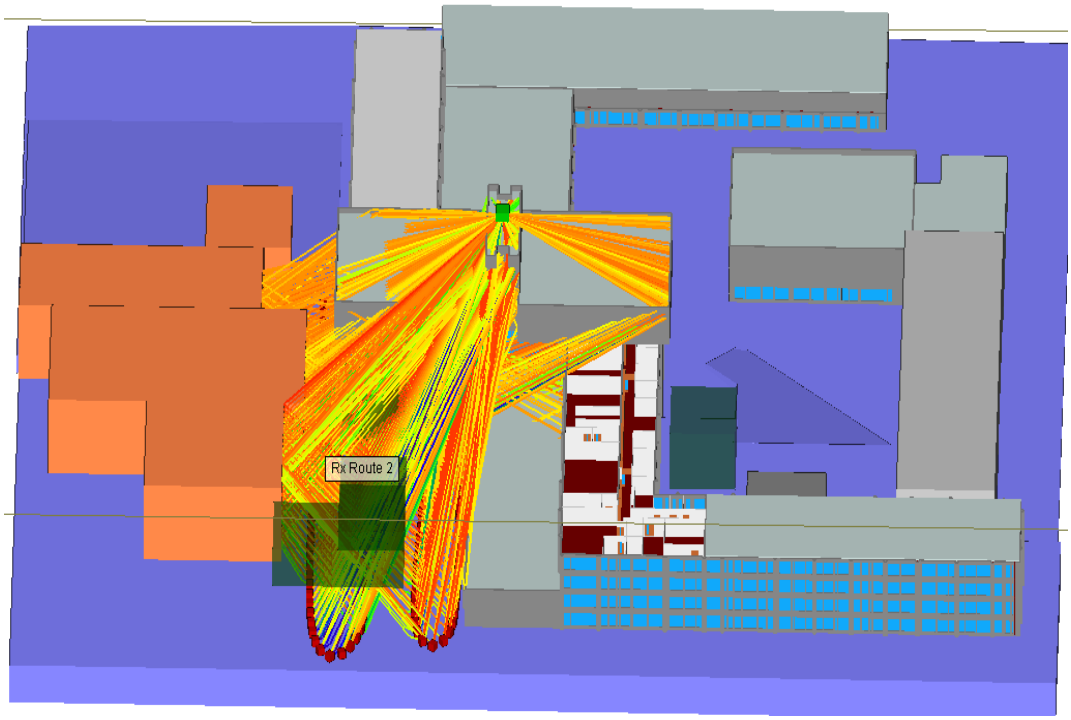

Figure 7. 10: 3D Campus Environment Model with Transmitters and Receivers locations including the multipath propagation rays.

The simulation was performed using the LTE [108] standard configuration at different bandwidths to calculate the throughput. Figure 7.11 shows the throughput of each receiver at any time instant using different bandwidth configurations. It is noticeable that higher bandwidth achieves higher throughput performance.

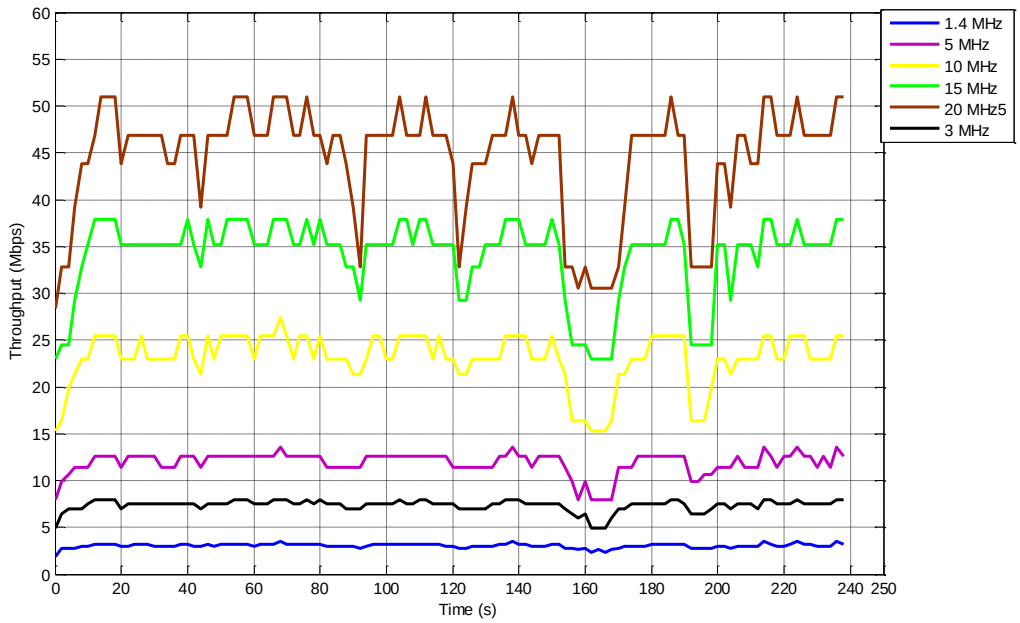

Figure 7. 11: Throughput (Mpbs) vs. Time (s).

Figure 7.12, 7.13 and 7.14 shows the received signal strength, path loss and delay spread for the receiver points at each corresponding time.

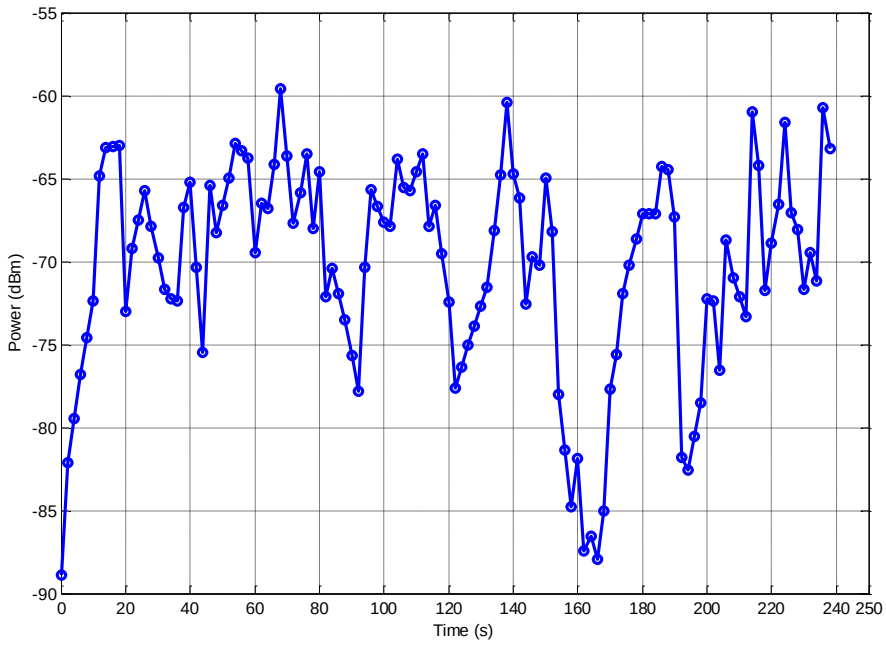

Figure 7.12: Received power (dBm) vs. Ttime (s).

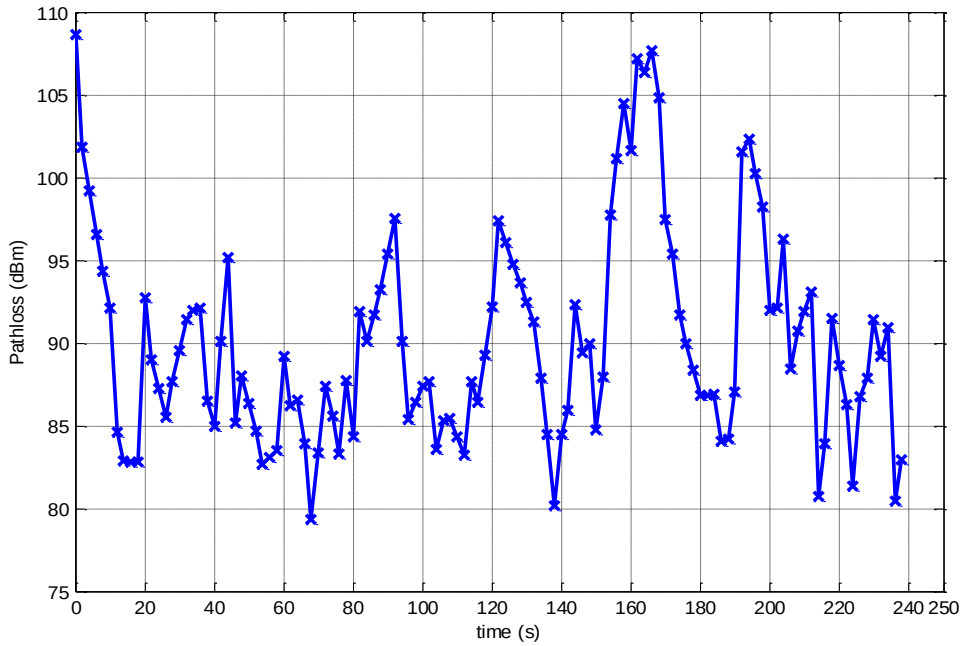

Figure 7.13: Path loss vs. time (s).

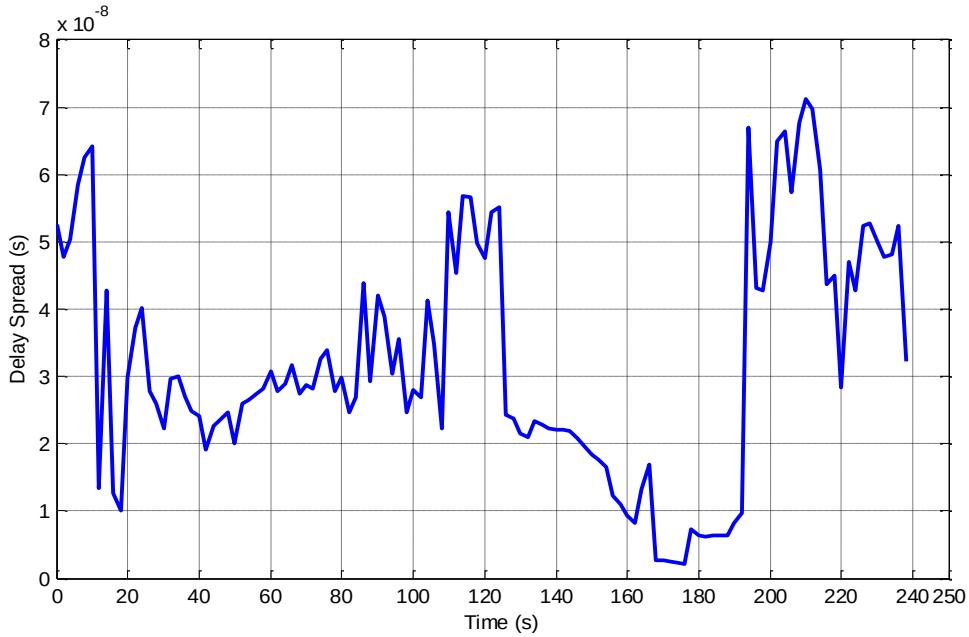

Figure 7.14: Delay Spread vs. time (s).

7.5 Conclusions

In this chapter, we introduced a deterministic multi scenario channel propagation model for University of Bradford campus; Indoor multi-storey propagation model was first evaluated in terms of the received signal strength and path loss for both scenarios LOS and NLOS, then Indoor-Outdoor Scenario using a moving receiver was created and evaluated. Finally Outdoor -Outdoor Scenario using a moving receiver was created and evaluated.

Wireless InSite's 3D model produces very accurate results, but at the cost of long run times. Run time is directly affected by the number of transmitters and receivers, and the number of faces in the building geometry. As the number of transmitters/receivers and building surfaces increases, then run time increases.

CHAPTER 8

An Exact Envelope Correlation Formula for Two-Antenna Systems Using Input Scattering Parameters and Including Power Losses

8.1 Introduction

As previously mentioned in Chapter 3, the capacity of SISO systems are limited by the Shannon-Nyquist criteria, but can be enhanced with the use of multiple antennas [109]. On the other hand in practical antenna arrays, mutual coupling between the antennas degrades the antenna system diversity performance; therefore designers try to minimize the mutual coupling of the antenna system while maintaining the matching requirements. MIMO systems are required to deliver maximum capacity with minimum bit error rate (BER). To achieve that, the antenna arrays should have high gain, narrow lobe patterns, and reasonable separation between the elements.

An important requirement for the MIMO system is that the antennas must be able to receive different signals even if they are closely spaced, i.e. diversity reception. Thus for maximum benefit of MIMO system the antennas should be spaced sufficiently in the arrays, but it is challenging and hard to implement multiple antennas in a very small area such as mobile handsets, PDA's and laptops. Therefore the spatial correlation properties of different antenna elements in arrays should be considered since this will affect the MIMO channel capacity.

In mobile communication the antenna spacing is usually small, thus the impact of the mutual coupling will not be negligible. Mutual coupling increases the spatial correlation between the array elements. Also, it deforms the radiation pattern of each array element, which affects the diversity gain.

A generalized analysis of signal correlation between any two array elements including non-identical elements and arbitrary load termination of passive antenna ports was presented in [110]. The method relates to the power balance concept and is based on the antenna impedance matrix. In [111], theoretical and simulation studies have been conducted to explain the experimentally observed effect that the correlation between signals of closely spaced antennas is smaller than that predicted using the well-known theoretical methods. A simple expression to compute the correlation coefficients from the far field pattern including the propagation environment characteristics and the terminating impedance was introduced in [112].

Three different methods are used to calculate the antenna correlation. The first method is based on the far field pattern [113], the second is based on the scattering parameters at

the antennas terminals [25] and the third method is based on Clarke's formula [114]. Calculating correlation using the radiation field pattern of the antenna system is a time consuming method, whether it is done by simulation or using experimental data.

A simple method for the computation of the envelope correlation for two antenna elements using scattering parameters was presented in [25]. This method avoids intensive computations using the radiation field patterns of the antenna system, and may be straightforwardly generalized to the envelope correlation of an N-antenna system [26].

This formulation has received widespread adoption in discussing antenna diversity issues [28, 115]. However, the computations in [25] and [26] do not include the power losses in the antenna structures. This accounts for the discrepancy between the envelope correlation results obtained by this method, from that computed directly from the radiation field patterns of the two antenna elements [116] using:

$$\rho_e = \frac{\left| \iint_{4\pi} d\Omega F_1(\theta,\phi).d\Omega F_2(\theta,\phi) \right|^2}{\iint_{4\pi} d\Omega \left|F_1(\theta,\phi)\right|^2 \iint_{4\pi} d\Omega \left|F_2(\theta,\phi)\right|^2} \tag{8.1}$$

where $F_i(\theta,\phi) = F_\theta^i(\theta,\phi)\hat{e}_\theta + F_\phi^i(\theta,\phi)\hat{e}_\phi$ is the radiation field of the ith antenna.

In practice it is required to identify envelope correlation between any two sensors in a given array. The correlation is sensitive to the intrinsic power losses in the radiating elements; the methodologies reported in [25] and [26] are based on ideal passive structures, i.e. without losses. Hallbjorner has presented a useful analysis on the effect of

antenna efficiency on spatial correlation estimates [116]. The analysis presented below provides an operational method, with a clear physical basis, for explicitly incorporating the intrinsic (Ohmic) losses into the estimation of the spatial correlation, using the scattering representation for a multi-beam array [117].

In this chapter, a simplified calculation of the envelope correlation in equation (8.1) for a lossy two-antenna system is completely evaluated in terms of the scattering parameters and the intrinsic power losses of the antenna structures. The power loss is presented in a matrix formulation, in order to match the presentation in [25, 26, 118, 119]. This represents a major simplification with respect to the conventional use of the radiation field patterns of the antennas. Two new illustrative examples are presented and discussed to show the contribution of the proposed method.

8.2 Summary of the Method

Consider the electromagnetic geometry suggested by Figure 8.1, the total power is given by:

$$P_{total} = P_{rad} + P_{loss} \tag{8.2}$$

where P_{rad} and P_{loss} are the total radiated power and power loss respectively; P_{tot} is sometimes called the accepted power, and may be computed in terms of the incident waves by $\left(a^{\dagger}a - b^{\dagger}b\right)$, where † is the Hermitian transpose.

The analysis developed below, and the subsequent case studies shown in Figure 2, have been presented for convenience in a wire antenna formulation and the solved using NEC.

It should be understood that the underlying concepts are fully general, and can readily be rewritten in terms of general surface and volume currents.

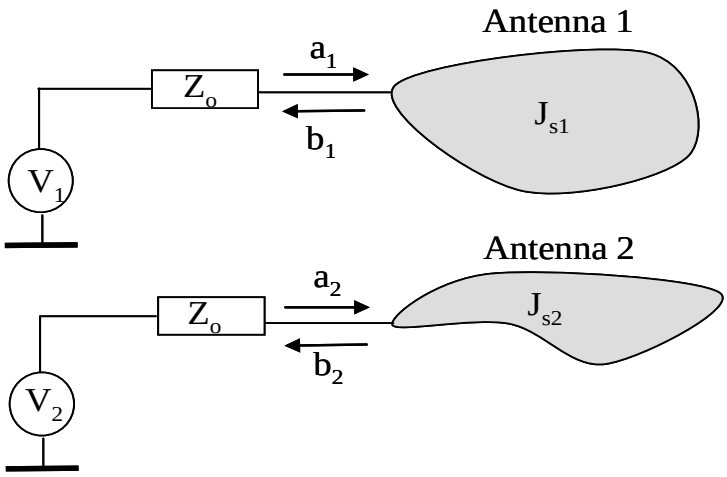

Figure 8. 1: Basic geometry for two antenna element system

The surface current density distributed on a radiating wire of radius r can be written as;

$$Js(\theta,l) = \frac{J_s(\theta,l)}{2\pi r} a_l \approx \frac{J_s(l)}{2\pi r} a_l \tag{8.3}$$

The power loss may be computed in terms of the surface currents on the antenna structures as follows. These currents may be expressed in terms of the incident waves a_1 and a_2:

$$J_{S1} = \frac{1}{\sqrt{R_S}} \left(a_1 \cdot \frac{J_{S1}^1(l)}{2\pi r} \hat{a}_l + a_2 \cdot \frac{J_{S1}^2(l)}{2\pi r} \hat{a}_l \right) \tag{8.4}$$

$$J_{S1} = \frac{1}{\sqrt{R_S}} \left(a_1 \cdot \frac{J_{S2}^1(l)}{2\pi r} \hat{a}_l + a_2 \cdot \frac{J_{S2}^2(l)}{2\pi r} \hat{a}_l \right) \tag{8.5}$$

J_{s1} and J_{s2} are the total currents on structures 1 and 2, respectively, J_{s1}^1 and J_{s1}^2 are the normalised currents on structures 1 and 2 due to the incident wave a_1, similarly J_{s2}^1 and J_{s2}^2 are due to the incident wave a_1 , R_s is the surface impedance of the antennas. Thus,

the power loss on structures 1 and 2 can be expressed by equation 8.6 and equation 8.7, respectively:

$$P_{l1} = \iint \left(a_1 J_{S1}^1(l) + a_2 J_{S1}^2(l)\right) \cdot \left(a_1 J_{S1}^1(l) + a_2 J_{S1}^2(l)\right)^* d\theta dl \tag{8.6}$$

$$P_{l2} = \iint \left(a_1 J_{S2}^1(l) + a_2 J_{S2}^2(l)\right) \cdot \left(a_1 J_{S2}^1(l) + a_2 J_{S2}^2(l)\right)^* d\theta dl \tag{8.7}$$

Expanding these expressions gives,

$$P_{l1} = \int |a_1|^2 J_{S1}^1(l) J_{S1}^{1*}(l) + a_1 a_2^* J_{S1}^1(l) J_{S1}^{2*}(l) + a_2 a_1^* J_{S1}^2(l) J_{S1}^{2*}(l) + |a_2|^2 a_1 a_2^* J_{S1}^2(l) J_{S1}^{2*}(l) dl \tag{8.8}$$

$$P_{l2} = \int |a_1|^2 J_{S2}^1(l) J_{S2}^{1*}(l) + a_1 a_2^* J_{S2}^1(l) J_{S2}^{2*}(l) + a_2 a_1^* J_{S2}^2(l) J_{S2}^{2*}(l) + |a_2|^2 a_1 a_2^* J_{S2}^2(l) J_{S2}^{2*}(l) dl \tag{8.9}$$

Hence, equation 8.8 and equation 8.9 can be expressed in matrix notation as,

$$P_{loss} = \left(a^\dagger L a\right) \tag{8.10}$$

where,

$$L = L' + L'' = \begin{pmatrix} L'_{11} & L'_{12} \\ L'_{21} & L'_{22} \end{pmatrix} + \begin{pmatrix} L''_{11} & L''_{12} \\ L''_{21} & L''_{22} \end{pmatrix} \tag{8.11}$$

The elements L'_{ij} may be read across as,

$$L'_{ij} = \begin{pmatrix} \frac{1}{2\pi} \int J_{S1}^1(l) J_{S1}^{1*}(l) dl & \frac{1}{2\pi} \int J_{S1}^1(l) J_{S1}^{2*}(l) dl \\ \frac{1}{2\pi} \int J_{S1}^2(l) J_{S1}^{2*}(l) dl & \frac{1}{2\pi} \int J_{S1}^2(l) J_{S1}^{2*}(l) dl \end{pmatrix} \tag{8.12}$$

and similarly for L''_{ij}. From the properties of the Hermitian inner product, it follows that $Li_j = L_{ij}^*$.

Equation 8.2 can now be expressed in terms of the incident waves a_1 and a_2.

$$a^\dagger \left(1 - S^\dagger S\right) a = \left(a^\dagger L a\right) + \left(a^\dagger R a\right) \tag{8.13}$$

where the scattering matrix S of the two-antenna system, including the power loss. R is the 2×2 matrix defined in [25] as,

$$R = \begin{pmatrix} \frac{D_1}{4\pi}\iint_{4\pi} d\Omega \left|F_1(\theta,\phi)\right|^2 & \frac{\sqrt{D_1 D_2}}{4\pi}\iint_{4\pi} d\Omega F_1(\theta,\phi)\cdot F_2^*(\theta,\phi) \\ \frac{\sqrt{D_2 D_1}}{4\pi}\iint_{4\pi} d\Omega F_2(\theta,\phi)\cdot F_1^*(\theta,\phi) & \frac{D_2}{4\pi}\iint_{4\pi} d\Omega \left|F_2(\theta,\phi)\right|^2 \end{pmatrix} \tag{8.14}$$

where D_i is the ith maximum directivity of the ith antenna. Therefore, from equation 8.13 the equivalent elements of equation 8.14 can be expressed as follows:

$$\frac{D_1}{4\pi}\iint_{4\pi} d\Omega \left|F_1(\theta,\phi)\right|^2 = 1-\left(1-\left|S_{11}\right|^2+\left|S_{21}\right|^2\right)-\left(L_{11}^{'}+L_{11}^{''}\right) \tag{8.15}$$

$$\frac{\sqrt{D_1 D_2}}{4\pi}\iint d\Omega F_1(\theta,\phi)\cdot F_2(\theta,\phi) = -\left(S_{11}^* S_{21}+S_{21}^* S_{22}\right)-\left(L_{12}^{'}+L_{12}^{''}\right) \tag{8.16}$$

Thus, the envelope correlation for the two-antenna system geometry (Figure 8.1) can be expressed in terms of the scattering parameters, and the intrinsic power losses, as in following:

$$\rho_e = \frac{\left|1-\left(S_{11}^* S_{12}+S_{21}^* S_{22}\right)-\left(L_{12}^{'}+L_{12}^{''}\right)\right|^2}{\left\{1-\left(\left|S_{11}\right|^2+\left|S_{21}\right|^2\right)-\left(L_{11}^{'}+L_{11}^{''}\right)\right\}\left\{1-\left(\left|S_{22}\right|^2+\left|S_{12}\right|^2\right)-\left(L_{22}^{'}+L_{22}^{''}\right)\right\}} \tag{8.17}$$

8.3 Simulation and Results Using Two Dipoles Antennas

In order to verify equation 8.17, the envelope correlation has been computed for two parallel half-wavelength wire dipoles in free space, as a function of their separation. The antenna far fields and scattering parameters were obtained using NEC [120]. The wire radius of each dipole was set at 0.002 wavelengths.

Two different sources of loss were considered for the purpose of validation. In the first instance, both dipoles were loaded by two lumped resistive loads, each of 25Ω, as in Figure 7.2. Secondly, the dipoles were loaded by surface conductivity along the antenna geometry.

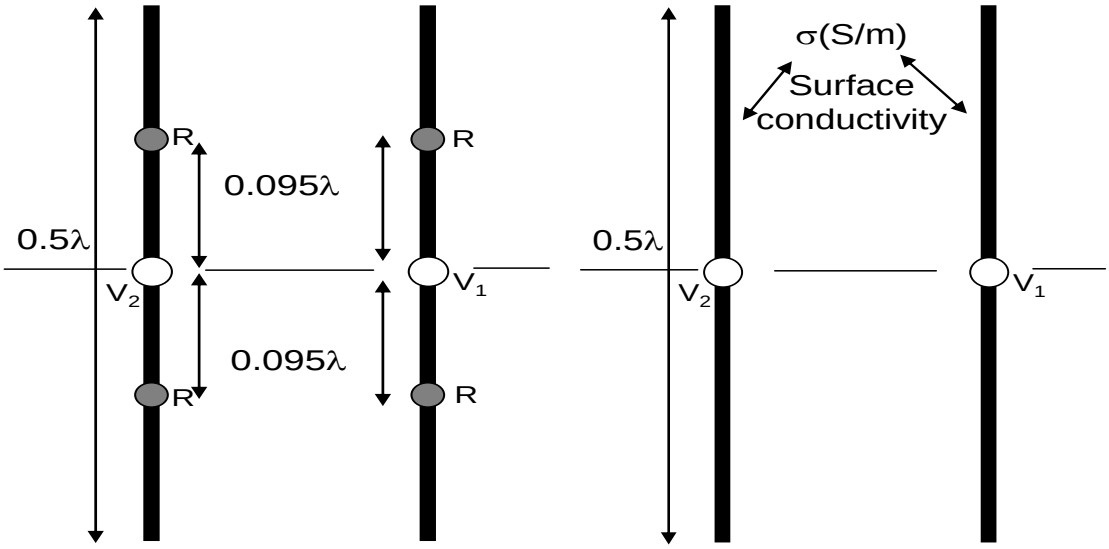

Figure 8. 2 : Examples under test; (left: antennas loaded by lumped resistive loads, right: antennas loaded by surface conductivity)

Variations between the proposed method and the lossless approach were checked by simulation. The spatial envelope correlations calculated using the far field parameters, versus the dipole separation distance, are given in Figure 8.3 for both lossless and lossy cases. There is good agreement between the proposed method and the results calculated from equation 8.1 for the lossy case. The envelope correlation for dipole separations less than 0.5 wavelengths can take values bigger than the achieved S_{21} values. It is also interesting to note that the nulls of the envelope correlation are shifted compared with those obtained for the lossless approach.

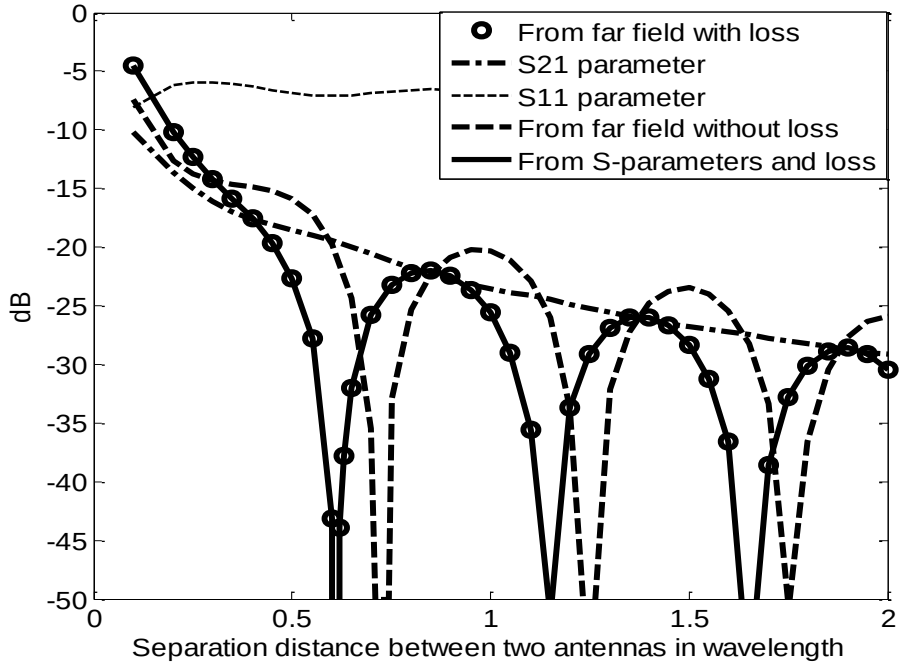

Figure 8. 3: Computed spatial envelope correlations and S-parameters for two half wavelength dipoles against their separated distance.

Figures 8.4 and 8.5 illustrate variations in the spatial envelope correlations, versus the lumped resistive loads, and surface conductivities, respectively.

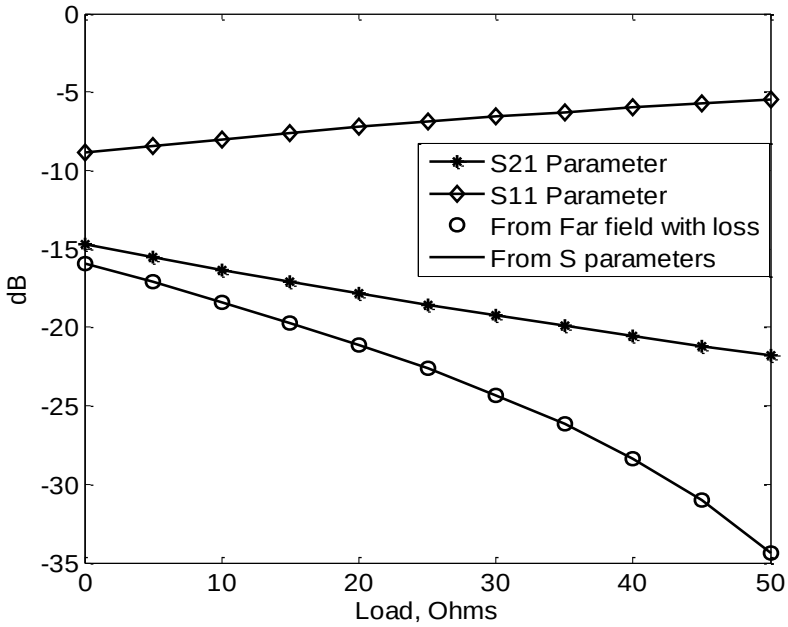

Figure 8. 4 : Envelope correlation and S-parameters for two half wavelength dipoles against the lumped resistive loads shown in Figure 8.2.

The dipole separation was kept constant at 0.5 wavelengths. These envelope correlation results prove the concept of the proposed method, i.e. equation 8.17, against those obtained from the far field patterns. It can be seen in Figure 8.4 that the envelope correlations values closely approach the S_{21} values as the load is reduced. For the surface conductivity case, they are much closer for small wire conductivity values.

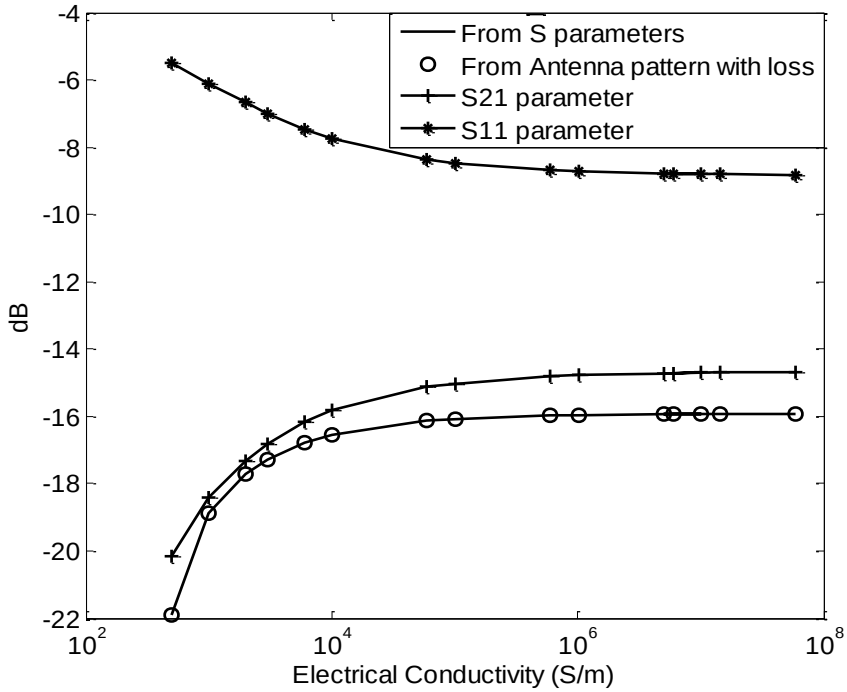

Figure 8. 5: Envelope correlation and S-parameters for two half wavelength dipoles against the surface electric conductivity on both dipoles.

8.4 Simulation and Results using two Planar Inverted F-antennas

The envelope correlation has also been computed for an array of two Planar Inverted F-antennas (PIFA) in free space, as a function of their separation distance 'd'. The antenna far fields and scattering parameters were obtained using NEC [120]. The wire radius used to create the whole system was set to 1 mm. Two different sources of loss were considered for the purpose of validation. In the first test, both antennas were loaded by lumped

resistive loads each of 10 Ω as shown in Figures 8.6a and 8.6b; whereas in the second a conducting surface resistivity was considered on both wires.

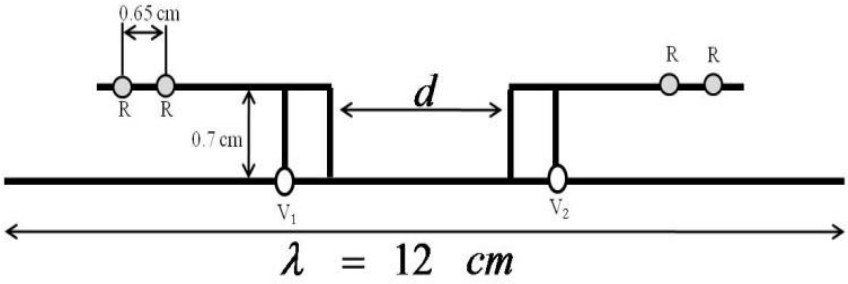

(a)

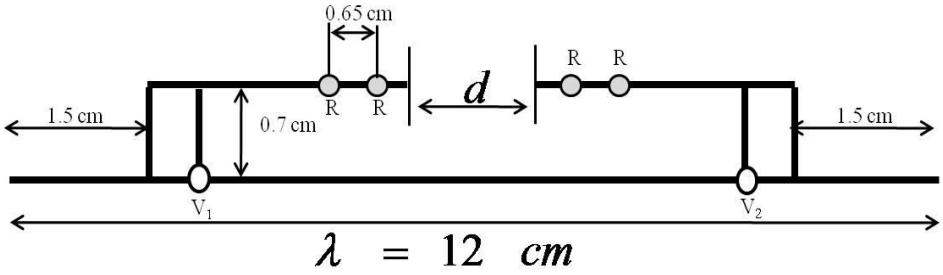

(b)

Figure 8. 6: Example under test: structure (a) and structure (b).

The spatial envelope correlation calculated using the far field parameters, versus the antenna separation distance d for the example shown in Figure 8.6a, is given in Figure 8.7 for both lossless and lossy case together with the result from the scattering parameters with loss.

From Figure 8.7 it is interesting to note that the S_{11} value varies between -0.2 and -1 dB. Figure 8.6a shows the two planar antennas with their feed ends adjacent, whilst in Figure 8.6b they are the other way round. For Figure 8.6a a strong mutual coupling will

presumably be introduced between the two antennas created by the high currents passing through the short feed pins. At almost all antenna separations the envelope correlation takes values higher than the S_{21} values.

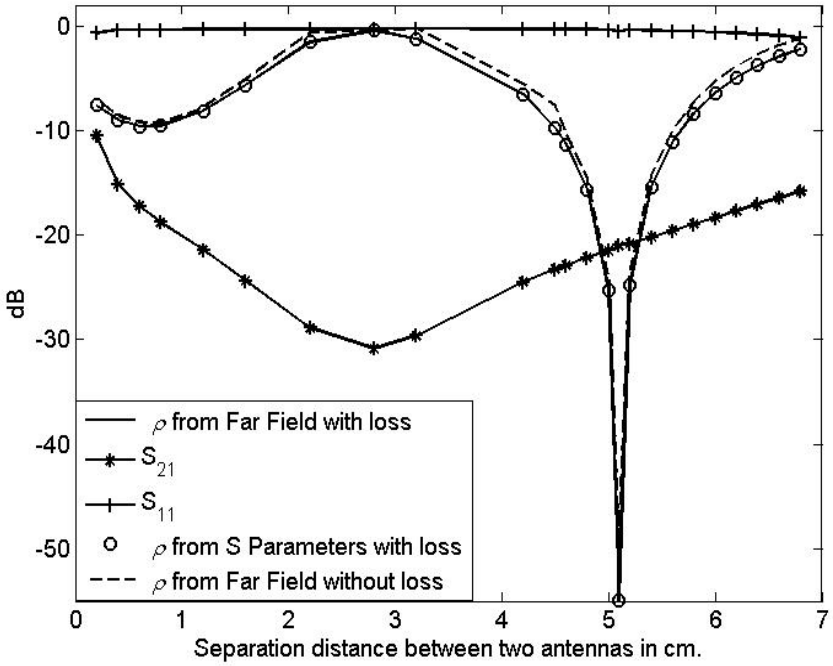

Figure 8. 7: Computed spatial envelope correlations and S-parameters for two PIFA antennas against their separated distance 'd' in centimetres.

Figure 8.8 illustrates variations in the spatial envelope correlations versus the antenna separation distance for the antenna array structure shown in Figure 8.6b. Again, the result shows a good agreement between the proposed method and the results calculated from equation 8.1 for the lossy case, it is noticeable from Figure 8.7 and 8.8 that the envelope correlation values computed by the proposed method and from equation 8.1 for the lossy case for antenna separations above 1 cm have a 1 dB difference. Note that for this configuration the S_{11} is much lower.

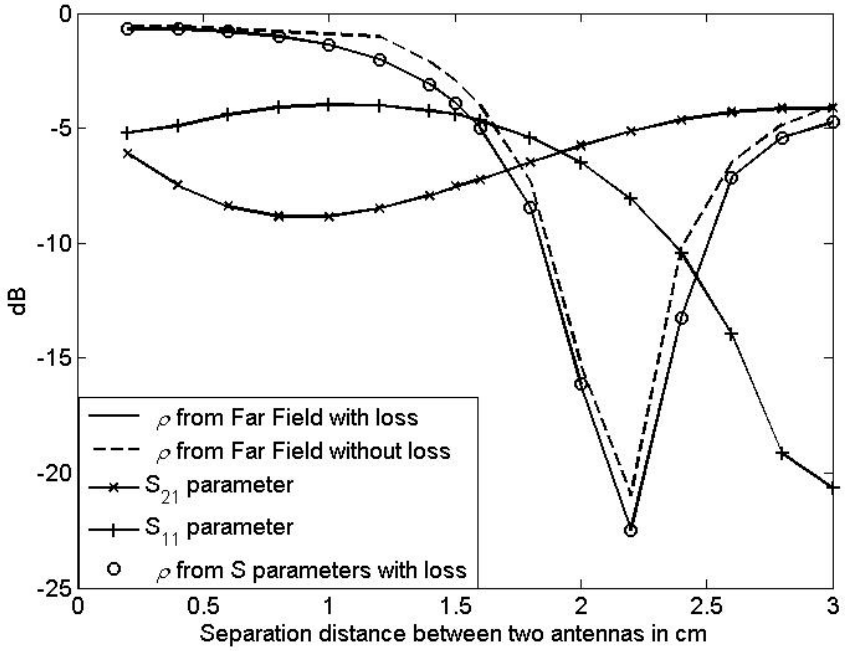

Figure 8. 8: Computed spatial envelope correlations and S-parameters for two PIFA antennas against their separated distance 'd' in centimetres.

Figure 8.9 illustrates the variation in the spatial envelope correlation versus the surface conductivities for the structure shown in Figure 8.6a. The antenna separation was kept constant at 3.2 cm. It can be seen in Figure 8.9 that the envelope correlation values are closer to the S_{11} values than to the S_{21}, there is no clear effect of the surface conductivity on the envelope correlation values.

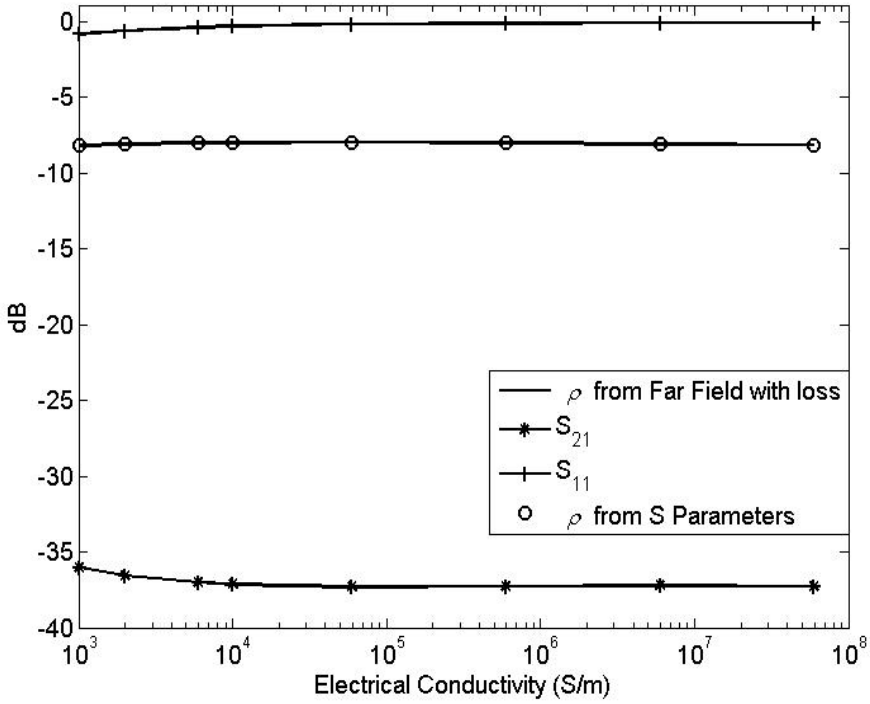

Figure 8. 9: Computed spatial envelope correlations and S-parameters for two PIFA antennas against surface electric conductivity on both antennas.

In summary, the analysis described here, based on the conceptual framework assumed by equation 8.17, provides a direct and accurate forecast of spatial envelope correlations, as compared with the far field analysis in equation 8.1.

It should be noted that several empirical approaches exist for the direct measurement of the radiation efficiency of passive antennas. These include radiometry [121, 122], random field analysis [123] and reverberation chamber techniques [124, 125], and when applied to multi-port passive structures can provide an independent check on the diagonal terms in the L-matrix (i.e. equation 8.11). Such practical implementations will be considered for future developments of this work.

8.5 Conclusions

A method of calculation, for the spatial envelope correlation of a two-antenna system, which includes losses, using the system scattering parameters has been presented. This new expression should reduce the complexity in predicting the spatial envelope correlation, and simplify antenna designs where a low envelope correlation is required. Four validation examples were presented, which demonstrate good agreement between the proposed method, and the explicit calculation using far field pattern data. The trend of this method represents a major engineering contribution to reduce the complexity of the conventional method that uses the radiation field patterns of the antennas.

CHAPTER 9

An Envelope Correlation Formula For (N, N) MIMO Antenna Arrays Using Input Scattering Parameters, And Including Power Losses

9.1 Introduction

MIMO systems employ multiple antennas at transmitter and receiver to improve the reliability and capacity of wireless links in a rich electromagnetic scattering environment. It is well known that the capacity of an (N,N) MIMO system increases with N, the number of antennas in the transmit and receive arrays on the assumption of independent Rayleigh fading between each pair of transmit and receive antennas [109]. In practice, the independence of the received signals will depend on the angular distribution in the channel, the arrangement and radiation pattern of the antennas and their polarization. It will be reduced by mutual coupling between antennas [126]. The avoidance of mutual coupling and the ability to distinguish between paths arriving at closely spaced angles is favoured by larger antenna spacing, whilst practical constraints often demand compact arrangements, especially in mobile systems.

To optimize the diversity performance of the array, antennas should be located so as to sample the channel at separations that exhibit minimum spatial correlation [118,127], taking account of mutual coupling effects [5-7]. (Note that in some circumstances, mutual coupling can enhance MIMO capacity [128, 129]). Since the optimum separation distance will depend on the angle-of-arrival distributions, practical systems may elect to optimize the separation for an average channel, for which a common assumption is of a rich scattering environment with scatterers uniformly distributed in angle. For this reason, it is useful in developing practical systems, to have a straightforward means to evaluate the spatial, complex-envelope correlation for the system of antennas [28, 130].

The theory presenting a generalized analysis of signal correlation between any two array elements to include non-identical elements and arbitrary load termination of passive antenna ports was presented in [112], the method is related to the power balance concept and based on the antenna impedance matrix. In [127,111], theoretical and simulation studies have been conducted to explain the experimentally observed effect that the correlation between signals of closely spaced antennas is smaller than that predicted using the well-known theoretical methods. A simple expression to compute the correlation coefficients from the far field pattern including the propagation environment characteristic and the terminating impedance was introduced in [110].

There are three possible methods to compute the envelope correlation. The first method is based on the use of far field pattern data [128], the use of actual or simulated radiation field data is time consuming, if spread over several design iterations. The second method employs the scattering parameters measured at the antenna terminals [25], and there is a third method based on Clarke's formula [114]. The calculation may also be formulated in

terms of a generalised impedance matrix [112]. In practice we require the correlation between any two antennas in an array. In [116] a useful relation was presented including the effect of the antenna efficiencies on the calculated spatial correlation. The correlation is sensitive to the intrinsic power losses in the radiating structures. The scattering formulation derived and tested in [25] and [26] does not include these losses and this provides the rationale for the method presented below.

The scattering parameter formulation for the envelope correlation in an (N,N) MIMO antenna array has been modified to take the intrinsic antenna power losses into account. This method of calculation provides a major simplification over the use of antenna radiation field patterns. Its accuracy is illustrated in three examples, which also show that the locations of the correlation minima are sensitive to the intrinsic losses.

9.2 Background Theory

The envelope correlation for two antennas may be calculated from equation (9.1):

$$\rho_e = \frac{\left|\iint_{4\pi} d\Omega F_1(\theta,\phi)\cdot F_2(\theta,\phi)\right|^2}{\iint_{4\pi} d\Omega \left|F_1(\theta,\phi)\right|^2 \iint_{4\pi} d\Omega \left|F_2(\theta,\phi)\right|^2} \tag{9.1}$$

where $F_i(\theta,\phi) = F_\theta^i(\theta,\phi)\hat{e}_\theta + F_\phi^i(\theta,\phi)\hat{e}_\phi$ is the radiation field of the ith antenna, and the surface integrations are over the 2-sphere [114]. On this basis, the envelope correlation between antennas i and j may be obtained from the equation (9.2), as described in [26],

$$\rho_e(i,j,N) = \frac{\left|C_{i,j}(N)\right|^2}{\prod_{k=(i,j)}\left[1-C_{k,k}(N)\right]} \tag{9.2}$$

where $C_{i,j}(N)$ is expressed as,

$$C_{i,j}(N) = \sum_{n=1}^{N} S_{i,n}^{*} S_{n,j} \tag{9.3}$$

Hence, from equations (9.2) and (9.3), the explicit scattering parameter formula for envelope correlation is [26]:

$$\rho_e(i,j,N) = \frac{\left| \sum_{n=1}^{N} S_{i,n}^{*} S_{n,j} \right|^2}{\prod_{k=(i,j)} \left[1 - \sum_{n=1}^{N} S_{i,n}^{*} S_{n,k} \right]} \tag{9.4}$$

Although equation (9.4) offers a simple approach compared with radiation pattern, it should be emphasized that this equation is limited by certain three assumptions as in [131].

In this chapter the computed envelope correlation for an (N, N) MIMO system will be evaluated from the scattering parameters and the intrinsic power losses in the radiating structures. This calculation represents a significant simplification over using the far field patterns in equation (9.1).

9.3 Summary of the Method

Consider the electromagnetic geometry in Figure 1, the total power is given by,.

$$P_{total} = P_{rad} + P_{loss} \tag{9.5}$$

where P_{rad} and P_{loss} are the total radiated power, and power loss, respectively. P_{total} is also known as the accepted power, and may be computed in terms of the incident wave, amplitude a and reflected amplitude b by $(a^{\dagger}a - b^{\dagger}b)$, where $\dagger$ is the Hermitian conjugate.

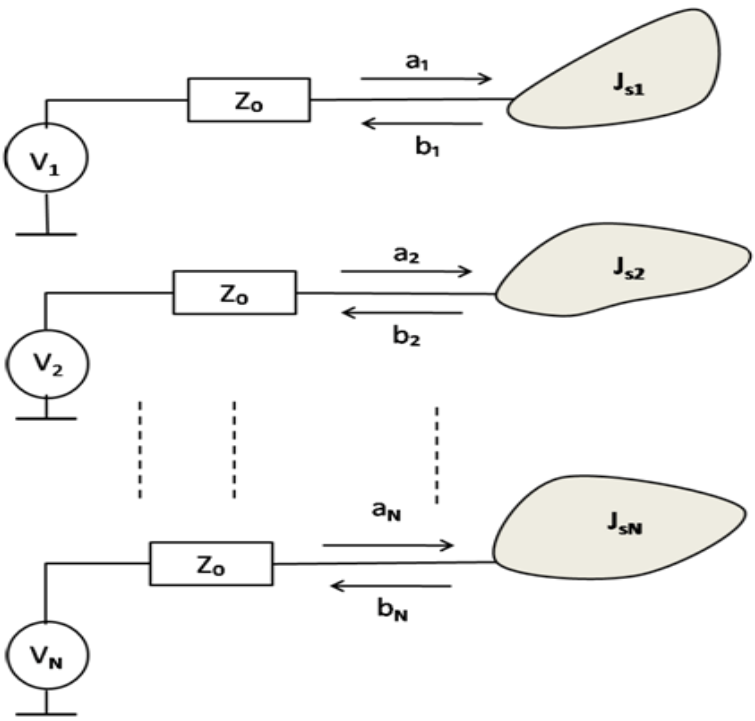

Figure 9. 1: The electromagnetic geometry for the N antenna element system.

The surface current density on the antenna structure can be written as:

$$Js(\theta,l) = \frac{I(\theta,l)}{2\pi r} a_l \approx \frac{I(l)}{2\pi r} a_l \tag{9.6}$$

where r is the radius of the dipole wire.

It should be noted that the use of equation (9.6) is to prove the concept of present work; however, equations from (9.6) till the end of this section could be redefined when the assumptions and approximation of the surface current distribution not exactly be given as equation 9.6 presents. One can use the actual surface current distribution on the antenna geometry surface. For example equation 6 simply could be defined on surface geometry of two orthogonal axes u and v as $J_s(u,v) = U_s(u,v)\hat{\boldsymbol{a}}_u + V_s(u,v)\hat{\boldsymbol{a}}_v$. Where $U_s(u,v)$ and $V_s(u,v)$ are the surface current densities in the directions of $\hat{\boldsymbol{a}}_u$ and $\hat{\boldsymbol{a}}_v$ respectively.

The power loss may be computed in terms of the surface currents on the antenna structures as follows. These currents may be expressed in terms of the incident waves $a_1, a_2, \cdots a_n$:

$$
\begin{aligned}
Js_1 &= \frac{1}{\sqrt{Rs}}\left(a_1 \cdot \frac{I_{11}(l)}{2\pi r} a_l + a_2 \cdot \frac{I_{12}(l)}{2\pi r} a_l + a_3 \cdot \frac{I_{13}(l)}{2\pi r} a_l + \cdots + a_N \cdot \frac{I_{1N}(l)}{2\pi r} a_l \right) \\
Js_2 &= \frac{1}{\sqrt{Rs}}\left(a_1 \cdot \frac{I_{21}(l)}{2\pi r} a_l + a_2 \cdot \frac{I_{22}(l)}{2\pi r} a_l + a_3 \cdot \frac{I_{23}(l)}{2\pi r} a_l + \cdots + a_N \cdot \frac{I_{2N}(l)}{2\pi r} a_l \right) \\
&\vdots \\
Js_i &= \frac{1}{\sqrt{Rs}}\left(a_1 \cdot \frac{I_{i1}(l)}{2\pi r} a_l + a_2 \cdot \frac{I_{i2}(l)}{2\pi r} a_l + a_3 \cdot \frac{I_{i3}(l)}{2\pi r} a_l + \cdots + a_N \cdot \frac{I_{iN}(l)}{2\pi r} a_l \right)
\end{aligned}
\tag{9.7}
$$

The I_{in} terms are the normalised currents on structure i due to the incident wave n, and R_s is the surface impedance of the antenna. The power loss on the ith antenna structures is calculated by,

$$
P_{loss_i} = \iint Js_i \cdot Js_i^* r d\theta dl
$$

$$
P_{loss_i} = \iint \left\{ \begin{array}{l}
a_1 \cdot a_1^* \dfrac{I_{i1}(l) I_{i1}^*(l)}{(2\pi r)^2} + a_1 \cdot a_2^* \dfrac{I_{i1}(l) I_{i2}^*(l)}{(2\pi r)^2} + \cdots + a_1 \cdot a_N^* \dfrac{I_{i1}(l) I_{iN}^*(l)}{(2\pi r)^2} \\
+ a_2 \cdot a_1^* \dfrac{I_{i2}(l) I_{i1}^*(l)}{(2\pi r)^2} + a_2 \cdot a_2^* \dfrac{I_{i2}(l) I_{i2}^*(l)}{(2\pi r)^2} + \cdots + a_2 \cdot a_N^* \dfrac{I_{i2}(l) I_{iN}^*(l)}{(2\pi r)^2} \\
+ a_N \cdot a_1^* \dfrac{I_{iN}(l) I_{i1}^*(l)}{(2\pi r)^2} + a_N \cdot a_2^* \dfrac{I_{iN}(l) I_{i2}^*(l)}{(2\pi r)^2} + \cdots + a_N \cdot a_N^* \dfrac{I_{iN}(l) I_{iN}^*(l)}{(2\pi r)^2}
\end{array} \right\} r d\theta dl
\tag{9.8}
$$

Solving for circumferential integral leads to,

$$
P_{loss_i} = \frac{1}{2\pi r} \int_l \left\{ \begin{array}{l}
a_1 \cdot a_1^* I_{i1}(l) I_{i1}^*(l) + a_1 \cdot a_2^* I_{i1}(l) I_{i2}^*(l) + \cdots + a_1 \cdot a_N^* I_{i1}(l) I_{iN}^*(l) + \\
a_2 \cdot a_1^* I_{i2}(l) I_{i1}^*(l) dl + a_2 \cdot a_2^* I_{i2}(l) I_{i2}^*(l) dl + \cdots + a_2 \cdot a_N^* I_{i2}(l) I_{iN}^*(l) + \\
a_N \cdot a_1^* I_{iN}(l) I_{i1}^*(l) + a_N \cdot a_2^* I_{iN}(l) I_{i2}^*(l) + \cdots + a_N \cdot a_N^* I_{iN}(l) I_{iN}^*(l)
\end{array} \right\} dl
\tag{9.9}
$$

Subject to equation (9), the power losses may be expressed in matrix notation as follows,

$$P_{loss} = a^{\dagger} L a \tag{9.10}$$

where the linear operator L can be defined by the following,

$$L = L^1 + L^2 + L^3 + \cdots + L^i \tag{9.11}$$

The matrix representations of the elements of L, as example L^1 and L^i can be written as below,

$$L^1 = \begin{bmatrix} \frac{1}{2\pi r}\int_l I_{11}(l)I_{11}^*(l)dl & \frac{1}{2\pi r}\int_l I_{11}(l)I_{12}^*(l)dl & \cdots & \frac{1}{2\pi r}\int_l I_{11}(l)I_{1N}^*(l)dl \\ \frac{1}{2\pi r}\int_l I_{12}(l)I_{11}^*(l)dl & \frac{1}{2\pi r}\int_l I_{12}(l)I_{12}^*(l)dl & \cdots & \frac{1}{2\pi r}\int_l I_{12}(l)I_{1N}^*(l)dl \\ \vdots & \vdots & \cdots & \cdots \\ \frac{1}{2\pi r}\int_l I_{1N}(l)I_{11}^*(l)dl & \frac{1}{2\pi r}\int_l I_{1N}(l)I_{12}^*(l)dl & \cdots & \frac{1}{2\pi r}\int_l I_{1N}(l)I_{1N}^*(l)dl \end{bmatrix}$$

$$\vdots$$

$$\vdots$$

$$L^i = \begin{bmatrix} \frac{1}{2\pi r}\int_l I_{i1}(l)I_{i1}^*(l)dl & \frac{1}{2\pi r}\int_l I_{i1}(l)I_{i2}^*(l)dl & \cdots & \frac{1}{2\pi r}\int_l I_{i1}(l)I_{iN}^*(l)dl \\ \frac{1}{2\pi r}\int_l I_{i2}(l)I_{i1}^*(l)dl & \frac{1}{2\pi r}\int_l I_{i2}(l)I_{i2}^*(l)dl & \cdots & \frac{1}{2\pi r}\int_l I_{i2}(l)I_{iN}^*(l)dl \\ \vdots & \vdots & \cdots & \cdots \\ \frac{1}{2\pi r}\int_l I_{iN}(l)I_{i1}^*(l)dl & \frac{1}{2\pi r}\int_l I_{iN}(l)I_{i2}^*(l)dl & \cdots & \frac{1}{2\pi r}\int_l I_{iN}(l)I_{iN}^*(l)dl \end{bmatrix} \tag{9.12}$$

Using the energy conservation law and its independence on array input coefficients [19], equation (9.5) including structure losses, can be expressed as

$$a^{\dagger}(1 - S^{\dagger}S)a = a^{\dagger}La + a^{\dagger}Ra \tag{9.13}$$

where $S \in \mathbb{c}^{N\times N}$ is the scattering matrix of the lossy N-antenna system, and R is an $N \times N$ matrix defined as,

$$R=\begin{pmatrix} \frac{D_1}{4\pi}\iint_{4\pi} d\Omega\left|F_1(\theta,\phi)\right|^2 & \frac{\sqrt{D_1D_2}}{4\pi}\iint_{4\pi} d\Omega F_1(\theta,\phi)\cdot F_2^*(\theta,\phi) & \cdots & \frac{\sqrt{D_1D_N}}{4\pi}\iint_{4\pi} d\Omega F_1(\theta,\phi)\cdot F_N^*(\theta,\phi) \\ \frac{\sqrt{D_2D_1}}{4\pi}\iint_{4\pi} d\Omega F_2(\theta,\phi)\cdot F_1^*(\theta,\phi) & \frac{D_2}{4\pi}\iint_{4\pi} d\Omega\left|F_2(\theta,\phi)\right|^2 & \cdots & \frac{\sqrt{D_2D_N}}{4\pi}\iint_{4\pi} d\Omega F_2(\theta,\phi)\cdot F_N^*(\theta,\phi) \\ \vdots & \vdots & \cdots & \cdots \\ \frac{\sqrt{D_ND_1}}{4\pi}\iint_{4\pi} d\Omega F_N(\theta,\phi)\cdot F_1^*(\theta,\phi) & \frac{\sqrt{D_ND_2}}{4\pi}\iint_{4\pi} d\Omega F_N(\theta,\phi)\cdot F_2^*(\theta,\phi) & \cdots & \frac{D_N}{4\pi}\iint_{4\pi} d\Omega\left|F_N(\theta,\phi)\right|^2 \end{pmatrix} \tag{9.14}$$

where D_i is the maximum directivity of the ith antenna.

Now, considering the above equations, the envelope correlation between the antennas i and j in the (N, N) MIMO system can be expressed in terms of the scattering parameters and the intrinsic power losses as follows,

$$\rho_e(i,j,N)=\frac{\left|\sum_{n=1}^{N} S_{i,n}^* S_{n,j}^* - \sum_{n=1}^{N} L_{ij}^n\right|^2}{\prod_{k=i,j}\left[1-\sum_{n=1}^{N} S_{k,n}^* S_{n,k} - \sum_{n=1}^{N} L_{kk}^n\right]} \tag{9.15}$$

As example, for a (3,3) MIMO system (i.e., three antennas at each end), the spatial correlation between antennas 1 and 2 may be calculated directly from the following,

$$\rho_e(1,2,3)=\frac{\left|S_{11}^*S_{12}+S_{12}^*S_{22}+S_{13}^*S_{32}-\left(L_{12}^1+L_{12}^2+L_{12}^3\right)\right|}{\left[1-\left(\left|S_{11}\right|^2+\left|S_{21}\right|^2+\left|S_{31}\right|^2\right)-\left(L_{11}^1+L_{11}^2+L_{11}^3\right)\right]\left[1-\left(\left|S_{22}\right|^2+\left|S_{12}\right|^2+\left|S_{32}\right|^2\right)-\left(L_{22}^1+L_{22}^2+L_{22}^3\right)\right]} \tag{9.16}$$

9.4 Simulation and Results

To verify equation 9.16, the spatial envelope correlation has been computed between two half wavelength dipole antennas, in free space for a three antenna system, as a function of their separation distance. The far field and scattering parameters have been computed using the NEC code.

For this example, the dipole radius for each structure was set to 0.002 wavelengths. Three different sources of loss were considered for validation purposes, and two distinct MIMO

configurations were investigated, namely a uniform linear array, and a circular (ring) array. In each case the three dipoles were loaded by two lumped 25 Ω resistive loads, separated by 0.095 wavelengths from the input source, as shown in Figure 8.2. The excitation was simply modelled by a voltage source at the centre of each dipole, and the applied termination load is 50 Ω.

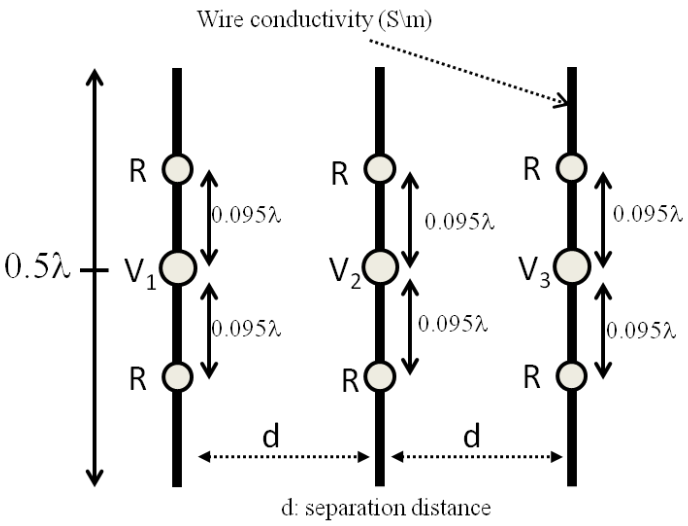

(a)

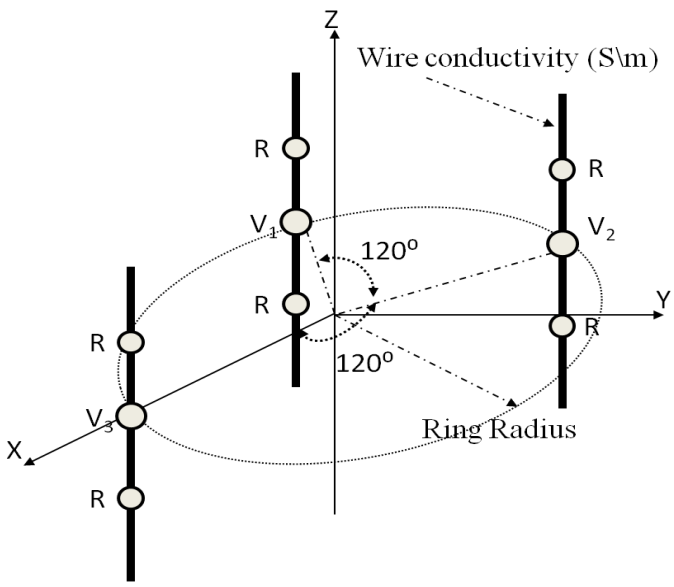

(b)

Figure 9. 2: Examples under test: (a) uniform linear array, (b) Ring array.

Departures between the results of this method and the lossless approach were checked through simulation. The spatial envelope correlations between the antenna elements 1 and 2 in the three element uniform linear array were calculated using the far field as a function of the dipole separation distances. The results are presented in Figure 8.3 for the lossy and lossless cases. Close agreement may be observed between the lossy analysis derived from equation (9.16), and the far field analysis in equation (9.1).

The envelope correlation for dipole separation distances less than 0.5 wavelengths and between each of the intervals from 0.8 to 0.9 wavelengths, 1.35 to 1.45 wavelengths and 1.85 to 1.95 wavelengths can take values bigger than the achieved S_{21} values. It is also interesting to note, that the nulls of the spatial envelope correlation are shifted as compared with those computed via the lossless approach.

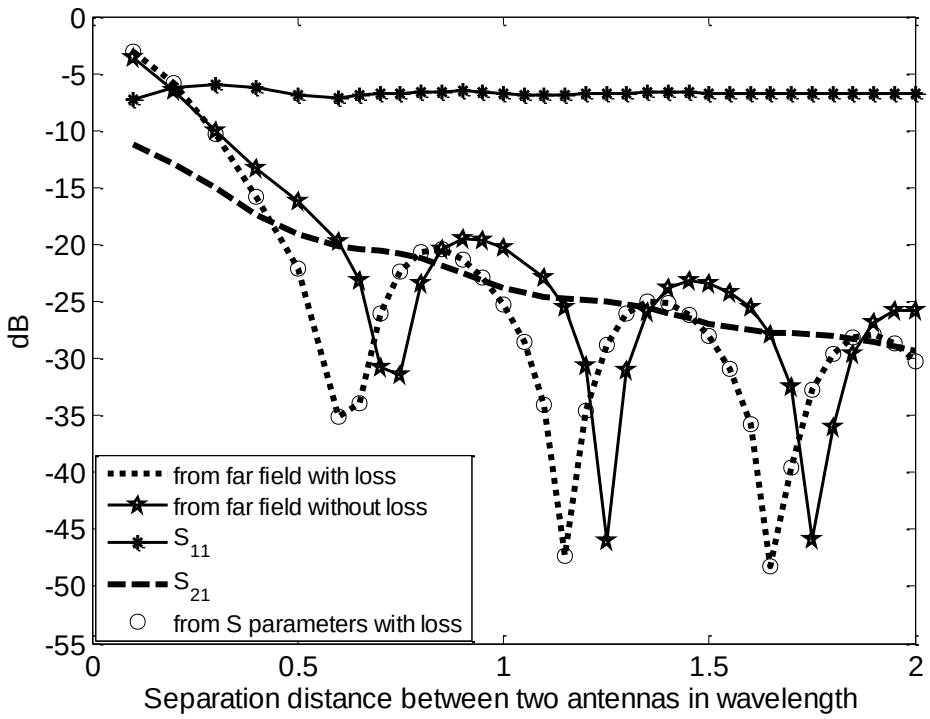

Figure 9. 3: The computed spatial envelope correlations and scattering parameters between dipoles 1 and 2 vs. their separation distance, in a MIMO system of three elements, arranged in a uniform linear array.

In Figure 9.4 the spatial envelope correlation between dipole elements 1 and 3 in the same uniform linear array are recorded, also as a function of their separation distance, for both lossy and lossless cases. It can be seen that the correlation values for the lossless case are smaller than for the lossy case, this is due to the middle element acting as a perfect reflector in the lossless case, thus contributing to a higher reflected power as compared to radiation power. The separation distance between the two radiators will affect the transmittance, $|S_{21}|$ which is associated with their mutual coupling.

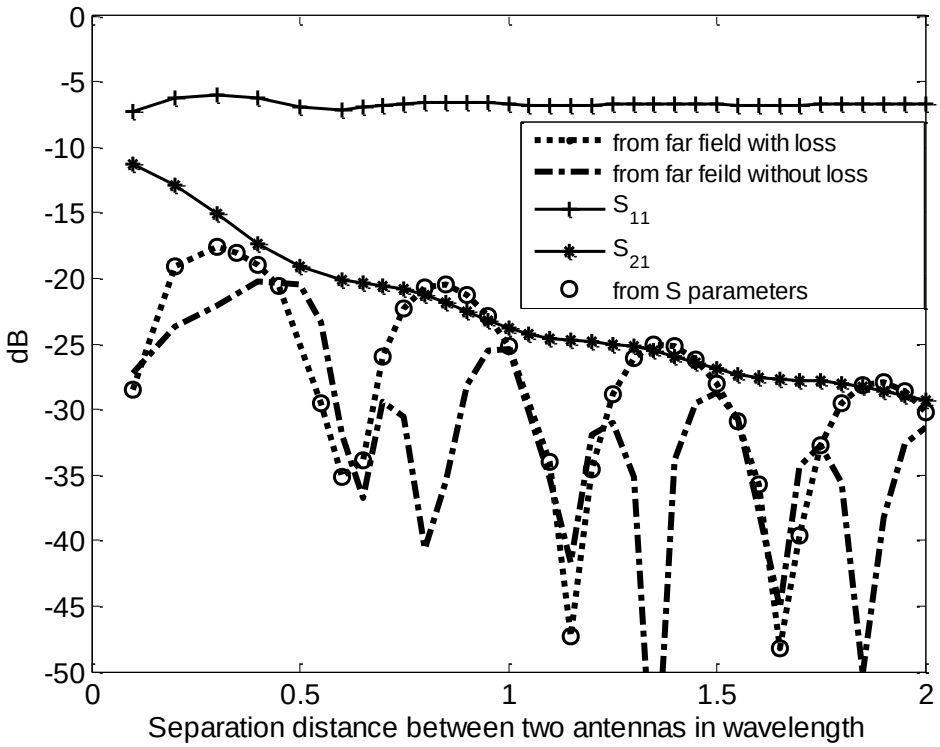

Figure 9. 4: The computed spatial envelope correlations and scattering parameters between dipoles 1 and 3 vs. their separation distance, in a MIMO system of three elements, arranged in a uniform linear array.

In Figure 9.5 the spatial envelope correlation between dipole elements 1 and 2 in a three antenna element ring array are recorded as a function of the ring radius in wavelengths, for both the lossy and lossless cases. These results show close agreement between the lossy analysis and the far field analysis from equation (9.1). For dipole separation less than 0.15 wavelengths and in the interval between 0.4 to 0.55 wavelengths the spatial envelope correlation can take values bigger than the S_{21} values. Furthermore the nulls of the envelope correlation calculated by the current method are shifted compared with the corresponding values from the lossless calculation, indicating the significance of including the intrinsic losses in the calculations. The spatial envelope correlations

between elements 2 and 3, and 1 and 3, in the ring array will be the same as for 1 and 2 due to symmetry.

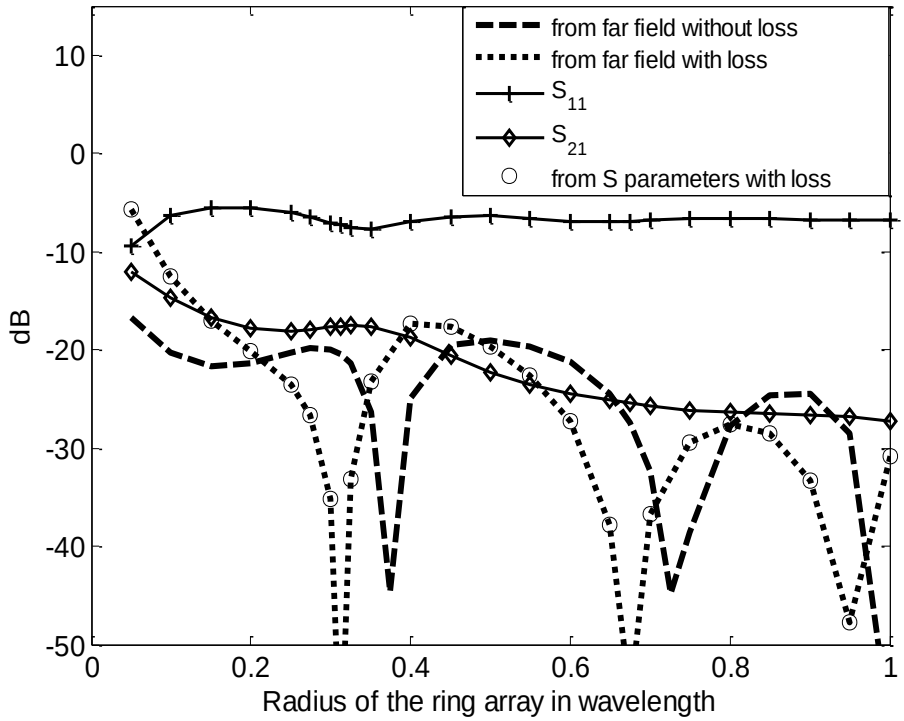

Figure 9. 5: The computed spatial envelope correlations and scattering parameters between dipoles 1 and 2 vs. their separation distance, in a MIMO system of three elements, arranged in a ring array.

Figure 9.6 depicts the variation of the spatial envelope correlation between dipole elements 1 and 2 versus the surface conductivities for a three antenna element uniform linear array and a ring array. The separation distance between the parallel dipoles in the case of the uniform linear array was kept constant at 0.5 wavelengths and in the case of the ring array the ring radius was set to 0.5 wavelengths.

It can be noted from Figure 9. 6 that the envelope correlation values become unaffected when the values of the surface conductivities get higher. Also it is noticeable from Fig. 6

that the envelope correlation values are within 1 dB and 0.5 dB of the S_{21} values for the uniform linear array and ring array respectively.

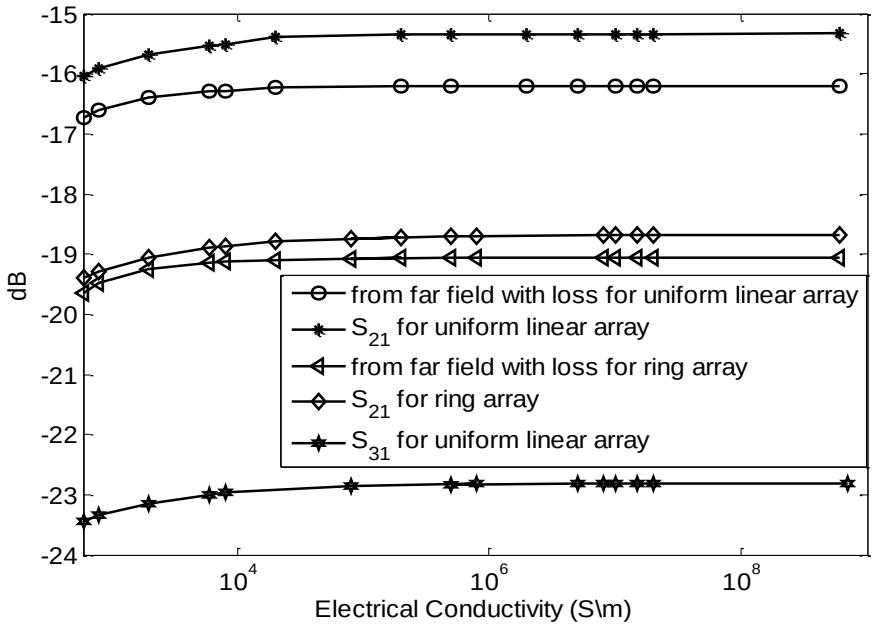

Figure 9. 6: The computed spatial envelope correlations and scattering parameters between dipoles 1 and 2 vs. their wire electric conductivity, in a MIMO system of three elements, arranged in a uniform linear array and in a ring array.

In summary, the analysis described here, based on the conceptual framework summarized in equation 9.16, provides a direct and accurate forecast of spatial envelope correlations, as compared with those obtained from the far field data in equation 9.1.

9.5 Conclusions

A direct calculation method has been presented for the spatial envelope correlation between any two antennas in a (N,N) MIMO array using the scattering parameters and intrinsic losses in the radiating structures. This formula should reduce the complexity and effort involved in spatial envelope correlation calculations for practical designs especially where low envelope correlation is required. Three examples have been presented to validate the technique. The results have shown close agreement between this method and the full computation using the far field pattern data. Several practical methods exist, e.g. radiometer [122], random field [124] and reverberation chamber [125], for direct measurement of the radiation efficiency of passive antennas. These can be used for multiport structures, and can provide independent checks of the diagonal terms in Equation (12). Such practical implementations of the proposed method will be considered further in future work

CHAPTER 10

Conclusions and Suggestions for Future Work

10.1 Conclusions

The necessary orientation in implementing a space-time coded OFDM transmitter over a multipath Rayleigh channel, and a receiver which uses a selection combining diversity technique has been reviewed and designed, the performance of this combined scenario is characterised in terms of the bit error rate and throughput. A novel four element QOSTBC scheme was introduced. It was developed by reforming the detection matrix of the original QOSTBC scheme, for which an orthogonal channel matrix was derived. The results exposed a computationally less complex linear decoding scheme as compared with the original QOSTBC. Space time coding schemes for three, four and eight transmitters were also derived using a Hadamard matrix.

The practical optimization of multi-antenna networks has been studied for realistic indoor and mixed propagation scenarios. A detailed analysis of the throughput and field strength distributions for a commercial dual band 802.11n MIMO radio operating indoors in a variety of line of sight and non-line of sight scenarios, were tested. The physical model of the geometry was based on architectural schematics, and realistic propagation data for the construction materials. The modelling concept was then extended and generalized to

a multi-storey indoor environment, and a large mixed site for indoor and outdoor channels based on the Bradford University campus.

The implications for the physical layer were also explored through the specification of antenna envelope correlation coefficients. Initially this was applied for an antenna module configuration with two independent antennas in close proximity. An operational method has been proposed using the scattering parameters of the system and which incorporates the intrinsic power losses of the radiating elements. The method was extended to estimate the envelope correlation coefficient for any two elements in a general (N,N) MIMO antenna array. Three examples are presented to validate and pioneer this technique, at which a very close agreement was shown to exist between the proposed method and the full electromagnetic analysis using the far field antenna radiation patterns.

10.2 Summary of the thesis

The conclusions of this work can be summarised by each Chapter as follows:

Chapter 2 presents the OFDM modulation technique in terms the influence of high data rate communication system and its mitigation towards the effect of ISI. OFDM was proved to be computationally efficient due to the use of IFFT and FFT technology to implement modulation and demodulation respectively. The OFDM was tested using MATLAB-SIMULINK over M-QAM digital modulation. It can be concluded that the BER for BPSK is less for low SNR compared to that achieved by QPSK and 16-QAM modulations. This is simply confirmed that the OFDM using BPSK is suitable for lower capacity and low power systems, whereas higher modulation schemes are suitable for high capacity and higher power systems.

Chapter 3 presents the diversity techniques that are used to improve the performance of the radio channel without any increase in the transmitted power. A summary of the receiver diversity techniques and their performances. Among different combining techniques MRC has the best performance and the highest complexity while SC has the least complexity. The focus was on general principles illustrated by a few simulation examples. The simple Alamouti code and its performance were discussed in detail, where it was shown that Alamouti scheme with two transmit and n_r receive antennas has the same diversity gain as an MRC receive diversity scheme with one transmit and $2n_r$ receive antennas.

Chapter 4 presents a novel QO-STBC scheme in terms of three and four transmit elements by reforming the detection matrix of the original QO-STBC scheme. An orthogonal channel matrix was derived that results in a linear decoding scheme simpler than the original OSTBC. The proposed scheme has shown a better operation performance than the conventional scheme, with performance gains of about 2 dB being achieved. In addition, a Diagonalzed Hadamard space time code for four transmit antennas was proposed, the proposed scheme outperformed the conventional one due to the orthogonality of the detection matrix.

Chapter 5 discusses the AMC as one of the interested technique for potentially maximizing the overall throughput of a wireless system; however there are some challenges associated with its implementation. For instance, the mobile channel can be considered to be time-varying, so the feedback mechanism of the system must be fast and reliable so the SNR information and thus will not be obsolete when the next transmission is due. This limits the performance of the AMC technique for a fast time-varying channel

because if the coherence time of the channel is too small, then there may be a discrepancy between the predicted and the actual channel condition when the next transmission is due. If this occurs, it may even lead to a worse network performance because the wrong modulation scheme will be used for the wrong channel condition per time. However, all simulations, results and analysis for the MIMO 2×3 antenna configuration with AMC show the best throughput performance potential of all the systems studied.

Chapter 6 presents the analysis of throughput values obtained from Line of Sight and Non-Line of Sight scenarios that provide an experimental insight into the performance of MIMO systems using the 802.11n standard in a typical multi-storey office building that reaches 250 and 296 Mbps for NLOS and LOS respectively (for 10 m distance). The achievable bit rate for a MIMO system was found much more reliable when compared to a SISO connection. Furthermore the 802.11n channel bonding option provides remarkable throughput increase, compared with 802.11a/b/g.

The Implementation of a simulated propagation model using 3D SBR in this chapter provides a good estimation of the channel propagation without demanding an extraordinary computational effort. The investigation found a high correlation for 2.4 GHz and 5.2 GHz frequencies (86% and 96% respectively) between measured and simulated data. By modelling a MIMO system in an indoor environment, it was possible to determine the signal strength distribution and its achievable throughput for different locations. Despite the accuracy of the results obtained in this investigation, the modelling process remains rather complex, which might limit its applicability in future work.

Finally, indoor furnished office environment was simulated using Wireless Insite and the results have been compared with the measurements of the received signals. The results

recorded showed a good degree of similarity with measurements. The results were quite encouraging to be adopted in supporting the practical implementation as they raised good estimation of a propagation channel and an accurate alternative for measurement, which takes a lot of time and is labour-intensive.

Chapter 7 presents a deterministic multi scenario channel propagation model for University of Bradford campus; Indoor multi-storey propagation model was first evaluated in terms of the received signal strength and path loss for both scenarios LOS and NLOS, then Indoor-Outdoor Scenario using a moving receiver was created and evaluated. Finally Outdoor -Outdoor Scenario using a moving receiver was created and evaluated.

InSite's 3D model was used to produce and confirm the accuracy of the results, but at the cost of long run times. Run time was found directly affected by the number of transmitters and receivers, and the number of faces in the building geometry. As the number of transmitters/receivers and building faces increases, run time increases.

Chapter 8 presents a method of calculation, for the spatial envelope correlation of a two-antenna system, which includes losses, using the system scattering parameters has been presented. This new expression should reduce the complexity in predicting the spatial envelope correlation, and simplify antenna designs where a low envelope correlation is required. Four validation examples were presented, which demonstrate good agreement between the proposed method, and the explicit calculation using far field pattern data. The trend of this method represents a major engineering contribution to reduce the

complicity of the conventional method that uses the radiation field patterns of the antennas.

Chapter 9 presents a direct calculation method for the spatial envelope correlation between any two antennas in a (N,N) MIMO array using the scattering parameters and intrinsic losses in the radiating structures. This formula should reduce the complexity and effort involved in spatial envelope correlation calculations for practical designs especially where low envelope correlation is required. Three examples have been presented to validate the technique. The results have shown close agreement between this method and the full computation using the far field pattern data.

10.3 Suggestions for Future Work

Throughout the course of this research it was observed that there were areas for further study that might be carried out:

- An important candidate for further development is testing the proposed space time coding over OFDM.
- The results in chapter 6 and 7 may be used in developing a new statistical propagation model for a targeted environment, including the full support of the measurements results.
- There would also be considerable research value in establishing a practical method, e.g. radiometer [121], random field [124] and reverberation chamber [125], for direct measurement of the radiation efficiency of passive antennas. These can be used for multiport structures, and can provide independent checks

of the diagonal terms in Equation (12) in chapter 8. Such practical implementations of the proposed method has already considered for patent application.

- One further possible study that might be considered using the achieved deterministic channel propagation models, by developing indoor and outdoor localization systems and making use of the huge data that can be collected and used towards such technique, e.g. Direction of arrival, Delay and Received signal strength [131, 132].

References

1. J.G. Proakis, *Digital Communications*, New York: McGraw-Hill, 1989.
2. C.E. Shannon, “A Mathematical Theory of Communication,” Bell Syst. Tech. J., Vol. 27, pp: 379-423, 623-656, July & Oct. 1948.
3. J. Winters, On the capacity of radio communication system with diversity in a Rayleigh fading environment, IEEE Journal on Selected Areas in Communications, vol. 5, no. 5, pp. 871-878, June 1987.
4. G.J. Foschini, “Layered space-time architecture for wireless communication in a fading environment when using multi-element antennas,” Bell Labs Tech J., vol. 1, no. 2, 41-59, 1996.
5. G.J. Foschini and M.J. Gans. On Limits of wireless Communications in a Fading Environment when Using Multiple Antennas. Wireless Personal Communications, 6:311-335, March 1998.
6. I.E. Telatar, Capacity of multi-antenna Gaussian channels, European Transaction on Telecommunications, vol. 10, no. 6, pp. 585-595, Nov/Dec 1999.
7. A.Paulraj, R.Nabar and D.Gore, Introduction to Space-Time Wireless Com munications, Cambridge University Press, 2003.
8. E. Telatar, Capacity of Multi-antenna Gaussian Channels, European Trans.Telecomm., vol. 10, no. 6, pp: 585-595, Nov/Dec1999.
9. E. Biglieri, *et al.*, *MIMO Wireless Communications*. Cambridge UK, 2007.
10. J. Mietzner, *et al.*, "Multiple-antenna techniques for wireless communications - a comprehensive literature survey," *Communications Surveys & Tutorials, IEEE,* vol. 11, pp. 87-105, 2009.

11. D. Gesbert, *et al.*, "From theory to practice: an overview of MIMO space-time coded wireless systems," *Selected Areas in Communications, IEEE Journal on,* vol. 21, pp. 281-302, 2003.
12. A. B. Gershman and N. D. Sidiropoulos, *Space- TIme Processing for MIMO Communications*. West Sussex, UK: John Wiley & Sons Ltd, 2005.
13. F. Fuschini, *et al.*, "Analysis of Multipath Propagation in Urban Environment Through Multidimensional Measurements and Advanced Ray Tracing Simulation," *Antennas and Propagation, IEEE Transactions on,* vol. 56, pp. 848-857, 2008.
14. A. Mendes Cavalcante, *et al.*, "A new computational parallel model applied in 3D ray-tracing techniques for radio-propagation prediction," in *Microwave Conference, 2006. APMC 2006. Asia-Pacific*, 2006, pp. 1859-1862.
15. M. Clemens and T. Weiland, "Discrete Electromagnetism with the Finite Integration Technique," *Progress In Electromagnetics Research,* vol. 32, pp. 65-87, 2001.
16. T. Rylander and A. Bondeson, "Stable FEM-FDTD hybrid method for Maxwell's equations," *Computer Physics Communications,* vol. 125, pp. 75-82, 2000.
17. Y. Huang and K. Boyle, *Antennas From Theory to Practice*. West Sussex, UK: John Wiley & Sons Ltd, 2008.
18. P. N. Zakharov, *et al.*, "Finite Integration Technique capabilities for indoor propagation prediction," in *Antennas & Propagation Conference, 2009. LAPC 2009. Loughborough*, 2009, pp. 369-372.
19. G. El Zein, *et al.*, "Characterization, modeling and simulation of the MIMO propagation channel," *Comptes Rendus Physique,* vol. 11, pp. 7-17, 2010.

20. L. C. Liechty, *et al.*, "Achieving practical MIMO network planning using the Two-Curve MIMO Performance Model," in *Antennas and Propagation Society International Symposium, 2009. APSURSI '09. IEEE*, 2009, pp. 1-4.
21. D. J. Love and R. W. Heath. Limited feedback unitary precoding for orthogonal space time block codes. IEEE Trans on signal processing, pp 64-73, January 2005.
22. H. Jafarkhani. A quasi orthogonal space-time block code. IEEE Trans. Comm., vol. 49, pp. 1-4, January 2001
23. O. Tirkkonen, A. Boariu, A. Hottinen. Minimal nonorthogonality rate one space-time block codes for 3+ Tx antennas. IEE International Symposium on Spread Spectrum Techniques and Applications (ISSSTA), vol. 2, New Jersey, USA, pp. 429-432, September 2000.
24. C. B. Papadias and G. J. Foschini. Capacity-approaching space-time codes for systems employing four transmitter antennas. *IEEE Trans. on Informution Theory*, vol. 49, pp. 726-733, March 2003.
25. S. Blanch, J. Romeu and I. Corbella, “Exact representation of antennas system diversity performance from input parameter description”, Electronics Letters, vol. 39, No. 9, 1st May 2003, pp. 705-707.
26. Thaysen, and K. B. Jakobsen, “Envelope correlation in (N, N) MIMO antenna array from scattering parameters”, Microwave and Optical Technology Letters, Vol. 48, No. 5, May 2006, pp. 832-834.
27. H. L. Zhang, Z. H. Wang, J. W. Yu, and J. Huang, “A Compact MIMO Antenna for Wireless Communication”, IEEE Antennas and Propagation Magazine, vol. 50, No. 6, Dec. 2008, pp. 104-107.

28. T. S. P. See and Z. N. Chen, “An Ultrawideband Diversity Antenna”, IEEE Trans on Antennas and Propagation, vol. 57, No. 6, June 2009, pp. 1957-1605.
29. J. G. Andrews, A. Ghosh, and R. Muhamed ‘Fundamentals of WiMAX Understanding Broadband Wireless Networking’, Prentice Hall Com. Eng. And Tech. Series, 2007.
30. Hanzo, L. and M. Munster, OFDM and MC-CDMA for broadband multi-user communications, WLANs and broadcasting. 2003, Chichester: Wiley. xxxiii, 978 pages.
31. Nee, R.V. and R. Prasad, OFDM for Wireless multimedia communications. 2000: Artech House Publisher. 260 pages.
32. Matic, D.M., Introduction to OFDM, II Edition. 1998, Interactive Multi-Media CD ROM, ISSN 1383-4231.
33. Proakis, J.G., Digital communications. 4th ed. McGraw-Hill series in electrical and computer engineering. 2001, London: McGraw-Hill. 1002 pages.
34. Sklar, B., Digital communications: fundamentals and applications. 1988, Englewood Cliffs, N.J.: Prentice-Hall. 776.
35. Gudmundson, M. and P.-O. Anderson. Adjacent channel interference in an OFDM system. in Vehicular Technology Conference, 1996. 'Mobile Technology for the Human Race'., IEEE 46th. 1996.
36. Yuping Zhao; Haggman, S.-G., ‘Intercarrier interference self-cancellation scheme for OFDM mobile communication systems’, IEEE Transactions on Communications, 2001. Vol 49, No.7, p. 1185 - 1191.
37. Wu, H.-C., ‘Analysis and characterization of intercarrier and interblock interferences for wireless mobile OFDM systems. Broadcasting’, IEEE Transactions on, 2006. Vol.52, No.2, p. 203-210.

38. Russell, M.S., G.L. ‘ Interchannel interference analysis of OFDM in a mobile environment’, In IEEE 45th Vehicular Technology Conference. 1995.
39. Akansu, A.N., et al., ‘Orthogonal transmultiplexers in communication: a review’, Signal Processing, IEEE Transactions on Signal Processing, vol.46, No. 4, April 1998. p. 979-995.
40. Shigeo NAKAJIMA, ‘Effects of Spectral Shaping on OFDM Transmission Performance in Nonlinear Channels’, IEEE conf. In mobile and wireless communications summit,2007, 16th IST.
41. Chang, K., K. Kim, and D.-H. Kim, ‘Reduction of Doppler effects in OFDM systems’, Consumer Electronics, IEEE Transactions on, 2006. Vol.52, No.4, p. 1159-1166.
42. Parsons, J.D., ‘The Mobile Radio Propagation Channel’, Second Edition ed, 2000, Wiley.
43. Colieri, S.E., M.; Puri, A.; Bahai A, ‘A study of channel estimation in OFDM systems’, IEEE 56th Vehicular Technology Conference, 2002. 2: p. 894 - 898.
44. Hutter, A.A.H., R.; Hammerschmidt, J.S. ‘Channel estimation for mobile OFDM systems’, in IEEE VTS 50th Vehicular Technology Conference. 1999.
45. A.V Oppenheim and R. W.Schafer, ‘Discrete Time Signal Processing’, Prentice Hall,1989.
46. A. Goldsmith, Wireless Communications, Cambridge University Press, 2005.
47. M. K. Simon and M.S. Alouini, Digital Communication over Fading channels: A Unified Approach to Performance Analysis, John Wiley&Sons, 200.
48. G. L. Rappaport, Principle of Mobile Communications, Norwell, K
49. J. H. Winter. “Switched diversity with feedback for DPSK mobile radio systems”, IEEE Trans. On Vehicular Tech., February, 1983.

50. D. J. Love and R. W. Heath. Limited feedback unitary precoding for orthogonal space time block codes. IEEE Trans on signal processing, pp 64-73, January 2005.
51. D. J. Love and R. W. Heath. Limited feedback unitary precoding for spatial multiplexing systems. IEEE Trans on Information Theory, pp 1967-1976, August 2005.
52. S. Alamouti. A Simple Transmitter Diversity Technique for Wireless Communications. IEEE Journal on Selected Areas of Communications, Special Issue on Signal Processing for Wireless Communications, vol.16, no.8, pp.1451-1458, Oct. 1998.
53. V. Tarokh, H. Jafarkhani and A. R. Calderbank. Space-time block codes from orthogonal designs. IEEE Trans. Inform. Theory, vol. 45, pp. 1456-1467, July 1999.
54. G. Ganesan, P. Stoica. Space-time diversity using orthogonal and amicable orthogonal design. Wireless Personal Communications, vol. 18, pp. 165-178, 2001.
55. V. Tarokh, N. Seshadri, A. R. Calderbank. Space-Time Codes for High Data Rate Wireless Communication: Performance Criterion and Code Construction. IEEE Trans. Inform. Theory, vol. 44, no. 2, pp. 744-765, March 1998.
56. G. G. Raleigh and J. M. Cioffi. Spatio-temporal coding for wireless communications, IEEE Trans Commun., Vol. 46, pp: 357-366, Mar. 1998.
57. H. Bölcskei, D. Gesbert, and A.J. Paulraj. On the capacity of OFDM-based spatial multiplexing systems, IEEE Trans. Commun., Vol. 50, pp: 225-234, Feb. 2002.
58. R. J. Piechocki, P.N. Fletcher, A.R. Nix, C.N. Canagarajah and J.P. McGeehan. Performance evaluation of BLAST-OFDM enhanced hiperland/2 using

simulated and measured channel data, IEE Electronic Letter, Vol. 37, No. 18, pp:1947- 1951, Aug 2001.

59. J. W. Wallace and M.A. Jensen. MIMO capacity variation with SNR and multipath richness from full-wave indoor FDTD simulations, IEEE Antenna and Propagation Society International Symposium, Vol. 2, pp: 523-526, June 2003.
60. A. F. Molish and M. Z. Wi. MIMO system with antenna selection- An overview, copyright Mitsubishi Electric Research Laboratories, Inc., 2004, 201 Broadway, Cambridge, Massachussetts 02139, TR-2004-014, March 2004.
61. U. Park, S. Kim, K. Lim and Jing Li, "A novel QO-STBC Scheme with Linear Decoding for Three and Four Transmit Antennas", IEEE communication letters Vol. 12, no. 12, December, 2008.
62. G.H. Golub and C.F. Van Loan, "Matrix Computations" (3rd ed.), Johns Hopkins University Press, 1996.
63. K. J. Horadam, "Hadamard Matrices and Their Applications", Princeton University Press, 2007.
64. H. J. Ryser, "Combinatorial Mathematics", John Wiley and Sons, 1963.
65. B. Vucetic and J. Yuan, "*Space-Time Coding"*. John Wiley and Sons, 2003
66. J. L. Byoung et al., "System-Level Performance of MIMO-based Mobile WiMAX System", in Mobile WiMAX Symposium, MWS IEEE, July 2009, pp. 189 – 194.
67. V.H Muntean and M. Otesteanu,"WiMAX versus LTE - An overview of technical aspects for Next Generation Networks technologies" in Electronics and Telecommunications (ISETC), 2010 9th International Symposium. 2010.

68. G. S. Khalid, “High Bit Rate Air Interface for Next Generation Mobile Communication Systems”, Ph.D. theses University of Bradford, 2007.

69. Y. L. Geoffrey and S. Gordon, Orthogonal Frequency Division Multiplexing for Wireless Communications, Springer Science Business Media, Inc, 2006.

70. Md. Ashraful Islam and Md. Zahid Hasan, Performance Evaluation of Wimax Physical Layer under Adaptive Modulation Techniques and Communication Channels, International Journal of Computer Science and Information Security, Vol. 5, No.1, 2009.

71. Sunil Joshi and Deepak Gupta, Throughput Quantification of MIMO based Correlated Rician fading Channel for a LTE downlink system, Special Issue of International Journal of Computer Applications (0975 – 8887) on Electronics, Information and Communication Engineering - ICEICE No.6, Dec 2011

72. Christian Mehlfuhrer, Sebastian Caban, and Markus Rupp, Experimental Evaluation of Adaptive Modulation and Coding in MIMO WiMAX with Limited Feedback, EURASIP Journal on Advances in Signal Processing, Volume 2008, Article ID 837102, 12 pages

73. Prabhakar Telagarapu, G.B.S.R.Naidu and K.Chiranjeevi, Analysis of Coding Techniques in WiMAX, International Journal of Computer Applications (0975 – 8887) Volume 22– No.3, May 2011

74. A. Maltsev et al., “Analysis of IEEE 802.16m and 3GPP LTE Release 10 technologies by Russian Evaluation Group for IMT-Advanced”, Ultra-Modern Telecommunications and Control Systems and Workshops (ICUMT), 2010 International Congress. 2010.

75. L. Garber, “Mobile WiMAX: The Next Wireless Battle Ground”, Computer, Vol.41, pp.16 – 18, June 2008.

76. Z. Hadj and F. Mohamed, “High Throughput of WiMAX MIMO-OFDM Including Adaptive Modulation and Coding”, (IJCSIS) International Journal of Computer Science and Information Security, Vol. 7, No. 1, 2010.

77. http://www.ieee802.org/16/tgd/

78. Y. O. Park and J. Park, “Design of FFT processor for IEEE802.16m MIMO-OFDM systems”, in Information and Communication Technology Convergence (ICTC), 2010 International Conference, Nov. 2010, pp. 191 – 194

79. M. Filippi, “SDR Implementation of an OFDM-MIMO Receiver” Aalborg University. 2008.

80. R. Amalia, “Implementation of a WiMAX simulator in Simulink”, Institute of Telecommunications, Vienna. 2007.

81. S. C. Yong et al, MIMO-OFDM Wireless Communications with MATLAB, John Wiley & Sons, 2010.

82. A. A. Goldsmith, Wireless Communication, Cambridge University Press, 2005.

83. V. Tarokh et al., “Space-Time Coding And Signal Processing For High Data Rate Wireless Communications”, AT&T Labs – Research. 2009.

84. P. N. Zakharov, *et al.*, "Finite Integration Technique capabilities for indoor propagation prediction," in *Antennas & Propagation Conference, 2009. LAPC 2009. Loughborough*, 2009, pp. 369-372.

85. P. Pajusco, "Propagation channel models for mobile communication," *Comptes Rendus Physique*, vol. 7, pp. 703-714, 2006.

86. M. Thiel and K. Sarabandi, "A Hybrid Method for Indoor Wave Propagation Modeling," *Antennas and Propagation, IEEE Transactions on*, vol. 56, pp. 2703-2709, 2008.

87. P. N. Zakharov, *et al.*, "Comparative Analysis of Ray tracing, finite integration technique and empirical models using ultra-detailed indoor environment model and measurements," in *Microwave, Antenna, Propagation and EMC Technologies for Wireless Communications, 2009 3rd IEEE International Symposium on*, 2009, pp. 169-176.

88. L. Nagy, "Short Range Device (SRD) propagation modeling for Indoor environment," in *Mobile and Wireless Communications Summit, 2007. 16th IST*, 2007, pp. 1-5.

89. J. D. Parsons, *The Mobile Radio Propagation Channel* vol. 2nd West Sussex, UK: John Wiley & Sons, Ltd., 2000.

90. Wave Propagation Standards Committee of the Antennas and Propagation Society, IEEE Standard DeÞnitions of Terms for Radio Wave Propagation, IEEE Std 211, 1997.

91. T. Rautiainen, *et al.*, "Measurements and 3D Ray Tracing Propagation Predictions of Channel Characteristics in Indoor Environments," in *Personal, Indoor and Mobile Radio Communications, 2007. PIMRC 2007. IEEE 18th International Symposium on*, 2007, pp. 1-5.

92. C. Saeidi, *et al.*, "Fast Ray Tracing Propagation Prediction Model For Indoor Environments," in *Antennas, Propagation & EM Theory, 2006. ISAPE '06. 7th International Symposium on*, 2006, pp. 1-4.

93. J. Nam-Ryul, *et al.*, "Performance of Channel Prediction Using 3D Ray-tracing Scheme Compared to Conventional 2D Scheme," in *Communications, 2006. APCC '06. Asia-Pacific Conference on*, 2006, pp. 1-6.

94. A. Toscano, *et al.*, "Fast ray-tracing technique for electromagnetic field prediction in mobile communications," *Magnetics, IEEE Transactions on*, vol. 39, pp. 1238-1241, 2003.

95. S. A. Hamzah, *et al.*, "Indoor channel prediction and measurement for wireless local area network (WLAN) system," in *Communication Technology, 2006. ICCT '06. International Conference on*, 2006, pp. 1-5.

96. R. A. Kipp and M. C. Miller, "Shooting-and-bouncing ray method for 3D indoor wireless propagation in WLAN applications," in *Antennas and Propagation Society International Symposium, 2004. IEEE*, 2004, pp. 1639-1642 Vol.2.

97. M. Lott and B. Walke, "The indoor radio channel at 5.2 GHz: prediction by means of ray tracing and measurements," in *Vehicular Technology Conference, 1999. VTC 1999 - Fall. IEEE VTS 50th*, 1999, pp. 2293-2297 vol.4.

98. W. Shihua, *et al.*, "Ray-tracing based channel model for 5GHz WLAN," in *Antennas and Propagation Society International Symposium, 2009. APSURSI '09. IEEE*, 2009, pp. 1-4.

99. Dlink, "Product External Specifications For 802.11n Wireless Poe Access Point (2.4GHz/5GHz) Atheros AR9132+AR9106 DAP-2553," Dlink Corporation 2010.

100. K. Aamodt, "Application Note AN042," Chipcon Products from Texas Instruments

101. MetaGeek. http://www.metageek.net/products/inssider.

102. Wavemon, "http://www.pointblanksecurity.com/wardriving-tools.php."

103. IEEE. (2010, August). *802.11n,* *http://standards.ieee.org/getieee802/download/802.11n-2009.pdf*.

104. Remcom, *The Wireless Insite Users Manual Release 2.5.11*. Pennsylvania, USA: Remcom Inc. , 2009.

105. Simon R. Saunders, "Antennas and Propagation for Wireless Communication Systems", second edition, Wiley, 2007.

106. Recommendation ITU-R P. 1238

107. J. D. Gupta, H. Suzuki and K. Z. Castro, "Effect of Pedestrian Movement on MIMO-OFDM Channel Capacity in an Indoor Environment", *IEEE Antennas and Wireless Propagation Letters, 2009, Vol. 8, pp.682 – 685.*

108. Motorola, "Long Term Evolution (LTE): A Technical Overview", Technical white paper. 2007.

109. G. J. Foschini and M. J. Gans, On Limits of Wireless Communications in a Fading Environment when UsingMultiple Antennas, *Wirel. Pers. Commun.*, vol. 6, *pp. 311-335, 1998.*

110. A. Derneryd and G. Kristensson, "Antenna signal correlation and its relation to the impedance matrix," *Electronics Letters,* vol. 40, pp. 401-402, 2004.

111. P. S. H. Leather and D. Parsons, "Antenna diversity for UHF handportable radio," *Electronics Letters,* vol. 39, pp. 946-948, 2003.

112. A. Derneryd and G. Kristensson, "Antenna signal correlation and its relation to the impedance matrix," *Electronics Letters,* vol. 40, pp. 401-402, 2004.

113. G. Lebru, S. Spiteri, and M. Falkner. MIMO complexity reduction through antenna selection, *Proc Australian Telecomm Cooperative Res. Center, ANNAC 03,2002, P.5.*

114. R. H. Clarke, "A statistical theory of mobile reception," vol. 47, pp. 957-1000., 1968.

115. H. L. Zhang, Z. H. Wang, J. W. Yu, and J. Huang, A Compact MIMO Antenna for Wireless Communication, *IEEE Antennas and Propagation Magazine,* vol. 50*, No. 6, Dec. 2008, pp. 104-107*

116. P. Hallbjorner, "The significance of radiation efficiencies when using S-parameters to calculate the received signal correlation from two antennas," *Antennas and Wireless Propagation Letters, IEEE,* vol. 4, pp. 97-99, 2005.

117. S. Stein, On cross coupling in multiple-beam antennas, *Antennas and Propagation, IRE Transactions on*, vol. 10*, pp. 548-557, 1962.*

118. R.G. Vaughan and J.B. Andersen, Antenna diversity in mobile communications, IEEE Trans Veh. Technology, 36, 1987, pp. 149-172.

119. Y. A. S. Dama, R. A. Abd-Alhameed, S. M. R. Jones, et al., An Envelope Correlation Formula for (N,N) MIMO Antenna Arrays Using Input Scattering Parameters, and Including Power Losses, *International Journal of Antennas and Propagation,* vol. 2011, *Article ID 421691, 7 pages, 2011. doi:10.1155/2011/421691*

120. G.L. Burke and A.J. Poggio, Numerical Electromagnetics Code (NEC)-Method of Moments, *Lawrence Livermore Laboratory, Livermore, CA, 1981.*

121. G.L. Burke and A.J. Poggio, Numerical Electromagnetics Code (NEC)-Method of Moments, *Lawrence Livermore Laboratory, Livermore, CA, 1981.*

122. N. J. McEwan, R. A. Abd-Alhameed, and M. N. Z. Abidin, "A modified radiometric method for measuring antenna radiation efficiency," *Antennas and Propagation, IEEE Transactions on,* vol. 51, pp. 2099-2105, 2003.

123. W.L. Schroeder and D. Gapski, Direct measurement of small antenna radiation efficiency by a calorimetric method, *IEEE Transactions on Antennas and Propagation*, 54, *9, 2646-2656, 2006.*

124. C. Qiang, *et al.*, "Comparison of experimental methods for measuring radiation efficiency of antennas for portable telephones," in *Antennas and Propagation Society International Symposium, 1998. IEEE*, 1998, pp. 149-152 vol.1.

125. K. Rosengren and P. S. Kildal, "Radiation efficiency, correlation, diversity gain and capacity of a six-monopole antenna array for a MIMO system: theory, simulation and measurement in reverberation chamber," *Microwaves, Antennas and Propagation, IEE Proceedings -*, vol. 152, pp. 7-16, 2005R. Janaswamy, "Effect of element mutual coupling on the capacity of fixed length linear arrays," *Antennas and Wireless Propagation Letters, IEEE,* vol. 1, pp. 157-160, 2002.

126. R. G. Vaughan and N. L. Scott, "Closely spaced monopoles for mobile ommunications," *Radio Sci.*, vol. 28, pp. 1259-1266, 1993.

127. S. S. G. Lebrun , M. Faulkner "MIMO complexity reduction through antenna selection," *Proc Australian Telecomm Cooperative Res. Centre,* vol. 5, pp. 1-5, 2003.

128. Z. Haili, *et al.*, "A compact MIMO antenna for wireless communication," *Antennas and Propagation Magazine, IEEE,* vol. 50, pp. 104-107, 2008.

129. T. S. P. See, *et al.*, "Correlation analysis of UWB MIMO antenna system configurations," in *Ultra-Wideband, 2008. ICUWB 2008. IEEE International Conference on*, 2008, pp. 105-108.

130. A. Diallo, *et al.*, "Diversity Characterization of Optimized Two-Antenna Systems for UMTS Handsets," *EURASIP Journal on Wireless Communications and Networking*, vol. 2007, 2007.

131. Chin-Heng Lim; Yahong Wan; Boon-Poh Ng; See, C.-M.S, “A Real-Time Indoor WiFi Localization System Utilizing Smart Antennas”, IEEE Transactions on Consumer Electronics, Vol. 53, No. 2, MAY 2007, pp. 618-622.

132. Gary F. Hatke, “Superresolution Source Location with Planar Arrays Superresolution Source Location with Planar Arrays”, The Lincoln Laboratory journal, Vol. 10, No. 2, 1997, pp. 127-146.

Author’s Publication Record

LIST OF PUBLICATIONS

REFEREED JOURNALS:

1. **Y.A.S. Dama,** R. A. Abd-Alhameed, S.M.R. Jones, D. Zhou, N.J. McEwan, M.B. Child and P.S. Excell, "An Envelope Correlation Formula For (N,N) MIMO Antenna Arrays Using Input Scattering Parameters, And Including Power Losses", International Journal of Antennas and Propagation, 2011, Article ID 421691, doi:10.1155/2011/421691
2. **Y. A. S Dama**, R. A. Abd-Alhameed, S. M. R Jones J.M. Noras, N.T.Ali ,"An Exact Envelope Correlation Formula for Two-Antenna Systems Using Input Scattering Parameters and Including Power Losses", International Journal on Communications Antenna and Propagation - February 2012, Vol. 2, No. 1, pp. 39-44
3. **Y.A.S Dama**, R A Abd-Alhameed, T S Ghazaany and S Zhu, "A New Approach for OSTBC and QOSTBC", International Journal of Computer Applications, 2013, Vol.67, No.6, pp.45-48.
4. R. Asif, R. A. Abd-Alhameed, O.O Anoh and **Y.A.S Dama**, "Performance Evaluation of DWT-OFDM and FFT-OFDM for Multicarrier Communications Systems using Time Domain Zero Forcing Equalization", International Jouranls of Computer Applications, 2012, Vol.4, No.4, pp.34-38.
5. Kelvin Anoh, Raed Abd-Alhameed, **Yousef Dama** and Steve Jones, "An Investigation of PMEPR of WPT-OFDM and OFDM Multicarrier Systems", Journal of Communications and Networking NWPJ-201307-07, July, 2013.
6. Kelvin Anoh, Raed Abd-Alhameed, **Yousef Dama** and Steve Jones, "Improved QO-STBC OFDM System Using Null Interference Elimination", International

Journal of Advanced Computer Science and Applications (IJACSA), Volume 4, No 8, August 2013.

REFEREED CONFERENCES:

1. **Y.A.S.Dama**, R. A. Abd-Alhameed, F. Salazar-Quiñonez, and SMR Jones, “3D SBR Simulation of Different Mobile Channel Propagation Scenarios over IEEE 802.11n”, The 29th International Review of Progress in Applied Computational Electromagnetics, ACES, Monterey, CA, March, 2013 (Accepted)
2. **Y. A. S. Dama**, R. Abd-Alhameed, F.Salazar-Quiñonez, D. Zhou, SMR. Jones, and S. Gao, "MIMO indoor propagation prediction using 3D shoot-and-bounce ray (SBR) tracing technique for 2.4 GHz and 5 GHz," in Antennas and Propagation (EUCAP), Proceedings of the 5th European Conference on, 2011, pp. 1655-1658, Italy.
3. **Y. A. S. Dama**, R. A. Abd-Alhameed, D. Zhou, S. M. R. Jones, M. B. Child, and P. S. Excell, "Calculation of the spatial envelope correlation between two antennas in terms of the system scattering parameters including conducting losses," in Antennas and Propagation Conference (LAPC), Loughborough, 2010, pp. 513-516, UK.
4. **Y.A.S Dama**, R. A. Abd-Alhameed, F.Salazar-Quiñonez, SMR Jones, K. N. Ramli and M.S.A. Al Khambashi “Experimental Throughput Analysis and MIMO Indoor Propagation Prediction for 802.11n System”, EMC, York, September, UK,2011.

5. **Y.A.S Dama**, R. A. Abd-Alhameed, F.Salazar-Quiñonez, SMR Jones and J.G. Gardiner, “Indoor Channel Measurement and Prediction for 802.11n System”, WIVEC2011, San Francisco, September, USA, 2011
6. **Y.A.S. Dama**, R. A. Abd-Alhameed, S.M.R. Jones, H.S.O. Migdadi and P.S. Excell, “A New Approach to Quasi-Orthogonal Space-Time Block Coding Applied to Quadruple MIMO Transmit Antennas “, ITA, Wales, September, UK, 2011.
7. **Y.A.S Dama**, R. A. Abd-Alhameed, SMR Jones, D Zhou and M.b.Child, “Experimental Throughput Analysis for 802.11n System and MIMO Indoor Propagation Prediction”, The XXX General Assembly and Scientific Symposium of the International Union of Radio Science (URSI), Istanbul, Turkey,2011
8. **Y.A.S. Dama**, R. A. Abd-Alhameed, S.M.R. Jones, N.J. McEwan, T. Sadeghpour, and M.B. Child “Envelope Correlation Formula For (N,N) MIMO Antenna Array Including Power Losse”, The IEEE International Conference on Electronics, Circuits, and Systems (ICECS), Lebanon, 2011
9. **Y.A.S Dama**, R.A. Abd-Alhameed, F.Salazar-Quiñonez, D. Zhou, SMR Jones, P.S. Excell, “Experimental Throughput Analysis for MIMO 802.11n Systems over LOS and NLOS Indoor Scenarios”, Mosharaka International Conference on Communications, Propagation, and Electronics (MIC-CPE2011), Jordan, 2011.
10. **Y.A.S Dama**, R.A. Abd-Alhameed, Ogbonnaya Anoh, SMR Jones, "MIMO INDOOR PROPAGATION PREDICTION USING 3D SHOOT-AND-BOUNCE RAY TRACING", Mosharaka International Conference on

Communications, Propagation, and Electronics (MIC-CPE2012), Turkey, 2012.

11. **Y.A.S Dama**, R. A. Abd-Alhameed, F Salazar-Quiñonez, O.O. Anoh and SMR Jones, "SIMULATION OF DIFFERENT CHANNEL PROPAGATION SCENARIOS", URSI Festival of Radio Science, University of Durham, April 2012, UK
12. **Y.A.S.Dama**, R. A. Abd-Alhameed, F. Salazar and SMR Jones, "3D SBR Simulation of Different Mobile Channel Propagation Scenarios over IEEE 802.11n", 29th Annual Review of Progress in Applied Computational Electromagnetics, pp. 863-868, 2013, USA.
13. D. Zhou, S. Gao, R. A. Abd-Alhameed, **Y.A.S Dama**, F. Zhu, J. Xu, "BAND-NOTCHED CHARACTERISTICS OF PLANAR ULTRA WIDEBAND ANTENNAS IN FREESPACE AND IN PROXIMITY TO METALLIC OBJEICTS", Mosharaka International Conference on Communications, Propagation, and Electronics (MIC-CPE2012), Turkey, 2012.
14. D. Zhou, F. Zhu, S. Gao, R. A. Abd-Alhameed, J. Xu, **Y.A.S Dama**, "Study and Analysis of Compact Planar Ultra Wideband Antenna with Band-Notched Characteristics"MIC-BEN2011, 1st International Conference on Biomedical Engineering, Electronics and Nanotechnology, Jordan,2011.
15. C.H. See, R. A. Abd-Alhameed, **Y.A.S Dama**, P. Excell, "Proposed Circuit Model for Calibration of Nonlinear Responses in Biological Media Exposed to RF Energy",1st International Conference on Biomedical Engineering, Electronics and Nanotechnology, Jordan,2011.

16. T. Sadeghpour, H. Karkhaneh, R. A. Abd-Alhameed, A. Ghorbani, I.T.E Elfergani, **Y.A.S Dama**, “Hammerstein predistorter for high power RF amplifiers in OFDM transmitters” General Assembly and Scientific Symposium, 2011 XXXth URSI pp: 1 – 4
17. M. Usman, R.A. Abd-Alhameed, **Y.A.S Dama**, P.S Excell, D. Zhou, B. Ibrahim, E.A. Elkhazmi, “New compact dual polarised dipole antenna for MIMO communications ” (WSA), 2010 International ITG Workshop on Smart Antennas, pp:326 – 330.
18. I.T.E Elfergani, R.A. Abd-Alhameed, C.H. See, T. Sadeghpour, **Y.A.S Dama**, S.M.R Jones, P.S. Excell, “A compact size reconfigurable PIFA antenna for use in mobile handset” General Assembly and Scientific Symposium, 2011 XXXth URSI, pp:1 – 4.
19. M.M. Abusitta, **Y.A.S. Dama**, R.A. Abd-Alhameed, C.H. See, J.M. Noras, A.D. Adebola, P.S. Excell, “Beam steering of horizontally polarized circular antenna arrays” Antennas and Propagation Conference (LAPC), 2011 Loughborough, pp:1 – 4.
20. Tahereh Sadeghpour, R. A. Abd-Alhameed, N. T. Ali, I. T. E. Elfergani, **Y.A.S. Dama**, O. O. Anoh, “Linear and nonlinear crosstalk in MIMO OFDM transceivers”, ICECS 2011, pp: 504-507
21. K.N. Ramli, R.A. Abd-Alhameed, **Y.A.S. Dama**, M.S.A. Alkhambashi, M.B. Child, P.S. Excell, “Interaction of EM fields to the human body using MoM-FDTD-SGFDTD hybrid computational method” EMC Europe, 2011, York, pp571 – 574.

22. T. Sadeghpour, R. A. Abd-Alhameed, H. Karkhaneh , I.E.T Elfergani, A. Ghorbani, P.S. Excell, **Y.A.S Dama**, “Memory Effects in RF Transmitters", ITA, Wales, September, UK, 2011.
23. O. O. Anoh, R.A. Abd-Alhameed, N.T. Ali, SMR. Jones and **Y.A.S. Dama**, “On the Performance of DWT and WPT Modulation for Multicarrier Systems”, CAMAD 2012, Barcelona, Spain.
24. Asif, R.; Abd-Alhameed, R.A.; Oanoh, O.; **Dama, Y**.; Migdadi, H.S.; Noars, J.M.; Hussaini, A.S.; Rodriguez, J, “Performance comparison between DWT-OFDM and FFT-OFDM using time domain zero forcing equalization”, International Conference on Telecommunications and Multimedia (TEMU), 2012, pp. 175 - 179

Selected Author's publications

Hindawi Publishing Corporation
International Journal of Antennas and Propagation
Volume 2011, Article ID 421691, 7 pages
doi:10.1155/2011/421691

Research Article

An Envelope Correlation Formula for (N, N) MIMO Antenna Arrays Using Input Scattering Parameters, and Including Power Losses

Y. A. S. Dama,[1] R. A. Abd-Alhameed,[1] S. M. R. Jones,[1] D. Zhou,[1] N. J. McEwan,[1] M. B. Child,[1] and P. S. Excell[2]

[1] *Shool of Engineering, Design and Technology, University of Bradford, West Yorkshire, BD7 1DP, UK*
[2] *Centre for Applied Internet Research, Glyndŵr University, Wrexham LL11 2AW, Wales, UK*

Correspondence should be addressed to Y. A. S. Dama, yasdama@bradford.ac.uk

Received 1 June 2011; Revised 3 August 2011; Accepted 5 August 2011

Academic Editor: Hon Tat Hui

The scattering parameter formulation for the envelope correlation in an (N, N) MIMO antenna array has been modified to take the intrinsic antenna power losses into account. This method of calculation provides a major simplification over the use of antenna radiation field patterns. Its accuracy is illustrated in three examples, which also show that the locations of the correlation minima are sensitive to the intrinsic losses.

1. Introduction

MIMO systems employ multiple antennas at transmitter and receiver to improve the reliability and capacity of wireless links in a rich electromagnetic scattering environment. It is well known that the capacity of an (N, N) MIMO system increases with N, the number of antennas in the transmit and receive arrays on the assumption of independent Rayleigh fading between each pair of transmit and receive antennas [1]. In practice, the independence of the received signals will depend on the angular distribution in the channel, the arrangement and radiation pattern of the antennas, and their polarization. It will be reduced by mutual coupling between antennas [2]. The avoidance of mutual coupling and the ability to distinguish between paths arriving at closely spaced angles is favored by larger antenna spacing, whilst practical constraints often demand compact arrangements, especially in mobile systems. To optimize the diversity performance of the array, antennas should be located so as to sample the channel at separations that exhibit minimum spatial correlation [3, 4], taking account of mutual coupling effects [5–7]. (Note that in some circumstances, mutual coupling can enhance MIMO capacity [8, 9].) Since the optimum separation distance will depend on the angle-of-arrival distributions, practical systems may elect to optimize the separation for an average channel, for which a common assumption is of a rich scattering environment with scatterers uniformly distributed in angle. For this reason, it is useful in developing practical systems to have a straightforward means to evaluate the spatial, complex-envelope correlation for the system of antennas [6, 10].

The theory presenting a generalized analysis of signal correlation between any two array elements to include non-identical elements and arbitrary load termination of passive antenna ports was presented in [11], the method is related to the power balance concept and based on the antenna impedance matrix. In [4, 12], theoretical and simulation studies have been conducted to explain the experimentally observed effect that the correlation between signals of closely spaced antennas is smaller than that predicted using the well-known theoretical methods. A simple expression to compute the correlation coefficients from the far field pattern including the propagation environment characteristic and the terminating impedance was introduced in [13].

There are three possible methods to compute the envelope correlation. The first method is based on the use of far field pattern data [8], and the use of actual or simulated radiation field data is time consuming if spread over several design iterations. The second method employs the scattering parameters measured at the antenna terminals [14], and

there is a third method based on Clarke's formula [15]. The calculation may also be formulated in terms of a generalised impedance matrix [11]. In practice, we require the correlation between any two antennas in an array. In [16] a useful relation was presented including the effect of the antenna efficiencies on the calculated spatial correlation. The correlation is sensitive to the intrinsic power losses in the radiating structures. The scattering formulation derived and tested in [14, 17] does not include these losses, and this provides the rationale for the method presented below.

2. Background Theory

The envelope correlation for two antennas may be calculated from (1):

$$\rho_e = \frac{\left|\iint_{4\pi} d\Omega F_1(\theta,\phi)^* \cdot F_2(\theta,\phi)\right|^2}{\iint_{4\pi} d\Omega \left|F_1(\theta,\phi)\right|^2 \iint_{4\pi} d\Omega \left|F_2(\theta,\phi)\right|^2}, \quad (1)$$

where $F_i(\theta,\phi) = F_\theta^i(\theta,\phi)\hat{a}_\theta + F_\phi^i(\theta,\phi)\hat{a}_\phi$ is the radiation field of the ith antenna and the surface integrations are over the 2-sphere [15]. On this basis, the envelope correlation between antennas i and j may be obtained from (2), as described in [16],

$$\rho_e(i,j,N) = \frac{\left|C_{i,j}(N)\right|^2}{\prod_{k=(i,j)}\left[1 - C_{k,k}(N)\right]}, \quad (2)$$

where $C_{i,j}(N)$ is expressed as

$$C_{i,j}(N) = \sum_{n=1}^{N} S_{i,n}^* S_{n,j}. \quad (3)$$

Hence, from (2) and (3), the explicit scattering parameter formula for envelope correlation is [17]:

$$\rho_e(i,j,N) = \frac{\left|\sum_{n=1}^{N} S_{i,n}^* S_{n,j}\right|^2}{\prod_{k=(i,j)}\left[1 - \sum_{n=1}^{N} S_{i,n}^* S_{n,k}\right]}. \quad (4)$$

Although (4) offers a simple approach compared with radiation pattern, it should be emphasized that this equation is limited by certain three assumptions as in [18].

In this paper, the computed two-antenna envelope correlation for an (N, N) MIMO system will be evaluated from the scattering parameters and the intrinsic power losses in the radiating structures. This calculation represents a significant simplification over using the far field patterns in (1).

3. Summary of the Method

Considering the electromagnetic geometry in Figure 1, the total power is given by

$$P_{\text{total}} = P_{\text{rad}} + P_{\text{loss}}, \quad (5)$$

where P_{rad} and P_{loss} are the total radiated power and power loss, respectively. P_{total} is also known as the accepted power and may be computed in terms of the incident wave,

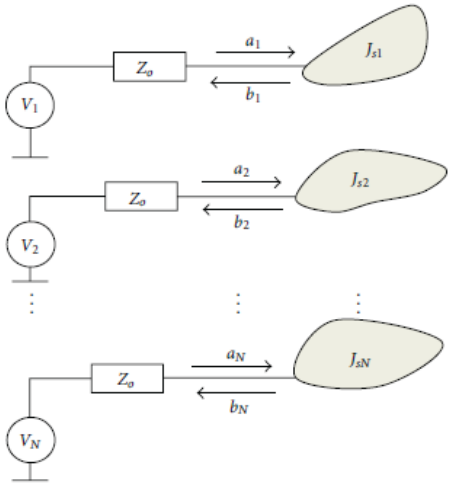

FIGURE 1: The electromagnetic geometry for the N antenna element system.

amplitude a and reflected amplitude b by $(a^\dagger a - b^\dagger b)$, where $\dagger$ denotes the Hermitian conjugate.

The analysis developed below, and the subsequent case studies shown in Figure 2, have been presented for convenience in a wire antenna formulation and the solved using NEC. It should be understood that the underlying concepts are fully general, and can be readily rewritten in terms of general surface and volume currents.

The surface current density on a wire antenna (dipole) structure can be written as

$$J_s(\theta,l) = \frac{I(\theta,l)}{2\pi r}\hat{a}_l \approx \frac{I(l)}{2\pi r}\hat{a}_l, \quad (6)$$

where r is the radius of the dipole wire.

The power loss may be computed in terms of the surface currents on the antenna structures as follows. These currents may be expressed in terms of the incident waves $a_1, a_2, \ldots a_n$

$$\begin{aligned}
J_{s1} &= \frac{1}{\sqrt{R_s}}\left(a_1 \cdot \frac{I_{11}(l)}{2\pi r}\hat{a}_l + a_2 \cdot \frac{I_{12}(l)}{2\pi r}\hat{a}_l + a_3 \cdot \frac{I_{13}(l)}{2\pi r}\hat{a}_l \right.\\
&\qquad \left. + \cdots + a_N \cdot \frac{I_{1N}(l)}{2\pi r}\hat{a}_l\right),\\
J_{s2} &= \frac{1}{\sqrt{R_s}}\left(a_1 \cdot \frac{I_{21}(l)}{2\pi r}\hat{a}_l + a_2 \cdot \frac{I_{22}(l)}{2\pi r}\hat{a}_l + a_3 \cdot \frac{I_{23}(l)}{2\pi r}\hat{a}_l \right.\\
&\qquad \left. + \cdots + a_N \cdot \frac{I_{2N}(l)}{2\pi r}\hat{a}_l\right),\\
&\vdots\\
J_{si} &= \frac{1}{\sqrt{R_s}}\left(a_1 \cdot \frac{I_{i1}(l)}{2\pi r}\hat{a}_l + a_2 \cdot \frac{I_{i2}(l)}{2\pi r}\hat{a}_l + a_3 \cdot \frac{I_{i3}(l)}{2\pi r}\hat{a}_l \right.\\
&\qquad \left. + \cdots + a_N \cdot \frac{I_{iN}(l)}{2\pi r}\hat{a}_l\right).
\end{aligned} \quad (7)$$

The I_{iN} terms are the normalised currents on structure i due to the incident wave N, and R_s is the surface impedance of

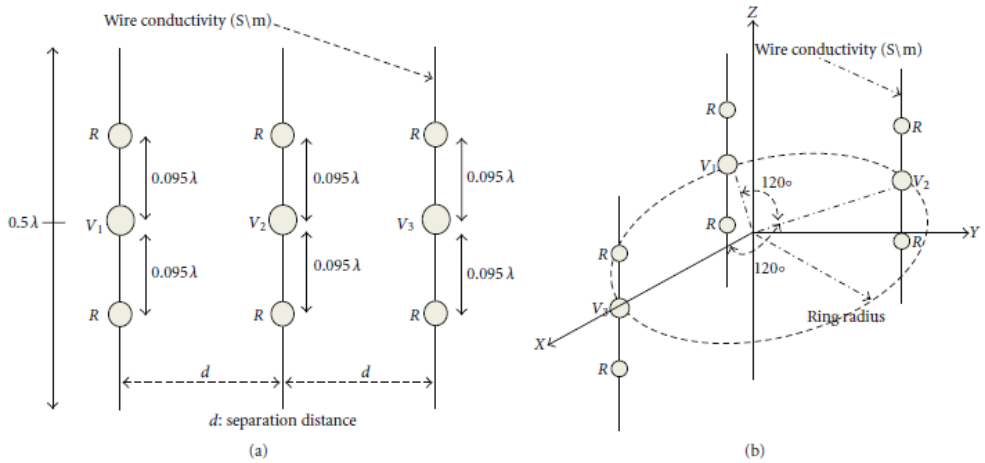

FIGURE 2: Examples under test: (a) Uniform linear array, (b) Ring array.

the antenna. The power loss on the ith antenna structure is calculated by

$$P_{\text{loss}_i} = \iint J_{si} \cdot J_{si}^* r d\theta dl,$$

$$\begin{aligned} P_{\text{loss}_i} = \iint \Bigg\{ & a_1 \cdot a_1^* \frac{I_{i1}(l) I_{i1}^*(l)}{(2\pi r)^2} + a_1 \cdot a_2^* \frac{I_{i1}(l) I_{i2}^*(l)}{(2\pi r)^2} \\ & + \cdots + a_1 \cdot a_N^* \frac{I_{i1}(l) I_{iN}^*(l)}{(2\pi r)^2} + a_2 \cdot a_1^* \frac{I_{i2}(l) I_{i1}^*(l)}{(2\pi r)^2} \\ & + a_2 \cdot a_2^* \frac{I_{i2}(l) I_{i2}^*(l)}{(2\pi r)^2} + \cdots + a_2 \cdot a_N^* \frac{I_{i2}(l) I_{iN}^*(l)}{(2\pi r)^2} \\ & + \cdots + a_N \cdot a_1^* \frac{I_{iN}(l) I_{i1}^*(l)}{(2\pi r)^2} + a_N \cdot a_2^* \frac{I_{iN}(l) I_{i2}^*(l)}{(2\pi r)^2} \\ & + \cdots + a_N \cdot a_N^* \frac{I_{iN}(l) I_{iN}^*(l)}{(2\pi r)^2} \Bigg\} r d\theta dl, \end{aligned} \tag{8}$$

solving for circumferential integral leads to

$$\begin{aligned} P_{\text{loss}_i} = \frac{1}{2\pi r} \int_l \Big\{ & a_1 \cdot a_1^* I_{i1}(l) I_{i1}^*(l) + a_1 \cdot a_2^* I_{i1}(l) I_{i2}^*(l) + \cdots \\ & + a_1 \cdot a_N^* I_{i1}(l) I_{iN}^*(l) + a_2 \cdot a_1^* I_{i2}(l) I_{i1}^*(l) dl \\ & + a_2 \cdot a_2^* I_{i2}(l) I_{i2}^*(l) dl + \cdots \\ & + a_2 \cdot a_N^* I_{i2}(l) I_{iN}^*(l) + a_N \cdot a_1^* I_{iN}(l) I_{i1}^*(l) \\ & + \cdots + a_N \cdot a_2^* I_{iN}(l) I_{i2}^*(l) + \cdots \\ & + a_N \cdot a_N^* I_{iN}(l) I_{iN}^*(l) \Big\} dl. \end{aligned} \tag{9}$$

Subject to (9), the power losses may be expressed in matrix notation as follows,

$$P_{\text{loss}} = a^\dagger L a, \tag{10}$$

where the linear operator L can be defined by the following:

$$L = L^1 + L^2 + L^3 + \cdots + L^i. \tag{11}$$

The matrix representations of the elements of L, as example L^1 and L^i can be written as below:

$$L^1 = \frac{1}{2\pi r} \begin{bmatrix} \int_l I_{11}(l) I_{11}^*(l) dl & \int_l I_{11}(l) I_{12}^*(l) dl & \cdots & \int_l I_{11}(l) I_{1N}^*(l) dl \\ \int_l I_{12}(l) I_{11}^*(l) dl & \int_l I_{12}(l) I_{12}^*(l) dl & \cdots & \int_l I_{12}(l) I_{1N}^*(l) dl \\ \vdots & \vdots & \cdots & \cdots \\ \int_l I_{1N}(l) I_{11}^*(l) dl & \int_l I_{1N}(l) I_{12}^*(l) dl & \cdots & \int_l I_{1N}(l) I_{1N}^*(l) dl \end{bmatrix},$$

$$\vdots$$

$$\vdots$$

$$L^i = \frac{1}{2\pi r} \begin{bmatrix} \int_l I_{i1}(l) I_{i1}^*(l) dl & \int_l I_{i1}(l) I_{i2}^*(l) dl & \cdots & \int_l I_{i1}(l) I_{iN}^*(l) dl \\ \int_l I_{i2}(l) I_{i1}^*(l) dl & \int_l I_{i2}(l) I_{i2}^*(l) dl & \cdots & \int_l I_{i2}(l) I_{iN}^*(l) dl \\ \vdots & \vdots & \cdots & \cdots \\ \int_l I_{iN}(l) I_{i1}^*(l) dl & \int_l I_{iN}(l) I_{i2}^*(l) dl & \cdots & \int_l I_{iN}(l) I_{iN}^*(l) dl \end{bmatrix}. \tag{12}$$

Hence the energy balance for the system expressed through (5) may be re-expressed fully in terms of the incident wave amplitudes, and the scattering matrix $S \in \mathbb{C}^{N\times N}$,

$$a^{\dagger}\left(1 - S^{\dagger}S\right)a = a^{\dagger}La + a^{\dagger}Ra. \tag{13}$$

This is essentially a modification of Stein's formulation for a multi-beam array [19], where R is a general $N \times N$ matrix. The explicit form of R is as follows,

$$R = \begin{pmatrix} \frac{D_1}{4\pi}\iint_{4\pi} d\Omega\,|F_1(\theta,\phi)|^2 & \frac{\sqrt{D_1D_2}}{4\pi}\iint_{4\pi} d\Omega F_1(\theta,\phi)\cdot F_2^*(\theta,\phi) & \cdots & \frac{\sqrt{D_1D_N}}{4\pi}\iint_{4\pi} d\Omega F_1(\theta,\phi)\cdot F_N^*(\theta,\phi) \\ \frac{\sqrt{D_2D_1}}{4\pi}\iint_{4\pi} d\Omega F_2(\theta,\phi)\cdot F_1^*(\theta,\phi) & \frac{D_2}{4\pi}\iint_{4\pi} d\Omega\,|F_2(\theta,\phi)|^2 & \cdots & \frac{\sqrt{D_2D_N}}{4\pi}\iint_{4\pi} d\Omega F_2(\theta,\phi)\cdot F_N^*(\theta,\phi) \\ \vdots & \vdots & \cdots & \cdots \\ \frac{\sqrt{D_ND_1}}{4\pi}\iint_{4\pi} d\Omega F_N(\theta,\phi)\cdot F_1^*(\theta,\phi) & \frac{\sqrt{D_ND_2}}{4\pi}\iint_{4\pi} d\Omega F_N(\theta,\phi)\cdot F_2^*(\theta,\phi) & \cdots & \frac{D_N}{4\pi}\iint_{4\pi} d\Omega\,|F_N(\theta,\phi)|^2 \end{pmatrix}, \tag{14}$$

where D_i is the maximum directivity of the ith antenna.

Now, considering the above equations, the envelope correlation between the antennas i and j in the (N,N) MIMO system can be expressed in terms of the scattering parameters and the intrinsic power losses as follows:

$$\rho_e(i,j,N) = \frac{\left|\sum_{n=1}^{N} S_{i,n}^{*}S_{n,j}^{*} - \sum_{n=1}^{N} L_{ij}^{n}\right|^2}{\prod_{k=i,j}\left[1 - \sum_{n=1}^{N} S_{k,n}^{*}S_{n,k} - \sum_{n=1}^{N} L_{kk}^{n}\right]}. \tag{15}$$

As an example, for a (3,3) MIMO system (i.e., three-antennas at each end), the spatial correlation between antennas 1 and 2 may be calculated directly from the following,

$$\rho_e(1,2,3) = \frac{\left|S_{11}^{*}S_{12} + S_{12}^{*}S_{22} + S_{13}^{*}S_{32} - \left(L_{12}^{1} + L_{12}^{2} + L_{12}^{3}\right)\right|}{\left[1 - \left(|S_{11}|^2 + |S_{21}|^2 + |S_{31}|^2\right) - \left(L_{11}^{1} + L_{11}^{2} + L_{11}^{3}\right)\right]\left[1 - \left(|S_{22}|^2 + |S_{12}|^2 + |S_{32}|^2\right) - \left(L_{22}^{1} + L_{22}^{2} + L_{22}^{3}\right)\right]}. \tag{16}$$

4. Simulation and Results

To verify (16), the spatial envelope correlation has been computed between two half wavelength dipole antennas, in free space for a three-antenna system, as a function of their separation distance. The far field and scattering parameters have been computed using the NEC code.

For this example, the dipole radius for each structure was set to 0.002 wavelengths. Three different sources of loss were considered for validation purposes, and two distinct MIMO configurations were investigated, namely, a uniform linear array, and a circular (ring) array. In each case, the three dipoles were loaded by two lumped 25 Ω resistive loads, separated by 0.095 wavelengths from the input source, as shown in Figure 2. The excitation was simply modeled by a voltage source at the centre of each dipole, and the applied termination load is 50 Ω.

Departures between the results of this method and the lossless approach were checked through simulation. The spatial envelope correlations between the antenna elements 1 and 2 in the three element uniform linear array were calculated using the far field as a function of the dipole separation distances. The results are presented in Figure 3 for the lossy and lossless cases. Close agreement may be observed between the lossy analysis derived from (16), and the far field analysis in (1). The envelope correlation for dipole separation distances less than 0.5 wavelengths and between each of the intervals from 0.8 to 0.9 wavelengths, 1.35 to 1.45 wavelengths and 1.85 to 1.95 wavelengths can take values bigger than the achieved S_{21} values. It is also interesting to note that the nulls of the spatial envelope correlation are shifted as compared with those computed via the lossless approach.

In Figure 4, the spatial envelope correlation between dipole elements 1 and 3 in the same uniform linear array are recorded, also as a function of their separation distance, for both lossy and lossless cases. It can be seen that the correlation values for the lossless case are smaller than for the lossy case, this is due to the middle element acting as a perfect reflector in the lossless case, thus contributing to a higher reflected power as compared to radiation power. The separation distance between the two radiators will affect the transmittance, $|S_{21}|$ which is associated with their mutual coupling.

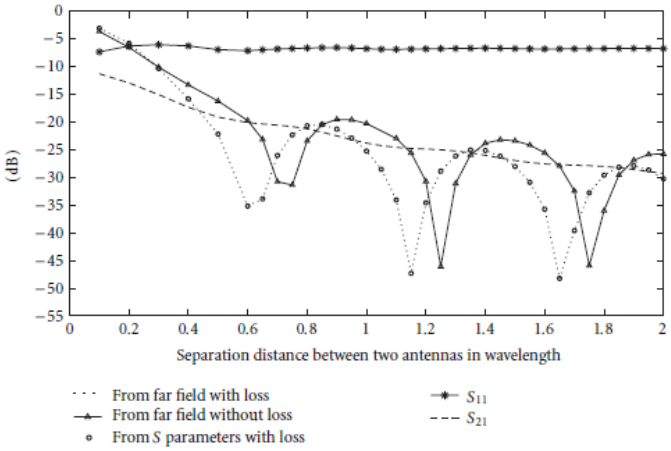

FIGURE 3: The computed spatial envelope correlations and scattering parameters between dipoles 1 and 2 versus their separation distance, in a MIMO system of three elements, arranged in a uniform linear array.

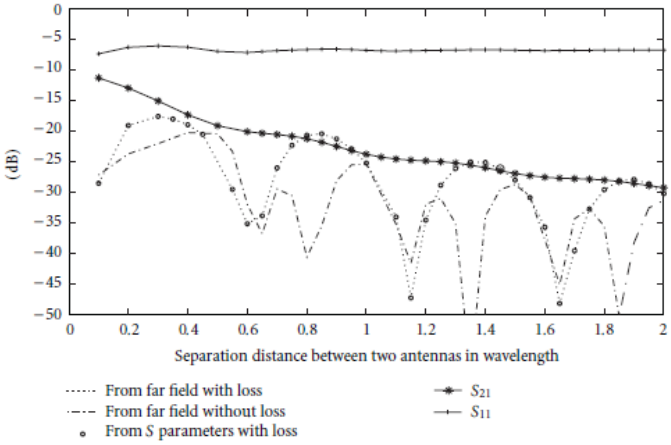

FIGURE 4: The computed spatial envelope correlations and scattering parameters between dipoles 1 and 3 versus their separation distance, in a MIMO system of three elements, arranged in a uniform linear array.

In Figure 5, the spatial envelope correlation between dipole elements 1 and 2 in a three-antenna element ring array are recorded as a function of the ring radius in wavelengths, for both the lossy and lossless cases. These results show close agreement between the lossy analysis and the far field analysis from (1). For dipole separation less than 0.15 wavelengths and in the interval between 0.4 to 0.55 wavelengths the spatial envelope correlation can take values bigger than the S_{21} values. Furthermore, the nulls of the envelope correlation calculated by the current method are shifted compared with the corresponding values from the lossless calculation, indicating the significance of including the intrinsic losses in the calculations. The spatial envelope correlations between elements 2 and 3, and 1 and 3, in the ring array will be the same as for 1 and 2 due to symmetry.

Figure 6 depicts the variation of the spatial envelope correlation between dipole elements 1 and 2 versus the surface conductivities for a three-antenna element uniform linear array and a ring array. The separation distance between the parallel dipoles in the case of the uniform linear array was kept constant at 0.5 wavelengths, and in the case of the ring array the ring radius was set to 0.5 wavelengths. It can be noted, from Figure 6 that the envelope correlation values become unaffected when the values of the surface conductivities get higher. Also, it is noticeable from Figure 6 that the envelope correlation values are within 1 dB and

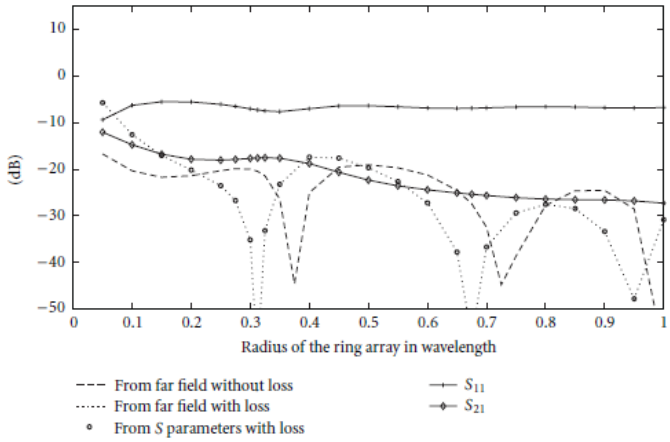

FIGURE 5: The computed spatial envelope correlations and scattering parameters between dipoles 1 and 2 versus their separation distance, in a MIMO system of three elements, arranged in a ring array.

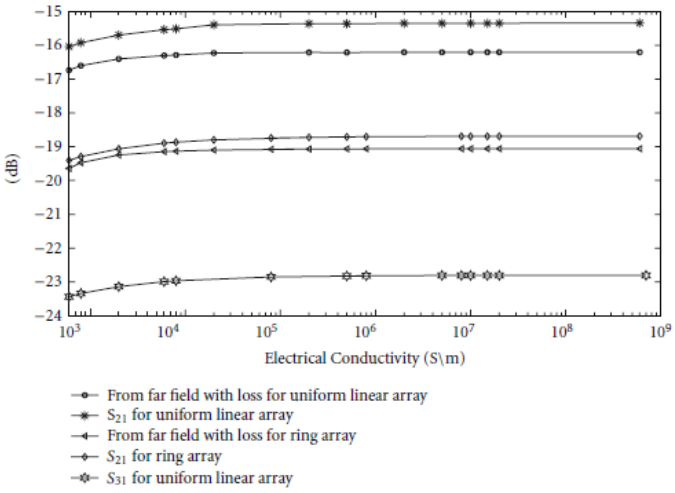

FIGURE 6: The computed spatial envelope correlations and scattering parameters between dipoles 1 and 2 versus their wire electric conductivity, in a MIMO system of three elements, arranged in a uniform linear array and in a ring array.

0.5 dB of the S_{21} values for the uniform linear array and ring array, respectively.

In summary, the analysis described here, based on the conceptual framework summarized in (16), provides a direct and accurate forecast of spatial envelope correlations, as compared with those obtained from the far field data in (1).

5. Conclusion

A direct calculation method has been presented for the spatial envelope correlation between any two antennas in a (N, N) MIMO array using the scattering parameters and intrinsic losses in the radiating structures. This formula should reduce the complexity and effort involved in spatial envelope correlation calculations for practical designs especially where low envelope correlation is required. Three examples have been presented to validate the technique. The results have shown close agreement between this method and the full computation using the far field pattern data. Several practical methods exist, for example, radiometer [20, 21], random field [22], and reverberation chamber [23], for direct measurement of the radiation efficiency of passive

antennas. These can be used for multiport structures and can provide independent checks of the diagonal terms in (12). Such practical implementations of the proposed method will be considered further in future work.

Acknowledgment

The authors would like to thank Pace PLC (Saltaire, West Yorkshire, BD18 3LF) for their financial support of the Knowledge Transfer Partnership (KTP no. 7277).

References

[1] G. J. Foschini and M. J. Gans, "On limits of wireless communications in a fading environment when using multiple antennas," *Wireless Personal Communications*, vol. 6, pp. 311–335, 1998.

[2] R. Janaswamy, "Effect of element mutual coupling on the capacity of fixed length linear arrays," *IEEE Antennas and Wireless Propagation Letters*, vol. 1, pp. 157–160, 2002.

[3] R. G. Vaughan and J. B. Andersen, "Antenna diversity in mobile communications," *IEEE Transactions on Vehicular Technology*, vol. 36, no. 4, pp. 149–172, 1987.

[4] R. G. Vaughan and N. L. Scott, "Closely spaced monopoles for mobile communications," *Radio Science*, vol. 28, no. 6, pp. 1259–1266, 1993.

[5] M. K. Ozdemir, H. Arslan, and E. Arvas, "On the correlation analysis of antennas in adaptive MIMO systems with 3-D multipath scattering," in *Proceedings of the IEEE Wireless Communications and Networking Conference (WCNC '04)*, vol. 1, pp. 295–299, 2004.

[6] T. S. P. See, A. M. L. Swee, and Z. N. Chen, "Correlation analysis of UWB MIMO antenna system configurations," in *Proceedings of the IEEE International Conference on Ultra-Wideband (ICUWB '08)*, pp. 105–108, Hannover, Germany, September 2008.

[7] A. A. H. Azremi, M. Kyro, J. Ilvonen et al., "Five-element in-verted-F antenna array for MIMO communications and radio direction finding on mobile terminal," in *Proceedings of the Loughborough Antennas and Propagation Conference (LAPC '09)*, pp. 557–560, November 2009.

[8] S. S. G. Lebrun and M. Faulkner, "MIMO complexity reduction through antenna selection," *Proceedings of the Australian Telecommunications Cooperative Research Centre*, vol. 5, pp. 1–5, 2003.

[9] H. Zhang, Z. Wang, J. Yu, and J. Huang, "A compact MIMO antenna for wireless communication," *IEEE Antennas and Propagation Magazine*, vol. 50, no. 6, pp. 104–107, 2008.

[10] T. S. P. See and Z. N. Chen, "An ultrawideband diversity antenna," *IEEE Transactions on Antennas and Propagation*, vol. 57, no. 6, pp. 1597–1605, 2009.

[11] A. Derneryd and G. Kristensson, "Signal correlation including antenna coupling," *Electronics Letters*, vol. 40, no. 3, pp. 157–159, 2004.

[12] P. S. H. Leather and D. Parsons, "Antenna diversity for UHF handportable radio," *Electronics Letters*, vol. 39, no. 13, pp. 946–948, 2003.

[13] A. Derneryd and G. Kristensson, "Antenna signal correlation and its relation to the impedance matrix," *Electronics Letters*, vol. 40, no. 7, pp. 401–402, 2004.

[14] S. Blanch, J. Romeu, and I. Corbella, "Exact representation of antenna system diversity performance from input parameter description," *Electronics Letters*, vol. 39, no. 9, pp. 705–707, 2003.

[15] R. H. Clarke, "A statistical theory of mobile reception," *Bell Systems Technical Journal*, vol. 47, pp. 957–1000, 1968.

[16] P. Hallbjörner, "The significance of radiation efficiencies when using S-parameters to calculate the received signal correlation from two antennas," *IEEE Antennas and Wireless Propagation Letters*, vol. 4, no. 1, pp. 97–99, 2005.

[17] J. Thaysen and K. B. Jakobsen, "Envelope correlation in (N,N) mimo antenna array from scattering parameters," *Microwave and Optical Technology Letters*, vol. 48, no. 5, pp. 832–834, 2006.

[18] A. Diallo, P. Le Thuc, C. Luxey et al., "Diversity characterization of optimized two-antenna systems for UMTS handsets," *Eurasip Journal on Wireless Communications and Networking*, vol. 2007, Article ID 37574, 9 pages, 2007.

[19] S. Stein, "On cross coupling in multiple-beam antennas," *IRE Transactions on Antennas and Propagation*, vol. 10, pp. 548–557, 1962.

[20] N. J. McEwan, R. A. Abd-Alhameed, and M. N. Z. Abidin, "A modified radiometric method for measuring antenna radiation efficiency," *IEEE Transactions on Antennas and Propagation*, vol. 51, no. 8, pp. 2099–2105, 2003.

[21] W. L. Schroeder and D. Gapski, "Direct measurement of small antenna radiation efficiency by calorimetric method," *IEEE Transactions on Antennas and Propagation*, vol. 54, no. 9, pp. 2646–2656, 2006.

[22] Q. Chen, H. Yoshioka, K. Igari, and K. Sawaya, "Comparison of experimental methods for measuring radiation efficiency of antennas for portable telephone," in *Proceedings of the IEEE Antennas and Propagation Society International Symposium*, vol. 1, pp. 149–152, June 1998.

[23] K. Rosengren and P.-S. Kildal, "Radiation efficiency, correlation, diversity gain and capacity of a six-monopole antenna array for a MIMO system: theory, simulation and measurement in reverberation chamber," *IEE Proceedings of Microwaves, Antennas and Propagation*, vol. 152, no. 1, pp. 7–16, 2005.

Indoor Channel Measurement and Prediction for 802.11n System

YAS Dama, R. A. Abd-Alhameed, F.Salazar-Quiñonez, SMR Jones and J.G. Gardiner
Mobile and Satellite Communications Research Centre
University of Bradford, Bradford, BD7 1DP, UK,yasdama@bardford.ac.uk, r.a.a.abd@bradford.ac.uk

***Abstract*— Significant improvements in the quality and reliability of indoor WLAN communications are claimed for devices with MIMO technology applying 802.11n standards, that allow users to achieve a theoretical data rate up to 300-600 Mbps on a single transmission. This paper presents an analysis of a commercial 802.11n MIMO 2×3 dual band (2.4 and 5 GHz) system focusing on the operational throughput performance over an indoor environment for Line of Sight (LOS) and Non Line of Sight (NLOS) scenarios. Efforts on combined field strength distribution, throughput, propagation-channel environments, of this system will be elucidated. The work is focusing on the operational performance of the physical measurements and results compared with simulation model over an indoor environment.**

Keywords-component; MIMO, WLAN, IEEE 802.11n, Channel Bonding

I. INTRODUCTION

This work is preliminary to an investigation of the use of 802.11 WLAN devices in multi-hop scenarios [1]. It is envisaged that by employing a distribution coordination function [2-3], to evaluate the channel conditions that determine the data rates and taking into consideration the effect of interference on a basic service set [4] there is a potential to correct the fairness level using dynamic network allocation vectors and forcing handoffs.

Recent studies have evaluated the commercial performance of hot-spot connections using 802.11abg [5] and 802.11e using simulations to identify the quality of the connection through the Medium Access Control (MAC) [6].

In the same context the recent release of the 802.11n standard needs to pass through similar studies for its in-depth evaluation. Researchers in [7], investigated throughput using one transmitted stream to determine how it behaves in the ISM bands in an office environment. Using the same approach and considering the application of commercial wireless devices as was presented in [8], to perform TCP/UDP (Transmission Control/ User Datagram Protcol) throughput analysis, this investigation elucidates the UDP throughput performance versus distance in the indoor environment.

Simulation of the received signal distribution provides valuable information for wireless system applications, in which the propagation models are designed using either statistical or deterministic approaches. Statistical methods present several limitations, including low accuracy in small cell sizes and are not applicable to spatio-temporal channel characterization required for many contemporary wireless systems (OFDM, MIMO, UWB etc.) [9]. Therefore deterministic methods have become the preferred technique for channel propagation simulations. These models can be performed through the application of Maxwell's equation, e.g. using Finite Integration Technique (FIT) or Finite Difference, Time Domain (FDTD) or Shoot and Bounce Ray tracing techniques (SBR). 2D and 3D simulations are usually performed in accurate computational scenarios due to the high number of interactions (multipath) calculated [10].

A 3D FIT approach was applied in [9] to radio propagation calculations over an area of 400 m^2. The modelling geometry was based on a building layout with a specified location of windows, doors and significant metallic furniture through a simulation supported by a single processor computer with computing time less than 3 hours and 400MHz-900MHz frequency range. Results showed that error standard deviation was in the range 2- 3.7 dB which demonstrates a useful level of accuracy for modelling. A similar approach was reported [11] in which the simulation frequencies considered were below 1GHz for compact scenarios providing insufficient reliability at higher frequencies or for greater areas.

Such techniques clearly require a substantial computational effort which provides a substantial limitation in applications where wider areas and higher frequencies are required, making the FIT model unpractical [12], especially in terms of prediction accuracy and spatial detail.

Finite Difference Time Domain (FDTD) methods may be used to compute the electromagnetic response of a variety of arrangements and types of walls in a building. This is done by the discretizing the wall, corners and terminal locations into finite size building blocks and calculating the iterative field over the multiple scattering on the structures. FDTD provides simple programming and simple data base structure; however the excessive running time (55 hours) and memory requirement makes this technique limited. Ray tracing can be used to model the propagation but usually requires complex programming to determine the geometry of the traced rays [13].

II. THROUGHPUT MEASUREMENTS SETUP

The throughput measurement campaign was developed to measure the data rate achievable at different locations on the 3rd floor corridor from Chesham Building B Block at the University of Bradford campus. The measurements were

978-1-4244-8325-9/11/$26.00 ©2011 IEEE

computed by two stationary personal computers (PC), each one connected via ethernet to a commercial 802.11n wireless router having a 1x3 MIMO antenna array, evaluating the throughput obtained from MIMO2 to MIMO1 as shown in Fig. 1, which can operate at different frequencies and bandwidths.

The evaluation of each set of measurements, was performed in compliance with the 802.11n standard [14] over 10m to 50m,

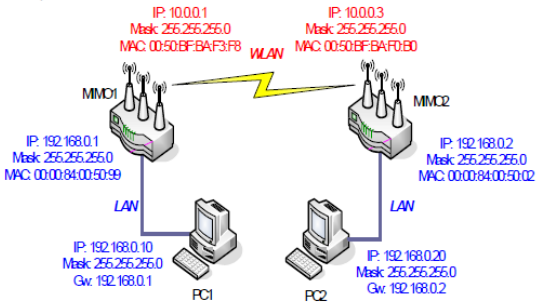

Figure 1. Throughput Measurements

A. *Software Implementation*

The throughput measurements were developed on UDP throughput mode due to the fast evaluation time for each position.

For this section, two different programs were applied to evaluate the throughput: IPERF [10] and IxChariot [11]. IPERF with its graphical interface (JPERF) provides a range of utilities to measure TCP and UDP characteristics and IxChariot is a sophisticated commercial package that enables performance assessment of network applications. Systems Structure

The PCs characteristics included 2 GB RAM memory and a 2.6 GHz single processor, using Windows XP professional operating system. Each PC was connected to a Dlink DAP2553 1x3 MIMO antenna via Ethernet using a Category 6 UTP cable, since it supports up to 10245 Mbps and the maximum throughput theoretically of a 2 stream MIMO systems is 300Mbps. The two antennas were linked together wirelessly in WDS mode. The software was deployed on both systems (PC1 and PC2).

B. *Scenarios*

Two different scenarios were established to evaluate the throughput performance on the MIMO antennas: the Line of Sight (LOS) Scenario, the Non Line of Sight (NLOS) Scenario. In each scenario, the antenna height was always 1m above the floor, for both the mobile (Rx) and the fixed unit (Tx).

The LOS scenario was implemented by installing the Tx antenna in a corridor in such a manner that all the measurement locations from the Rx antenna were able to achieve LOS reception. Five receiver locations were established for this scenario, separated by 10 m from each other in a linear distribution as shown in Fig. 2. The NLOS scenario was implemented by installing the Tx antenna in the corridor in a way that all measurement locations from the Rx antenna were able to achieve a NLOS reception. The same five receiver locations were established for the NLOS scenario as it was for the LOS scenario.

The aim of these scenarios is to evaluate the throughput over the distance in a LOS/NLOS setting for 2.4 and 5.2 GHz frequencies at 20 and 40 MHz bandwidth.

An additional throughput measurement was developed taking advantage of the LOS/NLOS scenarios and the configurable parameters from the antenna diversity analysis.

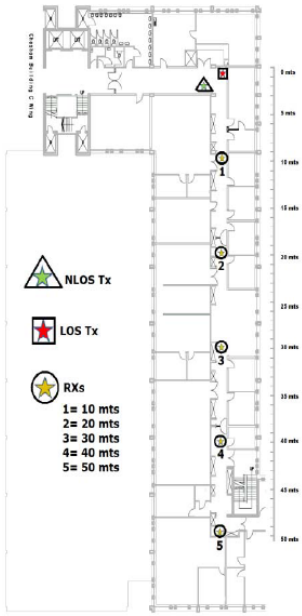

Figure 2. Line of sight Scenario

III. THROUGHPUT MEASUREMENT RESULTS

Each value represented in the following graphs was averaged over 5 measurements per location.

Fig. 3 describes the average (mean) and the maximum (peak) values obtained from the throughput measurements obtained from the LOS scenario at each of the 5 locations. A particular observation on the achievable throughput using 40MHz bandwidth is that at some points it doubles the 20 MHz throughput. In the majority of cases using 40 MHz, 5.2 GHz achieves higher date rates compared with the 2.4 GHz frequency configurations.

Fig. 4 shows the mean and the peak values obtained from the throughput measurements obtained from the NLOS scenario with the system operating at 2.4 and 5.2 GHz frequencies, using 20 and 40 MHz transmission bandwidth at each of the 5 locations. In this scenario there is a noticeable

decrease of throughput as the distance between the Tx and the Rx increases. Still at around 50 meters distance (location 5) the throughput is 90-100 Mbps (5GHz-40MHz), which is considered a very good performance for a NLOS scenario.

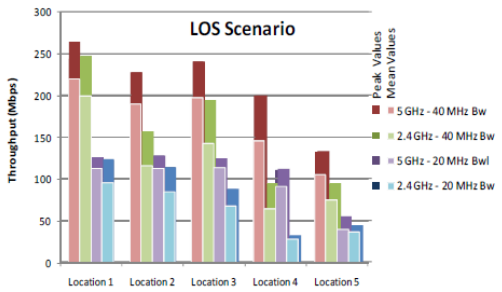

Figure 3. Averaged Throughput over Locations for LOS Scenario

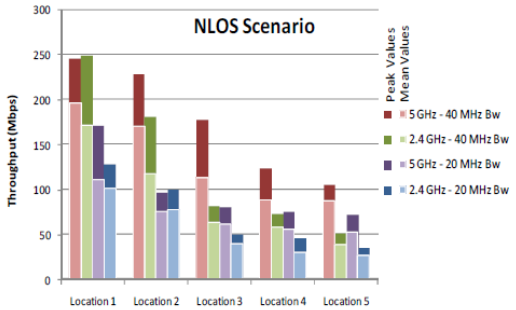

Figure 4. Averaged Throughput over Locations for NLOS Scenario

IV. SIMULATION MODEL

The simulation was performed through the 3D Shoot and Bounce Ray (3D SBR) technique, using 0.2° ray spacing, 7 reflections, 2 transmissions and 0 diffractions, which allowed evaluation of the paths launched from the transmitter. Following the basic multipath mechanisms (reflection, diffraction, transmission and scattering), it was possible to determine the rays reached by the receiver and therefore to calculate the path loss. Applying the image method approach the ray tracing technique captures precisely the large structure. The 2D and 3D simulations are performed in computational scenarios for accuracy due to the high number of multipaths calculated [10]. The Wireless InSite model included the configuration of specific parameters for its complete simulation: waveform, antenna, transmitter, receiver, model, materials and output.

The construction of the model was corroborated by the corridor layout used for the physical measurement. The model therefore has the same dimensions as the building corridor corresponding to 64 x 26 x 3 meters. The model was successfully completed by detailed modeling as shown in Fig. 5, establishing two types of walls: 20 cm thick and 12 cm thick (block material) according to the floor layout seen in table 1.

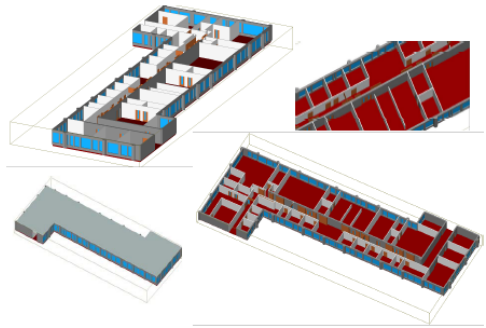

Figure 5. 3D Indoor Environment Model.

TABLE I
WALL TYPES FOR INDOOR DATABASE

Type	Layer Thickness
Wall	12cm - Block
Wall	20cm - Block
Door	6cm - Wood
Window	1cm - Glass

Two types of doors were identified, wood doors and crystal doors, the latter having two sub classifications: 2 glass crystal door and the 4 glass crystal door. The floor and the ceiling, 3m above the floor, were defined as block material. A second ceiling was simulated, 2.5m above the floor, acting as the foam ceiling tiles with 3cm thick of a soft dielectric material.

V. RSSI MEASURMENT AND SIMULATION RESULTS

The first measurement campaign was developed to evaluate the field distribution strength using a laptop and the MIMO 2×3 system along the corridor of Chesham Building section B, 3rd Floor, at the University of Bradford.

The physical model was performed in a layout with the total corridor space divided into $1m^2$ sections obtaining a total of 90 locations. Each section was evaluated for 5 Received Signal Strength Indicator (RSSI) values over two frequencies (2.4 and 5 GHz) using the 802.11n standard at 20 MHz bandwidth.

The 3D RSSI Scenario comprised of 90 receiver locations was divided into the Rx Route (69 locations), and the Rx Grid (21 locations) for practical analysis. The Rx Route is a route of receiver locations along the entire corridor; every single one with the same characteristics. The Rx Route has a part of LOS and NLOS receivers. The Rx Grid is a 7x3 Grid of receiver locations set in LOS as shown in Fig. 6.

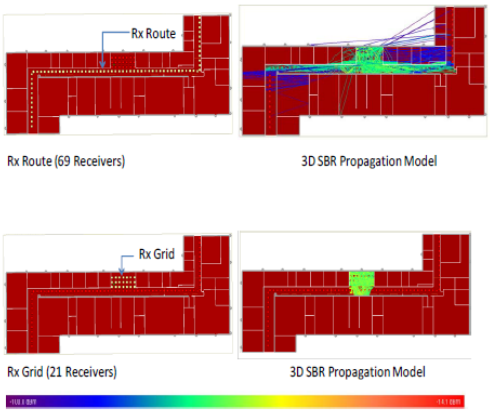

Figure 6. 3D RSSI Scenario Simulated Results.

Fig. 7 shows the field strength distribution obtained from RSSI measurements campaign along the corridor. The graph shows 13 scales from -9 to -100 dBm values, each scale using a 6.9 dBm range. The distribution was implemented for 2.4 and 5 GHz measurements. Both distributions show that in 5.2 GHz configuration, the signal strength is distributed over a less coverage area compared with 2.4 GHz, but achieving a higher intensity over closer areas.

Figure 7. RSSI Measurement Results for 2.4GHz and 5GHz.

Two simulations were averaged to analyze the propagation behaviour, the graphs in Fig. 8 show the comparison of the received signal strength measured per receiver location and the simulation of the 3D RSSI Scenario results. The simulated results are an average of the received signal of the maximum and minimum transmission power of the antennas. These are at 2.4 was from 17 to 11 dBm, and 5 GHz from 18 to 9 dBm, confirming the similarity of the values simulated.

Measured and simulated results were analyzed statistically concluding in a correlation between their signals of 86% at 2.4 GHz and 96% at 5 GHz. The total correlation of the physical and simulated model was of 92%. This indicates that the approximation from the simulation to the real world measurements were statistically similar.

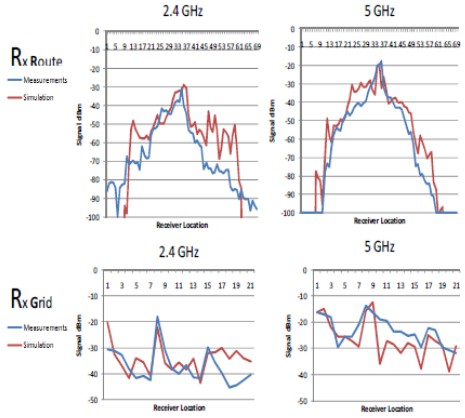

Figure 8. Measurements and Simulation Results Comparison

VI. CONCLUSIONS

The analysis of throughput values obtained from Line of Sight and Non-Line of Sight scenarios provide an experimental insight into the performance of MIMO systems deployed using the 802.11n standard in a typical multi-storey office building, reaching 250 and 296 Mbps for NLOS and LOS respectively (for 10 m distance). The achievable bit rate for a MIMO system is much more reliable when compared to a SISO connection. Furthermore the 802.11n channel bonding option provides remarkable throughput increase, compared with 802.11a/b/g.

The Implementation of a simulated propagation model using 3D SBR provides a good estimation of the channel propagation without demanding an extraordinary computational effort. Th investigation found a high correlation for 2.4 GHz and 5.2 GHz frequencies (86% and 96% respectively) between measured and simulated data . By modelling a MIMO system in an indoor environment, it was possible to determine the signal strength distribution and its achievable throughput for different locations. Despite the accuracy of the results obtained in this investigation, the modelling process remains rather complex, which might limit its applicability in future work.

REFERENCES

[1] S. H. Shah and K. Nahrstedt, "Guaranteeing throughput for real-time traffic in multi-hop IEEE 802.11 wireless networks," in

Military Communications Conference, 2005. MILCOM 2005. IEEE, 2005, pp. 371-377 Vol. 1.

[2] M. Laddomada, *et al.*, "On the throughput performance of multirate IEEE 802.11 networks with variable-loaded stations: analysis, modeling, and a novel proportional fairness criterion," *Wireless Communications, IEEE Transactions on,* vol. 9, pp. 1594-1607, 2010.

[3] W. Chiapin, *et al.*, "On Throughput Performance of Channel Inequality in IEEE 802.11 WLANs," *Wireless Communications, IEEE Transactions on,* vol. 7, pp. 4425-4431, 2008.

[4] Z. Dongmei, "Throughput Fairness in Infrastructure-Based IEEE 802.11 Mesh Networks," *Vehicular Technology, IEEE Transactions on,* vol. 56, pp. 3210-3219, 2007.

[5] C. Na, *et al.*, "Measured Traffic Statistics and Throughput of IEEE 802.11b Public WLAN Hotspots with Three Different Applications," *Wireless Communications, IEEE Transactions on,* vol. 5, pp. 3296-3305, 2006.

[6] J. del Prado Pavon and S. N. Shankar, "Impact of frame size, number of stations and mobility on the throughput performance of IEEE 802.11e," in *Wireless Communications and Networking Conference, 2004. WCNC. 2004 IEEE*, 2004, pp. 789-795 Vol.2.

[7] S. Fiehe, *et al.*, "Experimental study on performance of IEEE 802.11n and impact of interferers on the 2.4 GHz ISM band," presented at the Proceedings of the 6th International Wireless Communications and Mobile Computing Conference, Caen, France, 2010.

[8] V. Visoottiviseth, *et al.*, "An empirical study on achievable throughputs of IEEE 802.11n devices," in *Modeling and Optimization in Mobile, Ad Hoc, and Wireless Networks, 2009. WiOPT 2009. 7th International Symposium on*, 2009, pp. 1-6.

[9] P. N. Zakharov, *et al.*, "Finite Integration Technique capabilities for indoor propagation prediction," in *Antennas & Propagation Conference, 2009. LAPC 2009. Loughborough*, 2009, pp. 369-372.

[10] P. Pajusco, "Propagation channel models for mobile communication," *Comptes Rendus Physique,* vol. 7, pp. 703-714, 2006.

[11] M. Thiel and K. Sarabandi, "A Hybrid Method for Indoor Wave Propagation Modeling," *Antennas and Propagation, IEEE Transactions on,* vol. 56, pp. 2703-2709, 2008.

[12] P. N. Zakharov, *et al.*, "Comparative Analysis of Ray tracing, finite integration technique and empirical models using ultra-detailed indoor environment model and measurements," in *Microwave, Antenna, Propagation and EMC Technologies for Wireless Communications, 2009 3rd IEEE International Symposium on*, 2009, pp. 169-176.

[13] L. Nagy, "Short Range Device (SRD) propagation modeling for Indoor environment," in *Mobile and Wireless Communications Summit, 2007. 16th IST*, 2007, pp. 1-5.

[14] IEEE. (2010, August). *802.11n, http://standards.ieee.org/getieee802/download/802.11n-2009.pdf.*

International Journal on Communications Antenna and Propagation (I.Re.C.A.P.), Vol. 2, N. 1
February 2012

An Exact Envelope Correlation Formula for Two-Antenna Systems Using Input Scattering Parameters and Including Power Losses

Y.A.S Dama[1], R.A.Abd-Alhameed[1], S.M.R Jones[1] J.M. Noras[1] and N.T.Ali[2]

Abstract – *The calculation of the envelope correlation for a two antenna element system in terms of the system's scattering parameters is modified to include power losses. This new expression should reduce the complexity in predicting the spatial envelope correlation, and simplify antenna design where a low envelope correlation is required. This represents a major simplification with respect to the conventional use of the radiation field patterns of the antennas. The accuracy of the technique is illustrated by two examples.* ***Copyright © 2010 Praise Worthy Prize S.r.l. - All rights reserved.***

Keywords: *Antenna Diversity, Radiation Power, Envelope Correlation, Scattering Parameters*

Nomenclature

ρ_e Spatial envelope correlation.
$d\Omega$ Differential spherical area.
$F_\theta(\theta,\phi)$ Radiation field in $\hat{e}_\theta$ direction.
$F_\phi(\theta,\phi)$ Radiation field in $\hat{e}_\phi$ direction.
MIMO Multiple Input Multiple Output.
P_{total} Total power.
P_{rad} Radiated power.
P_{loss} Power loss .
† Hermitian transpose.
a Incident wave .
b Reflected wave .
$Js(\theta,l)$ Surface current density distribution .
J_{Si} The total currents on structures on the ith antenna structures.
a_i The incident wave on the ith antenna structures.
J_{S1}^1, J_{S1}^2 The normalised currents on structures 1 and 2 due to the incident wave a_1.
J_{S2}^1 and J_{S2}^2 The normalised currents on structures 1 and 2 due to the incident wave a_2.
P_{li} The power loss on the ith antenna structures.
L The losses matrix.
R Is 2x2 radiation matrix.
D_i The maximum directivity of the ith antenna.
D_i A lambed resistive element.
λ The wavelength.
σ Surface conductivity.

I. Introduction

Mobile communication systems where there is only one antenna at both the transmitter and the receiver are known as Single Input Single Output (SISO) systems. SISO system capacity is limited by the Shannon Nyquist criterion [1]. In order to increase the capacity of SISO systems to meet the high bit rate transmissions demanded by modern mobile communications, the bandwidth and/or the power have to increase significantly.

Fortunately, using MIMO systems (Multiple Input, Multiple Output) has the potential to increase the capacity of the wireless system without the need to increase the transmission power or the bandwidth [2]. On the other hand, mutual coupling between the antennas degrades the diversity performance of an antenna system; therefore designers try to minimize the mutual coupling of the antenna system whilst maintaining the matching requirements.

MIMO systems are required to deliver maximum capacity with minimum bit error rate (BER). They can exploit diversity, spatial multiplexing or beam forming and steering techniques, including null steering for interference rejection. Diversity gain requires independent or complementary fading at each antenna element and optimum spacing will depend on the angle of arrival spectrum in the multipath channel. Other techniques will benefit from an array radiation pattern that has high gain, a narrow beamwidth and low side or grating lobes in order to be able to resolve paths that are closely spaced in angle.

But it is challenging to implement multiple antennas in a very small volume such as mobile handsets, PDA's and laptops; therefore the spatial correlation properties of different antenna elements in the array should be considered since this will affect the MIMO channel capacity.

Manuscript received and revised January 2012, accepted February 2012

In mobile communication the antenna spacing is usually small, thus the impact of the mutual coupling will be not negligible. Mutual coupling increases the spatial correlation between the array elements. Also, it deforms the radiation pattern of each array element, which affects the diversity gain.

A generalized analysis of signal correlation between any two array elements including non-identical elements and arbitrary load termination of passive antenna ports was presented in [3]. The method is related to the power balance concept and is based on the antenna impedance matrix. In [5] theoretical and simulation studies have been conducted to explain the experimentally observed effect that the correlation between signals of closely spaced antennas is smaller than that predicted using the well known theoretical methods. A simple expression to compute the correlation coefficients from the far field pattern including the propagation environment characteristics and the terminating impedance was introduced in [5].

Three different methods are used to calculate the antenna correlation. The first method is based on the far field pattern [6], the second is based on the scattering parameters at the antennas terminals [7] and the third method is based on Clarke's formula [8]. Calculating correlation using the radiation field pattern of the antenna system is a time consuming method, whether it is done by simulation or using experimental data.

A simple method for the computation of the envelope correlation for two antenna elements using scattering parameters was presented in [7]. This method avoids intensive computations using the radiation field patterns of the antenna system, and may be straightforwardly generalized to the envelope correlation of an N-antenna system [9]. This formulation has been widely adopted in discussing antenna diversity issues [10, 11]. However, the computations in [7] and [9] do not include the power losses in the antenna structures. This accounts for the discrepancy between the envelope correlation results obtained by this method, from that computed directly from the radiation field patterns of the two antenna elements [12]:

$$\rho_e = \frac{\left| \iint_{4\pi} d\Omega F_1(\theta,\phi).d\Omega F_2(\theta,\phi) \right|^2}{\iint_{4\pi} d\Omega \left|F_1(\theta,\phi)\right|^2 \iint_{4\pi} d\Omega \left|F_2(\theta,\phi)\right|^2} \qquad (1)$$

where $F_i(\theta,\phi) = F_\theta^i(\theta,\phi)\hat{e}_\theta + F_\phi^i(\theta,\phi)\hat{e}_\phi$ is the radiation field of the ith antenna.

In practice it is required to identify envelope correlation between any two sensors in a given array. The correlation is sensitive to the intrinsic power losses in the radiating elements; the methodologies reported in [7] and [9] are based on ideal passive structures, i.e. without losses. Hallbjorner has presented a useful analysis on the effect of antenna efficiency on spatial correlation estimates [12]. The analysis presented below provides an operational method, with a clear physical basis, for explicitly incorporating the intrinsic (Ohmic) losses into the estimation of the spatial correlation, using the scattering representation for a multi-beam array [13].

The calculation of the envelope correlation for a (NxN) MIMO antenna array in terms of the system's scattering parameters is modified to include power losses [14]. This represents a major simplification with respect to the conventional use of the radiation field patterns of the antennas.

In this paper, a simplified calculation of the envelope correlation in (1) for a lossy two antenna system was intensively evaluated in terms of the scattering parameters and the intrinsic power losses of the antenna structures. The power loss is presented in a matrix formulation, in order to match the presentation in [7,9,14,15]. Two new illustrative examples are presented and discussed to show the contribution of the proposed method. .

I. Format of Manuscript

Consider the electromagnetic geometry suggested by Figure 1, the total power is given by:

$$P_{total} = P_{rad} + P_{loss} \qquad (2)$$

where P_{rad} and P_{loss} are the total radiated and loss power respectively; P_{tot} is sometimes called the accepted power, and may be computed in terms of the incident waves by $\left(a^\dagger a - b^\dagger b\right)$, where † denotes the Hermitian transpose.

The analysis developed below and the subsequent case studies shown in Figure 2, have been presented for convenience in a wire antenna formulation and the solved using NEC. It should be understood that the underlying concepts are fully general, and can be readily rewritten in terms of general surface and volume currents.

The surface current density distributed on a radiating wire of radius r can be written as;

$$Js(\theta,l) = \frac{J_s(\theta,l)}{2\pi r} a_l \approx \frac{J_s(l)}{2\pi r} a_l \qquad (3)$$

The power loss may be computed in terms of the surface currents on the antenna structures as follows. These currents may be expressed in terms of the incident waves a_1 and a_2:

$$J_{S1} = \frac{1}{\sqrt{R_S}} \left(a_1 \cdot \frac{J_{S1}^1(l)}{2\pi r} \hat{a}_l + a_2 \cdot \frac{J_{S1}^2(l)}{2\pi r} \hat{a}_l \right) \qquad (4)$$

$$J_{S2} = \frac{1}{\sqrt{R_S}} \left(a_1 \cdot \frac{J_{S2}^1(l)}{2\pi r} \hat{a}_l + a_2 \cdot \frac{J_{S2}^2(l)}{2\pi r} \hat{a}_l \right) \qquad (5)$$

Manuscript received and revised January 2012, accepted February 2012

J_{S1} and J_{S2} are the total currents on structures 1 and 2, respectively, J_{S1}^{1} and J_{S1}^{2} are the normalised currents on structures 1 and 2 due to the incident wave a_1, similarly J_{S2}^{1} and J_{S2}^{2} are due to the incident wave a_2, R_S is the surface impedance of the antennas. Thus, the power loss on structures 1 and 2 can be expressed by (6) and (7), respectively:

$$P_{l1} = \iint \left(a_1 J_{S1}^{1}(l) + a_2 J_{S1}^{2}(l)\right) \cdot \left(a_1 J_{S1}^{1}(l) + a_2 J_{S1}^{2}(l)\right)^{*} d\theta dl \quad (6)$$

$$P_{l2} = \iint \left(a_1 J_{S2}^{1}(l) + a_2 J_{S2}^{2}(l)\right) \cdot \left(a_1 J_{S2}^{1}(l) + a_2 J_{S2}^{2}(l)\right)^{*} d\theta dl \quad (7)$$

Expanding these expressions gives,

$$P_{l1} = \frac{1}{2\pi}\int |a_1|^2 J_{S1}^{1}(l) J_{S1}^{1*}(l) + a_1 a_2^{*} J_{S1}^{1}(l) J_{S1}^{2*}(l) + .. \quad (8)$$
$$...a_2 a_1^{*} J_{S1}^{2}(l) J_{S1}^{2*}(l) + |a_2|^2 J_{S1}^{2}(l) J_{S1}^{2*}(l) dl$$

$$P_{l2} = \frac{1}{2\pi}\int |a_1|^2 J_{S2}^{1}(l) J_{S2}^{1*}(l) + a_1 a_2^{*} J_{S2}^{1}(l) J_{S2}^{2*}(l) + .. \quad (9)$$
$$...a_2 a_1^{*} J_{S2}^{2}(l) J_{S2}^{2*}(l) + |a_2|^2 J_{S2}^{2}(l) J_{S2}^{2*}(l) dl$$

Hence, (8) and (9) can be expressed in the matrix notation as,

$$P_{loss} = (a, La) = \left(a^{\dagger} La\right) \quad (10)$$

where,

$$L = L' + L'' = \begin{pmatrix} L'_{11} & L'_{12} \\ L'_{21} & L'_{22} \end{pmatrix} + \begin{pmatrix} L''_{11} & L''_{12} \\ L''_{21} & L''_{22} \end{pmatrix} \quad (11)$$

The elements L'_{ij} may be read across as,

$$\begin{pmatrix} \frac{1}{2\pi}\int J_{S1}^{1}(l) J_{S1}^{1*}(l) dl & \frac{1}{2\pi}\int J_{S1}^{1}(l) J_{S1}^{2*}(l) dl \\ \frac{1}{2\pi}\int J_{S1}^{2}(l) J_{S1}^{2*}(l) dl & \frac{1}{2\pi}\int J_{S1}^{2}(l) J_{S1}^{2*}(l) dl \end{pmatrix} \quad (12)$$

and similarly for L''_{ij}. From the properties of the Hermitian inner product, it follows that $L_{ij} = L_{ij}^{*}$.

Equation (2) can now be expressed in terms of the incident waves a_1 and a_2.

$$a^{\dagger}\left(1 - S^{\dagger} S\right) a = \left(a^{\dagger} La\right) + \left(a^{\dagger} Ra\right) \quad (13)$$

where the scattering matrix S of the two-antenna system, includes the power loss. R is the 2×2 matrix defined in [7] as,

$$R = \begin{pmatrix} \frac{D_1}{4\pi}\iint_{4\pi} d\Omega |F_1(\theta,\phi)|^2 & \frac{\sqrt{D_1 D_2}}{4\pi}\iint_{4\pi} d\Omega F_1(\theta,\phi) \cdot F_2^{*}(\theta,\phi) \\ \frac{\sqrt{D_2 D_1}}{4\pi}\iint_{4\pi} d\Omega F_2(\theta,\phi) \cdot F_1^{*}(\theta,\phi) & \frac{D_2}{4\pi}\iint_{4\pi} d\Omega |F_2(\theta,\phi)|^2 \end{pmatrix} \quad (14)$$

Where D_i is the maximum directivity of the ith antenna. Therefore, from (13) the equivalent elements of (14) can be expressed as follows:

$$\frac{D_1}{4\pi}\iint_{4\pi} d\Omega |F_1(\theta,\phi)|^2 = 1 - \left(1 - |S_{11}|^2 + |S_{21}|^2\right) - \left(L'_{11} + L''_{11}\right) \quad (15)$$

$$\frac{\sqrt{D_1 D_2}}{4\pi}\iint d\Omega F_1(\theta,\phi) \cdot F_2(\theta,\phi) = -\left(S_{11}^{*} S_{21} + S_{21}^{*} S_{22}\right) \quad (16)$$
$$\ldots\ldots\ldots\ldots\ldots\ldots\ldots\ldots\ldots\ldots\ldots\ldots\ldots\ldots\ldots\ldots\ldots\ldots - \left(L'_{12} + L''_{12}\right)$$

Thus, the envelope correlation for the two-antenna system geometry (Fig. 1) can be expressed in terms of the scattering parameters, and the intrinsic power losses, as in (17).

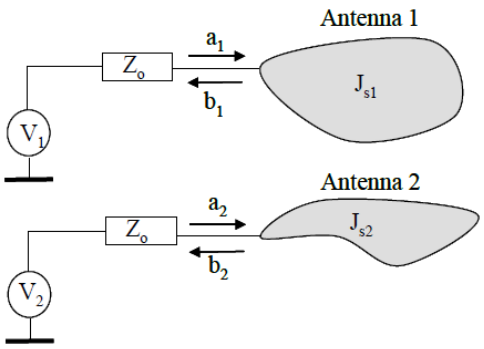

Fig. 1. Basic geometry for two antenna element system.

II. Simulation and Results

In order to verify (17), the envelope correlation has been computed for two parallel half-wavelength wire dipoles in free space, as a function of their separation. The antenna far fields and scattering parameters were obtained using NEC [8]. The wire radius of each dipole was set at 0.002 wavelengths.

Two different sources of loss were considered for the purpose of validation. In the first instance, both dipoles were loaded by two lumped resistive loads, each of 25Ω, as in Fig. 2. Secondly, the dipoles were loaded by surface conductivity along the antenna geometry.

Manuscript received and revised January 2012, accepted February 2012

$$\rho_e = \frac{\left|1-\left(S_{11}^{*}S_{12}+S_{21}^{*}S_{22}\right)-\left(L_{12}^{'}+L_{12}^{''}\right)\right|^2}{\left\{1-\left(\left|S_{11}\right|^2+\left|S_{21}\right|^2\right)-\left(L_{11}^{'}+L_{11}^{''}\right)\right\}\left\{1-\left(\left|S_{22}\right|^2+\left|S_{12}\right|^2\right)-\left(L_{22}^{'}+L_{22}^{''}\right)\right\}} \quad (17)$$

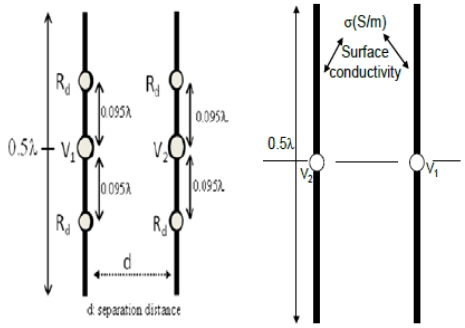

Fig. 2. Examples under test; (left: antennas loaded by lumped resistive loads, right: antennas loaded by surface conductivity)

Variations between the proposed method and the lossless approach were checked by simulation. The spatial envelope correlation calculated using the far field parameters, versus the dipole separation distance, are given in Fig. 3 for both lossless and lossy cases. There is good agreement between the proposed method and the results calculated from (1) for the lossy case. The envelope correlation for dipole separations less than 0.5 wavelengths can take values bigger than the achieved S_{21} values. It is also interesting to note that the nulls of the envelope correlation are shifted compared with those obtained for the lossless approach.

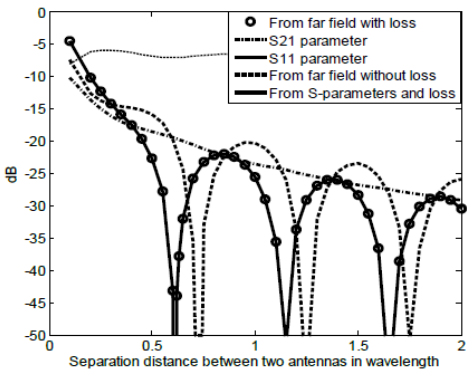

Fig. 3. Computed spatial envelope correlations and S-parameters for two half wavelength dipoles against their separated distance.

Figures 4 and 5 illustrate variations in the spatial envelope correlation, versus the lumped resistive loads, and surface conductivities, respectively.

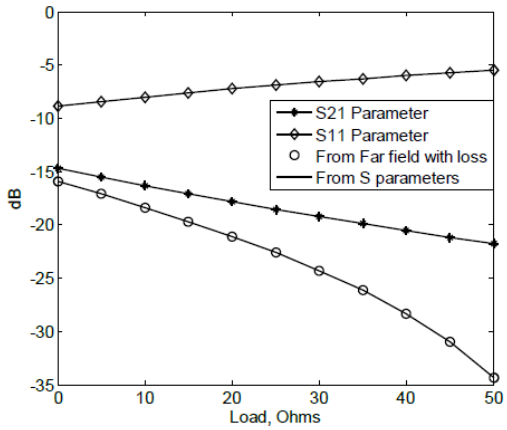

Fig. 4. Envelope correlation and S-parameters for two half wavelength dipoles against the lumped resistive loads shown in Fig. 2.

The dipole separation was kept constant at 0.5 wavelengths. These envelope correlation results prove the concept of the proposed method, i.e. equation (17), against those obtained from the far field patterns. It can be seen in fig. 4 that the envelope correlation values closely approach the S_{21} values as the load is reduced. For the surface conductivity case, they are much closer for small wire conductivity values.

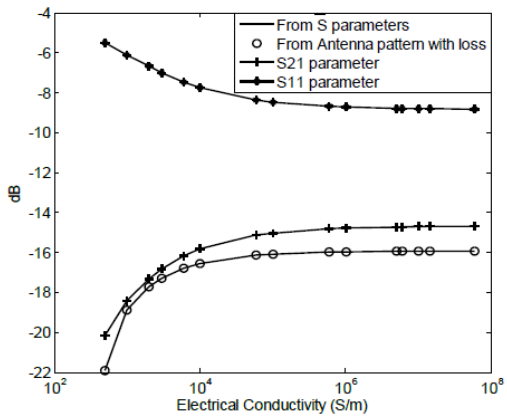

Fig.5. Envelope correlation and S-parameters for two half wavelength dipoles against the surface electric conductivity on both dipoles.

In summary, the analysis described here, based on the conceptual framework assumed by equation (17), provides a direct and accurate forecast of spatial

Manuscript received and revised January 2012, accepted February 2012

envelope correlation, as compared with the far field analysis in equation (1).

It should be noted that several empirical approaches exist for the direct measurement of the radiation efficiency of passive antennas. These include radiometry [17, 18], random field analysis [19] and reverberation chamber techniques [20], and when applied to multi-port passive structures they can provide an independent check on the diagonal terms in the L-matrix (i.e. equation (11)). Such practical implementations will be considered for future developments of this work.

III. Conclusions

A method of calculation, for the spatial envelope correlation of a two-antenna system, which includes losses, using the system scattering parameters has been presented. This new expression should reduce the complexity in predicting the spatial envelope correlation, and simplify antenna design where a low envelope correlation is required. Two validation examples were presented, which demonstrate good agreement between the proposed method, and the explicit calculation using far field pattern data. Two examples have been presented to validate the technique. The results have shown close agreement between the proposed method and the full computation using the far field pattern data.

Practical implementations for the direct measurement of the radiation efficiency of passive antennas will be the challenge for the future work.

Acknowledgment

The authors would like to thank Pace PLC (Saltaire, West Yorkshire, BD18 3LF) for their financial support of the Knowledge Transfer Partnership (KTP No: 7277).

References

[1] G. J. Foschini and M. J. Gans, On Limits of Wireless Communications in a Fading Environment when UsingMultiple Antennas, Wirel. Pers. Commun., vol. 6, pp. 311-335, 1998.

[2] J.G. Proakis, Digital Communications New York: McGraw-Hill, 1989.

[3] A. Derneryd and G. Kristensson. Antenna signal correlation and its relation to impedance matrix, Electronics Letter, Vol. 40, No.7, 1st April 2004.

[4] P. S. H Leather and D. Parsons. Antenna diversity for UHF handportable radio, Electronics Letters, Vol.39, No. 13, 26th June 2003

[5] A. Derneryd and G. Kristensson. Signal correlation including antenna coupling, Electronics letters, Vol.40, No.3, 5th February 2004.

[6] G. Lebru, S. Spiteri, and M. Falkner. MIMO complexity reduction through antenna selection, Proc Australian Telecomm Cooperative Res. Center, ANNAC 03,2002, P.5.

[7] S. Blanch, J. Romeu and I. Corbella, Exact representation of antennas system diversity performance from input parameter description, Electronics Letters, vol. 39, No. 9, 1st May 2003, pp. 705-707.

[8] R.H.Clarke. A statistical theory of mobile reception, Bell system Tech, 1968, 957-1000.

[9] J. Thaysen, and K. B. Jakobsen, Envelope correlation in (N, N) MIMO antenna array from scattering parameters, Microwave and Optical Technology Letters, Vol. 48, No. 5, May 2006, pp. 832-834.

[10] H. L. Zhang, Z. H. Wang, J. W. Yu, and J. Huang, A Compact MIMO Antenna for Wireless Communication, IEEE Antennas and Propagation Magazine, vol. 50, No. 6, Dec. 2008, pp. 104-107.

[11] T. S. P. See and Z. N. Chen, An Ultrawideband Diversity Antenna, IEEE Trans on Antennas and Propagation, vol. 57, No. 6, June 2009, pp. 1957-1605.

[12] P. Hallbjorner, The significance of radiation efficiencies when using S-parameters to calculate the received signal correlation from two antennas, Antennas and Wireless Propagation Letters, IEEE, vol. 4, pp. 97-99, 2005.

[13] S. Stein, On cross coupling in multiple-beam antennas, Antennas and Propagation, IRE Transactions on, vol. 10, pp. 548-557, 1962.

[14] R.G. Vaughan and J.B. Andersen, Antenna diversity in mobile communications, IEEE Trans Veh. Technology, 36, 1987, pp. 149-172.

[15] Y. A. S. Dama, R. A. Abd-Alhameed, S. M. R. Jones, et al., An Envelope Correlation Formula for (N,N) MIMO Antenna Arrays Using Input Scattering Parameters, and Including Power Losses, International Journal of Antennas and Propagation, vol. 2011, Article ID 421691, 7 pages, 2011. doi:10.1155/2011/421691.

[16] Y. A. S. Dama, R. A. Abd-Alhameed, D. Zhou, S. M. R. Jones, M. B. Child, and P. S. Excell, Calculation of the spatial envelope correlation between two antennas in terms of the system scattering parameters including conducting losses, in Antennas and Propagation Conference (LAPC), 2010 Loughborough, 2010, pp. 513-516

[17] G.L. Burke and A.J. Poggio, Numerical Electromagnetics Code (NEC)-Method of Moments, Lawrence Livermore Laboratory, Livermore, CA, 1981.

[18] N. J. McEwan, R. A. Abd-Alhameed, and M. N. Z. Abidin, A modified radiometric method for measuring antenna radiation efficiency, Antennas and Propagation, IEEE Transactions on, vol. 51, pp. 2099-2105, 2003.

[19] W.L. Schroeder and D. Gapski, Direct measurement of small antenna radiation efficiency by a calorimetric method, IEEE Transactions on Antennas and Propagation, 54, 9, 2646-2656, 2006.

[20] C. Qiang, H. Yoshioka, K. Igari, and K. Sawaya, Comparison of experimental methods for measuring radiation efficiency of antennas for portable telephones, in Antennas and Propagation Society International Symposium, 1998. IEEE, 1998, vol.1, pp. 149-152

[21] K. Rosengren and P. S. Kildal, Radiation efficiency, correlation, diversity gain and capacity of a six-monopole antenna array for a MIMO system: theory, simulation and measurement in reverberation chamber, Microwaves, Antennas and Propagation, IEE Proceedings -, vol. 152, pp. 7-16, 2005.

Authors' information

[1]Mobile and Satellite Communications Research Centre, University of Bradford, Bradford, West Yorkshire, BD7 1DP, UK

[2]Khalifa University, Sharjah, P.O.Box 573, UAE

Yousef Dama received B.S. degree in electrical engineering from An-Najah national University, Palestine, in 2005 and M.S.c degree in personal mobile and satellite communications from University of Bradford, UK, in 2006. He has been a research student with the Mobile and Satellite communications research centre since 2009 where he is currently working toward Ph.D degree, he contributed to several

Manuscript received and revised January 2012, accepted February 2012

referred conference papers and academic journals. His research focus includes OFDM, MIMO, Space Time Coding, mutual coupling and channel propagation.
Mr. Dama has been a member of the Jordanian engineering association since 2005.

Prof. Raed Abd-Alhameed is a Professor of Electromagnetic and Radio Frequency (RF) Engineering in the School of Engineering, Design and Technology at the University of Bradford, UK. He has over 20 years' research experience in RF designs, antennas and electromagnetic computational techniques and has published over 400 academic journals and referred conference papers. In particular his work has produced highly realistic analysis of RF and antennas design processes in the presence of large multi-layer scatterers, using the Bradford developed hybrid modeling techniques. He has led an EPSRC funded project "Multi-Band Balanced Antennas with Enhanced Stability and Performance for Mobile Handsets" and is also involved with several funded projects including nonlinear demodulation in biological tissue and assessment of effects of cellular phones on the nervous system. In addition, he has managed four KTP projects that focused on advanced RF and antenna designs and so has experience in working closely with industry. He is the chair of several successful workshops on Energy Efficient and Reconfigurable Transceivers (EERT): Approach towards Energy Conservation and CO_2 Reduction that addresses the biggest challenges for the future wireless systems. His current research interests include hybrid electromagnetic computational techniques, EMC, antenna design, low SAR antennas for mobile handset, bioelectromagnetics, RF mixers, active antennas, beam steering antennas, MIMO antennas, Energy efficient PAs, RF predistorter design including biological cell modelling for breast cancer applications. He is the Fellow of the Institution of Engineering and Technology, Fellow of Higher Education Academy and a Chartered Engineer.

Steve Jones is a lecturer in Telecommunications and is Director of Studies for programmes in Electronics and Telecommunications in the School of Engineering, Design and Technology at the University of Bradford. Since joining the University in 1987, he has worked on a wide variety of projects in the area of satellite slant-path propagation (e.g. 10 GHz bistatic-scatter, 11/14 GHz scintillation and ice depolarization with Olympus) and mobile radio propagation (notably Mobile VCE and TEAMS projects). He served as an Associate Editor for the IEEE Transactions on Antennas and Propagation 2004-8. Recently, he has worked on multiple-antenna technologies, signal processing and propagation modelling for broadband wireless access systems.

Dr. James M Noras is a Senior Lecturer in the School of Engineering, Design and Technology at the University of Bradford, UK. He has published 50 journal papers and 85 conference papers, in fundamental semiconductor Physics, analogue and digital circuit design, digital signal processing and RF system design and evaluation. He is the director of five internationally franchised BEng and MSc Courses in Electrical and Electronic Engineering, has successfully supervised 18 PhD students, and is currently supervising the research of 3 PhD students. His main research interests are now in digital system design and implementation, DSP and coding for communication systems, and localisation algorithms for mobile systems. He is a Member of the Institute of Physics and a Chartered Physicist.

Dr Nazar T Ali is an associate professor in the department of electronics at Khalifa University in the United Arab Emirates. He received his BSc degree in electrical and electronic engineering from the University of Mosul, Iraq, in 1984, and his PhD degree in the characterization and modeling of opto-electronic devices from the University of Bradford, UK, in 1990. He worked on many projects related to industry including UK-DTI and EPSRC funded projects. He has about 70 journals and refereed international conferences. His current research interests include design of analog CMOS integrated circuits, MIMO and various antenna structures and linearity problems associated with OFDM-based systems.

anuscript received and revised January 2012, accepted February 2012